

Dissertation zur Erlangung des Doktorgrades
der Fakultät für Chemie und Pharmazie
der Ludwig-Maximilians-Universität München

**Nitridoberyllates and
Nitridoberylloaluminates
for Solid-State Lighting**

Eugenia Elzer

aus

Kustanaj, Kasachstan

2022

Erklärung

Diese Dissertation wurde im Sinne von §7 der Promotionsordnung vom 28. November 2011 von Herrn Prof. Dr. Wolfgang Schnick betreut.

Eidesstattliche Versicherung

Diese Dissertation wurde eigenständig und ohne unerlaubte Hilfsmittel erarbeitet.

München, 24.05.2022

Eugenia Elzer

Dissertation eingereicht am	28.03.2022
1. Gutachter:	Prof. Dr. Wolfgang Schnick
2. Gutachter:	Prof. Dr. Dirk Johrendt
Mündliche Prüfung am	23.05.2022

Für meine Familie

I am among those who think that science has great beauty.

Marie Curie (1867-1934)

Danksagung

Mein ganz besonderer Dank gilt Herrn Prof. Dr. Wolfgang Schnick für die herzliche Aufnahme in seinem Arbeitskreis und die Möglichkeit meine Dissertation unter seiner fachlichen Anleitung anzufertigen. Die zur Verfügung gestellten Mittel, die hervorragenden Arbeitsbedingungen, die große Freiheit bei der inhaltlichen Gestaltung der Dissertation und die fachlichen Hilfestellungen und Ratschläge waren wertvolle Bausteine auf dem Weg zur Entstehung der vorliegenden Arbeit.

Herrn Prof. Dirk Johrendt danke ich ganz herzlich für die prompte Bereitschaft das Koreferat dieser Arbeit zu übernehmen.

Außerdem bedanke ich mich bei Prof. Dr. Thomas Klapötke, Prof. Dr. Achim Hartschuh, Prof. Dr. Hans-Christian Böttcher und Prof. Dr. Konstantin Karaghiosoff für die Bereitschaft Teil meiner Prüfungskommission während der mündlichen Prüfung zu sein.

Weiterhin danke ich Olga Lorenz, Wolfgang Wunschheim, Thomas Miller und Dieter Rau für ihre Hilfsbereitschaft in formalen und technischen Angelegenheiten jeder Art. Christian Minke danke ich für seine Geduld während der Durchführung zahlreicher EDX-Messungen. Ich danke weiterhin Dr. Peter Mayer für die Aufnahme der zahlreichen Einkristalldatensätze und PD Dr. Constantin Hoch, sowie Lucien Eisenburger für die Hilfestellung bei den komplexeren Strukturaufklärungen.

Bei meinen Praktikanten Thomas Rappenglitz, Niko Greither und Daniel Kraut möchte ich mich für die Unterstützung sowie das Interesse an meinen Forschungsprojekten bedanken.

Herzlicher Dank geht auch an die internen und externen Kooperationspartner, die mit ihrer fachlichen Expertise und Zusammenarbeit die vorliegende Arbeit bereichert haben. In diesem Zusammenhang bedanke ich mich insbesondere für die langjährige Kooperation mit Philipp Strobel, Volker Weiler und Peter J. Schmidt und für die fachliche Unterstützung rund um das Thema Leuchtstoffe.

Den Arbeitskollegen aus dem gesamten zweiten Stockwerk möchte ich für die entspannte Arbeitsatmosphäre und die stets unterhaltsamen Kaffeepausen der vergangenen Jahre danken. Mein besonderer Dank gilt hierbei Dr. Christine Pösl, die mich bereits während meiner Bachelorarbeit ganz herzlich in dem Arbeitskreis willkommen geheißen hat. Auch bei den Laborkollegen Dr.

Christian Maak, Dr. Philipp Strobel, Dr. Lukas Neudert, Dr. Robin Niklaus, Lucien Eisenburger, Monika Pointner und Sophia Wandelt möchte ich mich für die angenehme Arbeitsatmosphäre und den hilfsbereiten Umgang im Labor bedanken. Tobias Gifftthaler danke ich besonders für die entspannte Zusammenarbeit rund um das Thema Beryllium. Statt Konkurrenz und Wettbewerb habe ich mich jederzeit auf Unterstützung verlassen können, sei es bei der Arbeit an der Be-Glovebox und der HIP oder der Bereitschaft sowohl die Publikationen als auch große Teile dieser Arbeit Korrektur zu lesen.

Dr. Juliane Stahl und Dr. Bettina Rendenbach danke ich für das offene Ohr während des Promotionsalltags und für die amüsanten Gespräche am Abend. Es freut mich sehr, dass der gemeinsame Spieleabend auch über die Promotionszeit hinaus zu einem festen Termin im Kalender geworden ist. Bei Dr. Sebastian Wendl möchte ich mich für die Unterstützung, Aufheiterung, Motivation und wenn nötig auch Ablenkung im Verlauf der letzten Jahre, sowie die daraus entstandene Freundschaft bedanken.

Ganz herzlicher Dank geht auch an meine Freunde im Allgäu, die mich während der Zeit des Studierens und Promovierens unterstützt und begleitet haben. Ganz besonderer Dank gebührt an dieser Stelle Mike für das offene Ohr, egal wie ausufernd das Mitteilungsbedürfnis am Wochenende ausfiel und die unterhaltsamen Stunden am Brettspieletisch.

Zuletzt möchte ich mich bei meiner Familie für die bedingungslose Liebe und Unterstützung nicht nur während der Zeit in München, sondern ganz allgemein bedanken. Danke dafür, dass ihr mir stets den Rücken freigehalten habt, damit ich machen kann worauf ich Lust habe. Mama und Papa, bei euch kann ich mich nicht genug dafür bedanken, dass ihr das Wagnis eingegangen seid in ein neues Land zu ziehen, damit wir Kinder es besser haben. Ohne euren Mut und die Unterstützung von dir, mein kleines, großes Schwesterchen, wäre diese Arbeit so sicherlich nicht möglich gewesen. Danke!

Eugenia Elzer

Table of Contents

1. Introduction	1
1.1 LED – a technology that brightens up our daily life	1
1.2 Eu^{2+} luminescence	8
1.3 Nitrides – fundamentals	12
1.4 Beryllium and the structural chemistry of nitridoberyllates	14
1.5 Scope of this thesis	18
1.6 References	19
2. $\text{Eu}_3\text{Be}_{22}\text{N}_{16}\text{O}$: A Highly Condensed Oxonitridoberyllate	25
2.1 Introduction	25
2.2 Results and Discussion	27
2.3 Conclusion	33
2.4 Experimental Section	34
2.5 Acknowledgements	35
2.6 References	36
3. $M\text{Be}_{20}\text{N}_{14}:\text{Eu}^{2+}$ ($M = \text{Sr}, \text{Ba}$): Highly Condensed Nitridoberyllates with Exceptional Highly Energetic Eu^{2+} Luminescence	39
3.1 Introduction	40
3.2 Experimental Section	42
3.3 Results and Discussion	46
3.4 Conclusion	55
3.5 Acknowledgements	56
3.6 References	57
4. Illuminating Nitridoberylloaluminates: The Highly Efficient Red-Emitting Phosphor $\text{Sr}_2[\text{BeAl}_3\text{N}_5]:\text{Eu}^{2+}$	63
4.1 Introduction	64
4.2 Experimental Section	66
4.3 Results and Discussion	69

4.4	Conclusion.....	76
4.5	Acknowledgements.....	76
4.6	References.....	77
5.	Inverse-Tunable Red Luminescence and Electronic Properties of Nitridoberylaluminates $\text{Sr}_{2-x}\text{Ba}_x[\text{BeAl}_3\text{N}_5]:\text{Eu}^{2+}$ ($x = 0-2$).....	81
5.1	Introduction.....	82
5.2	Results and Discussion.....	84
5.3	Conclusion.....	96
5.4	Acknowledgements.....	97
5.5	References.....	98
6.	Summary.....	103
6.1	$\text{Eu}_3\text{Be}_{22}\text{N}_{16}\text{O}$: A Highly Condensed Oxonitridoberyllate.....	104
6.2	$M\text{Be}_{20}\text{N}_{14}:\text{Eu}^{2+}$ ($M = \text{Sr}, \text{Ba}$): Highly Condensed Nitridoberyllates with Exceptional Highly Energetic Eu^{2+} Luminescence	105
6.3	Illuminating Nitridoberylaluminates: The Highly Efficient Red-Emitting Phosphor $\text{Sr}_2[\text{BeAl}_3\text{N}_5]:\text{Eu}^{2+}$	106
6.4	Inverse-Tunable Red Luminescence and Electronic Properties of Nitridoberylaluminates $\text{Sr}_{2-x}\text{Ba}_x[\text{BeAl}_3\text{N}_5]:\text{Eu}^{2+}$ ($x = 0-2$).....	107
7.	Discussion and Outlook	109
7.1	References.....	115
A.	Supporting Information for Chapter 2.....	119
A.1	Results and Discussion.....	119
A.2	Author Contributions.....	127
A.3	References.....	127
B.	Supporting Information for Chapter 3.....	129
B.1	Results and Discussion.....	129
B.2	References.....	138
C.	Supporting Information for Chapter 4.....	139
C.1	Results and Discussion.....	139
C.2	References.....	145

D. Supporting Information for Chapter 5	147
D.1 Experimental Section.....	147
D.2 Results and Discussion.....	152
D.3 Author Contributions	162
D.4 References.....	163
E. Miscellaneous	167
E.1 List of Publications.....	167
E.2 Publications beyond this Thesis	169
E.3 Conference Contributions and Presentations	170
E.4 Deposited Crystallographic Data	171
E.5 Curriculum Vitae.....	172

1. Introduction

1.1 LED – a technology that brightens up our daily life

In 2014, I. Akasaki, H. Amano and S. Nakamura (Figure 1.1) jointly received the Nobel Prize in Physics “for the invention of efficient blue light-emitting diodes, which has enabled bright and energy-saving white light sources”.^[1] Twenty years after the invention of the efficient blue light emitting diode (LED), the Royal Swedish Academy of Sciences thus rewarded an invention of “*greatest benefit of mankind*”.^[1]



Figure 1.1: Winner of the Nobel Prize in Physics 2014. From left to right: I. Akasaki, H. Amano, S. Nakamura.^[2]

The LED is a semiconductor device consisting of a p-n junction and is based on a phenomenon called electroluminescence, i. e. the emission of light when an electrical current is applied. In a semiconductor, electrons from the conduction band (CB) can recombine with holes in the valence band (VB), releasing photons whose energy correspond to the energetic distance between the CB and VB (band gap). Doping – the targeted introduction of impurity atoms – increases the concentration of charge carriers. Doped materials are classified either as n-type or p-type materials. In an n-type material, an excess of electrons is achieved by introducing elements with more electrons, e. g. Si for n-GaN, while p-type materials are obtained by doping with an electron-deficient element, e. g. Zn or Mg for p-GaN. Besides elemental semiconductors (Si, Ge) there are also compound semiconductors, which are abbreviated as IV (SiC, SiGe) or III-V (GaAs, GaN) semiconductors, depending on the group of elements the semiconductors are comprised of. For LEDs, the III-V semiconductors are particularly relevant today.^[3]

The phenomenon of electroluminescence was first described by H. J. Round in 1907. He observed a “bright glow” when applying a current on a crystal of carborundum (silicon carbide, SiC).^[4] In the mid-1920s, a young Russian researcher named O. V. Losev also worked on SiC and published various articles regarding the invention of LEDs.^[5] Losev’s research did not receive much attention from the wider research community and it took several decades for further advancements to be made in the field of LED development.

While naturally occurring semiconductors such as SiC and ZnS (II-VI semiconductor) were studied in the first half of the last century, the era of III-V semiconductors began in the early 1950s.^[6] ^{7]} These semiconductors were not known before as they do not occur naturally. In 1961, J. Biard and G. Pittman developed and patented a GaAs-based infrared LED.^[8, 9] In the following year N. Holonyak Jr. introduced a red-emitting LED (GaAsP over GaAs substrate), representing the first LED to emit visible light.^[10] Further research followed, leading to the development of yellow and green LEDs by M. G. Craford in the early 1970s.^[11, 12] In the following years, LEDs slowly found their way into everyday life. Despite the variety of available colors and affordable prices through mass production, the use of LEDs was limited to indicator lights in telephones or control panels. The LEDs still suffered from low efficiency, limited current densities and therefore low brightness.

While an incandescent light bulb completely covers the entire visible spectrum, the LED is an almost monochromatic light source. The emitted wavelength – and as a result also the color – of an LED depends on the band gap of the used semiconductor. Hence, a white light LED (wLED) can be obtained through additive color mixing, e. g. of a blue, green and red LED as displayed in Figure 1.2.

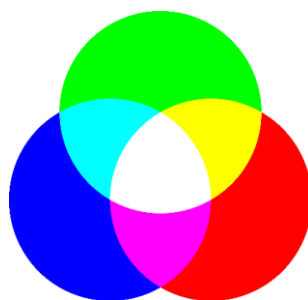


Figure 1.2: Illustration of additive color mixing with the primary colors blue, red and green.

Blue LEDs based on SiC were introduced as early as 1969 and even sold commercially until 1990.^[13] However, the latter showed very poor performance. Even the best SiC LEDs had an efficiency of 0.03%.^[14] In the 1970s GaN was investigated as a possible candidate for blue LEDs,

owing to its wide band gap (3.4 eV).^[15] GaN films exhibiting n-conductivity were grown successfully on sapphire (Al_2O_3) substrates using the hydride vapor phase epitaxy (HVPE). In order to make a p-n junction, various attempts were made to prepare Mg- or Zn-doped p-GaN.^[16] Despite successful Mg doping, the p-GaN showed no p-type conductivity, and the efficiency of the resulting blue LED was too low to be considered for any practical application. Finally, this led to a loss of interest in GaN-based blue LEDs among companies and researchers.^[16]

Only a few scientists regained interest, including the Japanese researchers I. Akasaki, H. Amano, and S. Nakamura. In 1986 I. Akasaki and H. Amano succeeded in synthesizing high quality GaN films using metalorganic vapor phase epitaxy (MOVPE).^[17] A few years later, while examining Zn-doped GaN with a scanning electron microscope (SEM), they accidentally discovered that irradiated samples showed more intense luminescence, without being able to exactly explain why.^[18] With this observation, Amano and Akasaki achieved p-type conduction in Zn- and Mg-doped GaN by low-energy electron beam irradiation (LEEBI) of the samples, thus enabling the two scientists to prepare their first ultra-violet (UV) and violet-blue LED.^[19, 20] In 1992, S. Nakamura identified the presence of ammonia (NH_3) as the cause of the inactivation of the Mg in the p-doped layers. He found out that NH_3 , which is used during the synthesis process, allows the formation of Mg-H complexes, thus inactivating the p-conductivity. Adding a thermal annealing step in a hydrogen free atmosphere allowed the release of hydrogen, thereby destroying the Mg-H complexes – a simple yet elegant step to facilitate and accelerate the synthesis process of p-type layers.^[21, 22] Improving the fabrication of InGaN and AlGaN and incorporating these materials into a double heterostructure LED were the next important steps on the way to a “*candela-class high-brightness InGaN/AlGaN*” blue LED with an external quantum efficiency of 2.7% and a “*high-brightness InGaN/AlGaN*” blue-green LED with an external quantum efficiency 2.4% (Figure 1.3a).^[23, 24] Both quantum efficiencies were the highest values reported for a blue and blue-green LED to that point. Since the invention of the first high-brightness blue LED the efficiency was further improved, e. g. by optimizing the device architecture. Today, alternative layouts, such as the thin-film flip-chip layout displayed in Figure 1.3b are common in state-of-the-art LEDs.

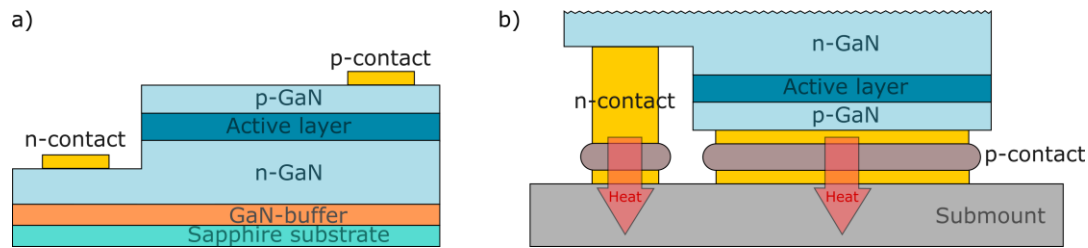


Figure 1.3. Schematic structure of the first blue-emitting LED (a) and a state-of-the-art flip-chip LED with a phosphor layer on top (b). In both schematics the active layer is a simplified representation of an InGaN/AlGaIn double heterostructure or a multi quantum well structure. Adapted from Ref.^[25]

In contrast to the structure of the first LED-chips (Figure 1.3ba), the chip is flipped, so the contacts no longer block part of the emission. In addition, the heat generated by ohmic losses can dissipate more easily through the contacts on the lower side. Finally, the GaN-buffer and the sapphire substrate are removed. All these advances allowed to increase the external quantum efficiency of InGaN LEDs (emission maximum $\lambda_{em} = 444 \text{ nm}$) up to 84.3%.^[26]

On the way to white LEDs (wLED), the invention of a high-efficiency blue LED was an important milestone. The efficient blue LED paved the way for lighting solutions that are not only long lasting, environmentally friendly, energy and cost efficient, but can also be specifically tailored to the demands of different application areas.^[27] As briefly mentioned earlier, white light is obtained by additive color mixing (Figure 1.2). There are various possibilities for the technical implementation. One way to obtain a wLED is to combine a blue, green and red LED. However, this solution has some disadvantages, one of which is the different life span of the respective LEDs. As a result, the color point of the wLED can change over time. Furthermore, the emission wavelength of some LEDs is strongly dependent on the chip temperature, which can rise up to 150 °C when the LED is operating.^[28] Additionally, the overall performance of this combination suffers from the low external quantum efficiency ($\approx 25\%$) of the green LED, known as the green gap.^[29]

Today, the lighting sector is dominated by another solution, namely phosphor converted LEDs (pc LEDs). Here, a blue-emitting LED is combined with a phosphor that absorbs blue light and re-emits light of lower wavelength, e. g. green, yellow or red.^[28] Although this type of LED suffers from energy loss, as blue light is down-converted by the phosphor into light of longer wavelength, this approach is superior to other approaches due to its simple design, cost effectiveness and versatility. An advantage of solid-state lighting (SSL) solutions, compared to conventional sources like incandescent and fluorescent sources, is the controllability of the spectral and spatial properties as well as the correlated color temperature (CCT). The LED chips can be assembled into different

lighting solutions, e. g. in the form of light bulbs, spotlights or as light strips. The combination of phosphors, on the other hand, determines whether the wLED emits warm (2500–3500 K), neutral (3500–4500 K) and cool (4500–5500 K) white or daylight (5500–7500 K).^[25,28]

The first wLED, manufactured by Nichia Company in 1996, was a single phosphor LED (1pc LED) and consisted of a blue LED coated with a yellow-emitting cerium-doped garnet phosphor ($\text{Y}_{3-x}\text{Gd}_x\text{Al}_{5-y}\text{Ga}_y\text{O}_{12}:\text{Ce}^{3+}$), often referred to as $\text{YAG}:\text{Ce}^{3+}$.^[30] The combination of a blue LED and a broad emission band of $\text{YAG}:\text{Ce}^{3+}$ covers almost the entire visible spectrum (Figure 1.4). However, parts in the red spectral range are missing, thus resulting in a cold-white light impression with a color rendering index below 75.^[31] The color rendering index (CRI) indicates the ability of a light source to render the colors of an object compared to sunlight (CRI = 100).^[27] A high value indicates a proper color rendering which is desirable for indoor lighting. Therefore, the low CRI of a 1pc LED with $\text{YAG}:\text{Ce}^{3+}$ is not acceptable for general illumination. Due to the high conversion efficiency this solution still remains attractive in areas such as automotive head lighting.^[29]

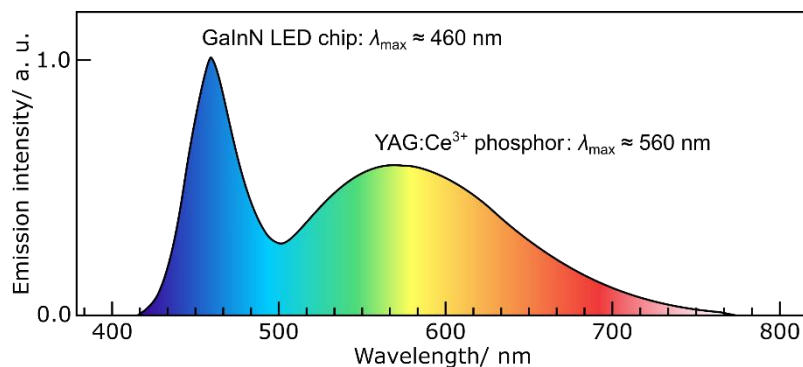


Figure 1.4. Emission spectrum of blue LED coated with a yellow emitting $\text{YAG}:\text{Ce}^{3+}$ phosphor. Adapted from Ref.^[30]

For illumination-grade lighting application, for example in residential lighting, however, LEDs with CRI values above 80 and CCTs in the range of 2700–4000 K are desired.^[25] Technically, this can be realized by coating a blue LED with different phosphors, for example a green-yellow and a red-emitting phosphor. This allows better coverage of the visible spectrum, resulting in higher CRI values. Red-emitting nitrides such as $(\text{Sr},\text{Ba})_2\text{Si}_5\text{N}_8:\text{Eu}^{2+}$ or $(\text{Ca},\text{Sr})\text{AlSiN}_3:\text{Eu}^{2+}$ already found their way into commercial application as phosphors in pc LEDs.^[32, 33] Both phosphors exhibit excellent photoluminescence properties, as well as chemical and thermal stability. A disadvantage, however, is the broad emission band of both phosphors, which leads to efficiency losses due to spill-over into the infrared region. To avoid this kind of efficiency loss red-emitting phosphor with a narrow-band

emission are desired. Figure 1.5 illustrates the difference between a state-of-the-art pc LED with a theoretical spectrum of a narrow-band emitting red phosphor (fwhm = 30 nm).

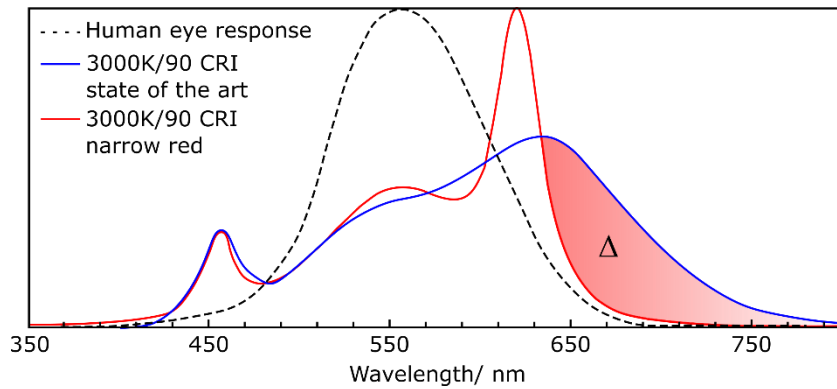


Figure 1.5. Comparison of the emission spectra of a state-of-the-art LED (90 CRI) and a modeled spectrum of a pc LED with a narrow-red phosphor (fwhm = 30 nm). The dotted line indicates the human eye response curve, while the colored red area in the deep red and IR region indicates the difference (Δ) between the emission in the red spectral region using a red phosphor with a broad emission band compared to a narrow-band red-emitting phosphor. Adapted from Ref^[34]

Accordingly, recent LED phosphor research is focused on the exploration of narrow-band emitting phosphors. In this context, structural prerequisites like a highly condensed anionic network, cation ordering, and a highly symmetric crystallographic site for the dopant with approximately equal dopant-ligand distances are discussed to be beneficial for narrow-band emitting phosphors. In fact, the structural properties of the narrow-band red-emitting phosphor $\text{Sr}[\text{LiAl}_3\text{N}_4]:\text{Eu}^{2+}$ (SLA), crystallizing in an ordered variant of the UCr_4C_4 -structure type, fulfilled almost all these prerequisites. SLA features a highly condensed anionic network with two crystallographic sites for the Eu^{2+} with very similar dopant-ligand distances, exhibiting an emission band with a maximum at $\lambda_{\text{em}} = 654 \text{ nm}$ and a full width at half maximum (fwhm) of $43 \text{ nm}/1170 \text{ cm}^{-1}$. The prototype pc LED with the narrow-band red-emitting phosphor SLA showed an increase in luminous efficacy of 14% compared to commercially available high CRI LED using red-emitting nitrides with a relatively broad emission band, such as $(\text{Sr},\text{Ba})_2\text{Si}_5\text{N}_8:\text{Eu}^{2+}$ or $(\text{Ca},\text{Sr})\text{AlSiN}_3:\text{Eu}^{2+}$ ^[35] SLA has not only gained much attention as a next-generation LED phosphor material but was also implemented in commercially available LEDs only a few years after its discovery.^[34, 35] Just recently, another promising candidate for a red phosphor which can be considered an isoelectronic substitution variant of SLA was discovered: $\text{Sr}[\text{Li}_2\text{Al}_2\text{O}_2\text{N}_2]:\text{Eu}^{2+}$ (SALON).^[36] The oxonitridoaluminate exhibits a slightly blue shifted emission maximum ($\lambda_{\text{em}} = 614 \text{ nm}$) and a comparable emission band width (fwhm = $48 \text{ nm}/1286 \text{ cm}^{-1}$) to SLA. The blue

shifted emission enables a gain in luminous efficacy of 16% compared to SLA.^[36] Both phosphors show excellent thermal performance, but the width of the emission band does not yet match the target value of 30 nm, proposed for a high-performance red phosphor.^[28]

In summary, it can be stated that the choice of the right phosphors in pc LEDs is highly relevant as the optical properties, such as spectral properties, luminous efficacy, CRI, CCT and lifetime all depend on them. While narrow-band red-emitting phosphors can contribute to the optimization of wLEDs, narrow-band blue and green-emitting phosphors are also relevant for the improvement of liquid crystal displays (LCD).^[37] To be considered for application in LEDs, phosphors must meet certain requirements: Efficient absorption of UV or blue light, suitable width of the emission band – usually expressed as full width at half maximum (fwhm) – and position of the emission maximum, high emission intensity and quantum efficiency, and high thermal and chemical stability.^[38, 39] These properties depend, among other things, on the chemical composition and compound structures. Nitrides have proven to be a suitable substance class with regard to the necessary properties. Starting from the substance class of nitridosilicates the search for suitable host lattices for doping with Eu^{2+} has been extended to adjacent elements in the periodic table. This led to the discovery of a variety of structures with different combinations of the elements Li, Mg, Al, Si and P forming the anionic networks. While a lot of research has already been done, it is still challenging to further explore new structures and substance classes to develop efficient, narrow-band emitting phosphors and enable LEDs with optimized phosphor properties. In this context, the incorporation of beryllium into the anionic networks can be beneficial, as already shown prior to this work by the blue-emitting oxoberyllates $A\text{E}\text{Li}_2[\text{Be}_4\text{O}_6]:\text{Eu}^{2+}$ ($A\text{E} = \text{Sr}, \text{Ba}$) and the cyan-emitting oxonitridoberyllate $\text{Sr}[\text{Be}_6\text{ON}_4]:\text{Eu}^{2+}$. These promising compounds were the starting point to investigate the synthesis of further Be containing compounds and to study their properties as potential phosphors within the scope of this thesis.

In Chapter 1.2 the Eu^{2+} luminescence and the influence of the host lattice on the luminescence will be discussed briefly. Chapter 1.3 will provide some fundamentals on nitrides, while Chapter 1.4 contains an introduction to the element beryllium and an overview of the nitridoberyllates known so far.

1.2 Eu^{2+} luminescence

The word luminescence was first proposed by the German physicist E. Wiedemann in 1888 as a term for substances that emit light not resulting from heat (in contrast to incandescence).^[40] The term luminescence includes both the process of light emission that occurs when a body is excited with radiation (fluorescence) and the process of light emission that is observed as an after-glow after the excitation has already ended (phosphorescence).^[41] Throughout this thesis, the more general term luminescence will be used most of the times.

For the development of luminescent materials, i. e. phosphors, it is helpful to understand which electronic processes are responsible for luminescence. Therefore, this chapter starts with an outline of the luminescence process in inorganic compounds in general followed by a discussion of the Eu^{2+} luminescence in inorganic host lattices.

Inorganic compounds with rigid host lattices and large band gaps ($> 3 \text{ eV}$) are of particular interest for application in LEDs. Undoped, these compounds are colorless, as they do not absorb visible light. Only after doping with activators, e. g. rare earth (*RE*) ions, luminescence is observed after excitation with UV or blue light.^[29, 38, 41] The processes responsible for the luminescence takes place at the activator ion and can be illustrated with the help of the configuration-coordinates diagram (Figure 1.6).^[42]

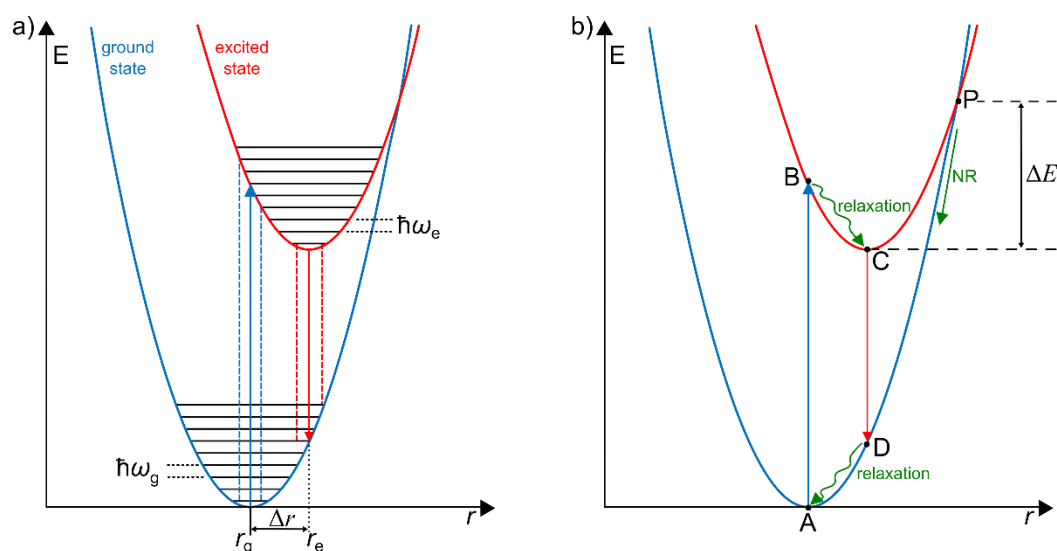


Figure 1.6: Configuration-coordinates diagram of a luminescent center. a) potential energy of the ground (blue) and first excited state (red) of a luminescent center; vibrational states are indicated as black horizontal lines, the absorption and emission as blue and red vertical arrows, respectively. b) simplified representation of the configuration-coordinates diagram. Adapted from Ref.^[41, 42]

Here, the potential energy of a luminescence center is plotted as a function of the configuration coordinate r for the ground state (blue) and the first excited state (red), where r represents the activator–ligand distance. Through vibrations of the ligands around the activator, the activator–ligand bond lengths can be shorter or longer, resulting in a higher energy of the system, with the lowest energy at the equilibrium distance r_g . When the system is in the excited state the equilibrium distance changes from r_g to r_e , which causes the upper parabola to be shifted by the amount Δr in respect to the ground state. The respective transition between ground state and excited state, i. e. absorption and emission, is shown as a vertical line (blue and red) and the vibrational states are drawn as horizontal lines (black). At temperatures at absolute zero, the lowest vibrational level will be occupied, while at higher temperatures, the higher vibrational states will also be populated, resulting in absorption and emission bands with certain bandwidths, indicated as dashed lines in Figure 1.6b on both side of the vertical arrows. Thus, the bandwidth increases with a larger Δr , while narrower band emission is observed for small values of Δr .^[42]

The phonon frequencies of the ground and excited state are given as $\hbar\omega_g$ and $\hbar\omega_e$, respectively, and depend on the atomic weight of the atoms in the host lattices.^[41] After the excitation (Figure 1.6b, A→B) the system returns to the energetically lowest point of the excited state through vibration (B→C) before returning to the ground state accompanied by emission (C→D), followed again by relaxation (D→A).^[41] Since a part of the energy is lost through heat dissipation, the observed emission is red-shifted compared to the absorption, which is known as Stokes shift and is quantified as $E_{\text{stokes}} = 2S \cdot \hbar\omega$. The Huang-Rhys factor S gives the number of phonons involved in the process of absorption and emission. Therefore, it is a measure for the electron-phonon coupling.^[41] Structures with a higher rigidity usually exhibit weaker electron-phonon coupling, and thus have smaller values of S . For that reason, the Stokes shift can be reduced through rigid host lattices and decreased lattice relaxation. The configuration-coordinate diagram also explains the process of luminescence quenching at higher temperatures. At the intersection of the two curves (point P in Figure 1.6b) a non-radiative return (NR) from the excited to the ground state (P→A) is possible. This state can be reached by a correspondingly high activation energy (ΔE), which would result in thermal quenching of the luminescence.^[42] Even though the processes are more complex in reality, this simple model can be used to explain the bandwidth of many activators, the Stokes shift of the emission, and temperature dependence of the emission.

As already discussed above, the luminescence in phosphors originates from electronic transitions of activator ions, with the rare earth ion Eu^{2+} and Ce^{3+} being the most common ones used in pc LEDs.^[38] The observed luminescence of these activators arises from the parity-allowed transition between the occupied $4f$ orbitals and unoccupied $5d$ orbitals.^[43] As the electronic configuration of Eu^{2+} is $[\text{Xe}]4f^7$, the electronic transition takes place between the $4f^7(^8\text{S}_{7/2})$ ground state and the $4f^6(^7\text{F})5d^1$ excited state. In contrast to $4f$ orbitals which are shielded by the outer $5s^2$ and $5p^6$ orbitals, the $5d$ orbitals, located in the outer orbit are strongly affected by their environment.^[44] The energetic position of the $5d$ orbitals of Eu^{2+} can be significantly modified by the nephelauxetic effect (measure of the covalence of activator–ligand bond) and the crystal field splitting as illustrated in Figure 1.7.

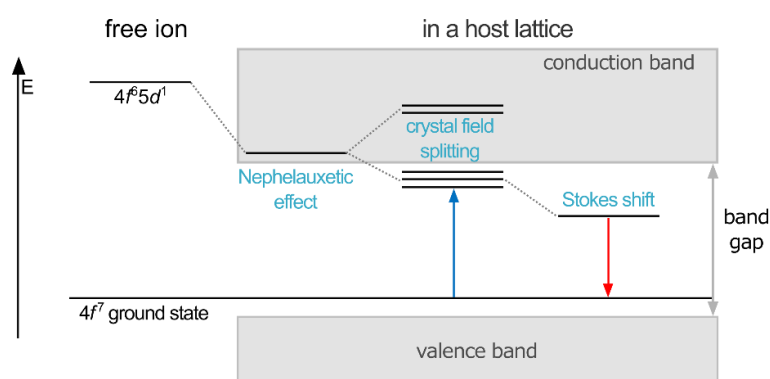


Figure 1.7: Schematic representation of the energy of the ground and excited state of Eu^{2+} in the free ion and in a host lattice. Adapted from Ref^[38]

A more covalent activator–ligand bonding and a strong crystal field splitting lowers the energetic position of the $5d$ orbitals resulting in a significantly red shifted emission. While the emission of a free Eu^{2+} is located in the ultra-violet region ($33856 \text{ cm}^{-1} / \approx 295 \text{ nm}$),^[43] the incorporation of Eu^{2+} into a host lattice shifts the position of the emission bands within the visible spectra region. Here, oxides, halides, borates and sulfates typically show emission in the blue-to-green spectral region.^[44] Due to the higher polarizability of nitrogen, Eu^{2+} doped nitrides exhibit a red-shifted emission compared to oxides. Even though the usual range is green-to-red, the high structural variety of the nitrides enables Eu^{2+} emission from blue to infrared.

The crystal field splitting is affected by the local environment of the activator ion, in particular by the activator–ligand bond lengths, the coordination number (CN) and the shape of the coordination polyhedron. Thus, the size of the cations substituted by Eu^{2+} can be used to modify the emission color of the phosphor. Replacing larger cations with smaller ones, for example Ba^{2+} with

Sr²⁺, the metal–ligand distance usually decreases, resulting in a stronger crystal field splitting, thus shifting the emission towards the red spectral region.^[44]

In summary, the high sensitivity of the 5*d* energy levels with respect to their local environment offers great potential for tuning position and shape of the emission band of Eu²⁺ doped phosphors. A more covalent activator–ligand bond and a stronger crystal field splitting in nitrides, compared to oxides reduces the energy of the 5*d* levels, resulting in red-shifted excitation and emission spectra. Furthermore, the incorporation of N³⁻ into the anionic network allows higher condensed structures (see also Chapter 1.4), which is beneficial for a smaller Stokes shift and narrower emission band widths.^[41]

1.3 Nitrides – fundamentals

Except for some occurrences in meteorites, (oxo)nitridometallates do not occur naturally, while oxidometallates – especially silicates – are a highly abundant substance class on our planet. The explanation for this can be found in the different chemical and physical properties of oxygen and nitrogen. N_2 molecules exhibit a very stable triple bond with a high bonding energy of $945 \text{ kJ}\cdot\text{mol}^{-1}$ and are considered to be unreactive at ambient temperature. This is why N_2 is often used as an inert gas to shield potentially reactive substances from oxygen. In comparison, the cleavage of a double bond between two oxygen atoms requires much less energy ($498 \text{ kJ}\cdot\text{mol}^{-1}$). Additionally, oxygen has a high electron affinity (-1.46 eV) and can easily be reduced to O^{2-} , while the reduction of N to N^{3-} is highly unfavorable, as nitrogen exhibits a positive electron affinity of 0.07 eV .^[45] As a result of these properties, the preparation of nitrides requires rigorous exclusion of water and oxygen during their synthesis to prevent hydrolysis and/or oxidation.

Structurally, not only nitridosilicates but also other nitridometallates, like nitridoaluminates or nitridophosphates, can be derived from silicates, to the extent that the structures of the substance classes are built up from more or less strongly linked TX_4 ($T = Al^{3+}, Si^{4+}, P^{5+}$; $X = O, N$) tetrahedra. However, while linkage in silicates usually occurs only via corners of SiO_4 tetrahedra, nitrogen allows linkage of tetrahedra via their corners and/or edges. This allows the formation of higher condensed anionic networks and therefore, also a significantly higher structural variety. A parameter that can be used to describe the increasing connectivity of the tetrahedral units is the degree of condensation κ . The latter is determined by dividing the number of network-building ions T by the number of coordinating anions X : $\kappa = n(T)/n(X)$. The maximum value to be achieved for the respective substance class corresponds to the ratio in the binary nitride and increases with decreasing formal charge of the tetrahedrally coordinated atom: $\kappa(P_3N_5) = 0.6$, $\kappa(Si_3N_5) = 0.75$, $\kappa(AlN) = 1.0$ (Figure 1.8) Thus, one could expect that nitridoaluminates can feature higher condensed structures compared to nitridosilicates or nitridophosphates. Until now, however, only a few ternary nitridoaluminates have been reported ($M_3Al_2N_4$ ($M = Sr, Ba$), $Ca_6[Al_2N_6]$, α - and β - $Ca_3[Al_2N_4]$) all with $\kappa = 0.5$ (Figure 1.8). Since κ increases with decreasing formal charge of the central atom T , a partial substitution of Al^{3+} by Mg^{2+} ($\kappa(Mg_3N_2) = 1.5$) or Li^+ ($\kappa(Li_3N) = 3$) should lead to an increase in the degree of condensation. In fact, this substitution resulted in the synthesis of several nitridomagneso- and nitridolithoaluminates, like $Sr_4[LiAl_{11}N_{14}]:Eu^{2+}$, $Sr[MgAl_5N_7]:Eu^{2+}$,

$\text{Ca}_{18.75}\text{Li}_{10.5}[\text{Al}_{39}\text{N}_{55}]:\text{Eu}^{2+}$, $M[\text{LiAl}_3\text{N}_4]:\text{Eu}^{2+}$ ($M = \text{Ca}, \text{Sr}$), $M[\text{Mg}_2\text{Al}_2\text{N}_4]:\text{Eu}^{2+}$ ($M = \text{Ca}, \text{Sr}, \text{Ba}$),
 $\text{CaBa}[\text{Li}_2\text{Al}_6\text{N}_8]:\text{Eu}^{2+}$ (Figure 1.8).^[35, 46-51]

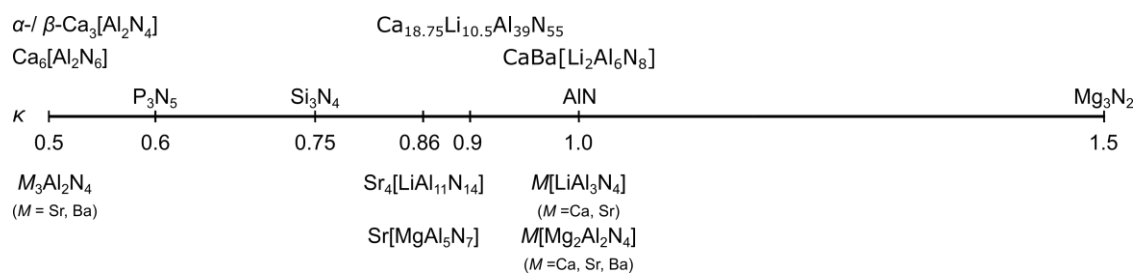


Figure 1.8. Overview of the degree of condensation κ for ternary and quaternary nitridoaluminates. Additionally, κ values of the binary nitrides P_3N_5 , Si_3N_4 , AlN and Mg_3N_2 are displayed.

In the search for new host lattices to be doped with Eu^{2+} and Ce^{3+} , the curiosity of preparative chemists extended to various combinations of the elements Li, Mg, Al, Si, and P as part of the anionic networks and led to the discovery of numerous previously unknown structures.^[52, 53] Interestingly, one element received only little attention until recently, even though it is directly situated between Li, Mg and Al in the periodic table. Yet, there are several reasons for the extension of synthetic investigations to Be. In contrast to the heavier homologues Ca^{2+} , Sr^{2+} and Ba^{2+} , Be^{2+} can be part of an anionic network comparable to Al^{3+} (nitridoaluminates), Si^{4+} (nitridosilicates) or P^{5+} (nitridophosphates). In addition to BeN_4 tetrahedra, Be^{2+} also can exhibit a 3-fold coordination forming trigonal-planar BeN_3 units, enabling a larger structural diversity. Comparing the binary nitrides Si_3N_4 and Be_3N_2 , a difference in the connectivity of the tetrahedra can be observed: Despite almost identical ionic radii in a tetrahedral coordination (Si^{4+} : 0.26 Å, Be^{2+} : 0.27 Å),^[54, 55] the formally lower charge of Be^{2+} allows edge- and vertex-sharing of the BeN_4 tetrahedra, while in Si_3N_4 only vertex-sharing SiN_4 tetrahedra are present.^[56] Thus, a higher degree of condensation can be realized, by introducing Be^{2+} into the anionic network, as was recently demonstrated for the highly condensed oxonitridoberyllate $\text{Sr}[\text{Be}_6\text{ON}_4]:\text{Eu}^{2+}$ and oxoberyllates $\text{AELi}_2[\text{Be}_4\text{O}_6]:\text{Eu}^{2+}$ ($\text{AE} = \text{Sr}, \text{Ba}$).^[57, 58]

1.4 Beryllium and the structural chemistry of nitridoberyllates

A 2016 minireview on beryllium started with the opening words: "What do you really know about beryllium and its compounds?".^[59] Although a comprehensive review of the previously known Be containing compounds is beyond the scope of this thesis, this chapter will give an answer to the above question in the form of a brief introduction of the element Be and the structures of the nitridoberyllates known so far.

Beryllium, sometimes called the most toxic non-radioactive element was first discovered by the French chemist L. N. Vauquelin in 1798,^[60] who was asked by a mineralogist to compare the chemical composition of Beryl and Emerald, as both stones exhibited the same weight and hardness. In his report L. N. Vauquelin emphasizes that the most interesting part of the analysis is his discovery of a new earth ("*terre nouvelle*").^[61] The chemical properties of the newly discovered compound (BeO) were compared in detail with those of Al₂O₃. Contrary to the chemical analysis used today, the chemist also carried out a taste test and found that the beryllium compounds tasted sweet, which is why glycine was suggested as a possible name.^[61] It took thirty years before metallic Be was prepared by heating a mixture of K and BeCl₂ by F. Wöhler and A. Bussy in 1828.^[62, 63] Another 70 years went by, until the French chemist, P. Lebeau obtained pure Be through the electrolysis of a mixture of BeF₂ and NaF.^[63]

The element Be is a gray, very hard metal with a low density (1.8477 g·cm⁻³) and a melting point of 1278 °C.^[45] In the periodic table, Be is located in the second main group. However, according to the diagonal relationship, it is more similar to Al from the third main group than to the heavier homologues of the AE group (Mg, Ca, Sr, and Ba). In nature, Be is most commonly found in minerals, such as beryl Be₃Al₂[Si₆O₁₈] and bertrandite Be₄(OH)₂[Si₂O₇], due to its high affinity to oxygen.^[64] Colored varieties of beryl are better known as gemstones like emerald, aquamarine, or golden beryl (sometimes called heliodore) (Figure 1.9). After his chemical analysis in 1798 L. N. Vauquelin stated that beryl and emerald are the same compound, differing only by a coloring component.^[61] The characteristic green color of emeralds stems from a substitution of Al³⁺ by Cr³⁺, while a substitution of Be²⁺ with Fe²⁺ and Si⁴⁺ with Fe³⁺ results in a light blue color characteristic for aquamarines and yellow color characteristic for golden beryl, respectively.^[64] Further beryllium containing gemstones are euclase BeAl(OH)[SiO₄], chrysoberyl Al₂[BeO₄] (with alexandrite as a known variety) and phenakit Be₂[SiO₄].^[45]



Figure 1.9: Photos of the gemstones beryl, emerald, aquamarine and golden beryl (from left to right).^[65]

As mentioned above, Be is classified as toxic, especially in case of inhalation of dusts and oral ingestion of soluble salts.^[59, 60, 66] Thus appropriate safety precautions are essential, when processing Be and Be containing substances. To prevent oral and dermal exposure, working under Schlenk-line-conditions or in gloveboxes is reasonable and required.^[59] However, once it has formed a stable compound with other elements, it can be expected to be safe, as illustrated by the use Be containing silicates and oxides as gemstones. Although its toxicity limits its practical use to some extent, Be is used in special applications due to its chemical and physical properties.

Due to its low absorption coefficient Be hardly interacts with X-rays, therefore the metal was used for the construction of windows for X-ray tubes.^[67] Its low weight and high stiffness (six times higher than steel) are particularly valued in space technology, e. g. in the construction of the James Webb Space Telescope, which was finally launched into space on December 25th, 2021.^[68] The use of Be contributes to the fact that the huge mirror weighs only 705 kg despite its surface area of 25 m². Almost more important in this context: Be has a high thermal conductivity and a thermal expansion coefficient at cryogenic temperatures of almost zero, which is particularly important for optics.^[69]

Further application-relevant examples of Be compounds include alloys and Be ceramics. By adding small amounts of the element (up to 2 wt%) to other metals such as Cu, alloys exhibiting high hardness and corrosion resistance are obtained. Moreover, tools made of Be-Cu alloys do not cause sparks and surgical instruments manufactured from it are non-magnetic.^[70] Be containing ceramics, like BeO, have high thermal conductivity and high band gap, making them suitable for both high-voltage and high-frequency applications.^[67]

Concerning the chemistry of Be containing nitrides, the number of compounds known so far is small. Prior to the start of this thesis, only the synthesis and structure of Be₃N₂,^[56, 71, 72] the ternary nitrides LiBeN and MBe₂N₂ (*M* = Mg, Ca, Sr, Ba) and the double nitrides BeSiN₂ and BeP₂N₄ were

known.^[73-77] Shortly thereafter, the structure of the quaternary nitridoberyllates $M[\text{BeSi}_2\text{N}_4]$ ($M = \text{Sr}, \text{Eu}$) and the high-pressure form of BeP_2N_4 were reported in our group.^[78, 79] In addition, some calculations reporting on two-dimensional $h\text{-BeN}_2$ and Be_3N_2 monolayers, as well as pressure-induced BeN_4 materials have been published in recent years.^[80-84] Finally, the publication of the high-pressure synthesis of BeN_4 polymorphs at the beginning of 2021, which should even contain BeN_6 octahedra, complete the overview.^[85]

Since the ternary nitridoberyllates and Be_3N_2 are of special relevance for this work, their syntheses and structures will be briefly discussed in the following. Reaction of elemental Be and N_2 at temperatures between 1100 and 1400 °C produces the colorless binary nitride Be_3N_2 in the cubic α -form,^[56] while above 1400 °C the hexagonal β -form is formed.^[71] $\alpha\text{-Be}_3\text{N}_2$ crystallizes in the *anti*- Mn_2O_3 (*anti*-bixbyite) structure, with Be tetrahedrally coordinated by four N atoms (Figure 1.10a). The structure can also be described as a defective anti-fluorite structure in which $\frac{1}{4}$ of the tetrahedral voids remain empty. While N^{3-} forms a distorted cubic close-packing of equal spheres, Be^{2+} occupies $\frac{3}{4}$ of the tetrahedrally coordinated sites.

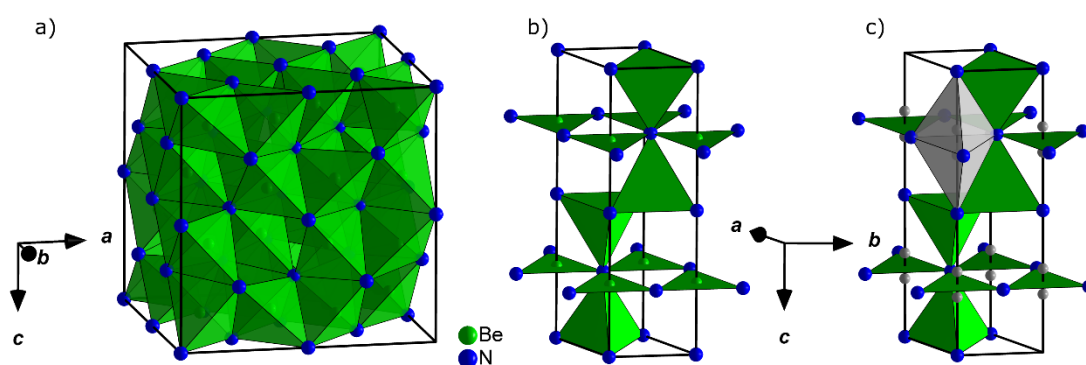


Figure 1.10. Crystal structure of Be_3N_2 with Be atoms in green or gray, N atoms in blue and the unit cell outlined in black. a) $\alpha\text{-Be}_3\text{N}_2$ with BeN_4 tetrahedra in green. b) structure of $\beta\text{-Be}_3\text{N}_2$ as determined in 1960 with BeN_4 tetrahedra and trigonal-planar BeN_3 units in green.^[71] c) structure of $\beta\text{-Be}_3\text{N}_2$ as re-determined in 1969,^[72] Be atoms in gray are distributed over two alternative tetrahedral sites (represented as gray polyhedra) adjacent to a trigonal site. At every time only one of the sites is fully occupied.

The structure determination of $\beta\text{-Be}_3\text{N}_2$ in 1960 initially suggested coexistence of BeN_4 tetrahedra and trigonal-planar BeN_3 units in the crystal structure (Figure 1.10b).^[71] A reexamination in 1969 led to the rebuttal of the originally assumed structure.^[72] According to Jeffrey *et al.*, $\beta\text{-Be}_3\text{N}_2$ contains only tetrahedrally coordinated Be^{2+} , with one of the Be atoms disordered between two mutually exclusive sites, which are indicated as gray atoms in Figure 1.10c. Hence, only one of the gray tetrahedra shown in Figure 1.10c is occupied at a time.

LiBeN can be obtained through reaction of Li_3N and Be in closed steel ampoules at 1000 °C. The crystal structure of LiBeN contains corrugated layers of corner- and edge-sharing BeN_3 units and layers of corner- and edge-sharing LiN_4 tetrahedra with $\kappa = 1.0$. For a clearer view, only some of the LiN_4 tetrahedra are displayed representatively in the LiN_4 layer (Figure 1.11a). By reacting Be_3N_2 with the nitrides Mg_3N_2 , Ca_3N_2 and the subnitrides Sr_2N and Ba_2N , respectively, at temperatures between 1100 and 1200 °C the nitridoberyllates with composition MBe_2N_2 ($M = \text{Mg, Ca, Sr, Ba}$) were obtained.^[73, 74] MgBe_2N_2 crystallizes in the anti- La_2O_3 structure exhibiting alternating layers of edge-sharing BeN_4 tetrahedra and MgN_6 octahedra as illustrated in Figure 1.11b. Due to the increasing size of the heavier homologues Ca–Ba, they do not crystallize in an anti- La_2O_3 structure but are isotypic to $\text{Ca}[\text{B}_2\text{C}_2]$ with planar layers of BeN_3 units and alkaline earth (AE) ion coordinated by eight N atoms in a distorted tetragonal prism (Figure 1.11c).

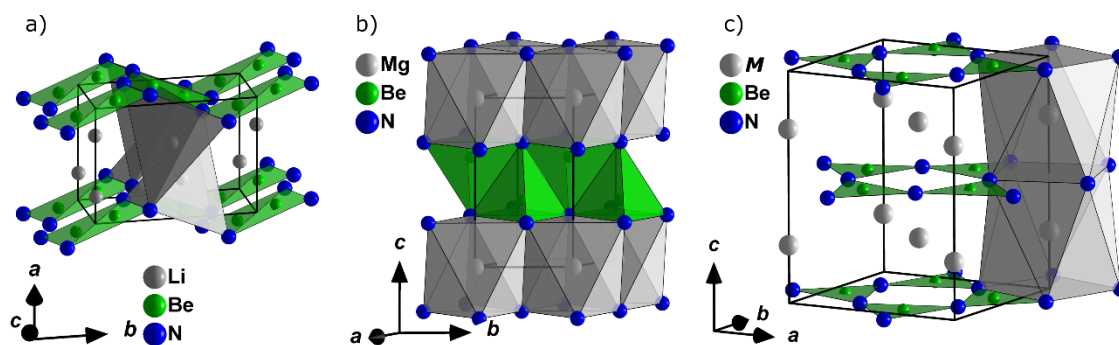


Figure 1.11. Crystal structure of LiBeN (a), MgBe_2N_2 (b) and MBe_2N_2 ($M = \text{Ca, Sr, Ba}$) (c) with BeN_4 tetrahedra and trigonal-planar BeN_3 units in green and Li-, Mg- or M -polyhedra depicted in gray.^[73, 74] Unit cells are outlined in black.

Recapitulating, the number of nitridoberyllates known so far is limited to a few compounds with a degree of condensation $\kappa = 1.0$. Adding the oxonitridoberyllate $\text{Sr}[\text{Be}_6\text{ON}_4]:\text{Eu}^{2+}$, the range expands to $\kappa = 1.2$. A greater structural diversity can be expected compared to other network building ions, as Be^{2+} can be either coordinated by four or three nitrogen atoms, building BeN_4 tetrahedra and trigonal-planar BeN_3 units, respectively. Moreover, it should be possible to synthesize Be containing structures with a degree of condensation $\kappa < 1.5$, as Be^{2+} features a lower formal charge compared to Al^{3+} and Si^{4+} .

1.5 Scope of this thesis

The main objective of this dissertation was the synthesis of new nitridoberyllates and nitridoberylloaluminates and the investigation of their luminescence properties after doping with Eu^{2+} . With regard to LED applications, structures with rigid host lattices are considered beneficial, since highly condensed anionic networks favor narrow-band emission.^[28] So far the highest value of $\kappa = 1.0$ is observed in LiBeN and $M\text{Be}_2\text{N}_2$ ($M = \text{Mg}, \text{Ca}, \text{Sr}, \text{Ba}$).^[73, 74] Taking oxygen into account and looking at the known compounds in the class of oxonitridoberyllates, the highest value reported so far is $\kappa = 1.2$ in $\text{Sr}[\text{Be}_6\text{ON}_4]:\text{Eu}^{2+}$.^[57] Therefore, the synthesis of ternary nitridoberyllates with a higher degree of condensation was targeted in the first part of this thesis.

Since beryllium is classified as toxic, it is advantageous for practical applications if a possible phosphor contains as little Be as possible. In the substance class of nitridoaluminates, efficient phosphors, which are even used commercially in pc LEDs as red phosphors, have been synthesized by incorporating additional network cations such as Mg^{2+} and Li^+ . In this context, the nitridolithoaluminate $\text{Sr}[\text{LiAl}_3\text{N}_4]:\text{Eu}^{2+}$ has gained much attention as a next-generation LED-phosphor due to its efficient narrow-band red emission and remarkable thermal stability of the luminescence.^[35] With these considerations in mind, the second part of this thesis focuses on the partial exchange of the higher charged Al^{3+} by the lower charged Be^{2+} , thus the synthesis of the first representatives of a new compound class, the nitridoberylloaluminates.

1.6 References

- [1] The Nobel Prize in Physics 2014 - Press Release. <https://www.nobelprize.org/uploads/2018/06/press-25.pdf> (accessed 18.02.2022).
- [2] The Nobel Prize in Physics 2014 - Summary. <https://www.nobelprize.org/prizes/physics/2014/summary/> (accessed 18.02.2022).
- [3] Colinge, J. P.; Colinge, C. A., *Physics of semiconductor devices*. Kluwer Academic Publishers New York, Boston, Dordrecht, London, Moskow, **2005**.
- [4] Round, H. J. A Note on Carborundum. *Electr. World* **1907**, *19*, 309.
- [5] Lossev, O. V. CII. Luminous carborundum detector and detection effect and oscillations with crystals. *London, Edinburgh Dublin Philos. Mag. J. Sci.* **1928**, *6*, 1024–1044.
- [6] Welker, H. Über neue halbleitende Verbindungen II. *Z. Naturforsch.* **1953**, *8a*, 248–251.
- [7] Welker, H. Über neue halbleitende Verbindungen. *Z. Naturforsch.* **1952**, *7a*, 744–749.
- [8] Biard, J. R.; Pittman, G. E. Semiconductor Radiant Diode. U.S. Patent 3293513, 1966.
- [9] Nair, G. B.; Dhoble, S. J., *The Fundamentals and Applications of Light-Emitting Diodes: The Revolution in the Lighting Industry*. Elsevier Science **2020**.
- [10] Holonyak, N.; Bevacqua, S. F. Coherent (visible) light emission from Ga(As_{1-x}P_x) junctions. *Appl. Phys. Lett.* **1962**, *1*, 82–83.
- [11] Craford, M. G.; Shaw, R. W.; Herzog, A. H.; Groves, W. O. Radiative recombination mechanisms in GaAsP diodes with and without nitrogen doping. *J. Appl. Phys.* **1972**, *43*, 4075–4083.
- [12] Groves, W. O.; Herzog, A. H.; Craford, M. G. The Effect of Nitrogen Doping on GaAs_{1-x}P_x Electroluminescent Diodes. *Appl. Phys. Lett.* **1971**, *19*, 184–186.
- [13] Potter, R. M.; Blank, J. M.; Addamiano, A. Silicon Carbide Light-Emitting Diodes. *J. Appl. Phys.* **1969**, *40*, 2253–2257.
- [14] Edmond, J. A.; Kong, H.-S.; Carter, C. H., Blue LEDs, UV photodiodes and high-temperature rectifiers in 6H-SiC. In *Wide-Band-Gap Semiconductors*, Van de Walle, C. G., Ed. Elsevier: Amsterdam, 1993; pp 453–460.
- [15] Schubert, E. F., *Light-emitting diodes*. E. Fred Schubert Rensselaer Polytech Institute Troy, New York, USA, **2018**.
- [16] Maruska, H. P.; Rhines, W. C. A modern perspective on the history of semiconductor nitride blue light sources. *Solid-State Electron.* **2015**, *111*, 32–41.
- [17] Amano, H.; Sawaki, N.; Akasaki, I.; Toyoda, Y. Metalorganic vapor phase epitaxial growth of a high quality GaN film using an AlN buffer layer. *Appl. Phys. Lett.* **1986**, *48*, 353–355.
- [18] Amano, H.; Akasaki, I.; Kozawa, T.; Hiramatsu, K.; Sawaki, N.; Ikeda, K.; Ishii, Y. Electron beam effects on blue luminescence of zinc-doped GaN. *J. Lumin.* **1988**, *40–41*, 121–122.
- [19] Amano, H.; Kito, M.; Hiramatsu, K.; Akasaki, I. P-Type Conduction in Mg-Doped GaN Treated with Low-Energy Electron Beam Irradiation (LEEBI). *Jpn. J. Appl. Phys* **1989**, *28*, L2112–L2114.
- [20] Akasaki, I.; Amano, H.; Kito, M.; Kazumasa, H. Photoluminescence of Mg-doped p-type GaN and electroluminescence of GaN p-n junction LED. *J. Lumin.* **1991**, *48–49*, 666–670.
- [21] Nakamura, S.; Iwasa, N.; Masayuki, S.; Mukai, T. Hole Compensation Mechanism of P-Type GaN Films. *Jpn. J. Appl. Phys* **1992**, *31*, 1258–1266.
- [22] Nakamura, S.; Mukai, T.; Senoh, M.; Iwasa, N. Thermal Annealing Effects on P-Type Mg-Doped GaN Films. *Jpn. J. Appl. Phys.* **1992**, *31*, L139–L142.
- [23] Nakamura, S.; Mukai, T.; Senoh, M. High-brightness InGaN/AlGaIn double-heterostructure blue-green-light-emitting diodes. *J. Appl. Phys.* **1994**, *76*, 8189–8191.

- [24] Nakamura, S.; Mukai, T.; Senoh, M. Candela-class high-brightness InGaN/AlGaIn double-heterostructure blue-light-emitting diodes. *Appl. Phys. Lett.* **1994**, *64*, 1687–1689.
- [25] Pust, P.; Schmidt, P. J.; Schnick, W. A revolution in lighting. *Nat. Mater.* **2015**, *14*, 454–458.
- [26] Narukawa, Y.; Ichikawa, M.; Sanga, D.; Sano, M.; Mukai, T. White light emitting diodes with super-high luminous efficacy. *J. Phys. D: Appl. Phys.* **2010**, *43*, 354002.
- [27] Schubert, E. F.; Kim, J. K. Solid-State Light Sources Getting Smart. *Science* **2005**, *308*, 1274–1278.
- [28] *2019 Lighting R&D Opportunities*; US Department of Energy, 2019.
- [29] Kitai, A. *Materials for Solid State Lighting and Displays*; Wiley: Chichester, U.K., 2017.
- [30] Bando, K.; Sakano, K.; Noguchi, Y.; Shimizu, Y. Development of High-bright and Pure-white LED Lamps. *J. Light Visual Environ.* **1998**, *22*, 2–5.
- [31] Setlur, A. A. Phosphors for LED-based Solid-State Lighting. *Electrochem. Soc. Interface* **2009**, *18*, 32–36.
- [32] Xie, R.-J.; Hirosaki, N.; Suehiro, T.; Xu, F.-F.; Mitomo, M. A Simple, Efficient Synthetic Route to $\text{Sr}_2\text{Si}_3\text{N}_8:\text{Eu}^{2+}$ -Based Red Phosphors for White Light-Emitting Diodes. *Chem. Mater.* **2006**, *18*, 5578–5583.
- [33] Watanabe, H.; Kijima, N. Crystal structure and luminescence properties of $\text{Sr}_x\text{Ca}_{1-x}\text{AlSiN}_3:\text{Eu}^{2+}$ mixed nitride phosphors. *J. Alloys Compd.* **2009**, *475*, 434–439.
- [34] *Narrow Red Phosphor Technology*; Lumileds Hoding B. V., 2016.
- [35] Pust, P.; Weiler, V.; Hecht, C.; Tucks, A.; Wochnik, A. S.; Henss, A. K.; Wiechert, D.; Scheu, C.; Schmidt, P. J.; Schnick, W. Narrow-band red-emitting $\text{Sr}[\text{LiAl}_3\text{N}_4]:\text{Eu}^{2+}$ as a next-generation LED-phosphor material. *Nat. Mater.* **2014**, *13*, 891–896.
- [36] Hoerder, G. J.; Seibald, M.; Baumann, D.; Schroder, T.; Peschke, S.; Schmid, P. C.; Tyborski, T.; Pust, P.; Stoll, I.; Bergler, M.; Patzig, C.; Reissaus, S.; Krause, M.; Berthold, L.; Hoche, T.; Johrendt, D.; Huppertz, H. $\text{Sr}[\text{Li}_2\text{Al}_2\text{O}_2\text{N}_2]:\text{Eu}^{2+}$ – A high performance red phosphor to brighten the future. *Nat. Commun.* **2019**, *10*, 1–9.
- [37] Liao, H.; Zhao, M.; Molokeev, M. S.; Liu, Q.; Xia, Z. Learning from a Mineral Structure toward an Ultra-Narrow-Band Blue-Emitting Silicate Phosphor $\text{RbNa}_3(\text{Li}_3\text{SiO}_4)_4:\text{Eu}^{2+}$. *Angew. Chem. Int. Ed.* **2018**, *57*, 11728–11731; *Angew. Chem.* **2018**, *130*, 11902–11905.
- [38] Wang, L.; Xie, R. J.; Suehiro, T.; Takeda, T.; Hirosaki, N. Down-Conversion Nitride Materials for Solid State Lighting: Recent Advances and Perspectives. *Chem. Rev.* **2018**, *118*, 1951–2009.
- [39] McKittrick, J.; Hannah, M. E.; Piquette, A.; Han, J. K.; Choi, J. I.; Anc, M.; Galvez, M.; Lugauer, H.; Talbot, J. B.; Mishra, K. C. Phosphor Selection Considerations for Near-UV LED Solid State Lighting. *ECS J. Solid State Sci. Technol.* **2013**, *2*, R3119–R3131.
- [40] Wiedemann, E. Ueber Fluorescenz und Phosphorescenz I. Abhandlung. *Ann. Phys.* **1888**, *270*, 446–463.
- [41] Yen, W. M.; Shinoya, S.; Yamamoto, H. *Phosphor Handbook*; CRS Press: 2007.
- [42] Blasse, G.; Bril, A. Characteristic luminescence. *Philips Tech. Rev.* **1970**, *31*, 303–332.
- [43] Dorenbos, P. f \rightarrow d transition energies of divalent lanthanides in inorganic compounds. *J. Phys.: Condens. Matter* **2003**, *15*, 575–594.
- [44] Dorenbos, P. Energy of the first $4f^7 \rightarrow 4f^65d$ transition of Eu^{2+} in inorganic compounds. *J. Lumin.* **2003**, *104*, 239–260.
- [45] Wiberg, E.; Wiberg, N., *Lehrbuch der anorganischen Chemie*. de Gruyter, Berlin **2007**, Vol. 102.

- [46] Wilhelm, D.; Baumann, D.; Seibald, M.; Wurst, K.; Heymann, G.; Huppertz, H. Narrow-Band Red Emission in the Nitridolithoaluminate $\text{Sr}_4[\text{LiAl}_{11}\text{N}_{14}]:\text{Eu}^{2+}$. *Chem. Mater.* **2017**, *29*, 1204–1209.
- [47] Wagatha, P.; Weiler, V.; Schmidt, P. J.; Schnick, W. Tunable Red Luminescence in Nitridomagnesoaluminates $\alpha\text{-Sr}_2[\text{MgAl}_5\text{N}_7]:\text{Eu}^{2+}$, $\beta\text{-Sr}_2[\text{MgAl}_5\text{N}_7]:\text{Eu}^{2+}$, and $\text{Sr}_8[\text{LiMg}_2\text{Al}_{21}\text{N}_{28}]:\text{Eu}^{2+}$. *Chem. Mater.* **2018**, *30*, 1755–1761.
- [48] Wagatha, P.; Pust, P.; Weiler, V.; Wochnik, A. S.; Schmidt, P. J.; Scheu, C.; Schnick, W. $\text{Ca}_{18.75}\text{Li}_{10.5}[\text{Al}_{39}\text{N}_{55}]:\text{Eu}^{2+}$ — Supertetrahedron Phosphor for Solid-State Lighting. *Chem. Mater.* **2016**, *28*, 1220–1226.
- [49] Wagatha, P.; Weiler, V.; Schmidt, P. J.; Schnick, W. Tailoring Emission Characteristics: Narrow-Band Red Luminescence from SLA to $\text{CaBa}[\text{Li}_2\text{Al}_6\text{N}_8]:\text{Eu}^{2+}$. *Chem. Mater.* **2018**, *30*, 7885–7891.
- [50] Pust, P.; Wochnik, A. S.; Baumann, E.; Schmidt, P. J.; Wiechert, D.; Scheu, C.; Schnick, W. $\text{Ca}[\text{LiAl}_3\text{N}_4]:\text{Eu}^{2+}$ — A Narrow-Band Red-Emitting Nitridolithoaluminate. *Chem. Mater.* **2014**, *26*, 3544–3549.
- [51] Pust, P.; Hintze, F.; Hecht, C.; Weiler, V.; Locher, A.; Zitnanska, D.; Harm, S.; Wiechert, D.; Schmidt, P. J.; Schnick, W. Group (III) Nitrides $M[\text{Mg}_2\text{Al}_2\text{N}_4]$ ($M = \text{Ca}, \text{Sr}, \text{Ba}, \text{Eu}$) and $\text{Ba}[\text{Mg}_2\text{Ga}_2\text{N}_4]$ — Structural Relation and Nontypical Luminescence Properties of Eu^{2+} Doped Samples. *Chem. Mater.* **2014**, *26*, 6113–6119.
- [52] Li, S.; Xie, R.-J.; Takeda, T.; Hirosaki, N. Critical Review—Narrow-Band Nitride Phosphors for Wide Color-Gamut White LED Backlighting. *ECS J. Solid State Sci. Technol.* **2018**, *7*, R3064–R3078.
- [53] Kloss, S. D.; Schnick, W. Nitridophosphates: A Success Story of Nitride Synthesis. *Angew. Chem. Int. Ed.* **2019**, *58*, 7933–7944; *Angew. Chem.* **2019**, *131*, 8015–8027.
- [54] Shannon, R. D. Revised effective ionic radii and systematic studies of interatomic distances in halides and chalcogenides. *Acta Crystallogr., Sect. A: Cryst. Phys., Diffr. Theor. Gen. Crystallogr.* **1976**, *32*, 751–767.
- [55] Popper, P.; Ruddlesden, S. N. Structure of the Nitrides of Silicon and Germanium. *Nature* **1957**, *179*, 1129.
- [56] Stackelberg, M. v.; Paulus, R. Untersuchungen über die Kristallstruktur der Nitride und Phosphide zweiwertiger Metalle. *Z. Phys. Chem.* **1933**, *22*, 305–322.
- [57] Strobel, P.; de Boer, T.; Weiler, V.; Schmidt, P. J.; Moewes, A.; Schnick, W. Luminescence of an Oxonitridoberyllate: A Study of Narrow-Band Cyan-Emitting $\text{Sr}[\text{Be}_6\text{ON}_4]:\text{Eu}^{2+}$. *Chem. Mater.* **2018**, *30*, 3122–3130.
- [58] Strobel, P.; Maak, C.; Weiler, V.; Schmidt, P. J.; Schnick, W. Ultra-Narrow-Band Blue-Emitting Oxoberyllates $\text{AELi}_2[\text{Be}_4\text{O}_6]:\text{Eu}^{2+}$ ($\text{AE} = \text{Sr}, \text{Ba}$) Paving the Way to Efficient RGB pc-LEDs. *Angew. Chem. Int. Ed.* **2018**, *57*, 8739–8743; *Angew. Chem.* **2018**, *130*, 8875–8879.
- [59] Naglav, D.; Buchner, M. R.; Bendt, G.; Kraus, F.; Schulz, S. Off the Beaten Track-A Hitchhiker's Guide to Beryllium Chemistry. *Angew. Chem. Int. Ed.* **2016**, *55*, 10562–10576; *Angew. Chem.* **2016**, *128*, 10718–10733.
- [60] Kumberger, O.; Schmidbaur, H. Warum ist Beryllium so toxisch? *Chem. Unserer Zeit* **1993**, *27*, 310–316.
- [61] Vauquelin, L.-N. Analyse de l'Aiguemarine, ou Béril; et découverte d'une terre nouvelle dans cette pierre. *Ann. Chim. Phys.* **1798**, *26*, 155–169.
- [62] Wöhler, F. Ueber das Beryllium und Yttrium. *Ann. Phys.* **1828**, *89*, 577–582.
- [63] Stock, A. Beryllium. *Angew. Chem.* **1929**, *42*, 637–652.

- [64] Wenk, H.-R.; Bulakh, A., *Minerals: their constitution and origin*. Cambridge University Press **2016**.
- [65] <https://www.mineralienatlas.de/index.php> (accessed 28.02.2022).
- [66] Agency for Toxic Substances and Disease Registry (ATSDR). *Toxicological Profile for Beryllium*; U.S. Department of Health and Human Services, P. H. S., Atlanta, GA, 1996.
- [67] Puchta, R. A brighter beryllium. *Nat. Chem.* **2011**, 3, 416.
- [68] <https://webb.nasa.gov/content/about/launch.html> (accessed 15.02.2021).
- [69] Feinberg, L. D.; Clampin, M.; Keski-Kuha, R.; Atkinson, C.; Texter, S.; Bergeland, M.; Gallagher, B. B. In *James Webb Space Telescope optical telescope element mirror development history and results*, Space Telescopes and Instrumentation 2012: Optical, Infrared, and Millimeter Wave, SPIE: 2012; pp 822-831.
- [70] Silliman, H. F. Beryllium-Copper Alloys. *Ind. Eng. Chem.* **1936**, 28, 1421–1428.
- [71] Eckerlin, P.; Rabenau, A. Zur Kenntnis des Systems $\text{Be}_3\text{N}_2\text{-Si}_3\text{N}_4$. Die Struktur einer neuen Modifikation von Be_3N_2 . *Z. Anorg. Allg. Chem.* **1960**, 304, 218–229.
- [72] Hall, D.; Gurr, G. E.; Jeffrey, G. A. Zur Kenntnis des Systems $\text{Be}_3\text{N-Si}_3\text{N}_4$. V. A Refinement of the Crystal structure of β -Beryllium Nitride. *Z. Anorg. Allg. Chem.* **1969**, 369, 108–112.
- [73] Somer, M.; Carrillo-Cabrera, W.; Peters, E.-M.; Peters, K.; von Schnering, H. Crystal structure of lithium beryllium nitride, LiBeN . *Z. Kristallogr.-Cryst. Mater.* **1996**, 211, 635–635.
- [74] Somer, M.; Yarasik, A.; Akselrud, L.; Leoni, S.; Rosner, H.; Schnelle, W.; Kniep, R. $\text{Ae}[\text{Be}_2\text{N}_2]$: nitridoberyllates of the heavier alkaline-earth metals. *Angew. Chem. Int. Ed.* **2004**, 43, 1088–1092; *Angew. Chem.* **2004**, 116, 1108–1112.
- [75] Eckerlin, P.; Rabenau, A.; Nortmann, H. Zur Kenntnis des Systems $\text{Be}_3\text{N}_2\text{-Si}_3\text{N}_4$. III. Darstellung und Eigenschaften von BeSiN_2 . *Z. Anorg. Allg. Chem.* **1967**, 353, 113–121.
- [76] Eckerlin, P. Zur Kenntnis des Systems $\text{Be}_3\text{N}_2\text{-Si}_3\text{N}_4$. IV. Die Kristallstruktur von BeSiN_2 . *Z. Anorg. Allg. Chem.* **1967**, 353, 225–235.
- [77] Pucher, F. J.; Römer, S. R.; Karau, F. W.; Schnick, W. Phenakite-type BeP_2N_4 – a possible precursor for a new hard spinel-type material. *Chem. Eur. J.* **2010**, 16, 7208–14.
- [78] Strobel, P.; Weiler, V.; Schmidt, P. J.; Schnick, W. $\text{Sr}[\text{BeSi}_2\text{N}_4]\text{:Eu}^{2+}/\text{Ce}^{3+}$ and $\text{Eu}[\text{BeSi}_2\text{N}_4]$: Nontypical Luminescence in Highly Condensed Nitridoberyllsilicates. *Chem. Eur. J.* **2018**, 24, 7243–7249.
- [79] Vogel, S.; Bykov, M.; Bykova, E.; Wendl, S.; Kloss, S. D.; Pakhomova, A.; Dubrovinskaia, N.; Dubrovinsky, L.; Schnick, W. Nitride Spinel: An Ultraincompressible High-Pressure Form of BeP_2N_4 . *Angew. Chem. Int. Ed.* **2020**, 59, 2730–2734; *Angew. Chem.* **2020**, 132, 2752–2756.
- [80] Ding, Y. M.; Ji, Y.; Dong, H.; Rujisamphan, N.; Li, Y. Electronic properties and oxygen reduction reaction catalytic activity of $h\text{-BeN}_2$ and MgN_2 by first-principles calculations. *Nanotechnology* **2019**, 30, 465202.
- [81] Zhang, C.; Sun, Q. A Honeycomb BeN_2 Sheet with a Desirable Direct Band Gap and High Carrier Mobility. *J. Phys. Chem. Lett.* **2016**, 7, 2664–70.
- [82] Chen, C.; Huang, B.; Wu, J. Be_3N_2 monolayer: A graphene-like two-dimensional material and its derivative nanoribbons. *AIP Adv.* **2018**, 8, 105105.
- [83] Zhang, X.; Xie, X.; Dong, H.; Zhang, X.; Wu, F.; Mu, Z.; Wen, M. Pressure-Induced High-Energy-Density BeN_4 Materials with Nitrogen Chains: First-Principles Study. *J. Phys. Chem. C* **2021**, 125, 25376–25382.
- [84] Zhang, S.; Zhao, Z.; Liu, L.; Yang, G. Pressure-induced stable BeN_4 as a high-energy density material. *J. Power Sources* **2017**, 365, 155–161.
- [85] Bykov, M.; Fedotenko, T.; Chariton, S.; Laniel, D.; Glazyrin, K.; Hanfland, M.; Smith, J. S.; Prakapenka, V. B.; Mahmood, M. F.; Goncharov, A. F.; Ponomareva, A. V.; Tasnadi, F.;

Abrikosov, A. I.; Bin Masood, T.; Hotz, I.; Rudenko, A. N.; Katsnelson, M. I.; Dubrovinskaia, N.; Dubrovinsky, L.; Abrikosov, I. A. High-Pressure Synthesis of Dirac Materials: Layered van der Waals Bonded BeN₄ Polymorph. *Phys. Rev. Lett.* **2021**, *126*, 175501.

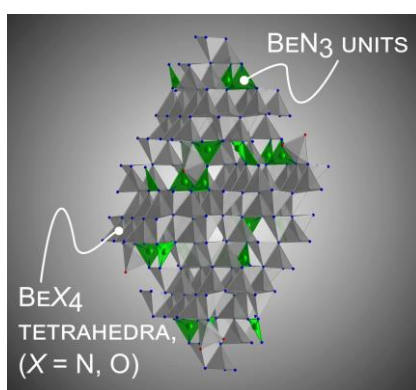
2. $\text{Eu}_3\text{Be}_{22}\text{N}_{16}\text{O}$: A Highly Condensed Oxonitridoberyllate

Eugenia Elzer, Martin Weidemann, and Wolfgang Schnick

Eur. J. Inorg. Chem. **2021**, 4979

DOI: 10.1002/ejic.202100807

Reprinted (adapted) with permission for non-commercial use from European Journal of Inorganic Chemistry (open access). Copyright 2021 John Wiley and Sons.



ABSTRACT: The oxonitridoberyllate $\text{Eu}_3\text{Be}_{22}\text{N}_{16}\text{O}$ was synthesized from $\text{Eu}(\text{NH}_2)_2$, Be_3N_2 and BeO in a W crucible under N_2 atmosphere in a radio-frequency furnace at $1400\text{ }^\circ\text{C}$. The crystal structure was solved and refined from X-ray diffraction data ($C2/c$ (no. 15), $a = 20.620(2)$, $b = 8.722(6)$, $c = 17.506(2)\text{ \AA}$, $\beta = 120.782(3)^\circ$) and confirmed with Rietveld refinement methods as well as lattice-energy calculations (Madelung part of lattice energy, MAPLE). $\text{Eu}_3\text{Be}_{22}\text{N}_{16}\text{O}$ consists of a rigid network of edge-sharing BeX_4 ($X = \text{N}, \text{O}$) tetrahedra and trigonal-planar BeN_3 units resulting in a high degree of condensation $\kappa = 1.29$. The charge of the anionic network is compensated by Eu^{2+} . Magnetic susceptibility measurements exhibit Curie-Weiss behavior above 2 K with an effective magnetic moment of $7.82\text{ }\mu_{\text{B}}/\text{f.u.}$, which is in accordance with the theoretical value for Eu^{II} .

2.1 Introduction

Over the past years, research on nitrides became an emerging and rapidly growing field in solid-state chemistry due to their intriguing chemical and physical properties, such as wide band gaps, or thermal and chemical stability.^[1] Especially, the application of Eu^{2+} and Ce^{3+} doped (oxo)nitrides as phosphors in solid-state lighting solutions has fueled the ongoing investigation of highly condensed

nitridosilicates, -aluminates and -phosphates as possible host lattices. Here, structures with a high degree of condensation are discussed to be favorable to narrow-band emitting phosphors.^[2]

Compared to oxides, (oxo)nitrides are considered to have a higher structural diversity, since nitrogen can connect up to four neighboring tetrahedra over common corners or even exhibit edge-sharing tetrahedra.^[3] This type of connectivity can give rise to highly condensed networks, whose degree of condensation κ is given as the fraction of the tetrahedral centers T to the coordinating anions N/O : $\kappa = n(T):n(N/O)$. In case of the binary nitrides of elements P, Si, Al and Mg it is apparent, that the degree of condensation increases with decreasing oxidation number of the tetrahedral center ($\kappa(\text{P}_3\text{N}_5) = 0.6$, $\kappa(\text{Si}_3\text{N}_4) = 0.75$, $\kappa(\text{AlN}) = 1.0$ and $\kappa(\text{Mg}_3\text{N}_2) = 1.5$). While the exploration of new structures in the class of nitrido(magnesio/litho)silicates and -(magnesio/litho)aluminates has been intensively pursued in the last decade, and led to the discovery of suitable candidates for application in LEDs (e. g., $(\text{Ba},\text{Sr})_2\text{Si}_5\text{N}_8:\text{Eu}^{2+}$,^[4, 5] $\text{Sr}[\text{LiAl}_3\text{N}_4]:\text{Eu}^{2+}$,^[6] or $\text{Sr}[\text{Li}_2\text{Al}_2\text{O}_2\text{N}_2]:\text{Eu}^{2+}$),^[7] the element beryllium has only recently moved into the focus of research. There are two aspects that make beryllium suitable for the discovery of new structures: the lower charge compared to Al^{3+} or Si^{4+} , and the possibility of both three- and fourfold coordination around Be^{2+} , thus making BeN_4 tetrahedra and trigonal-planar BeN_3 units possible.

Until 2018 only few representatives containing Be as a network building atom have been discovered: LiBeN and $M\text{Be}_2\text{N}_2$ ($M = \text{Mg}, \text{Ca}-\text{Ba}$).^[8-10] The crystal structure of LiBeN ($\kappa = 1.0$) contains corrugated layers of corner- and edge-sharing BeN_3 units and LiN_4 tetrahedra. MgBe_2N_2 ($\kappa = 1.0$) crystallizes in the *anti*- La_2O_3 structure type and forms a structure of alternating layers of edge-sharing BeN_4 tetrahedra and MgN_6 octahedra. Contrary, the heavier homologues Ca–Ba form $M\text{Be}_2\text{N}_2$ isotypic with $\text{Ca}[\text{B}_2\text{C}_2]$ containing planar layers of vertex-sharing BeN_3 units and AE^{2+} ions ($AE = \text{Ca}, \text{Sr}, \text{Ba}$).

Recent research in the field of oxonitridoberyllates has resulted in the discovery of two representatives exhibiting a high degree of condensation and luminescence upon doping with Eu^{2+} . While the oxonitridoberyllate $\text{Sr}[\text{Be}_6\text{ON}_4]:\text{Eu}^{2+}$ ($\kappa = 1.2$)^[11] contains both edge- and vertex-sharing BeN_4 and BeON_3 tetrahedra, the ternary nitridoberyllate $M\text{Be}_{20}\text{N}_{14}:\text{Eu}^{2+}$ ($M = \text{Sr}, \text{Ba}$) ($\kappa = 1.43$)^[12] consists solely of edge- and vertex-sharing BeN_4 tetrahedra and exhibits a degree of condensation very close to that of the binary nitride Be_3N_2 .

Here, we report on the preparation and characterization of $\text{Eu}_3\text{Be}_{22}\text{N}_{16}\text{O}$, an oxonitridoberyllate synthesized in a radio-frequency furnace exhibiting a previously not observed combination of BeN_4 and BeN_2O_2 tetrahedra and BeN_3 units in the crystal structure.

2.2 Results and Discussion

Synthesis and elemental analysis

The oxonitridoberyllate $\text{Eu}_3\text{Be}_{22}\text{N}_{16}\text{O}$ was synthesized in a high-temperature reaction (1400 °C) in a radio-frequency (rf) furnace under N_2 atmosphere starting from stoichiometric amounts of $\text{Eu}(\text{NH}_2)_2$, Be_3N_2 and BeO (Equation (1)). Detailed information on the synthesis is given in the Supporting Information (Table A.1).



The product was obtained as a crystalline powder with dark red color, which slowly undergoes hydrolysis under ambient conditions. For safety reasons, all manipulation of the samples were performed in a glovebox or under Schlenk conditions. Figure 2.1 shows the typical size ($<5 \mu\text{m}$) and appearance of the strongly intergrown small crystals, which impeded single-crystal XRD data acquisition.

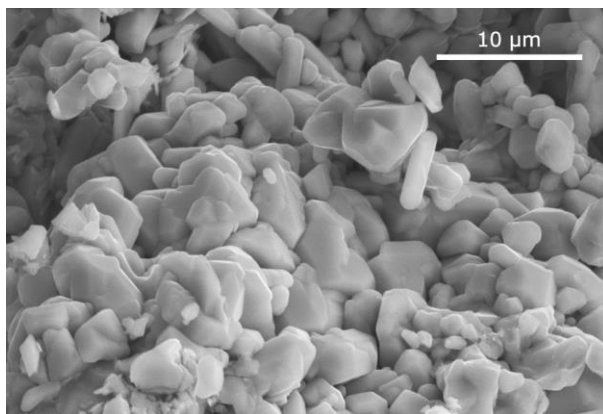


Figure 2.1. Sample morphology of $\text{Eu}_3\text{Be}_{22}\text{N}_{16}\text{O}$.

The atomic ratio $\text{Eu}:\text{N}:\text{O}$ obtained from EDX measurements (Table A.2) is 3:15.4:1.4 and corresponds well with the sum formula obtained from single-crystal X-ray data. Due to methodical limitations Be cannot be detected by EDX. As no other metals than Eu were detected, Be is assumed as the only possible central atom for the tetrahedra. The assignment of Be as central atoms for the tetrahedra and trigonal planar units is in the following further supported by analysis of the bond

distances in the structural model, lattice-energy calculations (Madelung part of lattice energy, MAPLE), and bond valence sum (BVS) calculations.^[13] The absence of N–H and O–H groups was confirmed by Fourier transform infrared (FTIR) spectroscopy (Figure A.1).

Structure determination

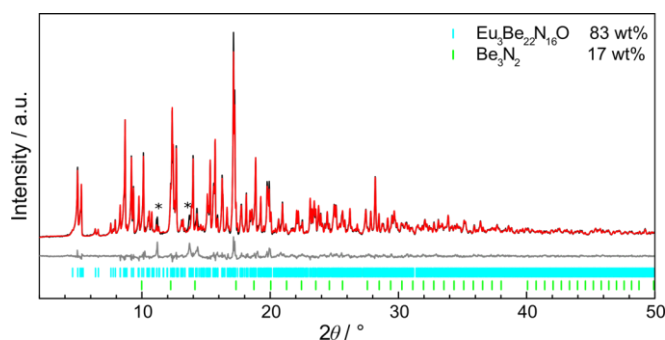
The crystal structure of the title compound was elucidated by X-ray diffraction experiments. Eu₃Be₂₂N₁₆O crystallizes in monoclinic space group *C2/c* (no. 15) with cell parameters $a = 20.620(2)$, $b = 8.722(6)$, $c = 17.506(2)$ Å, $\beta = 120.782(3)^\circ$. Crystallographic data are given in Table 2.1. The data set from a twinned crystal was merged with another crystal data set (overexposed) with different scale factors to fill in missing high angle data and improve and to improve the reflex determination of the light atoms compared to the heavy atoms. Further information (atomic coordinates, Wyckoff positions, isotropic and anisotropic displacement parameter) can be found in the Supporting Information (Table A.3 and Table A.4).

During refinement, two possibilities have been considered for a charge-balanced sum formula. One possible sum formula is a nitride with Eu in two different oxidation states: Eu^{II}₂Eu^{III}Be₂₂N₁₇ and the other is a substitution of one N³⁻ with O²⁻ leading to the sum formula Eu^{II}₃Be₂₂N₁₆O. Magnetic measurements and BVS calculations (Table A.5) revealed exclusively presence of Eu^{II}, therefore the compound was considered to be an oxonitridoberyllate Eu^{II}₃Be₂₂N₁₆O. Since X-rays cannot differentiate between O and N, the assignment of O to the position with the shortest Eu–*X* (*X* = O/N) distances was derived from MAPLE and BVS calculations (see below).

The electrostatic consistency of the entire crystal structure was further corroborated with MAPLE calculations. Here, electrostatic interactions, depending on the charge, distance and coordination spheres of the ions, were taken into account.^[14] MAPLE values were calculated for each ion type and for the complete structure and are summarized in Table A.6. The partial MAPLE values for Eu²⁺, Be²⁺, N³⁻ and O²⁻ are in good agreement with the literature.^[12, 14-16] The comparison of the MAPLE value (Table A.6) for the whole compound with values of constituent binary nitrides and oxides show only minor deviations. Rietveld refinement of powder X-ray diffraction data (Figure 2.2, Table A.7) identified Eu₃Be₂₂N₁₆O as the main phase, with Be₃N₂ as a side phase.

Table 2.1. Crystallographic data of $\text{Eu}_3\text{Be}_{22}\text{N}_{16}\text{O}$, standard deviations in parentheses.

	$\text{Eu}_3\text{Be}_{22}\text{N}_{16}\text{O}$
Formula mass/ $\text{g}\cdot\text{mol}^{-1}$	894.26
Crystal system	monoclinic
Space group	$C2/c$ (no. 15)
$a/\text{\AA}$	20.620(2)
$b/\text{\AA}$	8.722(6)
$c/\text{\AA}$	17.506(2)
$\beta/^\circ$	120.782(3)
Volume/ \AA^3	2704.69(4)
Z	8
$\rho_{\text{X-ray}}/\text{g}\cdot\text{cm}^{-3}$	4.392
Abs. coefficient/ $\mu\cdot\text{mm}^{-1}$	13.792
F(000)	3176
Crystal dimensions/ mm^3	$0.003 \times 0.002 \times 0.002$
Diffractometer	Bruker D8 Venture
Radiation	Mo- K_α ($\lambda = 0.71073 \text{\AA}$)
Temperature/ K	293(2)
Absorption correction	Multi-scan
θ range/ $^\circ$	2.79–29.572
Observed reflections	27106
Independent reflections	2453
Independent reflections with $I \geq 2\sigma(I)$	2449
Min./ max. transmission	0.927/ 1.000
Refined parameters	300
R_σ	0.0319
R indices ($F_0^2 \geq 2\sigma(F_0^2)$)	$R1 = 0.0369 / wR2 = 0.0967$
R indices (all data)	$R1 = 0.0452 / wR2 = 0.0962$
GoF	1.077
Data completeness	0.999
Min./ max. residual electron density/ $\text{e}\cdot\text{\AA}^{-3}$	-2.893/ 3.797

**Figure 2.2.** Rietveld refinement of $\text{Eu}_3\text{Be}_{22}\text{N}_{16}\text{O}$ (Mo $K_\alpha = 0.71073 \text{\AA}$). Observed (black), and calculated (red) powder X-ray diffraction pattern with the corresponding difference profile (gray). Respective positions of Bragg reflections of $\text{Eu}_3\text{Be}_{22}\text{N}_{16}\text{O}$ (cyan), and Be_3N_2 (green) are marked as vertical bars. Unidentified reflections are marked with an asterisk (*).

Structure description

$\text{Eu}_3\text{Be}_{22}\text{N}_{16}\text{O}$ can be described as a highly condensed oxonitridoberyllate with a degree of condensation of $\kappa = n(\text{Be}):n(\text{N}, \text{O}) = 1.29$. Compared to nitridosilicates or -aluminates, (oxo)nitridoberyllates can exhibit a higher degree of condensation, as BeN_4 tetrahedra can be connected over several edges due to the lower formal charge of Be^{2+} compared to Al^{3+} or Si^{4+} . The high connectivity of the tetrahedra are illustrated in Figure 2.3.

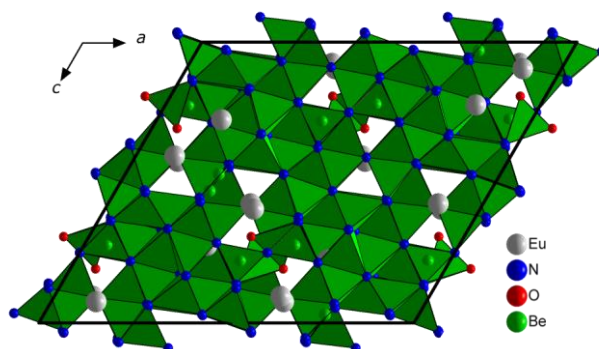


Figure 2.3. Crystal structure of $\text{Eu}_3\text{Be}_{22}\text{N}_{16}\text{O}$, with BeX_4 tetrahedra ($X = \text{N}, \text{O}$) and BeN_3 units in green, N atoms in blue, O atoms in red and Eu atoms in gray. The unit cell is outlined in black. Projection of the crystal structure along [010].

To describe the structure in more detail, the arrangement of the units can be formally deconstructed into layers consisting of trigonal planar BeN_3 units and BeN_4 or BeO_2N_2 tetrahedra, respectively (Figure 2.4 a). Figure 2.4 b shows the individual layers A (cyan), B (blue), C (gray) and D (green). Layers A, B and C are related by inversion centers with layers A', B' and C'. The representation of the individual layers in Figure 2.4 b also allows to see the trigonal-planar BeN_3 units, which appear as double units. Each one shares either a vertex or an edge to another BeN_3 unit, while the remaining corners are connected to BeN_4 tetrahedra. This arrangement creates a network of Be and N which has not been observed so far.

The unique topology of the anionic network exhibits the point symbol $\{3^{11}.4^{12}.5^5\}\{3^{13}.4^{10}.5^5\}\{3^{20}.4^{24}.5^{11}\}_2\{3^{25}.4^{32}.5^9\}\{3^{30}.4^{33}.5^3\}\{3^{30}.4^{34}.5^2\}\{3^{30}.4^{42}.5^6\}\{3^{31}.4^{40}.5^7\}_2\{3^{32}.4^{41}.5^5\}\{3^{36}.4^{51}.5^4\}\{3^{37}.4^{47}.5^7\}\{3^{38}.4^{49}.5^4\}\{3^{39}.4^{47}.5^5\}_2\{3^{40}.4^{49}.5^2\}\{3^{41}.4^{48}.5^2\}\{3^{41}.4^{58}.5^6\}_2\{3^{43}.4^{55}.5^7\}\{3^{46}.4^{66}.5^8\}$ as determined by TOPOS.^[17]

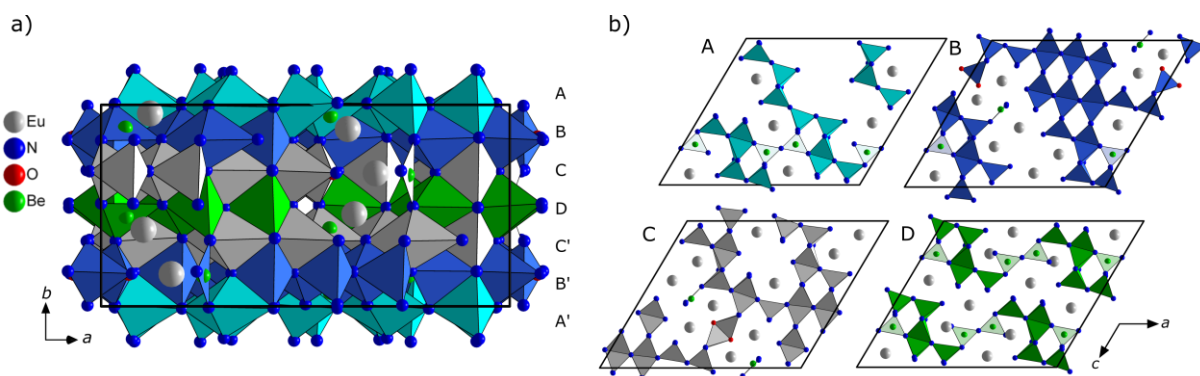


Figure 2.4. a) Projection of the crystal structure of $\text{Eu}_3\text{Be}_{22}\text{N}_{16}\text{O}$ along $[001]$ with layers of color coded BeX_4 ($X = \text{N}, \text{O}$) tetrahedra (darker color) and BeN_3 units (lighter color), N atoms in blue, O atoms in red and Eu atoms in gray; unit cell is outlined in black. b) A (cyan), B (blue), C (gray) and D (green) layer, view along $[010]$. BeN_3 units can be distinguished from BeX_4 tetrahedra through the visible Be central atom in green.

A selection of the interatomic distances in the anionic network is displayed in Table 2.2, while the entire list of interatomic distances can be found in the Supporting Information (Table A.8). As expected the Be–O distances are slightly shorter compared to those of Be–N, but overall the values correspond well to comparable compounds.^[8-12]

Table 2.2: Selection of interatomic distances in the anionic network of $\text{Eu}_3\text{Be}_{22}\text{N}_{16}\text{O}$ in Å.

	Be–N	Be–O
BeN_4 tetrahedra	1.68(2)–1.93(2)	-
BeN_2O_2 tetrahedra	1.87(2)–1.94(2)	1.65(2)–1.67(2)
BeN_3 units	1.58(2)–1.69(2)	-

As expected, the average bond length (Table A.9) within the tetrahedra (1.76 Å) is significantly longer than the average bond length within the trigonal planar units (1.65 Å), since the distances become larger with higher coordination numbers. To rule out that the trigonal-planar BeN_3 units were not highly distorted tetrahedra the distance to the nearest ligand was checked. The nearest N atom, which theoretically would lead to distorted tetrahedral coordination around Be20, Be21, and Be22, is at a distance larger than 2.4 Å, which is too long for typical bonding Be–N distances. Accordingly, trigonal-planar coordination around sites Be20, Be21, and Be22 is confirmed.

The angles (Table A.10) N–Be–N in the BeN_4 tetrahedra are in the range 100.5(6)–126.5(7)° and the angles of N–Be–N in the trigonal-planar BeN_3 units are in the range 106.6(7)–126.7(8)°, which is in good agreement with other nitridoberyllates.^[8-12] Only the BeN_2O_2 tetrahedra around Be19 show stronger deviations from these values (96.1(8)–118.4(8)°). Such deviations from the typical angle in a

tetrahedron are usually observed when two tetrahedra share a common edge, forming a so-called bow-tie units,^[18] which is also the case in this compound.

The charge of the anionic network is compensated by the incorporation of Eu^{2+} ions. Each Eu atom is surrounded by nine N atoms at a distance of 2.504(7)–3.174(6) Å and one O atom at a distance of 2.457(7)–2.482(8) Å (Table A.8, Figure A.2) in the form of a single-capped triangular cupola (Figure 2.5a). Three of such triangular cupola are further connected over edges and connected to each other over edges in all directions as illustrated in Figure 2.5b. Large distances are not unusual for Eu^{2+} surrounded by ten ligands and the average bond length of 2.82 Å agrees well with the sum of the Shannon radii (2.81 Å).^[19]

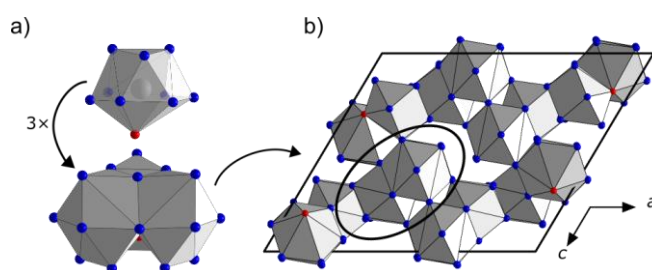


Figure 2.5. Coordination polyhedra around Eu^{2+} in the structure of $\text{Eu}_3\text{Be}_{22}\text{N}_{16}\text{O}$. a) top: one Eu^{2+} (gray) surrounded by nine N atoms (blue) and one O atom (red) forming a single capped triangle cupola around the central atom. down: display of three polyhedra around Eu^{2+} . b) projection of the coordination polyhedra around Eu^{2+} , view along [010], unit cell is outlined in black. The black ellipse indicates the triple pack already displayed in (a).

Magnetization Measurements

Magnetic susceptibility measurements of $\text{Eu}_3\text{Be}_{22}\text{N}_{16}\text{O}$ were performed to determine the oxidation state of Eu in the structure of $\text{Eu}_3\text{Be}_{22}\text{N}_{16}\text{O}$ (Figure 2.6). The compound exhibits a linear paramagnetic behavior following the Curie-Weiss law down to 6 K. The effective magnetic moment of $\mu_{\text{eff}} = 7.82 \mu_{\text{B}}$ was obtained from a Curie Weiss fit of the inverse molar susceptibility (inset of Figure 2.6) and is in good agreement with the theoretical value of $\mu_{\text{eff}} = 7.94 \mu_{\text{B}}$ for Eu^{2+} , confirming Eu^{2+} being the only species within the compound.^[20] Magnetization isotherms for 2.5 and 300 K are shown in Figure A.3. Paramagnetic saturation occurs at 2.5 K also tending towards the expected value $gJ(\text{Eu}^{2+}) = 6.5 \mu_{\text{B}}$.

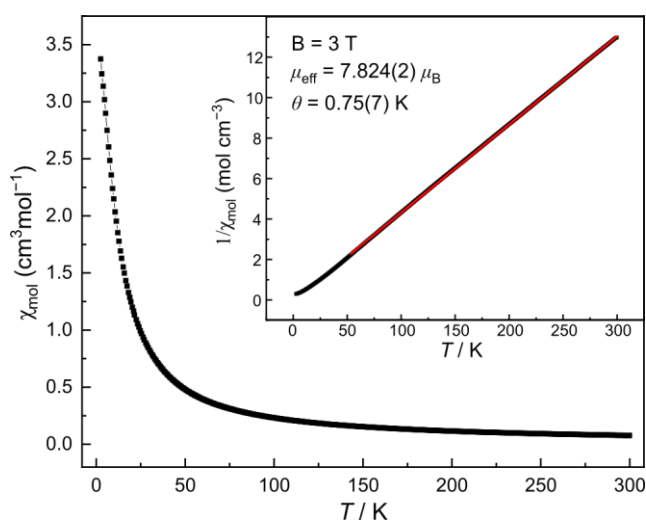


Figure 2.6. Magnetic susceptibility (black) and inverse susceptibility with the Curie-Weiss fit in red in the inset of $\text{Eu}_3\text{Be}_{22}\text{N}_{16}\text{O}$.

2.3 Conclusion

Simultaneous occurrence of trigonal-planar units and tetrahedral coordination of Be has already been observed in oxoberyllates, but not in nitridoberyllates. Until now, nitridoberyllates containing either trigonal-planar BeN_3 units (LiBeN , $M[\text{Be}_2\text{N}_2]$ with $M = \text{Ca}, \text{Sr}, \text{Ba}$) or BeN_4 tetrahedra ($\text{Mg}[\text{Be}_2\text{N}_2]$, or $M\text{Be}_{20}\text{N}_{14}$ with $M = \text{Sr}, \text{Ba}$) has been reported.

Here, we present the crystal structure of $\text{Eu}_3\text{Be}_{22}\text{N}_{16}\text{O}$ which contains BeN_4 and BeN_2O_2 tetrahedra and trigonal-planar BeN_3 units creating an anionic network with a high coordination degree of $\kappa = 1.29$. The crystal structure was solved using single-crystal diffraction data and supported by MAPLE and BVS calculations. With regard to the increasing interest in nitridoberyllates as host compounds for phosphors in solid-state lighting solutions, $\text{Eu}_3\text{Be}_{22}\text{N}_{16}\text{O}$ could be a stepping stone for the discovery of a luminescent compound, by substituting Eu with the alkaline earth metals Sr or Ba and adding only small amounts of Eu^{2+} as a dopant.

2.4 Experimental Section

Safety assessment

Since the element Be is declared as toxic and carcinogenic Be samples containing beryllium were handled with great caution.^[21, 22] To prevent exposure to Be, especially Be containing dusts, direct contact with the chemicals was prevented by using gloveboxes or working under Schlenk conditions.

Synthesis of $\text{Eu}_3\text{Be}_{22}\text{N}_{16}\text{O}$

$\text{Eu}_3\text{Be}_{22}\text{N}_{16}\text{O}$ was synthesized by a high temperature reaction in a radio frequency (rf) furnace under N_2 atmosphere. For safety reasons and due to the sensitivity of the starting materials to hydrolysis, all manipulation of the samples were performed in a glovebox (Unilab, MBraun, filled with dry Ar, $\text{H}_2\text{O} < 0.1$ ppm, and $\text{O}_2 < 0.1$ ppm). The starting materials $\text{Eu}(\text{NH}_2)_2$, Be_3N_2 (synthesized from Be (ABCR, 99+%, 325 mesh) at 1400°C under a N_2 atmosphere) and BeO (Alfa Aesar, 99.95%) were ground in a tungsten carbide mortar and filled into a tungsten crucible, which was transferred under Ar into a rf furnace. The sample was heated up to 1400°C in 1 h, kept at this temperature for 2 h and cooled down to room temperature in 1 h. The product was obtained as a crystalline powder with dark red body color.

Scanning electron microscopy (SEM) and energy-dispersive X-ray diffraction (EDX)

The morphology and chemical analysis was investigated with a Dual-beam Helios Nanolab G3 UC (FEI, Hillsboro) equipped with a X-Max 80 SDD detector (Oxford instruments, Abingdon). The EDX measurements were performed on carbon coated samples with an acceleration voltage of 20 keV.

FRIT spectroscopy

Fourier transform infrared (FTIR) spectra of $\text{Eu}_3\text{Be}_{22}\text{N}_{16}\text{O}$ were obtained using a Perkin WLMER BXII spectrometer with an attenuated total reflectance unit (ATR).

Single-crystal X-ray diffraction

Single crystals of $\text{Eu}_3\text{Be}_{22}\text{N}_{16}\text{O}$ were isolated from bulk samples, selected under an optical microscope and fixed on MicroMounts (MiTeGen, 20–30 μm). X-ray diffraction data were collected on a Bruker D8 Venture diffractometer with a rotating anode using $\text{Mo K}\alpha$ radiation. The program package APEX3 was used for the integration and absorption correction.^[23] The structure was solved by Direct Methods (SHELXS)^[24] and refined by least-square method (SHELXL).^[25, 26] Detailed crystallographic information can be accessed free of charge by the joint Cambridge Crystallographic Data Centre and Fachinformationszentrum Karlsruhe online deposition service by quoting the deposition number CSD 2104949.

Powder X-ray diffraction

Powder samples were finely ground and sealed in glass capillaries with 0.3 mm diameter (Hilgenberg, Germany). Powder X-ray diffraction data were collected on a STOE Stadi P diffractometer with a Ge(111) monochromator ($\text{Mo K}\alpha_1$ radiation) and a Mythen 1K detector in parafocusing Debye-Scherrer geometry. Rietveld refinements were carried out using the TOPAS Academic 6 package, applying the fundamental parameters approach.^[27-30]

Magnetization measurements

Magnetization isotherms and susceptibility measurements of powder samples were performed with a Quantum Design Inc. PPMS, equipped with a vibrating sample magnetometer (VSM) option. Data were collected with field strengths of ± 50 kOe between temperatures of 2.5–300 K using a PPMS MultiVu software package.^[31]

2.5 Acknowledgements

The authors thank Christian Minke for EDX measurements and Prof. Dr. D. Johrendt for the magnetic measurements. Great thanks and appreciations go to Sophia Wandelt, Reinhard Pritzl, Dr. Peter Mayer and Dr. Dieter Rau for the single-crystal measurements and to Lucien Eisenburger and Dr. Constantin Hoch (all at Department of Chemistry at LMU) for assistance with the single-crystal calculations.

2.6 References

- [1] Wang, L.; Xie, R. J.; Suehiro, T.; Takeda, T.; Hirosaki, N. Down-Conversion Nitride Materials for Solid State Lighting: Recent Advances and Perspectives. *Chem. Rev.* **2018**, *118*, 1951–2009.
- [2] Liao, H.; Zhao, M.; Molokeev, M. S.; Liu, Q.; Xia, Z. Learning from a Mineral Structure toward an Ultra-Narrow-Band Blue-Emitting Silicate Phosphor $\text{RbNa}_3(\text{Li}_3\text{SiO}_4)_4:\text{Eu}^{2+}$. *Angew. Chem. Int. Ed.* **2018**, *57*, 11728–11731; *Angew. Chem.* **2018**, *130*, 11902–11905.
- [3] Huppertz, H.; Schnick, W. Synthesis, Crystal Structure, and Properties of the Nitridosilicates $\text{SrYbSi}_4\text{N}_7$ and $\text{BaYbSi}_4\text{N}_7$. *Z. Anorg. Allg. Chem.* **1997**, *623*, 212–217.
- [4] Höpfe, H. A.; Lutz, H.; Morys, P.; Schnick, W.; Seilmeier, A. Luminescence in Eu^{2+} -doped $\text{Ba}_2\text{Si}_5\text{N}_8$: Fluorescence, Thermoluminescence, and Upconversion. *J. Phys. Chem. Solids* **2000**, *61*, 2001–2006.
- [5] Xie, R.-J.; Hirosaki, N.; Suehiro, T.; Xu, F.-F.; Mitomo, M. A Simple, Efficient Synthetic Route to $\text{Sr}_2\text{Si}_5\text{N}_8:\text{Eu}^{2+}$ -Based Red Phosphors for White Light-Emitting Diodes. *Chem. Mater.* **2006**, *18*, 5578–5583.
- [6] Pust, P.; Weiler, V.; Hecht, C.; Tucks, A.; Wochnik, A. S.; Henss, A. K.; Wiechert, D.; Scheu, C.; Schmidt, P. J.; Schnick, W. Narrow-band red-emitting $\text{Sr}[\text{LiAl}_3\text{N}_4]:\text{Eu}^{2+}$ as a next-generation LED-phosphor material. *Nat. Mater.* **2014**, *13*, 891–896.
- [7] Hoerder, G. J.; Seibald, M.; Baumann, D.; Schroder, T.; Peschke, S.; Schmid, P. C.; Tyborski, T.; Pust, P.; Stoll, I.; Bergler, M.; Patzig, C.; Reissaus, S.; Krause, M.; Berthold, L.; Hoche, T.; Johrendt, D.; Huppertz, H. $\text{Sr}[\text{Li}_2\text{Al}_2\text{O}_2\text{N}_2]:\text{Eu}^{2+}$ – A high performance red phosphor to brighten the future. *Nat. Commun.* **2019**, *10*, 1–9.
- [8] Somer, M.; Carrillo-Cabrera, W.; Peters, E.-M.; Peters, K.; von Schnering, H. Crystal structure of lithium beryllium nitride, LiBeN . *Z. Kristallogr.-Cryst. Mater.* **1996**, *211*, 635–635.
- [9] Somer, M.; Yarasik, A.; Akselrud, L.; Leoni, S.; Rosner, H.; Schnelle, W.; Kniep, R. $\text{Ae}[\text{Be}_2\text{N}_2]$: nitridoberyllates of the heavier alkaline-earth metals. *Angew. Chem. Int. Ed.* **2004**, *43*, 1088–1092; *Angew. Chem.* **2004**, *116*, 1108–1112.
- [10] Leoni, S.; Niewa, R.; Akselrud, L.; Prots, Y.; Schnelle, W.; Tahsin, G.; Cetinkol, M.; Somer, M.; Kniep, R. Novel Barium Beryllates $\text{Ba}[\text{Be}_2\text{N}_2]$ and $\text{Ba}_3[\text{Be}_5\text{O}_8]$: Syntheses, Crystal Structures and Bonding Properties. *Z. Anorg. Allg. Chem.* **2005**, *631*, 1818–1824.
- [11] Strobel, P.; de Boer, T.; Weiler, V.; Schmidt, P. J.; Moewes, A.; Schnick, W. Luminescence of an Oxonitridoberyllate: A Study of Narrow-Band Cyan-Emitting $\text{Sr}[\text{Be}_6\text{ON}_4]:\text{Eu}^{2+}$. *Chem. Mater.* **2018**, *30*, 3122–3130.
- [12] Elzer, E.; Niklaus, R.; Strobel, P. J.; Weiler, V.; Schmidt, P. J.; Schnick, W. $\text{MBe}_{20}\text{N}_{14}:\text{Eu}^{2+}$ (M = Sr, Ba) - Highly Condensed Nitridoberyllates with Exceptional Highly Energetic Eu^{2+} Luminescence. *Chem. Mater.* **2019**, *31*, 3174–3182.
- [13] Wills, A. S. *VaList*, Program available from www.ccp14.ac.uk.
- [14] Zeuner, M.; Pagano, S.; Schnick, W. Nitridosilicates and oxonitridosilicates: from ceramic materials to structural and functional diversity. *Angew. Chem. Int. Ed.* **2011**, *50*, 7754–7775; *Angew. Chem.* **2011**, *123*, 7898–7920.
- [15] Strobel, P.; Weiler, V.; Schmidt, P. J.; Schnick, W. $\text{Sr}[\text{BeSi}_2\text{N}_4]:\text{Eu}^{2+}/\text{Ce}^{3+}$ and $\text{Eu}[\text{BeSi}_2\text{N}_4]$: Nontypical Luminescence in Highly Condensed Nitridoberyllates. *Chem. Eur. J.* **2018**, *24*, 7243–7249.
- [16] Strobel, P.; Niklaus, R.; Schmidt, P. J.; Schnick, W. Oxoberyllates SrBeO_2 and $\text{Sr}_{12}\text{Be}_{17}\text{O}_{29}$ as Novel Host Materials for Eu^{2+} Luminescence. *Chem. Eur. J.* **2018**, *24*, 12678–12685.
- [17] Blatov, V. A.; Shevchenko, A. P.; Proserpio, D. M. Applied Topological Analysis of Crystal Structures with the Program Package ToposPro. *Cryst. Growth Des.* **2014**, *14*, 3576–3586.

-
- [18] Park, D. G.; Gál, Z. A.; DiSalvo, F. J. Synthesis and structure of $\text{Li}_4\text{Sr}_3\text{Ge}_2\text{N}_6$: a new quaternary nitride containing $\text{Ge}_2\text{N}_6^{10-}$ anions. *J. Solid State Chem.* **2003**, *172*, 166–170.
- [19] Shannon, R. D. Revised effective ionic radii and systematic studies of interatomic distances in halides and chalcogenides. *Acta Crystallogr., Sect. A: Cryst. Phys., Diffr. Theor. Gen. Crystallogr.* **1976**, *32*, 751–767.
- [20] Lueken, H., *Magnetochemie: Eine Einführung in Theorie und Anwendung*. Springer-Verlag Stuttgart, **1999**.
- [21] Naglav, D.; Buchner, M. R.; Bendt, G.; Kraus, F.; Schulz, S. Off the Beaten Track-A Hitchhiker's Guide to Beryllium Chemistry. *Angew. Chem. Int. Ed.* **2016**, *55*, 10562–10576; *Angew. Chem.* **2016**, *128*, 10718–10733.
- [22] Kumberger, O.; Schmidbaur, H. Warum ist Beryllium so toxisch? *Chem. Unserer Zeit* **1993**, *27*, 310–316.
- [23] BrukerAXS APEX3, version 2018.1-0.; 2018.
- [24] Sheldrick, G. M. SHELXS-97: A Program for Crystal structure solution. University of Göttingen, Germany, 1997.
- [25] Sheldrick, G. M. A short history of SHELX. *Acta Crystallogr., Sect. A: Found. Crystallogr.* **2008**, *64*, 112–122.
- [26] Sheldrick, G. M. SHELXL-97: A Program for Crystal structure refinement. University of Göttingen, Germany, 1997.
- [27] Cheary, R. W.; Coelho, A. A.; Cline, J. P. Fundamental Parameters Line Profile Fitting in Laboratory Diffractometers. *J. Res. Natl. Inst. Stand. Technol.* **2004**, *109*, 1–25.
- [28] Bergmann, J.; Kleeberg, R.; Haase, A.; Breidenstein, B. In *Advanced Fundamental Parameters Model for Improved Profile Analysis*, Materials Science Forum, Trans Tech Publications: 2000; pp 303–308.
- [29] Coelho, A. A. *TOPAS: A Program for Rietveld Refinement*, version 6; 2016.
- [30] Rietveld, H. M. A profile refinement method for nuclear and magnetic structures. *J. Appl. Crystallogr.* **1969**, *2*, 65–71.
- [31] Inc, Q. D. *PPMS MultiVu software* Version 1.5.11; San Diego, 2013.

3. $M\text{Be}_{20}\text{N}_{14}:\text{Eu}^{2+}$ ($M = \text{Sr}, \text{Ba}$): Highly Condensed Nitridoberyllates with Exceptional Highly Energetic Eu^{2+} Luminescence

Eugenia Elzer, Robin Niklaus, Philipp J. Strobel, Volker Weiler, Peter J. Schmidt, and Wolfgang Schnick

Chem. Mater. **2019**, *31*, 3174–3182

DOI: 10.1021/acs.chemmater.8b05133

Reprinted (adapted) with permission for non-commercial use from Chemistry of Materials. Copyright 2019 American Chemical Society.



ABSTRACT: The isotopic nitridoberyllates $M\text{Be}_{20}\text{N}_{14}$ with $M = \text{Sr}, \text{Eu}, \text{Ba}$ have been synthesized at high temperatures under a N_2 atmosphere. The crystal structures were solved and refined from single-crystal X-ray diffraction data ($I4/m$ (no. 87), $Z = 2$, $\text{SrBe}_{20}\text{N}_{14}:\text{Eu}^{2+}$, $a = 6.525(2)$, $c = 12.133(4)$ Å; $\text{EuBe}_{20}\text{N}_{14}$, $a = 6.524(8)$, $c = 12.136(2)$ Å; $\text{BaBe}_{20}\text{N}_{14}:\text{Eu}^{2+}$, $a = 6.540(6)$, $c = 12.214(11)$ Å). $M\text{Be}_{20}\text{N}_{14}$ contains a rigid network of multiply edge-sharing BeN_4 tetrahedra with a degree of condensation (i. e., atomic ratio Be/N) $\kappa = 1.43$. Eu^{2+} doped samples of $M\text{Be}_{20}\text{N}_{14}$ ($M = \text{Sr}, \text{Ba}$) show two emission bands in the blue-to-green spectral region: regular narrow-band blue Eu^{2+} emission ($\lambda_{\text{em}1} \approx 426\text{--}428$ nm, full width at half maximum (fwhm) $\approx 22\text{--}25$ nm/ $1180\text{--}1310$ cm^{-1}) and trapped exciton emission in the blue-green spectral region ($\lambda_{\text{em}2} \approx 530\text{--}540$ nm, fwhm > 100 nm). $M\text{Be}_{20}\text{N}_{14}$ show high chemical and thermal stability. For $\text{SrBe}_{20}\text{N}_{14}$ a wide band gap ($E_g = 4.6$ eV) and a high Debye temperature ($\theta_D = 1214$ K) were calculated. Large band gaps, chemical and thermal stability, and rigid networks make nitridoberyllates a promising class of host compounds for narrow-band emitting light emitting diode phosphors.

3.1 Introduction

Over the last years, Eu^{2+} doped compounds have been extensively investigated for application as luminescent materials (phosphors) in phosphor-converted light emitting diodes (pc LEDs).^[1-3] In most cases, the observed Eu^{2+} luminescence arises from the parity-allowed transition between the $4f^7(^8\text{S}_{7/2})$ ground state and the $4f^6(^7\text{F})5d^1$ excited state.^[4] The emission energies of this transition show a high sensitivity toward the local coordination environment, enabling the possibility to adjust the emission colors of Eu^{2+} doped phosphors in the entire visible spectral region by changing the crystal structure and thus the local chemical environment of the activator ion.^[4] The spectral position of the emission bands depend on the nephelauxetic effect (measure of the covalence of the activator–ligand bond) and the crystal field splitting of the $5d$ configuration. In general, a more covalent activator–ligand bonding interaction and a strong crystal field splitting lowers the energetic position of the $4f^65d^1$ excited state, resulting in a red shift of the emission. Hence, oxides, halides, borates, and sulfates typically show emission in the blue-to-green spectral region, whereas host lattices with more polarizable anions, such as nitrides and sulfides, can even exhibit green-to-red emission.^[5-8] In addition to normal $5d \rightarrow 4f\text{Eu}^{2+}$ emission, also anomalous Eu^{2+} trapped exciton (ETE) emission can occur, which is characterized by a large Stokes shift, an unusual temperature behavior, and a broad emission band. ETE is often observed when the activator atoms are incorporated on sites with a high coordination number and large activator–ligand bond lengths.^[5, 9-11]

Since the invention of efficient blue light-emitting diodes, the search for suitable phosphors with the purpose to down-convert the blue light and create energy-efficient warm-white LEDs has drawn much attention. The most common approach to generate white LEDs is to combine a blue-emitting InGaN chip with a yellow broadband phosphor (e. g., YAG:Ce).^[1] However, owing to the color deficiency in the red and blue-green regions, the color rendering index of such a 1pc LED is always less than 80 and thus the LED is not suitable for high-quality lightings. An option to realize superhigh color-rendering white LEDs with improved color point stability is the combination of a near-UV LED with highly efficient narrow-band emitting blue, green, and red phosphors.^[12] The ideal phosphors should have narrow emission profiles and no overlap of the multiple absorption and emission spectra, preventing reabsorption and thus contributing to increase the luminous efficacy. Conventional blue phosphors, such as $(\text{Sr},\text{Ba},\text{Ca})_{10}(\text{PO}_4)_6\text{Cl}_2:\text{Eu}^{2+}$ or $\text{BaMgAl}_{10}\text{O}_{17}:\text{Eu}^{2+}$, offer a high quantum efficiency but show a relatively large Stokes shift compared with narrow emitters like $\text{Sr}[\text{LiAl}_3\text{N}_4]:\text{Eu}^{2+}$.^[13-15] To minimize energy loss through the downconversion process, a rather small

Stokes shift is preferable. Narrow emission qualifies quantum dot materials to be possible converters in LEDs, but the application is limited among others due to the overlap of absorption and emission bands, poisonous elements such as Cd, and challenges for integrating them into the harsh LED environment.^[12,16]

Generally, phosphors used in pc LEDs should meet certain requirements, like efficient absorption of UV or blue light from the primary LED, high chemical and thermal stability, small thermal quenching, and high conversion efficiency.^[3, 14, 17, 18] Therefore, host lattices for efficient phosphors typically provide a wide band gap and a rigid host lattice with high atomic connectivity. By a targeted search for materials with a large band gap (E_g) and high Debye temperature (θ_D) (which is used as a proxy for the rigidity of a host lattice), new inorganic phosphors could already be identified.^[19-21] In the last decades, the field of suitable host lattices for doping with Eu^{2+} has been significantly extended to a magnitude of intriguing (oxo)nitridosilicates,^[22-26] nitridoalumosilicates,^[27-29] nitridomagnesosilicates,^[30-32] nitridolitho- and nitridomagnesoaluminates and quite recently also oxo(nitrido)beryllates.^[11,13,33-40] Since compounds such as $(\text{Sr,Ca})\text{AlSiN}_3:\text{Eu}^{2+}$, $(\text{Ba,Sr})_2\text{Si}_5\text{N}_8:\text{Eu}^{2+}$, and $\text{Sr}[\text{LiAl}_3\text{N}_4]:\text{Eu}^{2+}$ already have been commercially used,^[26, 27, 33] Eu^{2+} doped nitrides have proven their huge potential. In contrast to nitridosilicates (degree of condensation $\kappa = n(\text{Si}):n(\text{N}) \leq 0.75$) or nitridoaluminates ($\kappa \leq 1.0$), oxo(nitrido)beryllates can reach exceptionally high degrees of condensation (maximum $\kappa = 1.0$ in BeO and 1.5 in Be_3N_2). The potentially higher degree of condensation in nitridoberyllates results from the fact that the reduced formal charge of Be^{2+} compared with Si^{4+} with nearly the same ionic radius enables higher connectivity of BeN_4 tetrahedra over multiple common edges.^[41] The class of nitridoberyllates could even show a greater structural diversity than nitridosilicates since Be^{2+} can either be coordinated by four N atoms to form BeN_4 tetrahedra or by three N atoms to form trigonal planar BeN_3 units, respectively.^[11, 40, 42-44] Hitherto, there are only few known Be containing nitrides, such as the double nitride BeSiN_2 , $\text{Li}[\text{BeN}]$, $AE[\text{Be}_2\text{N}_2]$ ($AE = \text{Mg, Ca, Sr, Ba}$), $\text{Sr}[\text{BeSi}_2\text{N}_4]:\text{Eu}^{2+}/\text{Ce}^{3+}$, and $\text{Eu}[\text{BeSi}_2\text{N}_4]$.^[11, 42-44] However, recent investigations on oxo(nitrido)beryllates have proven that the scarcely studied material class is highly promising in search for further narrow-band emitting phosphors applicable in pc LEDs.^[13,40]

In this contribution, we report on synthesis and characterization of the nitridoberyllates $M\text{Be}_{20}\text{N}_{14}$ ($M = \text{Sr, Ba, Eu}$) with a remarkably high degree of condensation $\kappa = 1.43$. Their highly condensed network is made up of BeN_4 tetrahedra connected through common edges with only one crystallographic site for M. Upon doping with Eu^{2+} , $M\text{Be}_{20}\text{N}_{14}$ ($M = \text{Sr, Ba}$) unexpectedly shows two

emission bands: one narrow band in the blue spectral region and a second very broad band in the green spectral region. The narrow band can be attributed to the $4f^65d^1$ emission of the dopant, whereas the second emission probably originates from ETE emission.

3.2 Experimental Section

Safety Assessment

Exposure to Be and Be containing compounds is known to be harmful as it can cause diseases, such as acute berylliosis, chronic beryllium disease, and cancer. Although Beryllium is poorly absorbed, after oral and dermal exposure, the inhalation of Be dusts or soluble salts is especially hazardous.^[45] To prevent possible health detriment, working with Be in closed systems (gloveboxes and Schlenk lines) is reasonable and required.

Synthesis

All starting materials and samples were handled under the exclusion of moisture and oxygen in an Ar-filled glovebox (Unilab, MBraun, Garching, $\text{O}_2 < 1$ ppm, $\text{H}_2\text{O} < 1$ ppm) or in dry Schlenktype glassware attached to a vacuum line (10^{-3} mbar). Argon (Air Liquide, 5.0) was dried and purified in columns filled with silica gel (Merck), molecular sieve (Fluka, 4 Å), KOH (Merck, $\geq 85\%$), P_4O_{10} (Roth, $\geq 99\%$), and titanium sponge (700 °C, Johnsen Matthey, 99.5%).

Single crystals of $M\text{Be}_{20}\text{N}_{14}:\text{Eu}^{2+}$ ($M = \text{Sr}, \text{Ba}$) and $\text{EuBe}_{20}\text{N}_{14}$ were synthesized from $M(\text{NH}_2)_2$ ($M = \text{Sr}, \text{Ba}$) or $\text{Eu}(\text{NH}_2)_2$ and Be_3N_2 (synthesized from Be at 1400 °C under a N_2 atmosphere)^[46-48] (Table B.1 and Table B.2). In the case of $M = \text{Sr}, \text{Ba}$, small amounts of EuF_3 (2 mol% referred to M) were added as dopant for luminescence investigations. Starting materials were thoroughly ground in a tungsten carbide mortar under argon and filled into a tungsten crucible. The crucible was placed in a radio frequency (rf) furnace and subsequently heated in a nitrogen atmosphere in 0.5–1 h to 1400 °C and kept for 1 h, then cooled down to 500 °C in 0.5–1 h and subsequently quenched to room temperature by shutting down the furnace (Table B.3). The title compounds were obtained as colorless ($M = \text{Sr}, \text{Ba}$) or yellow ($M = \text{Eu}$) crystals, which show luminescence when irradiated with UV or blue light and are stable toward air, water, and against concentrated HCl.

Bulk samples of $M\text{Be}_{20}\text{N}_{14}:\text{Eu}^{2+}$ ($M = \text{Sr}, \text{Ba}$) were synthesized in a hot isostatic press under nitrogen pressure (50 MPa) at 1400 °C. Here, mixtures of Be_3N_2 (see above) and Sr_2N or Ba_2N and

small amounts of EuF_3 were used as starting materials (Table B.4). The preparation of the samples was carried out analogously to the abovementioned synthesis. The tungsten crucibles were placed in a corundum crucible and transferred to the hot isostatic press. The starting materials were heated in 4.7 h to $1400\text{ }^\circ\text{C}$, kept for 0.5 h, cooled down to $500\text{ }^\circ\text{C}$ in 1 h, and subsequently quenched to room temperature by shutting down the furnace. The obtained greyish powders were washed with concentrated HCl, water, and ethanol, to obtain off-white samples, suitable for further investigations.

Electron Microscopy

The examination of the chemical composition and morphology was carried out with a scanning electron microscope (SEM) NanoLab G3 (Helios), equipped with a X-Mas 80 SDD (Oxford Instruments) energy-dispersive X-ray (EDX) detector. The EDX data were obtained on several particles with an accelerating voltage of 20 kV.

Fourier Transform Infrared (FTIR) Spectroscopy

Fourier transform infrared (FTIR) spectroscopy was carried out using the attenuated total reflection method with a Perkin Elmer BXII spectrometer.

Single-Crystal X-ray Diffraction

Single crystals were isolated from the samples prepared in a rf furnace, with the aid of a microscope and mounted on MicroMounts (MiTeGen) with an aperture size of $20\text{--}30\text{ }\mu\text{m}$. X-ray diffraction data were collected on a Bruker D8 Venture diffractometer with a rotating anode (Mo K α radiation). Absorption correction was carried out using SADABS. The crystal structures were solved using direct methods and refined by least-squares method (SHELX-2014).^[49] Eu^{2+} in $M\text{Be}_{20}\text{N}_{14}:\text{Eu}^{2+}$ ($M = \text{Sr}, \text{Ba}$) was neglected for structure determination due to the insignificant scattering density resulting from the low content.

Crystallographic Data

Details on the single-crystal structure investigation on $M\text{Be}_{20}\text{N}_{14}:\text{Eu}^{2+}$ ($M = \text{Sr}, \text{Ba}$) and $\text{EuBe}_{20}\text{N}_{14}$ can be obtained from the Cambridge Crystallographic Data Centre (CCDC) upon quoting the depository codes CCDC 1883227 ($M = \text{Sr}$), CCDC 1883228 ($M = \text{Ba}$) and CCDC 1883229 ($\text{EuBe}_{20}\text{N}_{14}$).

Powder X-Ray Diffraction

Powder X-ray diffraction data were collected on a STOE Stadi P diffractometer with $\text{Cu K}\alpha_1$ radiation ($\lambda = 1.5406 \text{ \AA}$) or $\text{Mo K}\alpha$ radiation ($\lambda = 0.71073 \text{ \AA}$) in a parafocusing Debye–Scherrer geometry with a $\text{Ge}(111)$ monochromator and a Mythen 1K detector. Powder samples were sealed in a glass capillary with 0.1–0.3 mm diameter and 0.01 mm wall thickness (Hilgenberg, Germany). Rietveld refinements were carried out with the TOPAS Academic 6 package, applying the fundamental parameter approach (direct convolution of source emission profiles, axial instrument contributions, crystallite size, and microstrain effects).^[50–53]

Density Functional Theory (DFT) Calculations

All calculations were carried out with the Vienna ab initio simulation package^[54–56] utilizing the projector-augmented-wave method.^[57, 58] Structural relaxations of the unit cells of both Be_3N_2 and $\text{SrBe}_{20}\text{N}_{14}$ were done with a convergence criteria of 10^{-7} eV per atom for total energies, resulting in residual atomic forces below 1×10^{-3} eV \AA^{-1} . The plane-wave cutoff was set to 535 eV and Γ -centered k -meshes (Be_3N_2 : $7 \times 7 \times 7$; $\text{SrBe}_{20}\text{N}_{14}$: $8 \times 8 \times 5$) produced from the method of *Monkhorst and Pack* were used for sampling the Brillouin zone.^[59] Band structure calculations were performed on the basis of the primitive cell.^[60] Treatment of the exchange correlation was done with the generalized gradient approximation (GGA) of Perdew, Burke, and Ernzerhof,^[61, 62] whereas the modified Becke–Johnson formalism (GGA-mBJ) was used for band gap evaluation.^[63–65] Calculations of elastic tensors from six finite lattice distortions of the crystal utilizing displacements of $\pm 0.015 \text{ \AA}$ enabled the derivation of elastic constants and moduli from the stress-strain relationship.^[66]

UV-vis Spectroscopy

The diffuse reflectance UV-vis spectra were measured on a Jasco V-650 UV/vis spectrophotometer with a deuterium and a halogen lamp (JASCO, Pfungstadt, Germany, Czerny–Turner monochromator with 1200 lines/mm, concave grating, photomultiplier tube detector).

Luminescence

Measurements of single crystals were carried out with a HORIBA Fluoromax4 spectrofluorimeter system, attached via optical fibers to an Olympus BX51 microscope. Crystals were

sealed inside glass capillaries and measured with $\lambda_{\text{exc}} = 390$ nm. The emission spectra were captured with a 2 nm step size in a wavelength range between 400 and 800 nm.

Low-temperature luminescence measurements were recorded on a thick-bed powder layer between 300 and 6 K on an Ocean Optics HR2000 + ES spectrometer (2048 pixels, grating UA (200–1100 nm) slit 50) with the samples mounted in an evacuated cooling chamber, which was cooled by a liquid-He compressor system from Advance Research System Inc. (ARS4HW). Photoluminescence measurements on powder samples were carried out with an in-house-built system based on a 5.3" integrating sphere and a spectrofluorimeter equipped with a 150 W Xe lamp and two Czerny–Turner monochromators with a focal length of 500 mm (grating: 1800 g mm^{-1} , blazed at 250/500 nm) with a spectral range of 230–820 nm. The internal quantum efficiency (IQE) of the samples were determined by comparing integrated emission and absorption intensities at excitation wavelength with BaSO_4 white standard and $\text{SrSi}_2\text{O}_2\text{N}_2:\text{Eu}^{2+}$ (Lumileds) reference samples.

3.3 Results and Discussion

Synthesis and Chemical Analysis

The title compounds were synthesized at high temperatures in tungsten crucibles using an rf furnace and a hot isostatic press. The obtained blocklike crystals (Figure 3.1, Figure B.1), are colorless for $M\text{Be}_{20}\text{N}_{14}:\text{Eu}^{2+}$ ($M = \text{Sr}, \text{Ba}$) or light yellowish in the case of $\text{EuBe}_{20}\text{N}_{14}$.

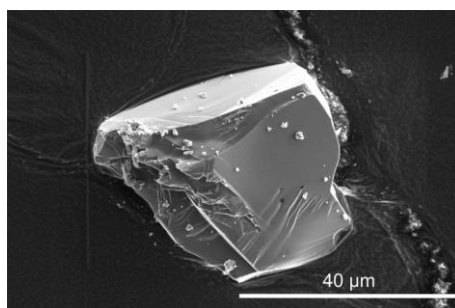


Figure 3.1. SEM image of $\text{EuBe}_{20}\text{N}_{14}$.

All samples are stable toward air, moisture, and concentrated HCl. The results of the EDX measurements (Table B.5) are in good agreement with the crystal structure refinement from single-crystal X-ray data. No O was detected, allowing drawing the conclusion of the formation of pure nitride phases. Other than Sr/Ba/Eu, no other metals were detected. This leaves Be, which cannot be determined by EDX, as the only possible element on tetrahedral centers. FTIR spectroscopy of $M\text{Be}_{20}\text{N}_{14}:\text{Eu}^{2+}$ ($M = \text{Sr}, \text{Ba}$) substantiated the absence of N–H and O–H groups (Figure B.2).

Crystal Structure Determination

The crystal structures of $M\text{Be}_{20}\text{N}_{14}$ ($M = \text{Sr}, \text{Eu}, \text{Ba}$) were solved and refined (SHELX-2014)^[49] in space group $I4/m$ (no. 87). The three compounds are isotypic with $Z = 2$ and $a = 6.525(2)$, $c = 12.133(4)$ Å for $\text{SrBe}_{20}\text{N}_{14}:\text{Eu}^{2+}$, $a = 6.5241(8)$, $c = 12.136(2)$ Å for $\text{EuBe}_{20}\text{N}_{14}$, and $a = 6.540(6)$, $c = 12.214(11)$ Å for $\text{BaBe}_{20}\text{N}_{14}:\text{Eu}^{2+}$. The slightly larger lattice parameters for the Ba containing phase originate from the larger ionic radius of Ba^{2+} compared to that of Sr^{2+} and Eu^{2+} , which are very similar.^[67] Crystallographic data are listed in Table 3.1. Atomic coordinates, Wyckoff positions and isotropic displacement parameters as well as anisotropic displacement parameters are summarized in the Supporting Information (Table B.6–Table B.11).

The consistency of the structure refinement is supported by lattice-energy calculations (MAPLE, Madelung Part of Lattice Energy) on $\text{SrBe}_{20}\text{N}_{14}:\text{Eu}^{2+}$, as a representative of the isotypic title

compounds. The results are summarized in the Supporting Information (Table B.12). The partial MAPLE values are in good agreement with reference data reported in the literature.^[7, 68] The MAPLE sum of $\text{SrBe}_{20}\text{N}_{14}:\text{Eu}^{2+}$ shows only a minor deviation of 0.09% from the value of a hypothetical synthesis from SrBe_2N_2 and $\alpha\text{-Be}_3\text{N}_2$.

Rietveld refinement of powder-diffraction data validates the structure of $M\text{Be}_{20}\text{N}_{14}:\text{Eu}^{2+}$ ($M = \text{Sr}, \text{Ba}$) obtained from single-crystal X-ray diffraction data (Figure 3.2, Table B.13, Figure B.3). Besides $M\text{Be}_{20}\text{N}_{14}:\text{Eu}^{2+}$, ($M = \text{Sr}, \text{Ba}$), $\alpha\text{-Be}_3\text{N}_2$ and WC (from the tungsten carbide mortar) were found as side phases. In the case of $\text{EuBe}_{20}\text{N}_{14}$, no Rietveld refinement was performed, due to a further not yet identified side phase. The obtained PXRD data and the simulated pattern from single-crystal data are included in the Supporting Information (Figure B.4).

Crystal Structure Description

The crystal structure of the title compounds stands out due to its highly condensed nitridoberyllate network with an exceptionally high degree of condensation of $\kappa = n(\text{Be}):n(\text{N}) = 1.43$. The few other known ternary nitridoberyllates possess a degree of condensation of $\kappa = 1.0$ (e. g., LiBeN , $A\text{Be}_2\text{N}_2$ ($A = \text{Ca}, \text{Sr}, \text{Ba}, \text{Mg}$)), leaving 1.43 in $M\text{Be}_{20}\text{N}_{14}$ as the highest observed value so far, apart from that of the binary nitride Be_3N_2 ($\kappa = 1.5$).

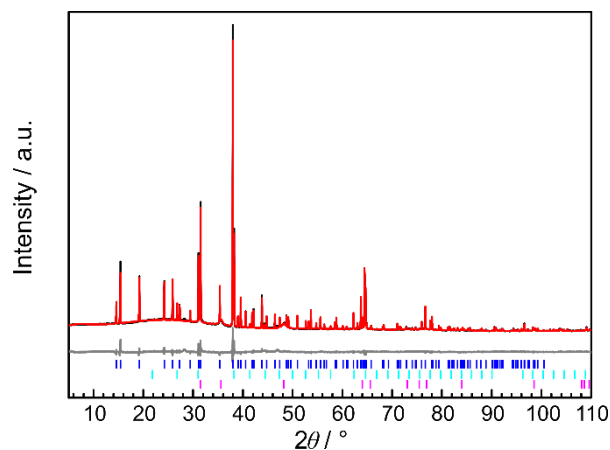


Figure 3.2. Rietveld refinement of $\text{SrBe}_{20}\text{N}_{14}$ ($\text{Cu K}\alpha 1 = 1.54056 \text{ \AA}$). Experimental data (black line), the calculated pattern (red line) and the difference curve (gray line). Tick marks: position of Bragg reflections of $\text{SrBe}_{20}\text{N}_{14}$ (blue), $\alpha\text{-Be}_3\text{N}_2$ (cyan), and WC (magenta).

The crystal structure of $M\text{Be}_{20}\text{N}_{14}$ consists of edge- and vertex-sharing BeN_4 tetrahedra, forming a highly condensed three-dimensional (3D) network with voids hosting the counterions Sr^{2+} , Eu^{2+} , or Ba^{2+} , respectively (Figure 3.3).

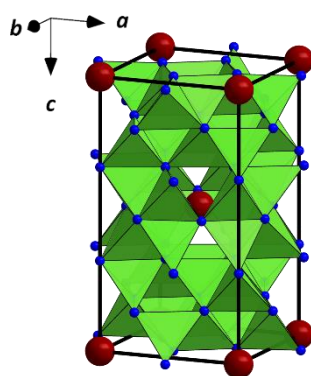


Figure 3.3. Crystal Structure of $M\text{Be}_{20}\text{N}_{14}$ ($M = \text{Sr}, \text{Eu}, \text{Ba}$) with BeN_4 tetrahedra (green), N atoms (blue), and M atoms (red); unit cell is outlined in black.

Table 3.1. Crystallographic data of $M\text{Be}_{20}\text{N}_{14}$ ($M = \text{Sr}, \text{Eu}, \text{Ba}$), standard deviations in parentheses.

	$\text{SrBe}_{20}\text{N}_{14}:\text{Eu}^{2+}$	$\text{EuBe}_{20}\text{N}_{14}$	$\text{BaBe}_{20}\text{N}_{14}:\text{Eu}^{2+}$
formula mass/ $\text{g}\cdot\text{mol}^{-1}$	463.96	528.30	513.68
crystal system		tetragonal	
space group		$I4/m$ (no. 87)	
cell parameters/ \AA	$a = 6.525(2)$ $c = 12.133(4)$	$a = 6.5241(8)$ $c = 12.136(2)$	$a = 6.540(6)$ $c = 12.214(11)$
Volume/ \AA^3	516.6(4)	516.5(2)	525.4(2)
formula units (cell)		2	
X-ray density/ $\text{g}\cdot\text{cm}^{-3}$	2.983	3.397	3.265
abs. coefficient/ $\mu\cdot\text{mm}^{-1}$	5.246	6.099	3.829
$F(000)$	432	482	468
crystal dimensions/ mm^3	$0.003 \times 0.003 \times 0.006$	$0.004 \times 0.003 \times 0.007$	$0.003 \times 0.005 \times 0.005$
diffractometer		Bruker D8 Venture	
radiation		Mo $K\alpha$ ($\lambda = 0.71073 \text{\AA}$)	
temperature/ K		293(2)	
absorption correction		multi-scan	
θ range/ $^\circ$	3.36–36.92	3.36–37.45	3.34–37.50
observed reflections	5965	9347	6913
independent reflections	642	712	722
independent reflections with $I \geq 2\sigma(I)$	580	709	719
min. / max. transmission	0.940/ 1.000	0.928/ 1.000	0.846/ 1.000
refined parameters	44	44	44
GoF	1.126	1.122	1.082
R indices ($F_0^2 \geq 2\sigma(F_0^2)$)	$R1 = 0.0324/$ $wR2 = 0.0520$	$R1 = 0.0160/$ $wR2 = 0.0320$	$R1 = 0.0271/$ $wR2 = 0.0580$
R indices (all data)	$R1 = 0.0409/$ $wR2 = 0.0542$	$R1 = 0.0161/$ $wR2 = 0.0320$	$R1 = 0.0274/$ $wR2 = 0.0581$
min./ max. residual electron density/ $\text{e}\cdot\text{\AA}^{-3}$	−0.610/ 0.546	−0.524/ 0.729	−0.844/ 1.642

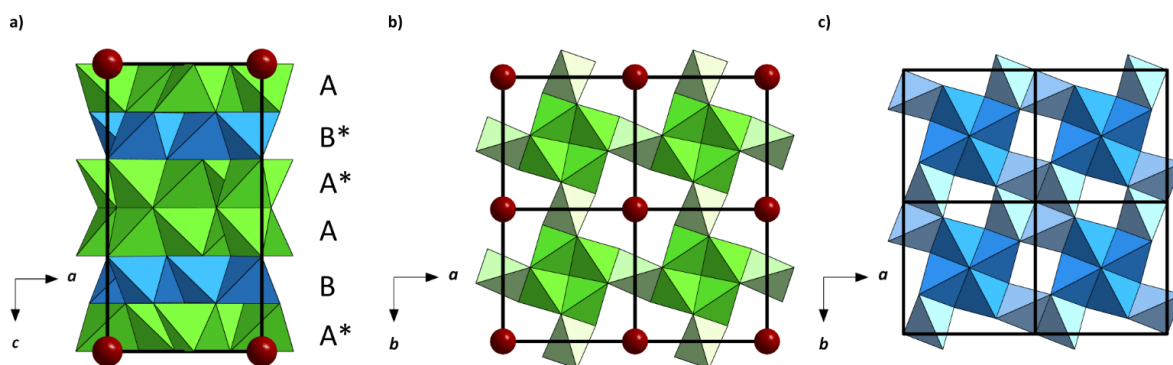


Figure 3.4. a) Three-dimensional beryllate network of $MBe_{20}N_{14}$ ($M = Sr, Eu, Ba$), view along $[0\bar{1}0]$ with a double layer consisting of layer A and A^* (green) and a separating layer B (blue); b) A layer, view along $[001]$ with M atoms ($M = Sr, Eu, Ba$; red) inside the voids; c) B layer, view along $[001]$.

For descriptive reasons the anionic network can formally be divided into two different layers: layer A, forming a double layer with its mirror image A^* and single layer B, which separates one double layer from the other (Figure 3.4a). Layer A consists of units of four edge-sharing BeN_4 tetrahedra (Figure 3.4b, dark green) interconnected by one further BeN_4 tetrahedra (Figure 3.4b, light green) over common edges and is transformed into A^* by a mirror plane parallel to $[010]$, creating a double layer with a cuboctahedral void occupied by the cation M . The second layer contains only units of four edge-sharing BeN_4 tetrahedra, alternately rotated by 180° , and connected over common edges (Figure 3.4c, dark and light blue). A and B layers are further interconnected via common edges and vertices, forming a highly condensed 3D network.

In $MBe_{20}N_{14}$ ($M = Sr, Eu, Ba$), the Be–N distances ($M = Sr$: 1.641(3)–1.968(3) Å; $M = Eu$: 1.640(2)–1.963(2) Å; $M = Ba$: 1.639(3)–1.975(4) Å) (Table B.14) correspond well to values in other nitridoberyllates ($AEBe_2N_2$ ($AE = Ca, Sr, Ba, Mg$), Be_3N_2) and the oxonitridoberyllate $Sr[Be_6ON_4]:Eu^{2+}$. Although the Be–N distances in the tetrahedron around Be3 are of about the same length (1.771(2)–1.800(4) Å), Be1 and Be2 atoms are displaced from the respective tetrahedron center, causing a strongly shortened (Be1–N1: 1.639(3)–1.641(3) Å and Be2–N1: 1.640(2)–1.661(3) Å) and a rather extended Be–N distance (Be1–N3: 1.963(3)–1.975(4) Å and Be2–N3: (1.858(3)–1.860(2) Å). The affected Be atoms are the central atoms of the BeN_4 tetrahedra forming the above mentioned units of four tetrahedra in the layers A (Figure 3.4b, dark green Be_2N_4 tetrahedra) and B (Figure 3.4c dark and light blue Be_1N_4 tetrahedra). The close physical proximity of the Be atoms likely causes a high electrostatic repulsion, resulting in a larger Be–N distance than that usually observed in known compounds.

The counterion M ($M = \text{Sr}, \text{Eu}, \text{Ba}$) occupies only one crystallographic site and is coordinated by 12 N atoms in a cuboctahedral arrangement, slightly compressed along c , resulting in two different $M\text{--N}$ distances of 2.915(2), 2.918(1) and 2.965(3) Å for $M1\text{--N}1$ and 3.169(2), 3.164(2) and 3.169(4) Å for $M1\text{--N}2$ ($M = \text{Sr}, \text{Eu}, \text{Ba}$) (Figure 3.5). Compared with the sum of the ionic radii,^[41, 67] the distances $\text{Sr}\text{--N}$ and $\text{Eu}\text{--N}$ are slightly elongated but in the same range as that for other known nitrides with $\text{Sr}^{2+}/\text{Eu}^{2+}$ in 12-fold coordination by N^{3-} ($\text{SrP}_2\text{N}_4:\text{Eu}^{2+}$ 2.50–3.38 Å;^[69] $\text{SrErAl}_3\text{SiN}_4\text{O}_3$: 3.109(6) Å;^[70] $\text{SrYbSi}_4\text{N}_7$: 2.931(3)–3.056(3) Å;^[71] EuYSi_4N_7 : 2.897–3.111 Å).^[72] The distance $\text{Ba}\text{--N}$ is in good agreement with the sum of the ionic radii and the value in BaBe_2N_2 (BaBe_2N_2 : 2.982(4) Å).^[42] Since only one nitridoberyllate containing Ba is known so far, other nitrides in which Ba is coordinated by 12 N atoms were used for comparison purposes. The $\text{Ba}\text{--N}$ distances also agree well with that in known nitrides ($\text{BaP}_2\text{N}_4:\text{Eu}^{2+}$: 2.78–3.48 Å;^[69] $\text{BaSr}_2\text{P}_6\text{N}_{12}:\text{Eu}^{2+}$: 2.80(1)–3.40(2) Å;^[69] $\text{BaYbSi}_4\text{N}_7$: 2.977(3)–3.052(3) Å).^[71]

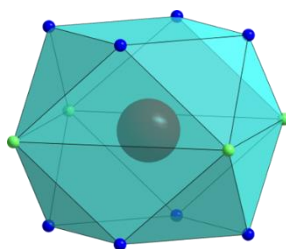


Figure 3.5. Coordination sphere of $M = \text{Sr}, \text{Ba}, \text{Eu}$ (red) in $M\text{Be}_{20}\text{N}_{14}$ with N1 atoms (blue, shorter $M1\text{--N}1$ distances) and N2 atoms (green, $M1\text{--N}2$ distances).

In most cases, the $M\text{--N}$ distances increase with increasing ionic radius. It is quite surprising that the title compounds show a rather small increase in the bond lengths from Sr/Eu to Ba (e. g., $\text{Ba}1\text{--N}1$: 0.02%). This can be explained by the highly condensed and therefore rigid network of BeN_4 tetrahedra, scarcely adjusting to the incorporation of smaller atoms like Sr^{2+} or Eu^{2+} compared with Ba^{2+} .

UV–Vis Spectroscopy

The optical band gaps of $M\text{Be}_{20}\text{N}_{14}:\text{Eu}^{2+}$ ($M = \text{Sr}, \text{Ba}$) were determined from diffuse reflectance UV–vis spectra of doped samples. The obtained reflectance spectra R (Figure B.5) were converted to pseudoabsorption spectra using the Kubelka–Munk function $F(R) = (1-R)^2/2R$.^[73] The optical band gaps were determined from Tauc plots by drawing tangents at the inflection points (Figure B.6).^[74] The Kubelka–Munk exponent $n = 2$ was chosen for the calculations, assuming indirect allowed

transitions for both compounds. The optical band gap for $M = \text{Sr}$ is about 4.1 eV, and for $M = \text{Ba}$, about 4.2 eV and is therefore slightly smaller than the values obtained from the DFT calculations.

Electronic Properties

To calculate the electronic band gap and mechanical properties of $\text{SrBe}_{20}\text{N}_{14}$ as a representative of the isotypic title compounds, DFT calculations were performed. The calculated band structure of $\text{SrBe}_{20}\text{N}_{14}$ is depicted in Figure 3.6. The calculation shows an indirect band gap of 4.6 eV, which is slightly larger than the determined optical band gap but shows a similar order of magnitude. The elastic constants, resulting elastic moduli, and Debye temperature (θ_D) are summarized in Table 3.2 and obtained from common relations.^[75-80]

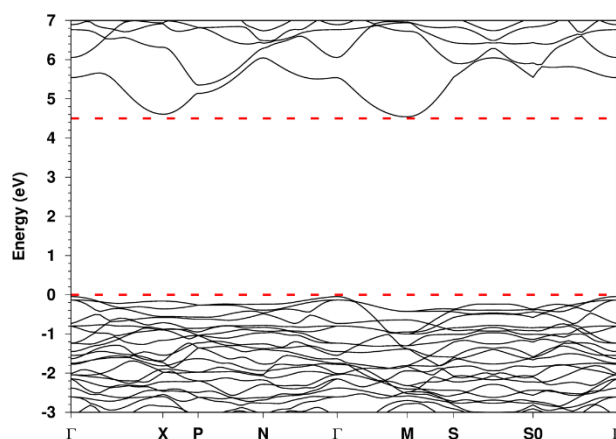


Figure 3.6. Calculated band structure of $\text{SrBe}_{20}\text{N}_{14}$ with the modified Becke–Johnson potential.

The calculations of the elastic constants demonstrate the high rigidity of the anionic network of $\text{SrBe}_{20}\text{N}_{14}$, as the values of the elastic constants in all three crystallographic directions are quite high and only slightly lower compared to those of $\alpha\text{-Be}_3\text{N}_2$ (Table B.15). C_{11} and C_{22} (a - and b -direction) are marginally increased with respect to C_{33} (c -direction). A recently discussed proxy for luminescent materials indicating the rigidity of the crystal structure is the Debye temperature (θ_D), which is rather high for $\text{SrBe}_{20}\text{N}_{14}$ ($\theta_D = 1214$ K) compared to that for other nitride compounds with a high degree of condensation ($\alpha\text{-Be}_3\text{N}_2$: $\theta_D = 1438.2$ K (Table B.15); $\text{SrLiAl}_3\text{N}_4$: $\theta_D = 716$ K; $\text{Sr}_2\text{Si}_5\text{N}_8$: $\theta_D = 702$ K).^{[20, 21,}

81]

Table 3.2. Calculated elastic constants C_{nm} , Bulk (B), Shear (G), and Young's (Y) Moduli in GPa, Debye Temperature (θ_D) in K and Poisson's ratio (ν) for $\text{SrBe}_{20}\text{N}_{14}$ ^a

elastic Moduli		elastic Constants	
B_V	187.9	C_{11}	408.9
B_R	187.9	C_{22}	408.9
B_{VRH}	187.9	C_{33}	403.8
G_V	154.9	C_{44}	148.8
G_R	154.5	C_{55}	148.8
G_{VRH}	154.7	C_{66}	148.2
Y_{VRH}	364.2	C_{12}	74.2
ν	0.18	C_{13}	80.5
θ_D	1214.1	C_{23}	80.5

^aBulk and shear moduli according to the Voigt (B_V , G_V); Reuss (B_R , G_R) and Voigt–Reuss–Hill (B_{VRH} , G_{VRH}) approach. C_{nm} obtained from C_{ijkl} according to the Voigt notation $xx \rightarrow 1$, $yy \rightarrow 2$, $zz \rightarrow 3$, $yz \rightarrow 4$, $zx \rightarrow 5$, $xy \rightarrow 6$.^[75]

Luminescence

Eu^{2+} doped samples (2% nominal Eu^{2+} concentration) of $M\text{Be}_{20}\text{N}_{14}:\text{Eu}^{2+}$ ($M = \text{Sr}, \text{Ba}$) show strong luminescence in the visible spectral region when excited with UV to blue light. Figure 3.7 shows excitation and emission spectra of single crystals of $M\text{Be}_{20}\text{N}_{14}:\text{Eu}^{2+}$ ($M = \text{Sr}, \text{Ba}$) and $\text{EuBe}_{20}\text{N}_{14}$.

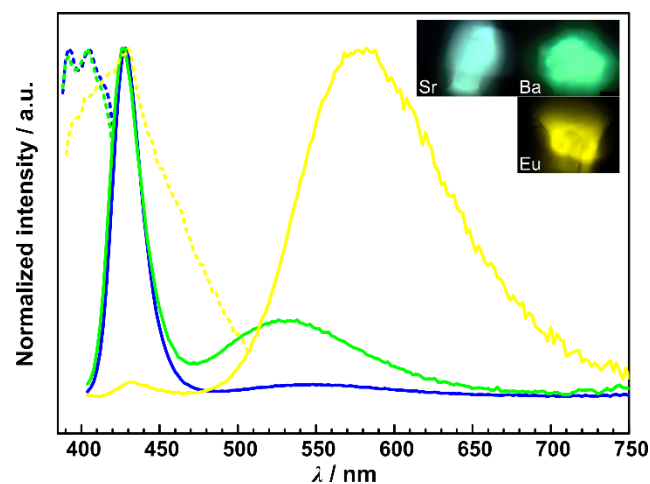


Figure 3.7. Luminescence spectra and photograph of single crystals of $M\text{Be}_{20}\text{N}_{14}:\text{Eu}^{2+}$ ($M = \text{Sr}, \text{Ba}$) and $\text{EuBe}_{20}\text{N}_{14}$. Normalized excitation spectra (dashed line) ($\lambda_{\text{exc}} = 390 \text{ nm}$) and emission spectra (line) for $M = \text{Sr}$ (blue), $M = \text{Ba}$ (green), and $\text{EuBe}_{20}\text{N}_{14}$ (yellow).

The luminescence in $M\text{Be}_{20}\text{N}_{14}:\text{Eu}^{2+}$ ($M = \text{Sr}, \text{Ba}$) and $\text{EuBe}_{20}\text{N}_{14}$ is assumed to originate solely from Eu^{2+} on the cuboctahedral coordinated site, owing to similar ionic radii of Eu^{2+} and Sr^{2+} and the highly condensed BeN_4 network leaving no other suitable position for a Eu^{2+} atom as a second luminescence center. $M\text{Be}_{20}\text{N}_{14}:\text{Eu}^{2+}$ ($M = \text{Sr}, \text{Ba}$) and $\text{EuBe}_{20}\text{N}_{14}$ exhibit one remarkably narrow

emission band in the blue spectral region and a second very broad red-shifted emission band. The emission maxima of $M\text{Be}_{20}\text{N}_{14}:\text{Eu}^{2+}$ ($M = \text{Sr}, \text{Ba}$) are located at $\lambda_{\text{em}1} = 428 \text{ nm}$ with a full width at half-maximum (fwhm) of $\approx 22 \text{ nm}/1180 \text{ cm}^{-1}$, $\lambda_{\text{em}2} \approx 540 \text{ nm}$ (fwhm $> 100 \text{ nm}$) for $M = \text{Sr}$, and $\lambda_{\text{em}1} = 426 \text{ nm}$ (fwhm $\approx 25 \text{ nm}/1310 \text{ cm}^{-1}$) and $\lambda_{\text{em}2} \approx 530 \text{ nm}$ (fwhm $> 110 \text{ nm}$) for $M = \text{Ba}$. Although a high concentration of Eu^{2+} often results in quenched luminescence due to nonradiative energy transfer between neighboring activators,^[12] a yellow luminescence is observed in $\text{EuBe}_{20}\text{N}_{14}$ at room temperature. The reason could be a long distance between two Eu atoms (shortest distance = 6.52 \AA). Therefore, energy transfer between Eu atoms occurs at low probability, resulting in a yellow luminescence in $\text{EuBe}_{20}\text{N}_{14}$.^[82] Following the trend of a shift of the emission toward longer wavelengths as the Eu^{2+} concentration increases the emission maxima in $\text{EuBe}_{20}\text{N}_{14}$ are located at $\lambda_{\text{em}1} \approx 430 \text{ nm}$ with a fwhm of $\approx 26 \text{ nm}/1380 \text{ cm}^{-1}$ and $\lambda_{\text{em}2} \approx 580 \text{ nm}$ (fwhm $> 110 \text{ nm}$).^[83]

As illustrated in Figure 3.5, the title compounds provide a highly symmetric, slightly distorted cuboctahedral coordination around M ($M = \text{Sr}, \text{Ba}$) and Eu, leading presumably to the remarkably narrow blue emission bands of $M\text{Be}_{20}\text{N}_{14}:\text{Eu}^{2+}$ ($M = \text{Sr}, \text{Ba}$) and $\text{EuBe}_{20}\text{N}_{14}$. The narrow blue emission is comparable to that of the narrow-band blue emitting oxoberyllates $A\text{ELi}_2[\text{Be}_4\text{O}_6]:\text{Eu}^{2+}$ ($AE = \text{Sr}, \text{Ba}$, $\lambda_{\text{em}} = 454\text{--}456 \text{ nm}$, fwhm $\approx 25 \text{ nm}/1200 \text{ cm}^{-1}$).^[13] Usually, emission of Eu^{2+} in nitrides is observed in the green-to-red spectral range. As already mentioned, the red-shift depends on the nephelauxetic effect and crystal field splitting.^[4] The high degree of condensation of the BeN_4 tetrahedra reduces the interaction between the anion N^{3-} and Eu^{2+} . Combined with the weak crystal field splitting, originating from the large coordination number (CN = 12), the red-shift is significantly reduced compared with known nitrides. $M\text{Be}_{20}\text{N}_{14}:\text{Eu}^{2+}$ ($M = \text{Sr}, \text{Ba}$) and $\text{EuBe}_{20}\text{N}_{14}$ are the first known ternary/ multinary nitrides with an emission band so far in the blue spectral region (e. g.: BaP_2N_4 : $\lambda_{\text{em}} = 460 \text{ nm}$;^[69] $\text{BaSr}_2\text{P}_6\text{N}_{12}$: $\lambda_{\text{em}} = 450 \text{ nm}$;^[69] SrSi_6N_8 : $\lambda_{\text{em}} = 450 \text{ nm}$).^[84]

In spite of only one crystallographic site for the dopant ion Eu^{2+} , the emission spectra show a second broadened and red-shifted emission band in the green spectral region, which is likely to originate from ETE emission. The emission spectra of Figure 3.7 show that the intensity of the large Stokes shift emission in the green spectral range is significantly smaller relative to the narrow band emission for $M = \text{Sr}$ compared to that of $M = \text{Ba}$ (for the same Eu doping level). This observation follows a trend typical for anomalous emission of the trapped exciton type, a higher probability for ETE for larger host lattice cation sizes.^[5] Only in $\text{EuBe}_{20}\text{N}_{14}$ the ETE emission is significantly stronger than the Eu^{2+} emission in the blue spectral region. The strong overlap of the red-shifted absorption

band of $\text{EuBe}_{20}\text{N}_{14}$ compared to that of $M\text{Be}_{20}\text{N}_{14}:\text{Eu}^{2+}$ ($M = \text{Sr}, \text{Ba}$) leads likely to a reabsorption of the normal Eu^{2+} emission, thus resulting in a strong ETE emission. In summary, the trend for the three compounds is that the ETE emission increases significantly from Sr via Ba to the Eu compound and the normal Eu^{2+} emission in $\text{EuBe}_{20}\text{N}_{14}$ disappears almost completely due to reabsorption.

To study the luminescence properties in more detail, temperature-dependent emission measurements were performed on $M\text{Be}_{20}\text{N}_{14}:\text{Eu}^{2+}$ ($M = \text{Sr}, \text{Ba}$) (Figure 3.8 and Figure B.8) from 6 to 300 K. As both compounds show a rather similar behavior, only the measurements of $\text{SrBe}_{20}\text{N}_{14}:\text{Eu}^{2+}$ are discussed in detail. The emission maximum of the broadened emission band of $\text{SrBe}_{20}\text{N}_{14}:\text{Eu}^{2+}$ shows a red shift of $\approx 820 \text{ cm}^{-1}$ when going from 300 to 6 K. A similar behavior has been reported in other compounds where ETE emission has been discussed ($M[\text{Mg}_2\text{Al}_2\text{N}_4]:\text{Eu}^{2+}$ ($M = \text{Ca}-\text{Ba}$), $\text{Ba}[\text{Mg}_3\text{SiN}_4]:\text{Eu}^{2+}$, $\text{Sr}[\text{BeSi}_2\text{N}_4]:\text{Eu}^{2+}$).^[11, 30, 38] As already discussed, trapped exciton emission probably occurs in our compounds due to long $M-\text{N}$ distances of 2.9–3.2 Å for $M\text{Be}_{20}\text{N}_{14}:\text{Eu}^{2+}$ ($M = \text{Sr}, \text{Ba}$).

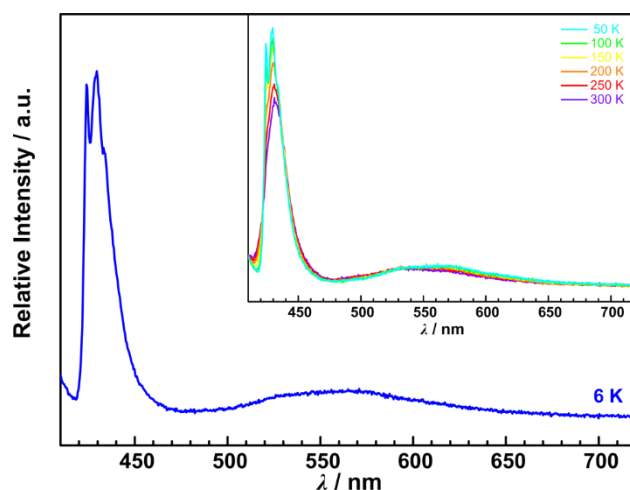


Figure 3.8. Photoluminescence spectrum of a powder sample of $\text{SrBe}_{20}\text{N}_{14}:\text{Eu}^{2+}$ at 6 K (blue line), $\lambda_{\text{exc}} = 380 \text{ nm}$. Inset: Photoluminescence spectra at different temperatures from 50 to 300 K.

The narrow blue emission maximum is slightly shifted to higher energies and starts to show a well-resolved vibronic structure of the emission transition below 150 K. At 6 K the zero phonon line (ZPL) is clearly visible at $\approx 425 \text{ nm}$. Hence, the Stokes shift can be accurately determined by $E_{\text{Stokes}} = 2E_{\text{max}}$ (twice the difference between the ZPL and the maximum of the absorption or emission band)^[85] to $\approx 660 \text{ cm}^{-1}$. The approximation by $\Gamma(T) = \Gamma(0)\sqrt{\coth(\hbar\omega/2kT)}$ ^[86] allows to obtain the average phonon energies of Eu on the only crystallographic site of Sr to be in the order of $\approx 250 \text{ cm}^{-1}$. Further information about the properties of $\text{SrBe}_{20}\text{N}_{14}:\text{Eu}^{2+}$ can be derived from the relative intensities of the respective vibration replicas. The ZPL seems to be the most intense transition,

followed by a higher vibronic replica only slightly intense than the ZPL pointing to a Huang–Rhys factor of ≈ 1 and therefore an outstandingly small electron–phonon coupling of Eu^{2+} in a crystalline matrix. As already discussed, Eu^{2+} on the Sr^{2+} site is incorporated in a highly condensed tetrahedral network. Consequently, lattice relaxation in the excited state is limited, thus, a small Stokes shift and a narrow emission in the blue spectral region can be observed for the normal $5d \rightarrow 4f \text{Eu}^{2+}$ emission.

Further luminescence properties were investigated on thick bed powder samples of $M\text{Be}_{20}\text{N}_{14}:\text{Eu}^{2+}$ ($M = \text{Sr}, \text{Ba}$). The internal and external quantum efficiencies (IQE/EQE) were determined with an excitation wavelength of $\lambda_{\text{exc}} = 380 \text{ nm}$. $\text{SrBe}_{20}\text{N}_{14}:\text{Eu}^{2+}$ exhibits a higher IQE of 35% (EQE: 28%) compared with 17% (15%) for $M = \text{Ba}$. Optimized synthesis conditions could help to obtain samples of $M\text{Be}_{20}\text{N}_{14}:\text{Eu}^{2+}$ ($M = \text{Sr}, \text{Ba}$) with improved emission properties, by reducing the side phases (WC, Be_3N_2), therefore increasing the IQE. The thermal quenching data (Figure B.7) for both phosphors show a relative photoemission intensity of ca. 80% ($M = \text{Sr}$) and 65% ($M = \text{Ba}$) at $100 \text{ }^\circ\text{C}$ compared to the initial emission intensity at 6 K .

3.4 Conclusion

In this contribution, we report on the crystal structure and the luminescence properties of the highly condensed nitridoberyllates $M\text{Be}_{20}\text{N}_{14}:\text{Eu}^{2+}$ ($M = \text{Sr}, \text{Ba}$) and $\text{EuBe}_{20}\text{N}_{14}$. The nitridoberyllates have been synthesized in high-temperature reactions. The crystal structure was solved and refined from single-crystal data and supported by X-ray diffraction data. The structure consists exclusively of edge-sharing BeN_4 tetrahedra, creating a highly condensed 3D network with solely one crystallographic site for M ($M = \text{Sr}, \text{Eu}, \text{Ba}$). The rigidity of the host lattice is reflected by a remarkably high Debye temperature ($\theta_D = 1212 \text{ K}$), compared with other known phosphors ($\text{SrLiAl}_3\text{N}_4$: $\theta_D = 716 \text{ K}$; $\text{Sr}_2\text{Si}_5\text{N}_8$: $\theta_D = 702 \text{ K}$) and the fact that the lattice constants for the isotypic Ba compound are nearly identical. As a consequence, $M\text{Be}_{20}\text{N}_{14}:\text{Eu}^{2+}$ ($M = \text{Sr}, \text{Ba}$) shows interesting luminescence properties upon excitation with UV/blue light. Due to the highly condensed host lattice and the cage-like substitutional site for the incorporation of Eu^{2+} , lattice relaxation is limited, resulting in a small Stokes shift and a narrow emission band in the blue spectral region (426–428 nm, fwhm $\approx 22\text{--}25 \text{ nm} / 1180\text{--}1310 \text{ cm}^{-1}$). Combined with weak crystal field splitting, originating from the large coordination number (CN = 12), the red shift in $M\text{Be}_{20}\text{N}_{14}:\text{Eu}^{2+}$ ($M = \text{Sr}, \text{Ba}$) is significantly reduced compared with known nitrides. In addition to normal Eu^{2+} emission, the nitridoberyllates show also a broad, red-shifted emission likely originating from trapped exciton emission. The fact

that the Sr compound only shows weak ETE intensities points toward directions for further improvements of the material's emission properties: (a) a further gradual reduction of the average alkaline earth cation size and (b) an increase of the energy difference between the $\text{Eu } 4f^65d^1$ state and the bottom of the conduction band by means of band gap engineering.^[5] In conclusion, $M\text{Be}_{20}\text{N}_{14}:\text{Eu}^{2+}$ ($M = \text{Sr}, \text{Ba}$) demonstrates the ability of beryllate structures to be highly promising candidates in the ongoing investigations for highly efficient narrow-band phosphors.

3.5 Acknowledgements

The authors thank Petra Huppertz and Detlef Wiechert (Lumileds Phosphor Center Aachen) for luminescence measurements, Christian Maak and Christian Minke for EDX measurements and Dr. Peter Mayer (all at Department of Chemistry, University of Munich (LMU)) for collecting single-crystal X-ray diffraction data.

3.6 References

- [1] Pust, P.; Schmidt, P. J.; Schnick, W. A revolution in lighting. *Nat. Mater.* **2015**, *14*, 454–458.
- [2] Takeda, T.; Xie, R.-J.; Suehiro, T.; Hirosaki, N. Nitride and oxynitride phosphors for white LEDs: Synthesis, new phosphor discovery, crystal structure. *Prog. Solid State Chem.* **2018**, *51*, 41–51.
- [3] Wang, L.; Xie, R. J.; Suehiro, T.; Takeda, T.; Hirosaki, N. Down-Conversion Nitride Materials for Solid State Lighting: Recent Advances and Perspectives. *Chem. Rev.* **2018**, *118*, 1951–2009.
- [4] Dorenbos, P. Energy of the first $4f^7 \rightarrow 4f^65d$ transition of Eu^{2+} in inorganic compounds. *J. Lumin.* **2003**, *104*, 239–260.
- [5] Dorenbos, P. Anomalous luminescence of Eu^{2+} and Yb^{2+} in inorganic compounds. *J. Phys.: Condens. Matter* **2003**, *15*, 2645–2665.
- [6] Höpfe, H. A. Recent developments in the field of inorganic phosphors. *Angew. Chem. Int. Ed.* **2009**, *48*, 3572–3582; *Angew. Chem.* **2009**, *121*, 3626–3636.
- [7] Zeuner, M.; Pagano, S.; Schnick, W. Nitridosilicates and oxonitridosilicates: from ceramic materials to structural and functional diversity. *Angew. Chem. Int. Ed.* **2011**, *50*, 7754–7775; *Angew. Chem.* **2011**, *123*, 7898–7920.
- [8] Kunkel, N.; Kohlmann, H.; Sayede, A.; Springborg, M. Alkaline-Earth Metal Hydrides as Novel Host Lattices for Eu^{II} Luminescence. *Inorg. Chem.* **2011**, *50*, 5873–5875.
- [9] Dutczak, D.; Ronda, C.; Jüstel, T.; Meijerink, A. Anomalous Trapped Exciton and d–f Emission in $\text{Sr}_4\text{Al}_{14}\text{O}_{25}:\text{Eu}^{2+}$. *J. Phys. Chem. A* **2014**, *118*, 1617–1621.
- [10] Moine, B.; Pedrini, C.; Courtois, B. Photoionization and luminescences in $\text{BaF}_2:\text{Eu}^{2+}$. *J. Lumin.* **1991**, *50*, 31–38.
- [11] Strobel, P.; Weiler, V.; Schmidt, P. J.; Schnick, W. $\text{Sr}[\text{BeSi}_2\text{N}_4]:\text{Eu}^{2+}/\text{Ce}^{3+}$ and $\text{Eu}[\text{BeSi}_2\text{N}_4]:$ Nontypical Luminescence in Highly Condensed Nitridoberyllsilicates. *Chem. Eur. J.* **2018**, *24*, 7243–7249.
- [12] Kitai, A. *Materials for Solid State Lighting and Displays*; Wiley: Chichester, U.K., 2017.
- [13] Strobel, P.; Maak, C.; Weiler, V.; Schmidt, P. J.; Schnick, W. Ultra-Narrow-Band Blue-Emitting Oxoberyllates $\text{AELi}_2[\text{Be}_4\text{O}_6]:\text{Eu}^{2+}$ (AE = Sr, Ba) Paving the Way to Efficient RGB pc-LEDs. *Angew. Chem. Int. Ed.* **2018**, *57*, 8739–8743; *Angew. Chem.* **2018**, *130*, 8875–8879.
- [14] McKittrick, J.; Hannah, M. E.; Piquette, A.; Han, J. K.; Choi, J. I.; Anc, M.; Galvez, M.; Lugauer, H.; Talbot, J. B.; Mishra, K. C. Phosphor Selection Considerations for Near-UV LED Solid State Lighting. *ECS J. Solid State Sci. Technol.* **2013**, *2*, R3119–R3131.
- [15] Piquette, A.; Bergbauer, W.; Galler, B.; Mishra, K. C. On choosing phosphors for near-UV and blue LEDs for white light. *ECS J. Solid State Sci. Technol.* **2016**, *5*, R3146–R3159.
- [16] Li, S.; Xie, R.-J.; Takeda, T.; Hirosaki, N. Critical Review—Narrow-Band Nitride Phosphors for Wide Color-Gamut White LED Backlighting. *ECS J. Solid State Sci. Technol.* **2018**, *7*, R3064–R3078.
- [17] George, N. C.; Denault, K. A.; Seshadri, R. Phosphors for Solid-State White Lighting. *Annu. Rev. Mater. Res.* **2013**, *43*, 481–501.
- [18] Xie, R.-J.; Hirosaki, N.; Takeda, T.; Suehiro, T. On the Performance Enhancement of Nitride Phosphors as Spectral Conversion Materials in Solid State Lighting. *ECS J. Solid State Sci. Technol.* **2013**, *2*, R3031–R3040.
- [19] Zhuo, Y.; Mansouri Tehrani, A.; Oliynyk, A. O.; Duke, A. C.; Brgoch, J. Identifying an efficient, thermally robust inorganic phosphor host via machine learning. *Nat. Commun.* **2018**, *9*, 1–10.

- [20] Brgoch, J.; DenBaars, S. P.; Seshadri, R. Proxies from Ab Initio Calculations for Screening Efficient Ce^{3+} Phosphor Hosts. *J. Phys. Chem. C* **2013**, *117*, 17955–17959.
- [21] Wang, Z.; Chu, I.-H.; Zhou, F.; Ong, S. P. Electronic Structure Descriptor for the Discovery of Narrow-Band Red-Emitting Phosphors. *Chem. Mater.* **2016**, *28*, 4024–4031.
- [22] Maak, C.; Durach, D.; Martiny, C.; Schmidt, P. J.; Schnick, W. Narrow-Band Yellow-Orange Emitting $\text{La}_{3-x}\text{Ca}_{1.5x}\text{Si}_6\text{N}_{11}:\text{Eu}^{2+}$ ($x \approx 0.77$): A Promising Phosphor for Next-Generation Amber pcLEDs. *Chem. Mater.* **2018**, *30*, 3552–3558.
- [23] Seibald, M.; Rosenthal, T.; Oeckler, O.; Maak, C.; Tücks, A.; Schmidt, P. J.; Wiechert, D.; Schnick, W. New Polymorph of the Highly Efficient LED-Phosphor $\text{SrSi}_2\text{O}_2\text{N}_2:\text{Eu}^{2+}$ – Polytypism of a Layered Oxonitridosilicate. *Chem. Mater.* **2013**, *25*, 1852–1857.
- [24] Maak, C.; Hoch, C.; Schmidt, P. J.; Schnick, W. Oxonitridosilicate Oxides $\text{RE}_{26}\text{Ba}_6[\text{Si}_{22}\text{O}_{19}\text{N}_{36}]\text{O}_{16}:\text{Eu}^{2+}$ ($\text{RE} = \text{Y}, \text{Tb}$) with a Unique Layered Structure and Orange-Red Luminescence for $\text{RE} = \text{Y}$. *Inorg. Chem.* **2018**, *57*, 2242–2248.
- [25] Seibald, M.; Rosenthal, T.; Oeckler, O.; Fahrnbauer, F.; Tücks, A.; Schmidt, P. J.; Schnick, W. Unexpected Luminescence Properties of $\text{Sr}_{0.25}\text{Ba}_{0.75}\text{Si}_2\text{O}_2\text{N}_2:\text{Eu}^{2+}$ -A Narrow Blue Emitting Oxonitridosilicate with Cation Ordering. *Chem. Eur. J.* **2012**, *18*, 13446–13452.
- [26] Höpfe, H. A.; Lutz, H.; Morys, P.; Schnick, W.; Seilmeier, A. Luminescence in Eu^{2+} -doped $\text{Ba}_2\text{Si}_5\text{N}_8$: Fluorescence, Thermoluminescence, and Upconversion. *J. Phys. Chem. Solids* **2000**, *61*, 2001–2006.
- [27] Watanabe, H.; Kijima, N. Crystal structure and luminescence properties of $\text{Sr}_x\text{Ca}_{1-x}\text{AlSiN}_3:\text{Eu}^{2+}$ mixed nitride phosphors. *J. Alloys Compd.* **2009**, *475*, 434–439.
- [28] Strobel, P.; Schmiechen, S.; Siegert, M.; Tücks, A.; Schmidt, P. J.; Schnick, W. Narrow-Band Green Emitting Nitridolithoalumosilicate $\text{Ba}[\text{Li}_2(\text{Al}_2\text{Si}_2)\text{N}_6]:\text{Eu}^{2+}$ with Framework Topology whj for LED/ LCD-Backlighting Applications. *Chem. Mater.* **2015**, *27*, 6109–6115.
- [29] Takeda, T.; Hirotsuki, N.; Funahshi, S.; Xie, R.-J. Narrow-Band Green-Emitting Phosphor $\text{Ba}_2\text{LiSi}_7\text{AlN}_{12}:\text{Eu}^{2+}$ with High Thermal Stability Discovered by a Single Particle Diagnosis Approach. *Chem. Mater.* **2015**, *27*, 5892–5898.
- [30] Schmiechen, S.; Strobel, P.; Hecht, C.; Reith, T.; Siegert, M.; Schmidt, P. J.; Huppertz, P.; Wiechert, D.; Schnick, W. Nitridomagnesosilicate $\text{Ba}[\text{Mg}_3\text{SiN}_4]:\text{Eu}^{2+}$ and Structure–Property Relations of Similar Narrow-Band Red Nitride Phosphors. *Chem. Mater.* **2015**, *27*, 1780–1785.
- [31] Strobel, P.; Weiler, V.; Hecht, C.; Schmidt, P. J.; Schnick, W. Luminescence of the Narrow-Band Red Emitting Nitridomagnesosilicate $\text{Li}_2(\text{Ca}_{1-x}\text{Sr}_x)_2[\text{Mg}_2\text{Si}_2\text{N}_6]:\text{Eu}^{2+}$ ($x = 0\text{--}0.06$). *Chem. Mater.* **2017**, *29*, 1377–1383.
- [32] Schmiechen, S.; Schneider, H.; Wagatha, P.; Hecht, C.; Schmidt, P. J.; Schnick, W. Toward New Phosphors for Application in Illumination-Grade White pc-LEDs: The Nitridomagnesosilicates $\text{Ca}[\text{Mg}_3\text{SiN}_4]:\text{Ce}^{3+}$, $\text{Sr}[\text{Mg}_3\text{SiN}_4]:\text{Eu}^{2+}$, and $\text{Eu}[\text{Mg}_3\text{SiN}_4]$. *Chem. Mater.* **2014**, *26*, 2712–2719.
- [33] Pust, P.; Weiler, V.; Hecht, C.; Tücks, A.; Wochnik, A. S.; Henss, A. K.; Wiechert, D.; Scheu, C.; Schmidt, P. J.; Schnick, W. Narrow-band red-emitting $\text{Sr}[\text{LiAl}_3\text{N}_4]:\text{Eu}^{2+}$ as a next-generation LED-phosphor material. *Nat. Mater.* **2014**, *13*, 891–896.
- [34] Pust, P.; Wochnik, A. S.; Baumann, E.; Schmidt, P. J.; Wiechert, D.; Scheu, C.; Schnick, W. $\text{Ca}[\text{LiAl}_3\text{N}_4]:\text{Eu}^{2+}$ — A Narrow-Band Red-Emitting Nitridolithoaluminate. *Chem. Mater.* **2014**, *26*, 3544–3549.
- [35] Wagatha, P.; Pust, P.; Weiler, V.; Wochnik, A. S.; Schmidt, P. J.; Scheu, C.; Schnick, W. $\text{Ca}_{18.75}\text{Li}_{10.5}[\text{Al}_{39}\text{N}_{55}]:\text{Eu}^{2+}$ — Supertetrahedron Phosphor for Solid-State Lighting. *Chem. Mater.* **2016**, *28*, 1220–1226.

- [36] Wilhelm, D.; Baumann, D.; Seibald, M.; Wurst, K.; Heymann, G.; Huppertz, H. Narrow-Band Red Emission in the Nitridolithoaluminate $\text{Sr}_4[\text{LiAl}_{11}\text{N}_{14}]:\text{Eu}^{2+}$. *Chem. Mater.* **2017**, *29*, 1204–1209.
- [37] Wagatha, P.; Weiler, V.; Schmidt, P. J.; Schnick, W. Tailoring Emission Characteristics: Narrow-Band Red Luminescence from SLA to $\text{CaBa}[\text{Li}_2\text{Al}_6\text{N}_8]:\text{Eu}^{2+}$. *Chem. Mater.* **2018**, *30*, 7885–7891.
- [38] Pust, P.; Hintze, F.; Hecht, C.; Weiler, V.; Locher, A.; Zitnanska, D.; Harm, S.; Wiechert, D.; Schmidt, P. J.; Schnick, W. Group (III) Nitrides $M[\text{Mg}_2\text{Al}_2\text{N}_4]$ ($M = \text{Ca}, \text{Sr}, \text{Ba}, \text{Eu}$) and $\text{Ba}[\text{Mg}_2\text{Ga}_2\text{N}_4]$ — Structural Relation and Nontypical Luminescence Properties of Eu^{2+} Doped Samples. *Chem. Mater.* **2014**, *26*, 6113–6119.
- [39] Wagatha, P.; Weiler, V.; Schmidt, P. J.; Schnick, W. Tunable Red Luminescence in Nitridomagnesoaluminates $\alpha\text{-Sr}_2[\text{MgAl}_5\text{N}_7]:\text{Eu}^{2+}$, $\beta\text{-Sr}_2[\text{MgAl}_5\text{N}_7]:\text{Eu}^{2+}$, and $\text{Sr}_8[\text{LiMg}_2\text{Al}_{21}\text{N}_{28}]:\text{Eu}^{2+}$. *Chem. Mater.* **2018**, *30*, 1755–1761.
- [40] Strobel, P.; de Boer, T.; Weiler, V.; Schmidt, P. J.; Moewes, A.; Schnick, W. Luminescence of an Oxonitridoberyllate: A Study of Narrow-Band Cyan-Emitting $\text{Sr}[\text{Be}_6\text{ON}_4]:\text{Eu}^{2+}$. *Chem. Mater.* **2018**, *30*, 3122–3130.
- [41] Baur, W. H. Effective Ionic Radii in Nitrides. *Crystallogr. Rev.* **1987**, *1*, 59–83.
- [42] Somer, M.; Yarasik, A.; Akselrud, L.; Leoni, S.; Rosner, H.; Schnelle, W.; Kniep, R. $\text{Ae}[\text{Be}_2\text{N}_2]$: nitridoberyllates of the heavier alkaline-earth metals. *Angew. Chem. Int. Ed.* **2004**, *43*, 1088–1092; *Angew. Chem.* **2004**, *116*, 1108–1112.
- [43] Eckerlin, P.; Rabenau, A.; Nortmann, H. Zur Kenntnis des Systems $\text{Be}_3\text{N}_2\text{-Si}_3\text{N}_4$. III. Darstellung und Eigenschaften von BeSiN_2 . *Z. Anorg. Allg. Chem.* **1967**, *353*, 113–121.
- [44] Somer, M.; Carrillo-Cabrera, W.; Peters, E.-M.; Peters, K.; von Schnering, H. Crystal structure of lithium beryllium nitride, LiBeN . *Z. Kristallogr.-Cryst. Mater.* **1996**, *211*, 635–635.
- [45] Agency for Toxic Substances and Disease Registry (ATSDR). *Toxicological Profile for Beryllium*; U.S. Department of Health and Human Services, P. H. S., Atlanta, GA, 1996.
- [46] Zeuner, M.; Hintze, F.; Schnick, W. Low temperature precursor route for highly efficient spherically shaped LED-phosphors $\text{M}_2\text{Si}_5\text{N}_8:\text{Eu}^{2+}$ ($M = \text{Eu}, \text{Sr}, \text{Ba}$). *Chem. Mater.* **2009**, *21*, 336–342.
- [47] Senker, J.; Jacobs, H.; Müller, M.; Press, W.; Müller, P.; Mayer, H.; Ibberson, R. Reorientational dynamics of amide ions in isotopic phases of strontium and calcium amide. 1. Neutron diffraction experiments. *J. Phys. Chem. B* **1998**, *102*, 931–940.
- [48] García-Gutiérrez, R.; Barboza-Flores, M.; Berman-Mendoza, D.; Contreras-López, O. E.; Ramos-Carrasco, A. Synthesis and characterization of highly luminescent beryllium nitride. *Mater. Lett.* **2014**, *132*, 179–181.
- [49] Sheldrick, G. M. Crystal structure refinement with SHELXL. *Acta Crystallogr., Sect. C: Struct. Chem.* **2015**, *71*, 3–8.
- [50] Cheary, R. W.; Coelho, A. A.; Cline, J. P. Fundamental parameters line profile fitting in laboratory diffractometers. *J. Res. Natl. Inst. Stand. Technol.* **2004**, *109*, 1–25.
- [51] Bergmann, J.; Kleeberg, R.; Haase, A.; Breidenstein, B. In *Advanced Fundamental Parameters Model for Improved Profile Analysis*, Materials Science Forum, Trans Tech Publications: 2000; pp 303–308.
- [52] Coelho, A. A. *TOPAS: A Program for Rietveld Refinement*, version 6; 2016.
- [53] Rietveld, H. M. A profile refinement method for nuclear and magnetic structures. *J. Appl. Crystallogr.* **1969**, *2*, 65–71.
- [54] Kresse, G.; Hafner, J. Ab initio molecular dynamics for liquid metals. *Phys. Rev. B* **1993**, *47*, 558–561.

- [55] Kresse, G.; Hafner, J. Ab initio molecular-dynamics simulation of the liquid-metal-amorphous-semiconductor transition in germanium. *Phys. Rev. B* **1994**, *49*, 14251–14269.
- [56] Kresse, G.; Furthmüller, J. Efficiency of ab-initio total energy calculations for metals and semiconductors using a plane-wave basis set. *Comput. Mater. Sci.* **1996**, *6*, 15–50.
- [57] Blöchl, P. E. Projector augmented-wave method. *Phys. Rev. B* **1994**, *50*, 17953–17979.
- [58] Kresse, G.; Joubert, D. From ultrasoft pseudopotentials to the projector augmented-wave method. *Phys. Rev. B* **1999**, *59*, 1758–1775.
- [59] Monkhorst, H. J.; Pack, J. D. Special points for Brillouin-zone integrations. *Phys. Rev. B* **1976**, *13*, 5188–5192.
- [60] Hinuma, Y.; Pizzi, G.; Kumagai, Y.; Oba, F.; Tanaka, I. Band structure diagram paths based on crystallography. *Comput. Mater. Sci.* **2017**, *128*, 140–184.
- [61] Perdew, J. P.; Burke, K.; Ernzerhof, M. Generalized Gradient Approximation Made Simple. *Phys. Rev. Lett.* **1996**, *77*, 3865–3868.
- [62] Perdew, J. P.; Burke, K.; Ernzerhof, M. Generalized Gradient Approximation Made Simple [Phys. Rev. Lett. 77, 3865 (1996)]. *Phys. Rev. Lett.* **1997**, *78*, 1396–1396.
- [63] Becke, A. D.; Johnson, E. R. A simple effective potential for exchange. *J. Chem. Phys.* **2006**, *124*, 221101.
- [64] Tran, F.; Blaha, P. Accurate Band Gaps of Semiconductors and Insulators with a Semilocal Exchange-Correlation Potential. *Phys. Rev. Lett.* **2009**, *102*, 226401.
- [65] Camargo-Martínez, J. A.; Baquero, R. Performance of the modified Becke-Johnson potential for semiconductors. *Phys. Rev. B* **2012**, *86*, 195106.
- [66] Le Page, Y.; Saxe, P. Symmetry-general least-squares extraction of elastic data for strained materials from ab initio calculations of stress. *Phys. Rev. B* **2002**, *65*, 104104.
- [67] Shannon, R. D. Revised effective ionic radii and systematic studies of interatomic distances in halides and chalcogenides. *Acta Crystallogr., Sect. A: Cryst. Phys., Diffr. Theor. Gen. Crystallogr.* **1976**, *32*, 751–767.
- [68] Strobel, P.; Niklaus, R.; Schmidt, P. J.; Schnick, W. Oxoberyllates SrBeO_2 and $\text{Sr}_{12}\text{Be}_{17}\text{O}_{29}$ as Novel Host Materials for Eu^{2+} Luminescence. *Chem. Eur. J.* **2018**, *24*, 12678–12685.
- [69] Pucher, F. J.; Marchuk, A.; Schmidt, P. J.; Wiechert, D.; Schnick, W. Luminescent nitridophosphates $\text{CaP}_2\text{N}_4:\text{Eu}^{2+}$, $\text{SrP}_2\text{N}_4:\text{Eu}^{2+}$, $\text{BaP}_2\text{N}_4:\text{Eu}^{2+}$, and $\text{BaSr}_2\text{P}_6\text{N}_{12}:\text{Eu}^{2+}$. *Chem. Eur. J.* **2015**, *21*, 6443–6448.
- [70] Schnick, W.; Huppertz, H.; Lauterbach, R. High temperature syntheses of novel nitrido- and oxonitrido-silicates and sialons using rf furnaces. *J. Mater. Chem.* **1999**, *9*, 289–296.
- [71] Huppertz, H.; Schnick, W. Synthesis, Crystal Structure, and Properties of the Nitridosilicates $\text{SrYbSi}_4\text{N}_7$ and $\text{BaYbSi}_4\text{N}_7$. *Z. Anorg. Allg. Chem.* **1997**, *623*, 212–217.
- [72] Li, Y. Q.; Fang, C. M.; de With, G.; Hintzen, H. T. Preparation, structure and photoluminescence properties of Eu^{2+} and Ce^{3+} -doped SrYSi_4N_7 . *J. Solid State Chem.* **2004**, *177*, 4687–4694.
- [73] López, R.; Gómez, R. Band-gap energy estimation from diffuse reflectance measurements on sol-gel and commercial TiO_2 : a comparative study. *J. Sol-Gel Sci. Technol.* **2012**, *61*, 1–7.
- [74] Tauc, J.; Grigorovici, R.; Vancu, A. Optical properties and electronic structure of amorphous germanium. *Phys. Status Solidi B* **1966**, *15*, 627–637.
- [75] Ashcroft, N. W.; Mermin, N. D., *Solid State Physics*. Saunders college Philadelphia, **1976**.
- [76] Hill, R. The elastic behaviour of a crystalline aggregate. *Proc. Phys. Soc. A* **1952**, *65*, 349–354.
- [77] Jiang, C.; Srinivasan, S.; Caro, A.; Maloy, S. Structural, elastic, and electronic properties of Fe_3C from first principles. *J. Appl. Phys.* **2008**, *103*, 043502.

-
- [78] Francisco, E.; Recio, J.; Blanco, M.; Pendás, A. M.; Costales, A. Quantum-mechanical study of thermodynamic and bonding properties of MgF_2 . *J. Phys. Chem. A* **1998**, *102*, 1595–1601.
- [79] Francisco, E.; Blanco, M.; Sanjurjo, G. Atomistic simulation of SrF_2 polymorphs. *Phys. Rev. B* **2001**, *63*, 094107.
- [80] Poirier, J.-P., *Introduction to the Physics of the Earth's Interior*. Cambridge University Press **2000**.
- [81] Denault, K. A.; Brgoch, J.; Kloss, S. D.; Gaultois, M. W.; Siewenie, J.; Page, K.; Seshadri, R. Average and local structure, debye temperature, and structural rigidity in some oxide compounds related to phosphor hosts. *ACS Appl. Mater. Interfaces* **2015**, *7*, 7264–72.
- [82] Liu, L.; Xie, R.-J.; Hirosaki, N.; Dierre, B.; Sekiguchi, T. Luminescence properties of a blue-emitting phosphor: $(\text{Sr}_{1-x}\text{Eu}_x)\text{Si}_9\text{Al}_{19}\text{ON}_{31}$ ($0 < x \leq 1$). *J. Solid State Chem.* **2013**, *207*, 49–54.
- [83] Xie, R.-J.; Hirosaki, N.; Yamamoto, Y.; Suehiro, T.; Mitomo, M.; Sakuma, K. Fluorescence of Eu^{2+} in Strontium Oxonitridoaluminosilicates (SiAlONS). *J. Ceram. Soc. Jpn.* **2005**, *113*, 462–465.
- [84] Shioi, K.; Hirosaki, N.; Xie, R.-J.; Takeda, T.; Li, Y. Luminescence properties of $\text{SrSi}_6\text{N}_8:\text{Eu}^{2+}$. *J. Mater. Sci.* **2008**, *43*, 5659–5661.
- [85] de Jong, M.; Seijo, L.; Meijerink, A.; Rabouw, F. T. Resolving the ambiguity in the relation between Stokes shift and Huang-Rhys parameter. *Phys. Chem. Chem. Phys.* **2015**, *17*, 16959–16969.
- [86] Curie, D., Absorption and emission spectra. In *Optical Properties of Ions in Solids*, Springer: 1975; pp 71–105.

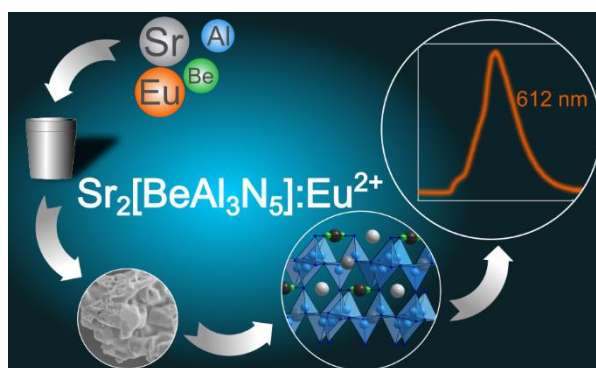
4. Illuminating Nitridoberylloaluminates: The Highly Efficient Red-Emitting Phosphor $\text{Sr}_2[\text{BeAl}_3\text{N}_5]:\text{Eu}^{2+}$

Eugenia Elzer, Philipp Strobel, Volker Weiler, Peter J. Schmidt, and Wolfgang Schnick

Chem. Mater. **2020**, *32*, 6611–6617

DOI: 10.1021/acs.chemmater.0c02037

Reprinted (adapted) with permission for non-commercial use from Chemistry of Materials. Copyright 2020 American Chemical Society.



ABSTRACT: The nitridoberylloaluminate $\text{Sr}_2[\text{BeAl}_3\text{N}_5]:\text{Eu}^{2+}$ was obtained through reaction of the binary nitrides in a hot isostatic press under a pressure of 50 MPa N_2 and a temperature of 1400 °C. The crystal structure was solved and refined from single-crystal X-ray diffraction data ($P\bar{1}$ (no. 2), $Z = 2$, $a = 6.061(2)$, $b = 6.982(3)$, $c = 7.872(4)$ Å and $\alpha = 102.22(3)$, $\beta = 112.62(2)$ and $\gamma = 104.02(2)^\circ$). The crystal structure of $\text{Sr}_2[\text{BeAl}_3\text{N}_5]:\text{Eu}^{2+}$ is made up out of a network of vertex- and edge-sharing AlN_4 tetrahedra and trigonal-planar BeN_3 units. The negative charge is compensated by Sr^{2+} ions occupying three crystallographic sites. Sr^{2+} ions are coordinated by seven and eight N atoms, respectively. After irradiation of Eu^{2+} doped samples with blue light (440–450 nm), strong red luminescence (emission maximum at ≈ 612 nm; full width at half-maximum (fwhm) 65–73 nm (1715 – 1966 cm^{-1}) is observed. Until now, $\text{Sr}_2[\text{BeAl}_3\text{N}_5]:\text{Eu}^{2+}$ is the only member of a compound class containing only beryllium and aluminum as network building atoms in a nitride, contributing to the range of red-emitting phosphors such as $\text{Sr}[\text{LiAl}_3\text{N}_4]:\text{Eu}^{2+}$ (SLA), $\text{Sr}[\text{Li}_2\text{Al}_2\text{O}_2\text{N}_2]:\text{Eu}^{2+}$ (SALON), $\text{Sr}_4[\text{LiAl}_{11}\text{N}_{14}]:\text{Eu}^{2+}$, or $\text{Sr}[\text{Mg}_3\text{SiN}_4]:\text{Eu}^{2+}$ (SMS).

4.1 Introduction

The search for new efficient and stable luminescent materials is an essential goal in solid-state chemistry, as these materials can significantly improve the quality of light emitting diodes (LEDs) for diverse applications. In the past years, nitrido(alumo)silicates have received much attention in solid-state lighting solutions, due to their thermal and chemical stability and promising optical properties. Eu^{2+} doped nitrido(alumo)silicates like $(\text{Ba},\text{Sr})_2\text{Si}_5\text{N}_8:\text{Eu}^{2+}$ and $M\text{AlSiN}_3:\text{Eu}^{2+}$ ($M = \text{Ca}, \text{Sr}$), show intense luminescence, which makes them suitable for implementation in phosphor converted LEDs.^[1-5]

The recent LED phosphor research is focused on exploration of narrow-band red-emitting phosphors to enhance luminous efficacy.^[6, 7] Here, structures based on highly condensed networks are discussed to be beneficial for narrow-band emission.^[8] The replacement of higher charged elements by lower charged ones, such as Be^{2+} , into solid-state host structures enables the discovery of highly condensed structures leading to a higher structural diversity, as has already been demonstrated for nitridoberyllosilicates ($M[\text{BeSi}_2\text{N}_4]$ ($M = \text{Sr}, \text{Eu}$)).^[9] Nitridoberylloaluminates, however, are unknown, thus far.

As a common structural feature, nitridoaluminates or -silicates contain condensed anionic networks of vertex- and edge-sharing TN_4 tetrahedra ($T = \text{Si}, \text{Al}$) including other metal cations as counterions. The degree of condensation κ is defined as the ratio of network-building ions T and coordinating anions N: $\kappa = n(T)/n(N)$ (e. g. $\kappa(\text{Si}_3\text{N}_4) = 0.75$; $\kappa(\text{AlN}) = 1$). In principle, nitridoaluminates can thus feature even higher condensed structures than nitridosilicates, therefore, acting as a promising compound class with intriguing properties and applications. Until now, however, only a few ternary nitridoaluminates have been reported, namely Li_3AlN_2 (rather a double-nitride than a nitridoaluminate), $M_3\text{Al}_2\text{N}_4$ ($M = \text{Sr}, \text{Ba}$), $\text{Ca}_6[\text{Al}_2\text{N}_6]$, and α - and β - $\text{Ca}_3[\text{Al}_2\text{N}_4]$.^[10-13]

In the last years, the structural diversity and κ of nitridoaluminates has been increased by partial substitution of Al^{3+} with Mg^{2+} or Li^+ ($\kappa(\text{Mg}_3\text{N}_2) = 1.5$, $\kappa(\text{Li}_3\text{N}) = 3$). These substitutions led to the discovery of a handful of quaternary nitridoaluminates, showing interesting luminescence properties upon doping with Eu^{2+} , namely $M[\text{Mg}_2\text{Al}_2\text{N}_4]:\text{Eu}^{2+}$ ($M = \text{Ca}, \text{Sr}, \text{Ba}$), $M[\text{LiAl}_3\text{N}_4]:\text{Eu}^{2+}$ ($M = \text{Ca}, \text{Sr}$), $\text{Ca}_{18.75}\text{Li}_{10.5}[\text{Al}_{39}\text{N}_{55}]:\text{Eu}^{2+}$, $\text{Sr}_4[\text{LiAl}_{11}\text{N}_{14}]:\text{Eu}^{2+}$, and α -/ β - $\text{Sr}_2[\text{MgAl}_5\text{N}_7]:\text{Eu}^{2+}$.^[14-19] The luminescence emerges from the parity-allowed transition from the $\text{Eu } 4f^6(^7\text{F})5d^1$ excited state to the $\text{Eu } 4f^7(^8\text{S}_{7/2})$ ground state and is significantly affected by the local environment of the dopant.^[20, 21] Especially, the

nitridolithoaluminate $\text{Sr}[\text{LiAl}_3\text{N}_4]:\text{Eu}^{2+}$ (SLA) that features outstanding luminescence properties, has gained much attention as a “next-generation LED-phosphor material”.^[16] Here, the high degree of condensation, a wide band gap and a dopant site with a high coordination number, lead to a very efficient narrow-band red emission and remarkable thermal stability of the luminescence behavior.^[16]

The search for new, highly condensed host lattices resulted in the investigation of introducing Be^{2+} into the anionic networks of nitridoaluminates. In contrast to Mg^{2+} , the incorporation of Be^{2+} in nitridoaluminates can lead to an even larger structural diversity, as Be can enter both, three- and fourfold coordination forming trigonal-planar BeN_3 units (e. g. $\text{Li}[\text{BeN}]$ and $AE[\text{Be}_2\text{N}_2]$ with $AE = \text{Mg}, \text{Ca}, \text{Sr}, \text{Ba}$) or BeN_4 tetrahedra (e. g. Be_3N_2 and BeSiN_2).^[22-25] Moreover, a high degree of condensation can be realized, as Be^{2+} features a lower formal charge when compared with Al^{3+} (or Si^{4+}). This principle has already been demonstrated for highly condensed (oxo)nitridoberyllates, as with the narrow-band cyan-emitting $\text{Sr}[\text{Be}_6\text{ON}_4]:\text{Eu}^{2+}$ ($\kappa = 1.2$), the ultra-narrow-band blue-emitting materials $AELi_2[\text{Be}_4\text{O}_6]:\text{Eu}^{2+}$ ($AE = \text{Sr}, \text{Ba}, \kappa = 0.67$), and the narrow-band blue-emitting $M\text{Be}_{20}\text{N}_{14}:\text{Eu}^{2+}$ ($M = \text{Sr}, \text{Ba}, \kappa = 1.43$).^[26-28] However, the incorporation of oxygen into the anionic network causes a reduction of the nephelauxetic effect, resulting in an emission shift towards the blue-cyan range. In contrast, nitride anions feature a higher covalence of the dopant-ligand interaction and cause a high crystal field splitting, which reduces the energy of the $5d$ levels of Eu^{2+} . Therefore, nitride-based host lattices feature a shift of the excitation and emission energies to higher wavelengths.^[20]

Recapitulating, the incorporation of Be^{2+} into nitridoaluminates, thus the preparation of nitridoberylloaluminates, can lead to the discovery of previously unknown structures. These new structures can have a high degree of condensation and an enhanced structural diversity, as not only BeN_4 tetrahedra but also trigonal-planar BeN_3 units may be formed. Here, we report on the first nitridoberylloaluminate. The crystal structure of $\text{Sr}_2[\text{BeAl}_3\text{N}_5]:\text{Eu}^{2+}$ is built up of AlN_4 tetrahedra and trigonal-planar BeN_3 units, resulting in a high degree of condensation. The nitridoberylloaluminate exhibit intense red luminescence after illumination with blue light.

4.2 Experimental Section

Safety Assessment

Working with compounds containing Be requires particular caution, as the element Be is toxic and can cause diseases, for example chronic beryllium disease (CBD), as well as being a carcinogen.^[29, 30] To prevent exposure to Be, especially the inhalation of Be containing dusts, all operations were conducted in closed systems (gloveboxes and Schlenk-type glassware).

Synthesis

The air and hydrolysis sensitivity of the starting materials and products made it a necessity to work in an Ar-filled glovebox (Unilab, MBraun, Garching, $\text{O}_2 < 1$ ppm, $\text{H}_2\text{O} < 1$ ppm) or in glassware filled with inert gas (Ar, (Air Liquide, 5.0)), which was attached to a Schlenk line. For desiccation and purification, Ar was flowing through columns filled with silica gel (Merck), molecular sieve (Fluka, 4 Å), KOH (Merck, $\geq 85\%$), P_4O_{10} (Roth, $\geq 99\%$), and titanium sponge (700 °C, Johnsen Matthey, 99.5%).

For the synthesis of $\text{Sr}_2[\text{BeAl}_3\text{N}_5]:\text{Eu}^{2+}$ stoichiometric amounts of the starting materials Sr_2N (Taiheiyō Cement Corp), AlN (ABCR, grade A) and Be_3N_2 (obtained from reaction of Be and N_2 at 1400 °C) were used.^[2, 31, 32] For doping a small amount of EuF_3 (Sigma-Aldrich) or $\text{Eu}(\text{NH}_2)_2$ was added to the reaction mixture. The exact amounts are summarized in Table C.1 and Table C.2. The starting materials were extensively ground using a tungsten carbide mortar and transferred into a tungsten crucible, which was transferred into a corundum crucible, before being placed into the hot isostatic press (HIP). The reactants were heated to 1400 °C with a rate of $300\text{ °C}\cdot\text{h}^{-1}$ and held at 1400 °C, while the N_2 pressure was kept at 50 MPa. After 2–5 h the temperature was reduced to 500 °C within 1–10 h. The products were cooled down to room temperature by shutting down the furnace.

The synthesis yielded heterogeneous products with orange crystals and some colorless and reddish side phases. The side phases could be identified as AlN, SrO, SrBe_2N_2 , and Be_3N_2 . A significant amount of the side phases can be removed by washing the samples under Ar atmosphere with a 1:2 mixture of acetic acid and isopropanol. The products were dried under vacuum and stored under Ar as the products are sensitive towards air and moisture. When irradiated with UV to blue light the compound shows red luminescence.

Electron Microscopy

The chemical composition, as well as the morphology, was analyzed using a scanning electron microscope (SEM) NanoLab G3 (Helios). To obtain the energy-dispersive X-ray (EDX) data the detector X-Mas 80 SDD (Oxford Instruments) was used. Several particles were examined with an accelerating voltage of 20 kV.

FTIR Spectroscopy

$\text{Sr}_2[\text{BeAl}_3\text{N}_5]:\text{Eu}^{2+}$ was examined with Fourier transform infrared (FTIR) spectroscopy on a Perkin WLMER BXII spectrometer (ATR method).

Single Crystal X-ray Diffraction

The selection of single crystals from the obtained samples was carried out under an optical microscope. Appropriate crystals were attached on MicroMounts (MiTeGen) with an aperture size of 20–30 μm . A Bruker D8 Venture diffractometer (rotating anode, Mo $K\alpha$ radiation) was used to collect the X-ray diffraction data. The program SADABS was utilized for absorption correction.^[33] The crystal structure was solved using Direct Methods and refined using least-squares methods (SHELX-2014). Due to the low content of Eu^{2+} , its contribution to the scattering density is irrelevant and was therefore neglected during the structure determination of $\text{Sr}_2[\text{BeAl}_3\text{N}_5]:\text{Eu}^{2+}$.

Crystallographic Data

Further information on the single-crystal structure data of $\text{Sr}_2[\text{BeAl}_3\text{N}_5]:\text{Eu}^{2+}$ can be requested from the Cambridge Crystallographic Data Centre by quoting the CSD number 2002561.

Powder X-ray Diffraction

For collection of powder X-ray diffraction data a STOE Stadi P diffractometer (Ge(111) monochromator, Mythen 1K detector) was used. The sample was enclosed in a glass capillary with 0.1–0.3 mm diameter (Hilgenberg, Germany) and irradiated with Cu $K\alpha_1$ radiation ($\lambda = 1.5406 \text{ \AA}$) in parafocusing Debye-Scherrer geometry. The TOPAS Academic 6 package was used for Rietveld refinements, by application of the fundamental parameters approach.^[34-37]

Luminescence

A HORIBA Fluoromax4 spectrofluorimeter system, which was connected to an Olympus BX51 microscope via optical fibers, was used to obtain luminescence spectra of single crystals (sealed in glass capillaries). The samples were excited with blue light ($\lambda_{\text{exc}} = 440 \text{ nm}$) and the emission spectra were collected between 400 and 800 nm (2 nm step size).

The collection of low temperature luminescence data on powder samples was conducted with an Ocean Optics HR2000 + ES spectrometer (2048 pixels, grating UA (200–1100 nm) slit 50). The powder samples were sealed in an evacuated chamber and cooled by a liquid-He compressor system (Advance Research System Inc., ARS4HW) in order to gather data between 6 and 300 K.

The measurements of the powder samples were performed on an in-house-built system. The spectrofluorimeter is equipped with a 150 W Xe lamp and two Czerny-Turner monochromators (focal length of 500 mm, grating: 1800 g/mm, blazed at 250/500 nm) with a spectral range of 230–820 nm. The system is based on a 5.3" integrating sphere. To determine the internal quantum efficiency (IQE), integrated emission and absorption intensities at the excitation wavelength of the samples were compared to reference samples (BaSO_4 white standard, and $\text{SrSi}_2\text{O}_2\text{N}_2:\text{Eu}^{2+}$ (Lumileds)).

UV-vis Spectroscopy

The collection of diffuse reflectance UV-vis spectra was carried out on a Jasco V-650 UV-vis spectrophotometer (Pfungstadt, Germany,) equipped with two different lamps (deuterium and halogen), a Czerny–Turner monochromator (1200 lines/mm, concave grating), and a photomultiplier tube detector.

4.3 Results and Discussion

Synthesis and Chemical Analysis

The above reported high-temperature synthesis gave access to the title compound $\text{Sr}_2[\text{BeAl}_3\text{N}_5]:\text{Eu}^{2+}$. The morphology of the crystals (Figure 4.1) and the atomic ratio of Sr:Al:N were determined by EDX measurements and correspond well with the sum formula (Table C.3).

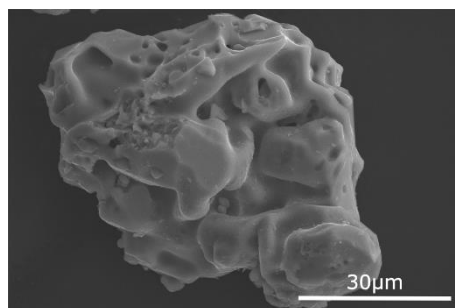


Figure 4.1. Morphology of $\text{Sr}_2[\text{BeAl}_3\text{N}_5]:\text{Eu}^{2+}$.

In washed samples no O was detected, confirming the formation of a pure nitride phase. The only detected metals were Sr, Al and Eu, as Be cannot be detected by EDX due to elemental limits. Therefore, it leaves Be as the only possible element for charge neutrality, based on the used starting materials. MAPLE calculations and bond lengths discussion, as discussed in detail below, support the assignment of Be as centers in the trigonal-planar BeN_3 units. No N–H and O–H groups could be observed by FTIR Spectroscopy of $\text{Sr}_2[\text{BeAl}_3\text{N}_5]:\text{Eu}^{2+}$ (Figure C.1).

Crystal Structure Determination

The crystal structures of $\text{Sr}_2[\text{BeAl}_3\text{N}_5]:\text{Eu}^{2+}$ was solved and refined (SHELX-2014)^[38] in space group $P\bar{1}$ (no. 2) with $Z=2$ and $a=6.061(2)$, $b=6.982(3)$, $c=7.872(4)$ Å, $\alpha=102.22(3)$, $\beta=112.62(2)$ and $\gamma=104.02(2)^\circ$. Crystallographic data are listed in Table 4.1. Wyckoff positions, atomic coordinates, and equivalent isotropic and anisotropic displacement parameters are listed in the Supporting Information (Table C.4–Table C.5).

Table 4.1: Crystallographic data of Sr₂[BeAl₃N₅]:Eu²⁺, standard deviations in parentheses.

	Sr ₂ [BeAl ₃ N ₅]:Eu ²⁺
formula mass/ g·mol ⁻¹	335.24
crystal system	triclinic
space group	$P\bar{1}$ (no. 2)
cell parameters/ Å, °	$a = 6.061(2)$ $b = 6.982(3)$ $c = 7.872(4)$ $\alpha = 102.22(3)$ $\beta = 112.62(2)$ $\gamma = 104.02(2)$
volume/ Å ³	280.5(2)
formula units/ cell	2
X-ray density/ g·cm ⁻³	3.969
abs. coefficient/ μ·mm ⁻¹	19.384
F(000)	308
crystal dimensions/ mm ³	0.004 × 0.003 × 0.002
diffractometer	Bruker D8 Venture
radiation	Mo Kα (λ = 0.71073 Å)
temperature/ K	293(2)
absorption correction	multi-scan
θ range/ °	2.981–44.976
observed reflections	14499
independent reflections	4490
independent reflections with $I \geq 4\sigma(I)$	3095
min./ max. transmission	0.829 / 1.000
refined parameters	103
GoF	1.004
R indices ($F_0^2 \geq 2\sigma(F_0^2)$)	$R1 = 0.0366 /$ $wR2 = 0.0570$
R indices (all data)	$R1 = 0.0720 /$ $wR2 = 0.0644$
min./max. residual electron density/ e·Å ⁻³	-1.316 / 1.119

The structure model obtained from X-ray data is supported by lattice-energy calculations (MAPLE, Madelung Part of Lattice Energy). Table C.6 in the Supporting Information contains the calculated values. The partial MAPLE values correspond well with reference data in literature, whereas the MAPLE sum of Sr₂[BeAl₃N₅]:Eu²⁺ deviates only slightly (1%) from the values of a hypothetical synthesis from SrBe₂₀N₁₄:Eu²⁺, AlN, and α-Be₃N₂. With respect to the different coordination of Be in Sr₂[BeAl₃N₅]:Eu²⁺ (trigonal- planar) compared with SrBe₂₀N₁₄ or α-Be₃N₂ (tetrahedral) and the decreased coordination of N^[4] in AlN or α-Be₃N₂ to N^[3] in Sr₂[BeAl₃N₅]:Eu²⁺, the deviation is small and therefore supports the crystal structure model.

Crystal Structure Description

The nitridoberylloaluminate $\text{Sr}_2[\text{BeAl}_3\text{N}_5]:\text{Eu}^{2+}$ exhibits a condensed three-dimensional network, made up of edge- and vertex-connected AlN_4 tetrahedra and trigonal-planar BeN_3 units (Figure 4.2). The degree of condensation is $\kappa = 0.8$

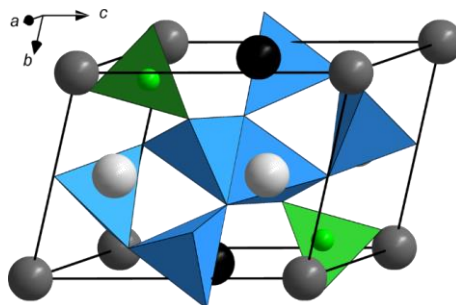


Figure 4.2: Unit cell of $\text{Sr}_2[\text{BeAl}_3\text{N}_5]:\text{Eu}^{2+}$ with AlN_4 tetrahedra (light blue), trigonal-planar BeN_3 units (green), and Sr atoms (Sr1: light gray, Sr2: gray, Sr3: black).

The structure consists of edge-sharing double tetrahedra $[\text{Al}_2\text{N}_6]^{12-}$, referred to as bow ties, and two edge-sharing trigonal-planar BeN_3 units, forming $[\text{Be}_2\text{N}_4]^{8-}$ units. The bow ties are further connected to each other over common vertices forming layers of bow ties (Figure 4.3a, blue), creating slightly distorted *sechser*-rings, which are filled with two $[\text{Be}_2\text{N}_4]^{8-}$ units, one above (Figure 4.3a, dark green) and one below the bow tie layer (Figure 4.3a, light green). The layers are further connected over common edges forming channels that are filled with Sr ions for charge neutrality (Figure 4.3b+c).

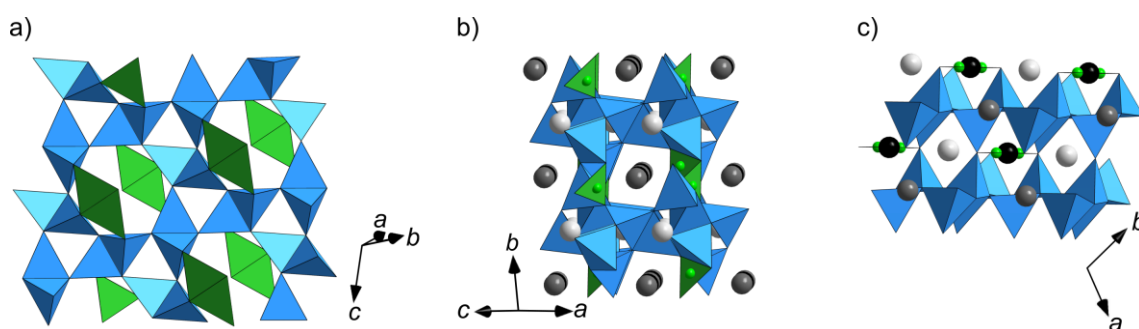


Figure 4.3: Crystal structure of $\text{Sr}_2[\text{BeAl}_3\text{N}_5]:\text{Eu}^{2+}$ with $[\text{Al}_2\text{N}_6]^{12-}$ units (blue) and $[\text{Be}_2\text{N}_4]^{8-}$ units (green) and Sr ions (Sr1: light gray, Sr2: gray, Sr3 black). a) top view of one layer of $[\text{Al}_2\text{N}_6]^{12-}$ and $[\text{Be}_2\text{N}_4]^{8-}$ units; b) view \perp to $[010]$; c) view of two bow tie layers along $[001]$.

The crystal structure of $\text{Sr}_2[\text{BeAl}_3\text{N}_5]:\text{Eu}^{2+}$ shows building units that are already known from nitridoberyllates as well as nitridoaluminates. $[\text{Be}_2\text{N}_4]^{8-}$ can be found in LiBeN or AEBe_2N_2 ($\text{AE} = \text{Ca}, \text{Sr}, \text{Ba}$),^[23, 24] while $[\text{Al}_2\text{N}_6]^{12-}$ units can be observed in α - and β - $\text{Ca}_3[\text{Al}_2\text{N}_4]$ (edge-sharing

bow ties)^[13] or $M_3\text{Al}_2\text{N}_4$ ($M = \text{Sr}, \text{Ba}$)^[11, 12] (chains of vertex sharing bow ties). Therefore, the structure of the title compound exhibits well-known building units that are, to the best of our knowledge, arranged in an unprecedented three-dimensional network.

In $\text{Sr}_2[\text{BeAl}_3\text{N}_5]:\text{Eu}^{2+}$ the Al–N distances (1.821(2)–1.926(2) Å) and the Be–N distances (1.647(3)–1.719(4) Å) (Table C.7) are in agreement with values in other known nitrides containing $[\text{Al}_2\text{N}_6]^{12-}$ bow tie units (e. g., $\text{AE}_3\text{Al}_2\text{N}_4$ ($\text{AE} = \text{Ca}, \text{Sr}, \text{Ba}$): 1.823(10)–1.985(9) Å,^[11-13] CaLiAlN_2 : 1.918(4)–1.959(4) Å,^[39] $\text{Ca}_5\text{Si}_2\text{Al}_2\text{N}_8$: 1.8332(11)–1.9521(10) Å)^[40] or nitridoberyllates containing $[\text{Be}_2\text{N}_4]^{8-}$ units (AEBe_2N_2 ($\text{AE} = \text{Ca}, \text{Sr}, \text{Ba}$): 1.632(6)–1.67(3) Å, LiBeN : 1.625(2)–1.6830(13) Å).^[23, 24] The Sr atoms occupy three crystallographically independent sites. The Sr1 atom is surrounded by seven N atoms, whereas the Sr2 and Sr3 atoms exhibit a hexagonal bipyramidal coordination and a distorted tetragonal prismatic coordination, respectively (Figure 4.4). The symmetric coordination around Sr2 and Sr3 plays a crucial role for a small Stokes shift and a reduction of the emission band width of the Eu^{2+} doped phosphor.

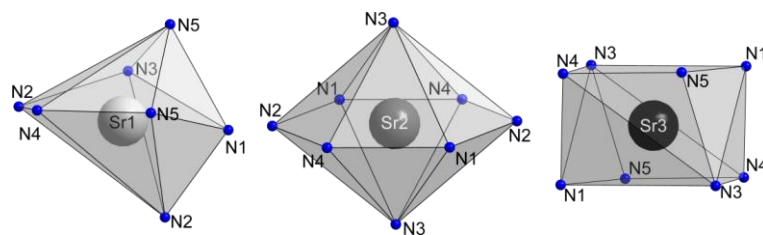


Figure 4.4: Coordination sphere of Sr1 (left, light gray), Sr2 (middle, gray) and Sr3 (right, black) atoms in $\text{Sr}_2[\text{BeAl}_3\text{N}_5]:\text{Eu}^{2+}$ with N atoms in blue.

The interatomic distances between Sr and N atoms vary between 2.682(2) and 3.186(3) Å. The values correspond well with the sum of the ionic radii (Sr–N: 2.67 (CN(Sr) = 7) or 2.72 Å (CN(Sr) = 8))^[41] and Sr–N distances in other nitridoaluminates containing Sr eight-fold coordination by N atoms (e. g. $\text{Sr}_4[\text{LiAl}_{11}\text{N}_{14}]:\text{Eu}^{2+}$, $\text{Sr}[\text{Mg}_2\text{Al}_2\text{N}_4]:\text{Eu}^{2+}$ or $\text{Sr}[\text{LiAl}_3\text{N}_4]:\text{Eu}^{2+}$ (SLA)).^{[14,}

16, 18]

Powder X-ray Diffraction

The bulk phase composition of the washed samples of $\text{Sr}_2[\text{BeAl}_3\text{N}_5]:\text{Eu}^{2+}$ was determined by Rietveld refinement of powder X-ray diffraction data (Table C.8). The refinements show that $\text{Sr}_2[\text{BeAl}_3\text{N}_5]:\text{Eu}^{2+}$ can be obtained as the main phase (Figure 4.5). In addition, the samples contain AlN, $\alpha\text{-Be}_3\text{N}_2$, as well as small amounts of SrO.

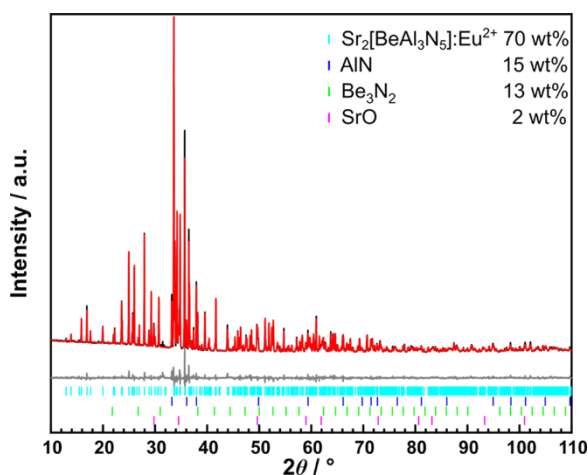


Figure 4.5: Rietveld refinement of $\text{Sr}_2[\text{BeAl}_3\text{N}_5]:\text{Eu}^{2+}$ ($\text{Cu K}\alpha_1$, $\lambda = 1.5406 \text{ \AA}$). Observed (black line) and calculated X-ray diffraction pattern (red line) with the difference curve (gray line). Tick marks correspond to the position of Bragg reflections of $\text{Sr}_2[\text{BeAl}_3\text{N}_5]:\text{Eu}^{2+}$ (cyan), AlN (blue), and Be_3N_2 (green), and SrO (magenta).

UV-vis Spectroscopy

Undoped samples of $\text{Sr}_2[\text{BeAl}_3\text{N}_5]$ (Figure C.2a) were used to determine the optical band gap from diffuse reflectance UV-vis spectra. The samples contained small amounts of SrBe_2N_2 (yellow body color) and thus absorb in the visible spectral range. Therefore, UV-Vis spectra of purified $\text{Sr}_2[\text{BeAl}_3\text{N}_5]$ samples were recorded to assign the correct transition to $\text{Sr}_2[\text{BeAl}_3\text{N}_5]$. Converting the measured reflectance spectra R to pseudoabsorption spectra was achieved by using the Kubelka-Munk function $F(R) = (1-R)^2/2R$.^[42] Through a linear fit of the data at the inflection point from the Tauc plot (Figure C.2b), the optical band gap was determined. This provides, that a direct allowed transition ($n = 1/2$) takes place. The optical band gap for $\text{Sr}_2[\text{BeAl}_3\text{N}_5]$ was determined to be around 3.8 eV and can be compared to other nitrides (e. g. $M[\text{Mg}_2\text{Al}_2\text{N}_4]$ ($M = \text{Ca}, \text{Sr}, \text{Ba}$): 3.65–3.8 eV).^[14]

Luminescence

$\text{Sr}_2[\text{BeAl}_3\text{N}_5]:\text{Eu}^{2+}$ (2% nominal Eu^{2+} concentration) shows strong red emission upon excitation with UV to blue light with maximum absorption around 440 nm. To study the luminescence properties, measurements on powder samples and single crystals were conducted. The obtained spectra are presented in Figure 4.6 and clearly show, that the luminescence properties can be associated with $\text{Sr}_2[\text{BeAl}_3\text{N}_5]:\text{Eu}^{2+}$ and rule out a possible contribution of the side phase $\text{SrO}:\text{Eu}^{2+}$ to the measured spectra. The sample exhibits an emission maximum at $\lambda_{\text{em}} \approx 612 \text{ nm}$, and an fwhm of $\approx 71 \text{ nm}/1899 \text{ cm}^{-1}$. At room temperature, the internal quantum efficiency (IQE) was determined as 33%.

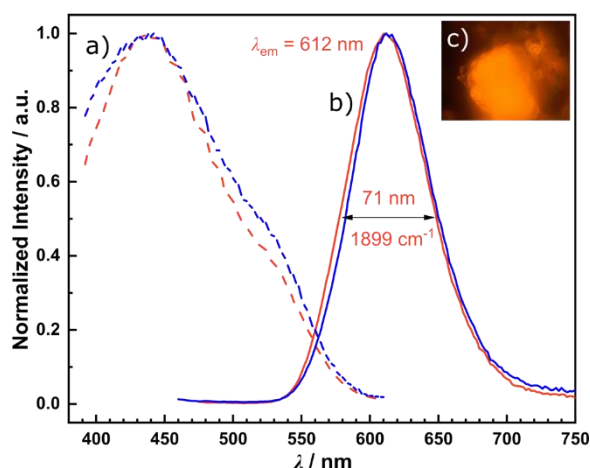


Figure 4.6: Normalized photoluminescence spectra of a bulk sample (red) and a single crystal (blue) of $\text{Sr}_2[\text{BeAl}_3\text{N}_5]:\text{Eu}^{2+}$ (2 mol-% Eu^{2+} concentration referred to Sr). a) Excitation spectra ($\lambda_{\text{obs}} = 622 \text{ nm}$); b) Emission spectra ($\lambda_{\text{exc}} = 440 \text{ nm}$); c) Photograph of a single crystal of $\text{Sr}_2[\text{BeAl}_3\text{N}_5]:\text{Eu}^{2+}$ irradiated with blue light ($\lambda_{\text{exc}} = 420 \text{ nm}$).

Emission maxima and fwhm are comparable to other nitrides like $M[\text{Mg}_2\text{Al}_2\text{N}_4]:\text{Eu}^{2+}$ ($M = \text{Ca}$ and Sr : $\lambda_{\text{em}} = 606$ and 612 nm , $\text{fwhm} \approx 67 \text{ nm}/1815 \text{ cm}^{-1}$ and $82 \text{ nm}/1823 \text{ cm}^{-1}$),^[14] $\text{Sr}_{0.99}\text{Eu}_{0.01}\text{AlSiN}_3$ ($\lambda_{\text{em}} = 610 \text{ nm}$, $\approx 72 \text{ nm}$),^[43] and the narrow-red emitting $\text{Sr}[\text{Mg}_3\text{SiN}_4]:\text{Eu}^{2+}$, ($\lambda_{\text{em}} = 615 \text{ nm}$, $\text{fwhm} \approx 43 \text{ nm}/1170 \text{ cm}^{-1}$).^[44] Compared with the remarkably narrow emission band of red-emitting phosphors like SMS ($\text{fwhm} \approx 1170 \text{ cm}^{-1}$), SLA ($\text{fwhm} \approx 1180 \text{ cm}^{-1}$) or the oxonitride $\text{Sr}[\text{Li}_2\text{Al}_2\text{O}_2\text{N}_2]:\text{Eu}^{2+}$ (SALON) (1286 cm^{-1})^[45] the emission band of $\text{Sr}_2[\text{BeAl}_3\text{N}_5]:\text{Eu}^{2+}$ is slightly broadened. These three phosphors crystallize in variants of the UCr_4C_4 structure type with one (SMS, SALON) or two crystallographic sites for a Sr atom (SLA). The coordination sphere of Sr contains 8 N atoms (SMS and SLA) or 4 N and 4 O atoms (SALON) in a cube-like coordination, reducing the inhomogeneous broadening of the emission due to chemically different dopant sites to a minimum. As already discussed in the crystal structure description the structure of $\text{Sr}_2[\text{BeAl}_3\text{N}_5]:\text{Eu}^{2+}$ provides three independent Sr^{2+} sites with varying Sr–N distances (Figure 4.4, Table C.7). Different Eu–N distances lead to broadened emission bands composed from emission transitions of the individual dopant sites. Considering the difference between the shortest Sr–N and the longest Sr–N distance at the respective sites ($\Delta\text{Sr–N}$: Sr1: 0.289 \AA , Sr2: 0.589 \AA , Sr3: 0.487 \AA), it is even more surprising that the band broadening of the emission in $\text{Sr}_2[\text{BeAl}_3\text{N}_5]:\text{Eu}^{2+}$ turns out to be relatively moderate.

In order to determine the influence of dopant concentration on the luminescence properties, samples with varying Eu^{2+} concentration (1, 2, 3 and 4 mol-% Eu^{2+} concentration referred to Sr) were synthesized. The synthesis of samples with up to 4 mol-% Eu^{2+} referred to the amount of Sr^{2+} were successful. A larger amount of Eu^{2+} prevented the formation of the title compound. The emission

band width shows a slight narrowing up to an fwhm of ≈ 65 nm/ 1715 cm^{-1} and a shift of the emission band to higher wavelengths with increasing Eu^{2+} concentration from 608 to 612 nm most likely due to reabsorption effects. The spectra and values for all samples can be found in the Supporting Information (Figure C.1, Table C.9).

For the investigation of the thermal behavior of $\text{Sr}_2[\text{BeAl}_3\text{N}_5]:\text{Eu}^{2+}$ (2 mol-% Eu^{2+} concentration referred to Sr), temperature dependent luminescence spectra were recorded. Figure 4.7 show the photoluminescence (PL) spectra of a bulk sample.

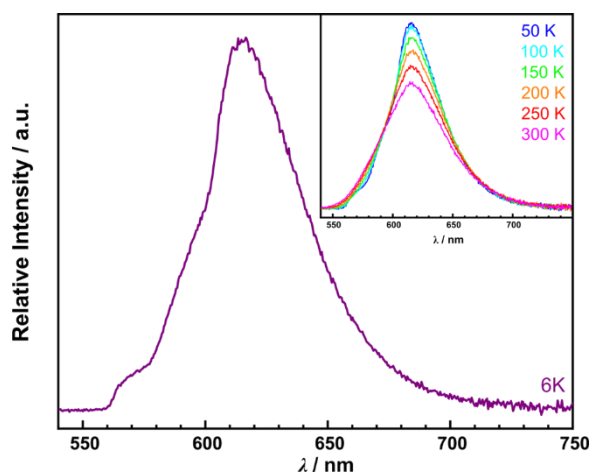


Figure 4.7: PL spectrum of $\text{Sr}_2[\text{BeAl}_3\text{N}_5]:\text{Eu}^{2+}$ with 2 mol-% Eu^{2+} concentration referred to Sr at 6 K (violet line). Inset in the right corner: PL spectra at varying temperatures (50–300 K). Measurements were collected on a powder sample.

As expected, the sample shows band narrowing with decreasing temperature and no significant shift in the emission maxima at lower temperatures. Therefore, the luminescence in $\text{Sr}_2[\text{BeAl}_3\text{N}_5]:\text{Eu}^{2+}$ can be assigned to normal Eu^{2+} emission whereas anomalous luminescence behavior with trapped exciton emission, as was observed for e. g. $\text{Sr}[\text{Mg}_2\text{Al}_2\text{N}_4]:\text{Eu}^{2+}$, can be ruled out.^[14] The emission spectrum at 6 K exhibits three superimposing emission peaks (≈ 570 , 590 and 612 nm) in $\text{Sr}_2[\text{BeAl}_3\text{N}_5]:\text{Eu}^{2+}$ which probably originate from the three different crystallographic sites for $\text{Sr}^{2+}/\text{Eu}^{2+}$. The relative photoluminescence intensity at 473 K (200 °C) with respect to the emission intensity at 6 K (Figure C.4) is ca. 60%. Therefore, the phosphor shows only moderate thermal quenching.

4.4 Conclusion

Here, we present the first representative in the class of nitridoberylloaluminates, namely $\text{Sr}_2[\text{BeAl}_3\text{N}_5]:\text{Eu}^{2+}$. The compound exhibits intense luminescence in the red spectral range upon doping with Eu^{2+} . It was synthesized in a high-pressure/high-temperature reaction in a HIP. The crystal structure of $\text{Sr}_2[\text{BeAl}_3\text{N}_5]:\text{Eu}^{2+}$ was solved and refined from single-crystal data and supported by X-ray diffraction data and MAPLE calculations. The highly condensed 3D network of $\text{Sr}_2[\text{BeAl}_3\text{N}_5]:\text{Eu}^{2+}$ is made up of edge- and vertex-sharing AlN_4 tetrahedra and trigonal-planar BeN_3 units and provides three crystallographically independent sites for Sr. Eu^{2+} doped samples exhibit an emission maximum at ≈ 612 nm and an fwhm of ≈ 71 nm/ 1899 cm^{-1} . The luminescence properties can be compared to compounds like $M[\text{Mg}_2\text{Al}_2\text{N}_4]:\text{Eu}^{2+}$ ($M = \text{Ca}, \text{Sr}$), $\text{Sr}_{0.99}\text{Eu}_{0.01}\text{AlSiN}_3$, or SALON. In contrast to narrow-band red-emitting SMS, SLA or SALON the fwhm in $\text{Sr}_2[\text{BeAl}_3\text{N}_5]:\text{Eu}^{2+}$ is slightly broader, likely due to three different substitutional lattice sites for Eu^{2+} with different Eu–N distances. This leads to broadened emission bands composed from emission transitions of the individual dopant sites. Nevertheless, $\text{Sr}_2[\text{BeAl}_3\text{N}_5]:\text{Eu}^{2+}$, as the first member of the class of nitridoberylloaluminates, contributes to the class of red-emitting phosphors and can potentially serve as a stepping stone for the further search for highly efficient narrow-band red-emitting phosphors in the class of nitridoberylloaluminates.

For the future, next to studies on the luminescence properties of this novel compound class, the structural chemistry of nitride materials incorporating Al and Be is especially interesting, since the diagonal relationship of both main group elements should have a large effect on cation ordering phenomena as well as coordination eventually leading to novel, not yet observed crystal structures.

4.5 Acknowledgements

The authors are grateful to Christian Minke for EDX measurements and Dr. Peter Mayer (both Department of Chemistry, University of Munich (LMU)) for collecting single-crystal X-ray diffraction data, as well as Petra Huppertz and Detlef Wiechert (Lumileds Phosphor Center Aachen) for luminescence measurements.

4.6 References

- [1] Höpfe, H. A.; Lutz, H.; Morys, P.; Schnick, W.; Seilmeier, A. Luminescence in Eu^{2+} -doped $\text{Ba}_2\text{Si}_5\text{N}_8$: Fluorescence, Thermoluminescence, and Upconversion. *J. Phys. Chem. Solids* **2000**, *61*, 2001–2006.
- [2] Zeuner, M.; Hintze, F.; Schnick, W. Low temperature precursor route for highly efficient spherically shaped LED-phosphors $\text{M}_2\text{Si}_5\text{N}_8:\text{Eu}^{2+}$ ($\text{M} = \text{Eu}, \text{Sr}, \text{Ba}$). *Chem. Mater.* **2009**, *21*, 336–342.
- [3] Uheda, K.; Hirosaki, N.; Yamamoto, Y.; Naito, A.; Nakajima, T.; Yamamoto, H. Luminescence properties of a red phosphor, $\text{CaAlSiN}_3:\text{Eu}^{2+}$, for white light-emitting diodes. *Electrochem. Solid-State Lett.* **2006**, *9*, H22-H25.
- [4] Xie, R.-J.; Hirosaki, N.; Suehiro, T.; Xu, F.-F.; Mitomo, M. J. C. o. m. A Simple, Efficient Synthetic Route to $\text{Sr}_2\text{Si}_5\text{N}_8:\text{Eu}^{2+}$ -Based Red Phosphors for White Light-Emitting Diodes. *Chem. Mater.* **2006**, *18*, 5578–5583.
- [5] Watanabe, H.; Kijima, N. Crystal structure and luminescence properties of $\text{Sr}_x\text{Ca}_{1-x}\text{AlSiN}_3:\text{Eu}^{2+}$ mixed nitride phosphors. *J. Alloys Compd.* **2009**, *475*, 434–439.
- [6] *Solid-state lighting R&D plan*; US Department of Energy, 2016.
- [7] *2019 Lighting R&D Opportunities*; US Department of Energy, 2019.
- [8] Liao, H.; Zhao, M.; Molochev, M. S.; Liu, Q.; Xia, Z. Learning from a Mineral Structure toward an Ultra-Narrow-Band Blue-Emitting Silicate Phosphor $\text{RbNa}_3(\text{Li}_3\text{SiO}_4)_4:\text{Eu}^{2+}$. *Angew. Chem. Int. Ed.* **2018**, *57*, 11728–11731; *Angew. Chem.* **2018**, *130*, 11902–11905.
- [9] Strobel, P.; Weiler, V.; Schmidt, P. J.; Schnick, W. $\text{Sr}[\text{BeSi}_2\text{N}_4]:\text{Eu}^{2+}/\text{Ce}^{3+}$ and $\text{Eu}[\text{BeSi}_2\text{N}_4]$: Nontypical Luminescence in Highly Condensed Nitridoberyllsilicates. *Chem. Eur. J.* **2018**, *24*, 7243–7249.
- [10] Juza, R.; Hund, F. Metal Amides and Metal Nitrides. XVII. The Ternary Nitrides Li_3AlN_2 and Li_3GaN_2 . *Z. Anorg. Chem.* **1948**, *257*, 13–25.
- [11] Blase, W.; Cordier, G.; Ludwig, M.; Kniep, R. $\text{Sr}_3[\text{Al}_2\text{N}_4]$: A Nitridoaluminate with Corrugated Tetrahedral Chains $1^\infty[\text{AlN}_{4/2}^{3-}]$. *Z. Naturforsch., B: J. Chem. Sci.* **1994**, *49*, 501–505.
- [12] Ludwig, M.; Niewa, R.; Kniep, R. Dimers $[\text{Al}_2\text{N}_6]^{12-}$ and Chains $[\text{AlN}_{4/2}^{3-}]$ in the Crystal Structures of $\text{Ca}_6[\text{Al}_2\text{N}_6]$ and $\text{Ba}_3[\text{Al}_2\text{N}_4]$. *Z. Naturforsch., B: J. Chem. Sci.* **1999**, *54*, 461–465.
- [13] Ludwig, M.; Jäger, J.; Niewa, R.; Kniep, R. Crystal Structures of Two Polymorphs of $\text{Ca}_3[\text{Al}_2\text{N}_4]$. *Inorg. Chem.* **2000**, *39*, 5909–5911.
- [14] Pust, P.; Hintze, F.; Hecht, C.; Weiler, V.; Locher, A.; Zitnanska, D.; Harm, S.; Wiechert, D.; Schmidt, P. J.; Schnick, W. Group (III) Nitrides $M[\text{Mg}_2\text{Al}_2\text{N}_4]$ ($M = \text{Ca}, \text{Sr}, \text{Ba}, \text{Eu}$) and $\text{Ba}[\text{Mg}_2\text{Ga}_2\text{N}_4]$ —Structural Relation and Nontypical Luminescence Properties of Eu^{2+} Doped Samples. *Chem. Mater.* **2014**, *26*, 6113–6119.
- [15] Pust, P.; Wochnik, A. S.; Baumann, E.; Schmidt, P. J.; Wiechert, D.; Scheu, C.; Schnick, W. $\text{Ca}[\text{LiAl}_3\text{N}_4]:\text{Eu}^{2+}$ — A Narrow-Band Red-Emitting Nitridolithoaluminate. *Chem. Mater.* **2014**, *26*, 3544–3549.
- [16] Pust, P.; Weiler, V.; Hecht, C.; Tucks, A.; Wochnik, A. S.; Henss, A. K.; Wiechert, D.; Scheu, C.; Schmidt, P. J.; Schnick, W. Narrow-band red-emitting $\text{Sr}[\text{LiAl}_3\text{N}_4]:\text{Eu}^{2+}$ as a next-generation LED-phosphor material. *Nat. Mater.* **2014**, *13*, 891–896.
- [17] Wagatha, P.; Pust, P.; Weiler, V.; Wochnik, A. S.; Schmidt, P. J.; Scheu, C.; Schnick, W. $\text{Ca}_{18.75}\text{Li}_{10.5}[\text{Al}_{39}\text{N}_{55}]:\text{Eu}^{2+}$ —Supertetrahedron Phosphor for Solid-State Lighting. *Chem. Mater.* **2016**, *28*, 1220–1226.

- [18] Wilhelm, D.; Baumann, D.; Seibald, M.; Wurst, K.; Heymann, G.; Huppertz, H. Narrow-Band Red Emission in the Nitridolithoaluminate Sr₄[LiAl₁₁N₁₄]:Eu²⁺. *Chem. Mater.* **2017**, *29*, 1204–1209.
- [19] Wagatha, P.; Weiler, V.; Schmidt, P. J.; Schnick, W. Tunable Red Luminescence in Nitridomagnesoaluminates α -Sr₂[MgAl₅N₇]:Eu²⁺, β -Sr₂[MgAl₅N₇]:Eu²⁺, and Sr₈[LiMg₂Al₂₁N₂₈]:Eu²⁺. *Chem. Mater.* **2018**, *30*, 1755–1761.
- [20] Dorenbos, P. Energy of the first 4f⁷ → 4f⁶5d transition of Eu²⁺ in inorganic compounds. *J. Lumin.* **2003**, *104*, 239–260.
- [21] Tolhurst, T. M.; Strobel, P.; Schmidt, P. J.; Schnick, W.; Moewes, A. Direct Measurements of Energy Levels and Correlation with Thermal Quenching Behavior in Nitride Phosphors. *Chem. Mater.* **2017**, *29*, 7976–7983.
- [22] Stackelberg, M. v.; Paulus, R. Untersuchungen über die Kristallstruktur der Nitride und Phosphide zweiwertiger Metalle. *Z. Phys. Chem.* **1933**, *22*, 305–322.
- [23] Somer, M.; Carrillo-Cabrera, W.; Peters, E.-M.; Peters, K.; von Schnering, H. Crystal structure of lithium beryllium nitride, LiBeN. *Z. Kristallogr.-Cryst. Mater.* **1996**, *211*, 635–635.
- [24] Somer, M.; Yarasik, A.; Akselrud, L.; Leoni, S.; Rosner, H.; Schnelle, W.; Kniep, R. Ae[Be₂N₂]: nitridoberyllates of the heavier alkaline-earth metals. *Angew. Chem. Int. Ed.* **2004**, *43*, 1088–1092; *Angew. Chem.* **2004**, *116*, 1108–1112.
- [25] Eckerlin, P.; Rabenau, A.; Nortmann, H. Zur Kenntnis des Systems Be₃N₂–Si₃N₄. III. Darstellung und Eigenschaften von BeSiN₂. *Z. Anorg. Allg. Chem.* **1967**, *353*, 113–121.
- [26] Strobel, P.; de Boer, T.; Weiler, V.; Schmidt, P. J.; Moewes, A.; Schnick, W. Luminescence of an Oxonitridoberyllate: A Study of Narrow-Band Cyan-Emitting Sr[Be₆ON₄]:Eu²⁺. *Chem. Mater.* **2018**, *30*, 3122–3130.
- [27] Strobel, P.; Maak, C.; Weiler, V.; Schmidt, P. J.; Schnick, W. Ultra-Narrow-Band Blue-Emitting Oxoberyllates AELi₂[Be₄O₆]:Eu²⁺ (AE = Sr, Ba) Paving the Way to Efficient RGB pc-LEDs. *Angew. Chem. Int. Ed.* **2018**, *57*, 8739–8743; *Angew. Chem.* **2018**, *130*, 8875–8879.
- [28] Elzer, E.; Niklaus, R.; Strobel, P. J.; Weiler, V.; Schmidt, P. J.; Schnick, W. MBe₂₀N₁₄:Eu²⁺ (M = Sr, Ba) - Highly Condensed Nitridoberyllates with Exceptional Highly Energetic Eu²⁺ Luminescence. *Chem. Mater.* **2019**, *31*, 3174–3182.
- [29] Kumberger, O.; Schmidbaur, H. Warum ist Beryllium so toxisch? *Chem. Unserer Zeit* **1993**, *27*, 310–316.
- [30] Naglav, D.; Buchner, M. R.; Bendt, G.; Kraus, F.; Schulz, S. Off the Beaten Track-A Hitchhiker's Guide to Beryllium Chemistry. *Angew. Chem. Int. Ed.* **2016**, *55*, 10562–10576; *Angew. Chem.* **2016**, *128*, 10718–10733.
- [31] Senker, J.; Jacobs, H.; Müller, M.; Press, W.; Müller, P.; Mayer, H.; Ibberson, R. Reorientational dynamics of amide ions in isotopic phases of strontium and calcium amide. 1. Neutron diffraction experiments. *J. Phys. Chem. B* **1998**, *102*, 931–940.
- [32] García-Gutiérrez, R.; Barboza-Flores, M.; Berman-Mendoza, D.; Contreras-López, O. E.; Ramos-Carrasco, A. Synthesis and characterization of highly luminescent beryllium nitride. *Mater. Lett.* **2014**, *132*, 179–181.
- [33] Sheldrick, G. M. *SADABS, Multi-Scan Absorption Correction, Bruker AXS*, version 2; Madison, WI, USA, 2012.
- [34] Cheary, R. W.; Coelho, A. A.; Cline, J. P. Fundamental parameters line profile fitting in laboratory diffractometers. *J. Res. Natl. Inst. Stand. Technol.* **2004**, *109*, 1–25.

- [35] Bergmann, J.; Kleeberg, R.; Haase, A.; Breidenstein, B. In *Advanced Fundamental Parameters Model for Improved Profile Analysis*, Materials Science Forum, Trans Tech Publications: 2000; pp 303–308.
- [36] Coelho, A. A. *TOPAS: A Program for Rietveld Refinement*, version 6; 2016.
- [37] Rietveld, H. M. A profile refinement method for nuclear and magnetic structures. *J. Appl. Crystallogr.* **1969**, *2*, 65–71.
- [38] Sheldrick, G. M. Crystal structure refinement with SHELXL. *Acta Crystallogr., Sect. C: Struct. Chem.* **2015**, *71*, 3–8.
- [39] Pust, P.; Pagano, S.; Schnick, W. Ca[LiAlN₂]: A Quaternary Nitridoaluminate. *Eur. J. Inorg. Chem.* **2013**, *2013*, 1157–1160.
- [40] Ottinger, F.; Cuervo-Reyes, E.; Nesper, R. Synthesis, Crystal and Electronic Structure of the Nitridoaluminosilicate Ca₅[Si₂Al₂N₈] *Z. Anorg. Allg. Chem.* **2010**, *636*, 1085–1089.
- [41] Shannon, R. D. Revised effective ionic radii and systematic studies of interatomic distances in halides and chalcogenides. *Acta Crystallogr., Sect. A: Cryst. Phys., Diffr. Theor. Gen. Crystallogr.* **1976**, *32*, 751–767.
- [42] López, R.; Gómez, R. Band-gap energy estimation from diffuse reflectance measurements on sol–gel and commercial TiO₂: a comparative study. *J. Sol-Gel Sci. Technol.* **2012**, *61*, 1–7.
- [43] Watanabe, H.; Yamane, H.; Kijima, N. Crystal Structure and Luminescence of Sr_{0.99}Eu_{0.01}AlSiN₃. *J. Solid State Chem.* **2008**, *181*, 1848–1852.
- [44] Schmiechen, S.; Schneider, H.; Wagatha, P.; Hecht, C.; Schmidt, P. J.; Schnick, W. Toward New Phosphors for Application in Illumination-Grade White pc-LEDs: The Nitridomagnesosilicates Ca[Mg₃SiN₄]:Ce³⁺, Sr[Mg₃SiN₄]:Eu²⁺, and Eu[Mg₃SiN₄]. *Chem. Mater.* **2014**, *26*, 2712–2719.
- [45] Hoerder, G. J.; Seibald, M.; Baumann, D.; Schroder, T.; Peschke, S.; Schmid, P. C.; Tyborski, T.; Pust, P.; Stoll, I.; Bergler, M.; Patzig, C.; Reissaus, S.; Krause, M.; Berthold, L.; Hoche, T.; Johrendt, D.; Huppertz, H. Sr[Li₂Al₂O₂N₂]:Eu²⁺ – A high performance red phosphor to brighten the future. *Nat. Commun.* **2019**, *10*, 1–9.

5. Inverse-Tunable Red Luminescence and Electronic Properties of Nitridoberyllaluminates $\text{Sr}_{2-x}\text{Ba}_x[\text{BeAl}_3\text{N}_5]:\text{Eu}^{2+}$ ($x = 0-2$)

Eugenia Elzer, Philipp Strobel, Volker Weiler, Muhammad R. Amin, Peter J. Schmidt, Alexander Moewes and Wolfgang Schnick

Chem. Eur. J. **2022**, e202104121

DOI: 10.1002/chem.202104121

Reprinted (adapted) with permission for non-commercial use from Chemistry – A European Journal (open access). Copyright 2022 John Wiley and Sons.



ABSTRACT: The nitridoberyllaluminate $\text{Ba}_2[\text{BeAl}_3\text{N}_5]:\text{Eu}^{2+}$ and solid solutions $\text{Sr}_{2-x}\text{Ba}_x[\text{BeAl}_3\text{N}_5]:\text{Eu}^{2+}$ ($x = 0.5, 1.0, 1.5$) were synthesized in a hot isostatic press (HIP) under 50 MPa N_2 atmosphere at 1200 °C. $\text{Ba}_2[\text{BeAl}_3\text{N}_5]:\text{Eu}^{2+}$ crystallizes in triclinic space group $P\bar{1}$ (no. 2) ($Z = 2$, $a = 6.1869(10)$, $b = 7.1736(13)$, $c = 8.0391(14)$ Å, $\alpha = 102.754(8)$, $\beta = 112.032(6)$, $\gamma = 104.765(7)^\circ$), which was determined from single-crystal X-ray diffraction data. The lattice parameters of the solid solution series have been obtained from Rietveld refinements and show a nearly linear dependence on the atomic ratio Sr:Ba. The electronic properties and the band gaps of $M_2[\text{BeAl}_3\text{N}_5]$ ($M = \text{Sr}, \text{Ba}$) have been investigated by a combination of soft X-ray spectroscopy and density functional theory (DFT) calculations. Upon irradiation with blue light (440–450 nm), the nitridoberyllaluminates exhibit intense orange to red luminescence, which can be tuned between 610 and 656 nm (fwhm = 1922–2025 cm^{-1} (72–87 nm)). In contrast to the usual trend, the substitution of the smaller Sr^{2+} by larger Ba^{2+} leads to an inverse-tunable luminescence to higher wavelengths. Low-temperature luminescence measurements have been performed to exclude anomalous emission.

5.1 Introduction

In recent years, the constant search for new phosphors pushed solid-state lighting, based on light-emitting diodes (LEDs), to one of the most popular lighting solutions. Especially, further improving luminous efficacy of white phosphor-converted (pc) LEDs with high color rendition depends on phosphor materials with optimized luminescence properties.^[1] The combination of a high color rendering index without compromising luminous efficacy is a key factor in the optimization of pc-LEDs.^[2] Here, particularly the emission maximum and the width of the emission band of the red-emitting phosphor play a significant role to avoid emission in the deep red spectral area.

In this context, Eu^{2+} doped nitrides are intensively investigated, as they do not only show good thermal and chemical stability, but also promising optical properties.^[3] The luminescence observed in Eu^{2+} activated phosphors can be generally attributed to transitions between the $4f^6(^7\text{F})5d^1$ excited state and the $4f^7(^8\text{S}_{7/2})$ ground state and is highly sensitive towards the local environment of the activator ion.^[4] Red-emitting nitrides like $(\text{Sr},\text{Ba})_2\text{Si}_5\text{N}_8:\text{Eu}^{2+}$ ^[5] or $(\text{Ca},\text{Sr})\text{AlSiN}_3:\text{Eu}^{2+}$ ^[6] already found their way into commercial application as phosphors in pc-LEDs, due to their excellent photoluminescence properties. However, since both compounds exhibit rather broad emission bands, the luminous efficacy is limited due to spill-over to the infrared region. Structures based on highly condensed anionic networks are shown to be beneficial for narrow-band emission.

The degree of condensation κ is defined as the ratio of tetrahedral centers T to coordinating N atoms ($\kappa = n(T):n(\text{N})$). In theory κ can be increased (κ by replacing higher charged tetrahedral centers (Al^{3+} , Si^{4+}) with lower charged ones like Li^+ or Mg^{2+} . Indeed, these substitutions led to the discovery of promising narrow-band red-emitting phosphors, such as $\text{Sr}[\text{LiAl}_3\text{N}_4]:\text{Eu}^{2+}$ (SLA),^[7] $\text{Sr}[\text{Mg}_3\text{SiN}_4]:\text{Eu}^{2+}$ (SMS),^[8] or $\text{Sr}[\text{Li}_2\text{Al}_2\text{O}_2\text{N}_2]:\text{Eu}^{2+}$ (SALON).^[9] Even though SMS exhibits an emission maximum in the desired spectral region at $\lambda_{\text{max}} = 615$ nm and a very narrow emission band with a full width at half-maximum (fwhm) of 43 nm/ 1170 cm^{-1} , high thermal quenching prevents its application in pc-LEDs. SLA ($\lambda_{\text{max}} = 654$ nm, fwhm = 50 nm/ 1180 cm^{-1}) and the recently reported SALON ($\lambda_{\text{max}} = 614$ nm, fwhm = 48 nm/ 1286 cm^{-1}) show better thermal performance, but emission band widths of both compounds do not yet match the target value of 30 nm, proposed for a high-performance red phosphor.^[1]

In the pursuit of Eu^{2+} doped host lattices with an even narrower emission band, the incorporation of Be^{2+} into the anionic networks of nitrides may evolve as a viable solution also for narrow-red emitting materials. Compared to Al^{3+} or Si^{4+} , Be^{2+} has a lower formal charge, which can lead to host lattices with a large κ , as already demonstrated with the discovery of the cyan-emitting oxonitridoberyllate $\text{Sr}[\text{Be}_6\text{ON}_4]:\text{Eu}^{2+}$,^[10] the blue-emitting oxoberyllates $A\text{ELi}_2[\text{Be}_4\text{O}_6]:\text{Eu}^{2+}$ ($A = \text{Sr}, \text{Ba}$),^[11] the blue-emitting nitridoberyllates $M\text{Be}_{20}\text{N}_{14}:\text{Eu}^{2+}$ ($M = \text{Sr}, \text{Ba}$),^[12] or the red-emitting nitridoberylaluminates $\text{Sr}_2[\text{BeAl}_3\text{N}_5]:\text{Eu}^{2+}$.^[13]

As already mentioned, the $5d$ energy levels are highly sensitive towards the local environment of the activator ion. This enables tuning of the shape and position of the emission band by tailoring the local structure around the activator. With respect to a free Eu^{2+} ion, the energy of the lowest excited state of Eu^{2+} ions in a host lattice is affected by the nephelauxetic effect and the crystal field splitting. Usually, a covalent activator–ligand bond and a strong crystal field result in a significant lowering of the energetic position of the $5d$ orbitals. Therefore, the distance between the ground state and the excited state is reduced, resulting in a red-shifted emission. The crystal field splitting depends on the local environment, especially the activator–ligand bond length, the coordination number and the shape of the coordination polyhedron around the activator. Thus, the size of the cations substituted by Eu^{2+} can be used to modify the emission color of a phosphor. If smaller cations (for example, Sr^{2+}) are replaced by larger ones (for example, Ba^{2+}), the metal–ligand distances and the volume of the coordination polyhedra usually increase, leading to a weaker crystal field splitting, shifting the emission bands towards the blue spectral region. The opposite case is seen in $M[\text{Mg}_3\text{SiN}_4]:\text{Eu}^{2+}$ ($M = \text{Sr}, \text{Ba}$),^[8, 14] and $M[\text{Mg}_2\text{Al}_2\text{N}_4]:\text{Eu}^{2+}$ ($M = \text{Ca}, \text{Sr}, \text{Ba}$),^[15] where a trend to red-shifted emission in the sequence $\text{Ca} < \text{Sr} < \text{Ba}$ has been observed. The emission of both phosphors with $M = \text{Ba}$ is discussed to originate from two emission processes: regular $4f^5d^1 \rightarrow 4f^7$ Eu^{2+} emission accompanied by trapped exciton emission, which is characterized by a large Stokes shift, a broad emission band and unusual temperature behavior.^[14, 15] Trapped-exciton emission has also been observed in nitridoberyllate phosphors, such as $\text{SrBeSi}_2\text{N}_4:\text{Eu}^{2+}$ and $M\text{Be}_{20}\text{N}_{14}:\text{Eu}^{2+}$ ($M = \text{Sr}, \text{Ba}$).^[12, 16] The compounds exhibiting such anomalous luminescence show unexpected behavior at low temperatures: The emission maximum is shifted to longer wavelengths at lower temperatures compared to the values obtained at room temperature.^[14, 15, 17, 18]

In the pursuit of the discovery of new phosphors with optimized luminescence properties different strategies have been proposed, for example mineral prototype evolution strategy, single-particle diagnosis approach, machine learning or cation substitution strategy.^[19-22] The relation of Eu^{2+} luminescence and the crystal structure of the host lattice motivates substitution in already known structures as well as exploration of completely new structures to contribute to the understanding of structure-property relationships.

In this contribution, we report on optical luminescence of $\text{Ba}_2[\text{BeAl}_3\text{N}_5]:\text{Eu}^{2+}$ and the solid solution series $\text{Sr}_{2-x}\text{Ba}_x[\text{BeAl}_3\text{N}_5]:\text{Eu}^{2+}$ ($x = 0.5, 1.0, 1.5$), as well as their syntheses and electronic properties. Upon irradiation with blue light, the nitridoberylloaluminates exhibit intense orange to red luminescence. In contrast to the usual trend, the emission maximum in the nitridoberylloaluminates $\text{Sr}_{2-x}\text{Ba}_x[\text{BeAl}_3\text{N}_5]:\text{Eu}^{2+}$ ($x > 0$) is inversely shifted to higher wavelengths by the incorporation of the larger cation Ba^{2+} . This contribution shows that even small changes in the local environment in the investigated nitridoberylloaluminates have a significant effect on the luminescence, since activator concentration and anomalous emission can be ruled out as causes for the unexpected red-shifted emission with increasing size of the alkaline earth element.

5.2 Results and Discussion

Synthesis and Chemical Analysis

A modification of the reported synthesis for $\text{Sr}_2[\text{BeAl}_3\text{N}_5]:\text{Eu}^{2+}$,^[13] gave access to a solid solution series with the nominal composition $\text{Sr}_{2-x}\text{Ba}_x[\text{BeAl}_3\text{N}_5]:\text{Eu}^{2+}$ ($x = 0.5, 1.0$ and 1.5) and $\text{Ba}_2[\text{BeAl}_3\text{N}_5]:\text{Eu}^{2+}$. The products were obtained as crystalline powders with orange body color and red luminescence upon irradiation with blue light. The morphology of the crystals is shown in Figure D.2. The atomic ratio of Sr:Ba:Al:N (Table 5.1), as obtained from EDX measurements, range within the estimated standard deviations from the intended sum formulas for the solid solution series $\text{Sr}_{2-x}\text{Ba}_x[\text{BeAl}_3\text{N}_5]:\text{Eu}^{2+}$.

Table 5.1. EDX results of $\text{Sr}_{2-x}\text{Ba}_x[\text{BeAl}_3\text{N}_5]:\text{Eu}^{2+}$ ($x = 0, 0.5, 1.0, 1.5, 2.0$). Theoretical values (th.) and experimental values (exp.) in mol% for each composition with standard deviations in parentheses.

x	$\text{Sr}_{2-x}\text{Ba}_x[\text{BeAl}_3\text{N}_5]:\text{Eu}^{2+}$									
	0		0.5		1.0		1.5		2.0	
	th.	exp.	th.	exp.	th.	exp.	th.	exp.	th.	exp.
Sr	20	25(3)	15	11(3)	10	9(1)	5	5(1)	0	0
Ba	0	0	5	7(2)	10	12(2)	15	14(1)	20	16(3)
Al	30	30(4)	30	32(4)	30	34(3)	30	33(2)	30	36(2)
N	50	45(6)	50	43(4)	50	44(3)	50	48(3)	50	49(3)
O	0	0	0	7(7)	0	1(1)	0	0	0	0

Beryllium usually cannot be detected with this method. The oxygen content is insignificant within the estimated standard deviations and was only detected for the Sr-rich representatives of the solid solution series ($x = 0.5, 1.0$). A possible reason might be the hydrolysis sensitivity of the investigated powder samples. As already mentioned in the experimental section the formation of $M\text{Be}_2\text{N}_2$ ($M = \text{Sr}, \text{Ba}$) and SrO as impurity phases hampered the preparation of a defined composition with regard to the atomic ratio of Sr:Ba for the solid solution phases.

Crystal Structure

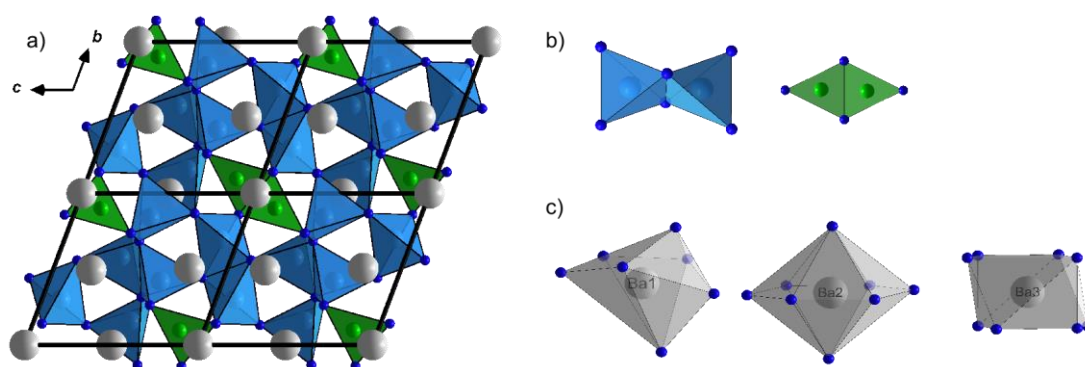
Based on the crystal structure solution and refinement (SHELX-2014),^[23] $\text{Ba}_2[\text{BeAl}_3\text{N}_5]:\text{Eu}^{2+}$ crystallizes in space group $P\bar{1}$ (no. 2) isotypical to $\text{Sr}_2[\text{BeAl}_3\text{N}_5]:\text{Eu}^{2+}$.^[13] During the refinement of the crystal structure the small amount of Eu^{2+} was neglected, due to the insignificant contribution to the scattering density. Crystallographic data of the Ba containing phase show an increase of the unit cell volume (~7%) compared to $\text{Sr}_2[\text{BeAl}_3\text{N}_5]:\text{Eu}^{2+}$, due to the incorporation of the larger Ba^{2+} ion (Table 5.2).

Detailed crystallographic data, atomic coordinates, Wyckoff positions, isotropic displacement parameters, anisotropic displacement parameters and selected distances and angles of $\text{Ba}_2[\text{BeAl}_3\text{N}_5]:\text{Eu}^{2+}$ are summarized in the Supporting Information (Table D.3–Table D.7). Detailed information on the single-crystal data of $\text{Ba}_2[\text{BeAl}_3\text{N}_5]:\text{Eu}^{2+}$ are provided free of charge by the joint Cambridge Crystallographic Data Centre and Fachinformationszentrum Karlsruhe Access Structures service. Deposition Number CSD 2121521 (for $\text{Ba}_2[\text{BeAl}_3\text{N}_5]:\text{Eu}^{2+}$) contains the supplementary crystallographic data for this paper.

Table 5.2: Crystallographic data of $\text{Ba}_2[\text{BeAl}_3\text{N}_5]:\text{Eu}^{2+}$ compared to reported values for $\text{Sr}_2[\text{BeAl}_3\text{N}_5]:\text{Eu}^{2+}$.^[13] Standard deviations in parentheses.

	$\text{Sr}_2[\text{BeAl}_3\text{N}_5]:\text{Eu}^{2+}$	$\text{Ba}_2[\text{BeAl}_3\text{N}_5]:\text{Eu}^{2+}$
Formula mass/ $\text{g}\cdot\text{mol}^{-1}$	335.24	434.68
Crystal system	triclinic	
Space group	$P\bar{1}$ (no. 2)	
Formula units/ cell	2	
Cell parameters/ \AA , $^\circ$	$a = 6.061(2)$	$a = 6.1869(10)$
	$b = 6.982(3)$	$b = 7.1736(13)$
	$c = 7.872(4)$	$c = 8.0391(14)$
	$\alpha = 102.22(3)$	$\alpha = 102.754(8)$
	$\beta = 112.62(2)$	$\beta = 112.032(6)$
	$\gamma = 104.02(2)$	$\gamma = 104.765(7)$
Volume/ \AA^3	280.5(2)	299.24(9)
X-ray density/ $\text{g}\cdot\text{cm}^{-3}$	3.969	4.824

The crystal structure of $\text{Ba}_2[\text{BeAl}_3\text{N}_5]:\text{Eu}^{2+}$ (Figure 5.1a) consists of edge- and vertex-sharing AlN_4 tetrahedra and trigonal-planar BeN_3 units. Each AlN_4 tetrahedron shares one edge with another AlN_4 tetrahedron building a bow-tie unit ($[\text{Al}_2\text{N}_6]^{12-}$) and each BeN_3 unit is connected to a second BeN_3 unit over a common edge, building a planar $[\text{Be}_2\text{N}_4]^{8-}$ unit (Figure 5.1b). These building units are further connected by common vertices forming a three-dimensional anionic network, which contains channels filled with Ba^{2+} (and Eu^{2+} , when doped) for charge neutrality. The alkaline earth (AE) ions are distributed over three different coordination sites (Ba1, Ba2 and Ba3) and coordinated by seven (Ba1) and eight (Ba2 and Ba3) N atoms, respectively (Figure 5.1c).

**Figure 5.1.** Crystal structure representation of $\text{Ba}_2[\text{BeAl}_3\text{N}_5]:\text{Eu}^{2+}$ with Al atoms (light blue), Be atoms (green), N atoms (blue) and Ba atoms (gray). a) view of $2 \times 2 \times 2$ unit cells along $[100]$; b) bow-tie unit $[\text{Al}_2\text{N}_6]^{12-}$ (top, light blue) and $[\text{Be}_2\text{N}_4]^{8-}$ unit (bottom, green); c) coordination polyhedra (gray) around Ba1 (top), Ba2 (middle) and Ba3 (bottom).

The interatomic distances between Ba atoms and N atoms are in the range of 2.719(5)–3.243(4) Å, which is comparable with other Ba containing nitrides with a coordination number (CN) of eight (Figure D.3). The increase of the distances in the sequence $d_{\text{Ba1-N}} < d_{\text{Ba2-N}} < d_{\text{Ba3-N}}$ corresponds well with the higher CN around Ba2 and Ba3. Both effects explain the increased thermal displacements of the Ba2/Ba3 sites in comparison to Ba1 (Table D.4). The different distances are also reflected in the polyhedral volumes, which are significantly smaller around Ba1 (31.64 Å³) relative to Ba2 (46.15 Å³) and Ba3 (44.41 Å³).

The bulk phase composition of the samples was determined by Rietveld refinement of powder X-ray diffraction data (Table D.8). For the refinement of $\text{Sr}_{2-x}\text{Ba}_x[\text{BeAl}_3\text{N}_5]:\text{Eu}^{2+}$ ($x > 0$), the structural model of $\text{Ba}_2[\text{BeAl}_3\text{N}_5]:\text{Eu}^{2+}$ from single-crystal X-ray diffraction data was used. Representative for all samples, the plot of the Rietveld refinement of $\text{Ba}_2[\text{BeAl}_3\text{N}_5]:\text{Eu}^{2+}$ is shown in Figure 5.2, confirming $\text{Ba}_2[\text{BeAl}_3\text{N}_5]:\text{Eu}^{2+}$ as the main phase. The sample contains small amounts of AlN and BaBe_2N_2 as impurity phases. Rietveld refinement plots for $\text{Sr}_{2-x}\text{Ba}_x[\text{BeAl}_3\text{N}_5]:\text{Eu}^{2+}$ ($x > 0$) are provided in the Supporting Information (Figure D.4).

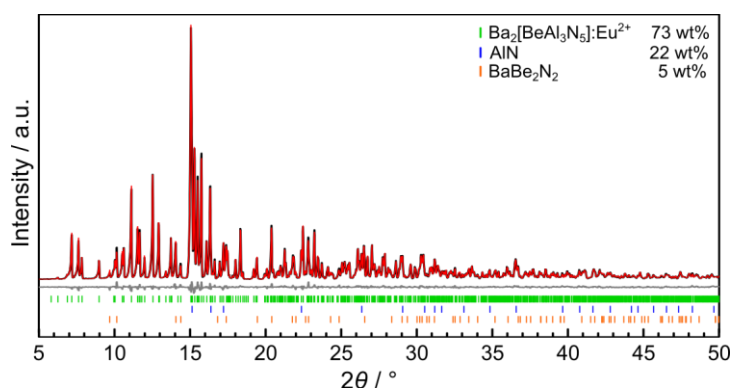


Figure 5.2: Rietveld refinement of $\text{Ba}_2[\text{BeAl}_3\text{N}_5]:\text{Eu}^{2+}$ ($\text{Mo K}\alpha_1 = 0.71073 \text{ \AA}$). Experimental data (black line), calculated pattern (red line) and difference curve (gray line). Tick marks: position of Bragg reflections of $\text{Ba}_2[\text{BeAl}_3\text{N}_5]:\text{Eu}^{2+}$ (green), AlN (blue), and BaBe_2N_2 (orange).

Due to the larger ionic radius of Ba^{2+} compared to Sr^{2+} , the lattice parameters of the samples are increasing with Ba^{2+} partially or completely occupying the Sr sites. Comparing the lattice parameters (Figure 5.3), an almost linear dependence on the atomic ratio Ba:Sr is observed.

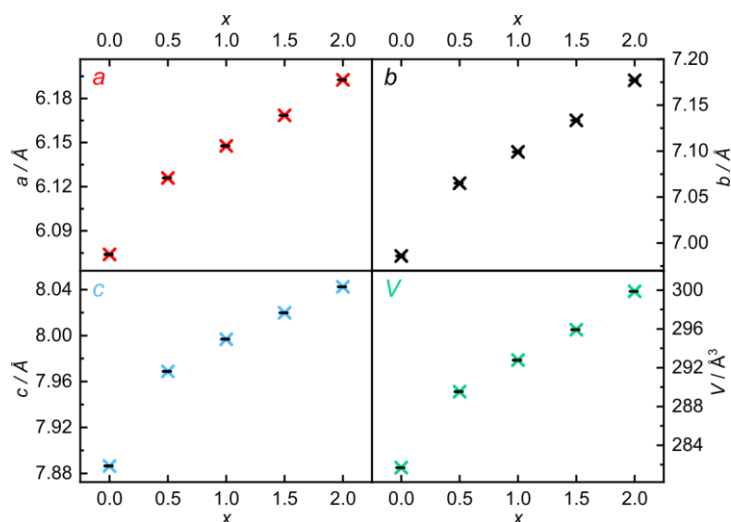


Figure 5.3: Comparison of the lattice parameters a (red), b (black), and c (light blue), and the volume of the unit cell V (green) of $\text{Sr}_{2-x}\text{Ba}_x[\text{BeAl}_3\text{N}_5]:\text{Eu}^{2+}$ with $x = 0, 0.5, 1.0, 1.5$ and 2.0 obtained from Rietveld refinements.

As already discussed above, the structure provides three crystallographically independent AE^{2+} ($AE^{2+} = \text{Sr}, \text{Ba}$) sites (Figure 5.1c) with coordination polyhedra of different sizes and shapes. Since the local coordination around the cation replaced by Eu^{2+} can have a strong influence on the photoluminescence properties of the nitridoberylloaluminates, the occupation of Sr/Ba1, Sr/Ba2 and Sr/Ba3 sites was investigated using Rietveld refinements. A graphical representation of the site occupation factors is illustrated in Figure 5.4, indicating a mixed occupancy of all three sites.

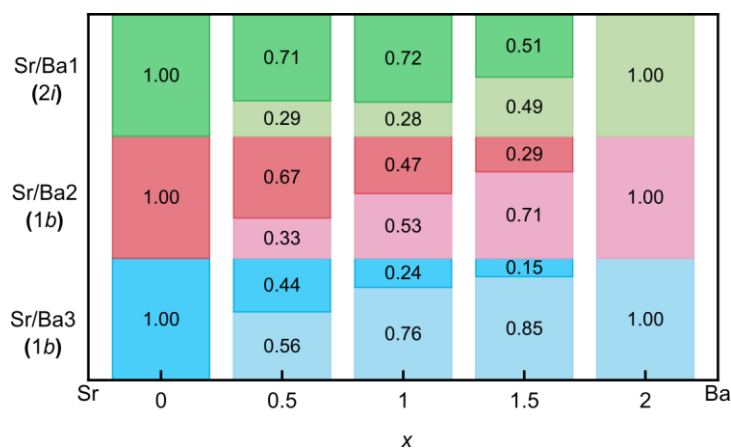


Figure 5.4: Graphical representation of the site occupation factors of the three crystallographic sites occupied by Sr and/or Ba in the solid solution series $\text{Sr}_{2-x}\text{Ba}_x[\text{BeAl}_3\text{N}_5]:\text{Eu}^{2+}$. Wyckoff positions of the respective sites are given in brackets. The darker color represents Sr, while the lighter color stands for Ba.

The refinement was restrained to allow only electroneutral sum formula. Therefore, the three crystallographic sites were assumed to be fully occupied while the Sr:Ba ratio was refined. According to the refinements, the atomic ratios of Sr:Ba are 1.3:0.7 ($x = 0.5$), 1.1:0.9 ($x = 1.0$) and 0.7:1.3 ($x = 1.5$).

Due to the different ionic radii of Ba^{2+} (1.42 Å, CN = 8) and Sr^{2+} (1.26 Å, CN = 8),^[24] an ordering of the heavy atoms is plausible. The members of the solid solution, however, do not show ordering of the AE^{2+} ions, but indicate a mixed occupancy of all three sites (Figure 5.4). But the distribution of the larger Ba^{2+} ion is uneven across the possible sites. Ba^{2+} ions prefer the occupation of Sr/Ba2 and Sr/Ba3, probably based on the larger polyhedral volumes compared to the Sr/Ba1 site. The impact of these results will be further discussed in the luminescence section.

Electronic Properties

The electronic properties of $M_2[\text{BeAl}_3\text{N}_5]:\text{Eu}^{2+}$ ($M = \text{Sr}, \text{Ba}$) were investigated by a combination of synchrotron-based soft X-ray absorption spectroscopy (XAS) and X-ray emission spectroscopy (XES), as well as DFT calculations. As the results for both compounds are quite similar, the XES, XAS, resonant inelastic X-ray scattering spectra (RIXS) and a non-resonant X-ray emission spectrum (NXES) for $\text{Sr}_2[\text{BeAl}_3\text{N}_5]:\text{Eu}^{2+}$ are shown in Figure 5.5, while the spectra for $\text{Ba}_2[\text{BeAl}_3\text{N}_5]:\text{Eu}^{2+}$ can be found in the Supporting Information (Figure D.5). The solid black line shown in Figure 5.5b corresponds to the experimental PFY for $\text{Sr}_2[\text{BeAl}_3\text{N}_5]:\text{Eu}^{2+}$, which is compared to core hole (solid orange line) and ground state (dash-dotted orange line) calculations.

It is found that the experimental XAS spectrum is in good agreement with the core hole calculations, as all major features are reproduced at the correct energy positions and approximately at the correct peak heights. The comparison of the two calculated absorption spectra (Figure 5.5b, orange) to the measured spectrum (Figure 5.5b, black) makes it clear that the core hole concentration in the experiment lies somewhere between the two calculated cases. Therefore, the core hole concentration should be more dilute than the case we calculated, and which reflects 1 of 20 atoms in the supercell missing a 1s electron. A more diluted core hole concentration (and hence larger supercell) was computationally not feasible due to the increased cpu time that would be required.

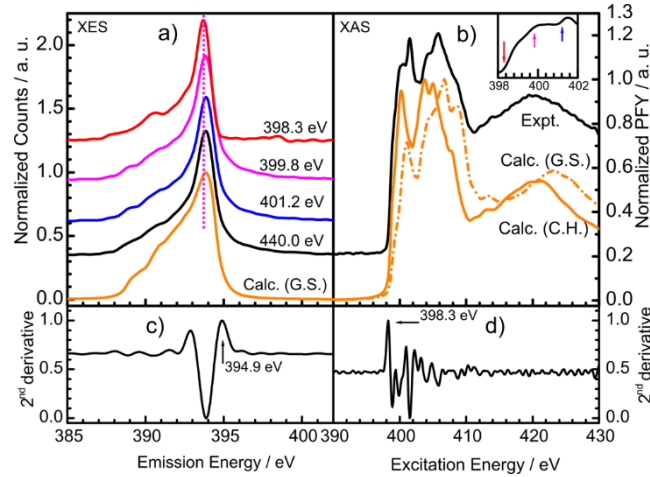


Figure 5.5: Experimental and calculated N K-edge XES and XAS spectra of $\text{Sr}_2[\text{BeAl}_3\text{N}_5]:\text{Eu}^{2+}$. a) NXES spectrum (black) excited at 440.0 eV and RIXS spectra (red, magenta, and blue) collected at 398.3 eV, 399.8 eV, and 401.2 eV are compared with ground state calculations (orange). The vertical dotted magenta line indicates that the highest emission energy is observed at the highest excitation energy in the RIXS spectra, which indicates an indirect band gap; b) Comparison of experimental PFY (black), core hole (C.H.) and ground state (G.S.) calculations of N K-edge XAS spectra. The small color coded arrows in the embedded figure indicate where in the conduction band (CB) the N 1s electron was excited to obtain the emission spectra of the corresponding color; c) Second derivatives of the NXES spectrum, with peaks that are above the noise level and are corresponding to the valence band edge indicated by the arrow; d) Second derivative of PFY of XAS spectrum with peaks corresponding to CB edge indicated by the arrow.

As the absorption and emission spectra are proportional to the unoccupied and occupied pDOS, respectively their separation can be used to determine the electronic band gap, using the second derivative method. Here, the valence band (VB) and the conduction band (CB) edges are taken to be the first peaks in the second derivative above the noise at the upper edge of the NXES and lower edge of the XAS spectra, respectively, as indicated by the arrows in Figure 5.5c+d. From the band edges (Figure 5.5 and Figure D.5) the estimated band gap is found to be 3.4 ± 0.3 eV for $\text{Sr}_2[\text{BeAl}_3\text{N}_5]:\text{Eu}^{2+}$ and 3.1 ± 0.3 eV for $\text{Ba}_2[\text{BeAl}_3\text{N}_5]:\text{Eu}^{2+}$, respectively. This result must be adjusted to account for the effect of the N 1s core hole that is created during the excitation process. Applying a DFT-derived correction of 0.1 eV the final experimental band gaps are found to be 3.5 ± 0.3 eV ($M = \text{Sr}$) and 3.2 ± 0.3 eV ($M = \text{Ba}$), respectively. The calculated band gap using PBE-GGA is found to be 2.8 eV ($M = \text{Sr}$) and 2.56 eV ($M = \text{Ba}$), respectively. This underestimation is typical for DFT and can be improved by using the modified Becke-Johnson (mBJ) exchange-correlation potential.^[25] In this case, the calculated band gaps are found to be 4.2 eV ($M = \text{Sr}$) and 3.6 eV ($M = \text{Ba}$). A summary of the band gap values can be found in Table 5.3.

Table 5.3: Determined band gap (Δ) values for $M_2[\text{BeAl}_3\text{N}_5]:\text{Eu}^{2+}$ ($M = \text{Sr}, \text{Ba}$) in eV obtained from X-ray spectroscopy (XES/XAS), DFT-calculations (GGA/mBJ) and UV-Vis spectroscopy (Tauc, direct and indirect).

M	$\Delta_{\text{XES/XAS}}$	Δ_{GGA}	Δ_{mBJ}	$\Delta_{\text{Tauc, direct}}$	$\Delta_{\text{Tauc, indirect}}$
Sr	3.5 ± 0.3	2.8	4.2	$3.8^{[13]}$	3.1
Ba	3.2 ± 0.3	2.6	3.6	3.5	3.0

The band structure of $M_2[\text{BeAl}_3\text{N}_5]:\text{Eu}^{2+}$ ($M = \text{Sr}, \text{Ba}$) was calculated using the mBJ exchange-correlation potentials (Figure D.6). The calculations indicate an indirect band gap for both materials with the valence band (VB) maximum at the T point for both compounds and the conduction band (CB) minimum at the Γ point for $\text{Sr}_2[\text{BeAl}_3\text{N}_5]:\text{Eu}^{2+}$ and Z point for $\text{Ba}_2[\text{BeAl}_3\text{N}_5]:\text{Eu}^{2+}$, respectively. The pDOS of both compounds (Figure D.7) show high similarity with other materials based on XN_4 ($X = \text{Li}, \text{Al}, \text{Mg}, \text{Si}$) tetrahedra, for example, $\text{SLA}^{[26]}$ $\text{Li}_2\text{Ca}_2[\text{Mg}_2\text{Si}_2\text{N}_6]:\text{Eu}^{2+}$,^[27] or $\text{Ba}[\text{Li}_2[\text{Al}_2\text{Si}_2\text{N}_6]:\text{Eu}^{2+}$,^[27] where the upper VB is dominated by N p states and the lower VB is characterized by X s/p states. Meanwhile, the alkaline earth ion d states strongly contribute to the lower CB. Based on the definition of Dorenbos, there are two types of compounds: type I compounds, where the bottom of the CB is dominated by alkaline earth ions which are replaced by rare earth ions, and type II compounds, where the lower CB is dominated by ions that are not replaced by the rare earth ion.^[28] Typically, type I compounds show an increasing band gap with smaller size of the alkaline earth, which is in accordance with the values obtained for $M_2[\text{BeAl}_3\text{N}_5]:\text{Eu}^{2+}$ ($M = \text{Sr}, \text{Ba}$), where the Sr containing phosphors show larger band gap values (Table 5.3).

UV-Vis Spectroscopy

Additionally, the optical band gaps of $\text{Sr}_2[\text{BeAl}_3\text{N}_5]:\text{Eu}^{2+}$ and $\text{Ba}_2[\text{BeAl}_3\text{N}_5]:\text{Eu}^{2+}$ were estimated from reflectance data and compared to the ones obtained from XAS/XES experiments and DFT calculations. The reflectance spectra R were converted to pseudoabsorption spectra using the Kubelka–Munk function $F(R) = (1-R)^2/(2R)$ (Figure D.8).^[29-31] The optical band gaps were determined through a linear fit of the data at the inflection point from the Tauc plots ($[F(R) h\nu]^{1/n}$ with $n = 1/2$ for a direct and $n = 2$ for an indirect allowed transition for a better comparison with the literature (direct band gap for $\text{Sr}_2[\text{BeAl}_3\text{N}_5]:\text{Eu}^{2+}$ of 3.8 eV),^[13] The values are summarized in Table 5.3 and are approximately in the same range, as the calculated (GGA and mBJ) and experimentally (XES/XAS) determined band gaps.

Luminescence

Luminescence measurements were carried out on samples with various compositions. Excitation and emission spectra of single particles of the solid solution series $\text{Sr}_{2-x}\text{Ba}_x[\text{BeAl}_3\text{N}_5]:\text{Eu}^{2+}$ ($x = 0-2.0$) are displayed in Figure 5.6 (2 mol% Eu^{2+} concentration referred to Sr/Ba).

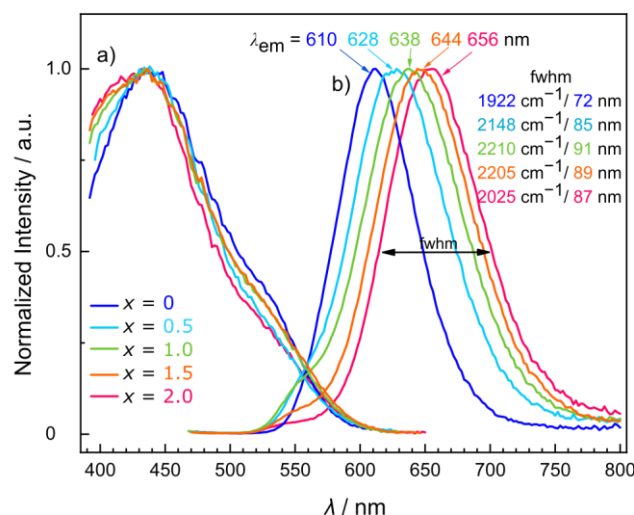


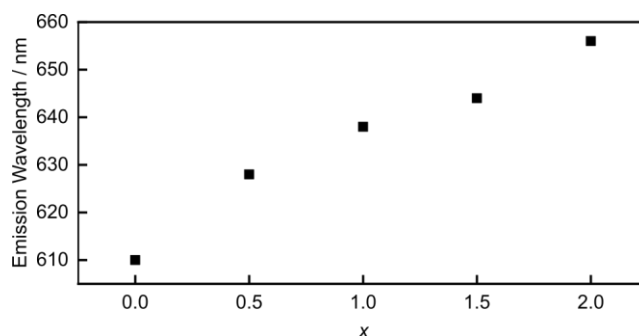
Figure 5.6: Normalized photoluminescence spectra of single particles of $\text{Sr}_{2-x}\text{Ba}_x[\text{BeAl}_3\text{N}_5]:\text{Eu}^{2+}$ with $x = 0$ (dark blue), 0.5 (light blue), 1.0 (green), 1.5 (orange), 2.0 (pink). a) Excitation spectra ($\lambda_{\text{obs}} = 626-670$ nm), b) Emission spectra ($\lambda_{\text{exc}} = 440-450$ nm).

The excitation spectra in Figure 5.6a show that all members of the solid solution series can be excited with blue light with a maximum absorption around 440 nm. Compared to the Sr containing nitridoberylloaluminate, $\text{Ba}_2[\text{BeAl}_3\text{N}_5]:\text{Eu}^{2+}$ exhibits a red-shifted emission maximum at $\lambda_{\text{em}} = 656$ nm with a fwhm of ≈ 87 nm/ 2025cm^{-1} . The position of the emission maximum and the shape of the emission band obtained from single particles are comparable to the ones obtained from bulk samples (Supporting Information, Figure D.10). Therefore, the luminescence properties of the bulk samples can be assigned to $\text{Ba}_2[\text{BeAl}_3\text{N}_5]:\text{Eu}^{2+}$, which rules out a possible contribution to the red emission by the side phase BaBe_2N_2 . The value of the internal quantum efficiency (IQE) at room temperature for $\text{Ba}_2[\text{BeAl}_3\text{N}_5]:\text{Eu}^{2+}$ is 44%, which is similar to $\text{Sr}_2[\text{BeAl}_3\text{N}_5]:\text{Eu}^{2+}$ (33%).^[13] Overall, the photoluminescence properties for $\text{Ba}_2[\text{BeAl}_3\text{N}_5]:\text{Eu}^{2+}$ are comparable to other nitrides, some of which are summarized in Table 5.4.

Table 5.4: Luminescence properties and coordination number (CN) of selected orange-red emitting Eu^{2+} doped (oxo)nitrides.

Compound	$\lambda_{\text{em}}/\text{nm}$	$\lambda_{\text{exc}}/\text{nm}$	fwhm/nm	fwhm/ cm^{-1}	CN	Ref.
$\text{Ba}_2[\text{BeAl}_3\text{N}_5]$	656	440	87	2025	7, 8	
$\text{Ca}[\text{Mg}_2\text{Al}_2\text{N}_4]$	606	440	67	1815	8	[15]
$\text{Sr}[\text{Mg}_2\text{Al}_2\text{N}_4]$	612	440	82	1823	8	[15]
$\text{Sr}_2[\text{BeAl}_3\text{N}_5]$	612	440	71	1899	7, 8	[13]
$\text{Sr}[\text{Li}_2\text{Al}_2\text{O}_2\text{N}_2]$	614	460	48	1286	8	[9]
$\text{Sr}[\text{Mg}_3\text{SiN}_4]$	615	440	43	1170	8	[8]
$\text{Sr}_2[\text{MgAl}_5\text{N}_7]$	633	440	78	1940	8	[32]
$\text{Sr}[\text{LiAl}_3\text{N}_4]$	654	440	50	1180	8	[7]
$\text{Ba}[\text{Mg}_2\text{Al}_2\text{N}_4]$	666	440	104	2331	8	[15]
$\text{Sr}_4[\text{LiAl}_{11}\text{N}_{14}]$	670	460	85	1880	8	[33]

To investigate the effect of the substitution of Sr^{2+} with Ba^{2+} on the Eu^{2+} luminescence in $\text{Sr}_{2-x}\text{Ba}_x[\text{BeAl}_3\text{N}_5]:\text{Eu}^{2+}$, luminescence emission spectra of samples with $x = 0, 0.5, 1.0, 1.5$ and 2.0 were measured (Figure 5.6b). The emission maxima obtained from samples of the solid solution series show tunable emission between 610 to 656 nm through the compositional variable x (Figure 5.7).

**Figure 5.7:** Correlation between the increasing Ba content with different x values and the emission wavelength from the luminescence measurements of bulk samples.

The fwhm values for $x = 0$ (72 nm/ 1922 cm^{-1}) and $x = 2$ (87 nm/ 2025 cm^{-1}) are slightly smaller with values around 2000 cm^{-1} , while in $\text{Sr}_{2-x}\text{Ba}_x[\text{BeAl}_3\text{N}_5]:\text{Eu}^{2+}$ with $x = 0.5, 1.0$ and 1.5 the fwhm is increased up to 2200 cm^{-1} . The fwhm broadening is caused by varying Eu–N distances, resulting from mixed occupation of the three alkaline earth sites as discussed in the crystal structure section. Furthermore, in the samples with mixed occupation of the Sr/Ba sites, a second emission maximum occurs at shorter wavelengths, peaking around 550 nm. The intensity of this second emission maximum is very weak and almost identical for the samples with $x = 0.5$ and 1.0 and decreases even further in the sample with $x = 1.5$. Comparing the low-temperature measurements of

$\text{Sr}_2[\text{BeAl}_3\text{N}_5]:\text{Eu}^{2+}$ ^[13] and $\text{Ba}_2[\text{BeAl}_3\text{N}_5]:\text{Eu}^{2+}$ (Figure D.12) only one broad emission band is observed for the Ba compound, while the superposition of three emission maxima is observed at 6 K for $\text{Sr}_2[\text{BeAl}_3\text{N}_5]:\text{Eu}^{2+}$. In the mixed phases (Figure D.10 and Figure D.11), it can be observed that this second emission maximum also decreases in intensity as the Sr content of the compound decreases. Therefore, the assumption is that this emission maximum originates from Eu^{2+} on the Sr/Ba1 site with the highest Sr content according to the Rietveld refinement (Figure 5.4).

Cationic substitution is often used to alter the emission color of nitride phosphors, as the emission is strongly influenced by the local environment around the activator Eu^{2+} . Generally, the substitution of a smaller ion by a bigger one should lead to a smaller crystal field splitting and therefore shifting the emission color to shorter wavelengths.^[3] Contrary to such observations, the emission of the solid solution series $\text{Sr}_{2-x}\text{Ba}_x[\text{BeAl}_3\text{N}_5]:\text{Eu}^{2+}$ is inversely shifted from 610 towards 656 nm with increasing Ba content as illustrated in Figure 5.7. The small leap in the position of the emission maximum observed between $x = 0$ and $x = 0.5$ is consistent with the interval observed analyzing the lattice parameter dependence on the Ba:Sr ratio, displayed in Figure 5.3.

Possible reasons for the uncommon, inverse-tunable red emission of $\text{Sr}_{2-x}\text{Ba}_x[\text{BeAl}_3\text{N}_5]:\text{Eu}^{2+}$ will be discussed in the following section. Such a red-shifted emission can be associated with the activator concentration, the occurrence of anomalous trapped exciton emission or occur due to a change in the local environment around Eu^{2+} without necessarily changing the crystal structure of the compound.^[17, 34-37]

In crystal structures with multiple crystallographic sites for the incorporation of the activator, the activator can act as donor and acceptor, enabling energy transfer between the activator ions. Typically, the probability for an energy transfer depends on the distance between the Eu^{2+} atoms, therefore a red-shift of the emission with increasing activator concentration can take place, as already observed in different phosphors (e. g., $M_2\text{Si}_5\text{N}_8:\text{Eu}^{2+}$ ($M = \text{Sr}, \text{Ba}$),^[34, 38] or $\text{Ca}_{2-x}\text{Eu}_x\text{SiO}_4$ ^[39]). Luminescence spectra of bulk samples of $\text{Ba}_2[\text{BeAl}_3\text{N}_5]:\text{Eu}^{2+}$ with a nominal Eu^{2+} concentrations of 0.3, 1, 2, 3, and 4 mol% referred to Ba are shown in the Supporting information (Figure D.9) and were compared with the reported spectra for $\text{Sr}_2[\text{BeAl}_3\text{N}_5]:\text{Eu}^{2+}$.^[13]

In the literature, it has been reported that the location of the emission maximum does not change as the Eu content increases for $\text{Sr}_2[\text{BeAl}_3\text{N}_5]:\text{Eu}^{2+}$.^[13] A comparable behavior was observed for $\text{Ba}_2[\text{BeAl}_3\text{N}_5]:\text{Eu}^{2+}$. Phase-pure samples will be necessary to further investigate luminescence properties in even more detail. Based on the current data, a red-shift of the emission due to increasing activator concentrations seems to be rather unlikely.

As anomalous trapped exciton emission is known to occur more likely in phosphors with Eu^{2+} on sites with high coordination number and large activator–ligand bond lengths,^[34] temperature-dependent emission measurements were performed to investigate the luminescence properties of the title compounds at lower temperatures (Figure D.10–Figure D.12). The obtained spectra show no significant shift of the emission maxima at lower temperatures, suggesting that anomalous emission is an unlikely explanation for the unusual inverse shift of the emission maxima to higher wavelengths.

The third option to discuss is the dependence of the emission on structurally related properties, especially of Eu^{2+} states influenced by its surrounding ligands. As already stated in the introduction, the $4f$ - $5d$ transition, which defines the excitation and emission properties of Eu^{2+} doped phosphors, is highly sensitive toward the local coordination environment around the activation ion. When Eu^{2+} replaces Sr^{2+} in $\text{Sr}_2[\text{BeAl}_3\text{N}_5]:\text{Eu}^{2+}$, no structural changes are expected, as the ionic radii of both ions are quite similar (Eu^{2+} : 1.25 Å (CN = 8) and 1.20 Å (CN = 7); Sr^{2+} : 1.26 Å (CN = 8) and 1.21 Å (CN = 7)).^[24] The situation is quite different with Ba^{2+} , as the ionic radius is larger than that of Eu^{2+} (Ba^{2+} : 1.42 Å (CN = 8) and 1.38 Å (CN = 7)).^[24] Therefore, incorporation of Eu^{2+} on a larger crystallographic site can lead to red-shifted emission due to local lattice rearrangement. Considering the stepwise substitution of the lighter alkaline earth ion by the heavier homologue in the solid solution series, the activator Eu^{2+} preferentially replaces Sr atoms due to the similar ionic radii. When the neighboring Sr atoms are gradually replaced by the larger Ba^{2+} , the strain of the Ba–N bond distances increases leading to shorter Sr–N and Eu–N bond lengths, in order to release lattice strain. The more Sr atoms are replaced by Ba^{2+} , the shorter the Eu–N (and Sr–N) distances become. Shorter activator–ligand distances increase the crystal field splitting of the $5d$ orbitals resulting in a continuous red-shifted emission, as discussed for example for $(\text{Sr}_{0.98-x}\text{Ba}_x\text{Eu}_{0.02})\text{Si}_2\text{O}_2\text{N}_2$ ($x = 0$ – 0.63).^[35] Especially in crystal structures, where cations have a close proximity to each other, it is reasonable that the successive substitution of the smaller cations by a larger one can lead to local distortion and an increased lattice strain.^[35] As discussed in the crystal structure the anionic network

of the nitridoberyllo-aluminates contains several channels which are filled with the alkaline-earth ions, therefore, replacing Sr^{2+} by Ba^{2+} would have a strong impact on several neighboring ions in this crystal structure. Therefore, it seems most likely, that the uncommon, inverse-tunable red emission of $\text{Sr}_{2-x}\text{Ba}_x[\text{BeAl}_3\text{N}_5]:\text{Eu}^{2+}$ is the result of a change in the local Eu^{2+} coordination, depending on the Sr:Ba ratio.

5.3 Conclusion

In this contribution we report on the synthesis of $\text{Ba}_2[\text{BeAl}_3\text{N}_5]:\text{Eu}^{2+}$ and the solid solution series $\text{Sr}_{2-x}\text{Ba}_x[\text{BeAl}_3\text{N}_5]:\text{Eu}^{2+}$ ($x = 0.5, 1.0, 1.5$) by high-temperature reaction in a hot isostatic press under 50 MPa N_2 . The crystal structure of $\text{Ba}_2[\text{BeAl}_3\text{N}_5]:\text{Eu}^{2+}$ was solved and refined from a single-crystal and is supported by powder X-ray diffraction data, while the lattice parameters of the members of the solid solution series were determined by Rietveld refinement. The crystal structure is isotypic to the recently discovered nitridoberyllaluminate $\text{Sr}_2[\text{BeAl}_3\text{N}_5]:\text{Eu}^{2+}$ and consists of edge- and vertex-sharing AlN_4 tetrahedra and trigonal-planar BeN_3 units creating a highly condensed 3D network with three mixed occupied crystallographic Sr/Ba sites. $\text{Ba}_2[\text{BeAl}_3\text{N}_5]:\text{Eu}^{2+}$ shows an emission maximum at $\lambda_{\text{em}} = 656$ nm with a fwhm of ≈ 87 nm/ 2025 cm^{-1} , which is comparable to other narrow-band red-emitting phosphors like $M[\text{Mg}_2\text{Al}_2\text{N}_4]:\text{Eu}^{2+}$ ($M = \text{Sr}, \text{Ba}$), $M\text{AlSiN}_3$ ($M = \text{Ca}, \text{Sr}$),^[40] α - and β - $\text{Sr}_2[\text{MgAl}_5\text{N}_7]:\text{Eu}^{2+}$, or $\text{Sr}_8[\text{LiMg}_2\text{Al}_{21}\text{N}_{28}]:\text{Eu}^{2+}$.^[32] The Eu^{2+} emission can be continuously tuned from 610 to 656 nm by increasing the Ba content. Compared to narrow-band red-emitting phosphors like $\text{Sr}[\text{LiAl}_3\text{N}_4]:\text{Eu}^{2+}$, the members of the solid solution series show somewhat broader emission bands, most probably due to the convolution of the emission from three differently coordinated Eu^{2+} sites. In contrast to the usual trend, the emission maximum in the nitridoberyllaluminates $\text{Sr}_{2-x}\text{Ba}_x[\text{BeAl}_3\text{N}_5]:\text{Eu}^{2+}$ ($x = 0-2$) is inversely shifted to higher wavelengths by the incorporation of the larger cation Ba^{2+} . This fact emphasizes the importance of studies regarding the structures and properties of potential phosphors, since the Eu^{2+} emission can be significantly influenced by small local changes and distortions of the environment without necessarily changing the symmetry of the crystal.

In summary, the synthesis of the presented compounds and the study of their electronic and optical properties contributes to the elucidation of the so far little explored class of nitridoalumoberyllates and emphasizes their role in the discovery and development of new luminescent materials.

5.4 Acknowledgements

The authors thank Karl Adriaan Zijtveld (Lumileds Phosphor Center Aachen) for luminescence measurements, Dr. Christian Maak and Christian Minke for EDX measurements and Dr. Peter Mayer (all Department of Chemistry, University of Munich (LMU)) for collecting single-crystal X-ray diffraction data. The soft X-ray spectroscopy measurements were performed at the Canadian Light Source (CLS), which is funded by the Canada Foundation for Innovation, the Natural Science and Engineering Research Council of Canada (NSERC), the National Research Council Canada, the Canadian Institutes of Health Research, the Government of Saskatchewan, Western Economic Diversification Canada, and the University of Saskatchewan. The authors also acknowledge Compute Canada. The calculations presented in this paper were performed on the Cedar high-performance computing cluster, which is part of the WestGrid (www.westgrid.ca) and Compute Canada Calcul Canada (www.computecanada.ca).

5.5 References

- [1] *2019 Lighting R&D Opportunities*; US Department of Energy, 2019.
- [2] Leño Jr., J. L.; Fang, M.-H.; Liu, R.-S. Review—Narrow-Band Emission of Nitride Phosphors for Light-Emitting Diodes: Perspectives and Opportunities. *ECS J. Solid State Sci. Technol.* **2018**, *7*, R3111–R3133.
- [3] Wang, L.; Xie, R. J.; Suehiro, T.; Takeda, T.; Hirosaki, N. Down-Conversion Nitride Materials for Solid State Lighting: Recent Advances and Perspectives. *Chem. Rev.* **2018**, *118*, 1951–2009.
- [4] Meijerink, A.; Blasse, G. Luminescence properties of Eu^{2+} -activated alkaline earth haloborates. *J. Lumin.* **1989**, *43*, 283–289.
- [5] Xie, R.-J.; Hirosaki, N.; Suehiro, T.; Xu, F.-F.; Mitomo, M. A Simple, Efficient Synthetic Route to $\text{Sr}_2\text{Si}_5\text{N}_8:\text{Eu}^{2+}$ -Based Red Phosphors for White Light-Emitting Diodes. *Chem. Mater.* **2006**, *18*, 5578–5583.
- [6] Watanabe, H.; Kijima, N. Crystal structure and luminescence properties of $\text{Sr}_x\text{Ca}_{1-x}\text{AlSiN}_3:\text{Eu}^{2+}$ mixed nitride phosphors. *J. Alloys Compd.* **2009**, *475*, 434–439.
- [7] Pust, P.; Weiler, V.; Hecht, C.; Tucks, A.; Wochnik, A. S.; Henss, A. K.; Wiechert, D.; Scheu, C.; Schmidt, P. J.; Schnick, W. Narrow-band red-emitting $\text{Sr}[\text{LiAl}_3\text{N}_4]:\text{Eu}^{2+}$ as a next-generation LED-phosphor material. *Nat. Mater.* **2014**, *13*, 891–896.
- [8] Schmiechen, S.; Schneider, H.; Wagatha, P.; Hecht, C.; Schmidt, P. J.; Schnick, W. Toward New Phosphors for Application in Illumination-Grade White pc-LEDs: The Nitridomagnesosilicates $\text{Ca}[\text{Mg}_3\text{SiN}_4]:\text{Ce}^{3+}$, $\text{Sr}[\text{Mg}_3\text{SiN}_4]:\text{Eu}^{2+}$, and $\text{Eu}[\text{Mg}_3\text{SiN}_4]$. *Chem. Mater.* **2014**, *26*, 2712–2719.
- [9] Hoerder, G. J.; Seibald, M.; Baumann, D.; Schroder, T.; Peschke, S.; Schmid, P. C.; Tyborski, T.; Pust, P.; Stoll, I.; Bergler, M.; Patzig, C.; Reissaus, S.; Krause, M.; Berthold, L.; Hoche, T.; Johrendt, D.; Huppertz, H. $\text{Sr}[\text{Li}_2\text{Al}_2\text{O}_2\text{N}_2]:\text{Eu}^{2+}$ – A high performance red phosphor to brighten the future. *Nat. Commun.* **2019**, *10*, 1–9.
- [10] Strobel, P.; de Boer, T.; Weiler, V.; Schmidt, P. J.; Moewes, A.; Schnick, W. Luminescence of an Oxonitridoberyllate: A Study of Narrow-Band Cyan-Emitting $\text{Sr}[\text{Be}_6\text{ON}_4]:\text{Eu}^{2+}$. *Chem. Mater.* **2018**, *30*, 3122–3130.
- [11] Strobel, P.; Maak, C.; Weiler, V.; Schmidt, P. J.; Schnick, W. Ultra-Narrow-Band Blue-Emitting Oxoberyllates $\text{AELi}_2[\text{Be}_4\text{O}_6]:\text{Eu}^{2+}$ (AE = Sr, Ba) Paving the Way to Efficient RGB pc-LEDs. *Angew. Chem. Int. Ed.* **2018**, *57*, 8739–8743; *Angew. Chem.* **2018**, *130*, 8875–8879.
- [12] Elzer, E.; Niklaus, R.; Strobel, P. J.; Weiler, V.; Schmidt, P. J.; Schnick, W. $\text{MBe}_{20}\text{N}_{14}:\text{Eu}^{2+}$ (M = Sr, Ba) - Highly Condensed Nitridoberyllates with Exceptional Highly Energetic Eu^{2+} Luminescence. *Chem. Mater.* **2019**, *31*, 3174–3182.
- [13] Elzer, E.; Strobel, P.; Weiler, V.; Schmidt, P. J.; Schnick, W. Illuminating Nitridoberylloaluminates: The Highly Efficient Red-Emitting Phosphor $\text{Sr}_2[\text{BeAl}_3\text{N}_5]:\text{Eu}^{2+}$. *Chem. Mater.* **2020**, *32*, 6611–6617.
- [14] Schmiechen, S.; Strobel, P.; Hecht, C.; Reith, T.; Siegert, M.; Schmidt, P. J.; Huppertz, P.; Wiechert, D.; Schnick, W. Nitridomagnesosilicate $\text{Ba}[\text{Mg}_3\text{SiN}_4]:\text{Eu}^{2+}$ and Structure–Property Relations of Similar Narrow-Band Red Nitride Phosphors. *Chem. Mater.* **2015**, *27*, 1780–1785.
- [15] Pust, P.; Hintze, F.; Hecht, C.; Weiler, V.; Locher, A.; Zitnanska, D.; Harm, S.; Wiechert, D.; Schmidt, P. J.; Schnick, W. Group (III) Nitrides $M[\text{Mg}_2\text{Al}_2\text{N}_4]$ (M = Ca, Sr, Ba, Eu) and $\text{Ba}[\text{Mg}_2\text{Ga}_2\text{N}_4]$ — Structural Relation and Nontypical Luminescence Properties of Eu^{2+} Doped Samples. *Chem. Mater.* **2014**, *26*, 6113–6119.

- [16] Strobel, P.; Weiler, V.; Schmidt, P. J.; Schnick, W. Sr[BeSi₂N₄]:Eu²⁺/Ce³⁺ and Eu[BeSi₂N₄]: Nontypical Luminescence in Highly Condensed Nitridoberyllosilicates. *Chem. Eur. J.* **2018**, *24*, 7243–7249.
- [17] Dorenbos, P. Anomalous luminescence of Eu²⁺ and Yb²⁺ in inorganic compounds. *J. Phys.: Condens. Matter* **2003**, *15*, 2645–2665.
- [18] Sommerdijk, J. L.; Bril, A. Divalent Europium Luminescence in Perovskite-Like Alkaline-Earth Fluorides. *J. Lumin.* **1976**, *11*, 363–367.
- [19] Zhao, M.; Zhang, Q.; Xia, Z. Structural Engineering of Eu²⁺-Doped Silicates Phosphors for LED Applications. *Acc. Mater. Res.* **2020**, *1*, 137–145.
- [20] Zhuo, Y.; Mansouri Tehrani, A.; Oliynyk, A. O.; Duke, A. C.; Brgoch, J. Identifying an efficient, thermally robust inorganic phosphor host via machine learning. *Nat. Commun.* **2018**, *9*, 1–10.
- [21] Hirosaki, N.; Takeda, T.; Funahashi, S.; Xie, R.-J. Discovery of New Nitridosilicate Phosphors for Solid State Lighting by the Single-Particle-Diagnosis Approach. *Chem. Mater.* **2014**, *26*, 4280–4288.
- [22] Zhou, X.; Qiao, J.; Xia, Z. Learning from Mineral Structures toward New Luminescence Materials for Light-Emitting Diode Applications. *Chem. Mater.* **2021**, *33*, 1083–1098.
- [23] Sheldrick, G. M. Crystal structure refinement with SHELXL. *Acta Crystallogr., Sect. C: Struct. Chem.* **2015**, *71*, 3–8.
- [24] Shannon, R. D. Revised effective ionic radii and systematic studies of interatomic distances in halides and chalcogenides. *Acta Crystallogr., Sect. A: Cryst. Phys., Diffr. Theor. Gen. Crystallogr.* **1976**, *32*, 751–767.
- [25] Tran, F.; Blaha, P. Accurate Band Gaps of Semiconductors and Insulators with a Semilocal Exchange-Correlation Potential. *Phys. Rev. Lett.* **2009**, *102*, 226401.
- [26] Tolhurst, T. M.; Boyko, T. D.; Pust, P.; Johnson, N. W.; Schnick, W.; Moewes, A. Investigations of the Electronic Structure and Bandgap of the Next-Generation LED-Phosphor Sr[LiAl₃N₄]:Eu²⁺—Experiment and Calculations. *Adv. Opt. Mater.* **2015**, *3*, 546–550.
- [27] Tolhurst, T. M.; Strobel, P.; Schmidt, P. J.; Schnick, W.; Moewes, A. Designing Luminescent Materials and Band Gaps: A Soft X-ray Spectroscopy and Density Functional Theory Study of Li₂Ca₂[Mg₂Si₂N₆]:Eu²⁺ and Ba[Li₂(Al₂Si₂)N₆]:Eu²⁺. *J. Phys. Chem. C* **2017**, *121*, 14296–14301.
- [28] Dorenbos, P. Thermal Quenching of Eu²⁺5d–4f Luminescence in Inorganic Compounds. *J. Phys.: Condens. Matter* **2005**, *17*, 8103–8111.
- [29] López, R.; Gómez, R. Band-gap energy estimation from diffuse reflectance measurements on sol–gel and commercial TiO₂: a comparative study. *J. Sol-Gel Sci. Technol.* **2012**, *61*, 1–7.
- [30] Tauc, J.; Grigorovici, R.; Vancu, A. Optical properties and electronic structure of amorphous germanium. *Phys. Status Solidi B* **1966**, *15*, 627–637.
- [31] Kubelka, P. New Contributions to the Optics of Intensely Light-Scattering Materials Part I. *J. Opt. Soc. Am* **1948**, *38*, 448–457.
- [32] Wagatha, P.; Weiler, V.; Schmidt, P. J.; Schnick, W. Tunable Red Luminescence in Nitridomagnesoaluminates α -Sr₂[MgAl₅N₇]:Eu²⁺, β -Sr₂[MgAl₅N₇]:Eu²⁺, and Sr₈[LiMg₂Al₂₁N₂₈]:Eu²⁺. *Chem. Mater.* **2018**, *30*, 1755–1761.
- [33] Wilhelm, D.; Baumann, D.; Seibald, M.; Wurst, K.; Heymann, G.; Huppertz, H. Narrow-Band Red Emission in the Nitridolithoaluminate Sr₄[LiAl₁₁N₁₄]:Eu²⁺. *Chem. Mater.* **2017**, *29*, 1204–1209.

- [34] Li, Y. Q.; van Steen, J. E. J.; van Krevel, J. W. H.; Botty, G.; Delsing, A. C. A.; DiSalvo, F. J.; de With, G.; Hintzen, H. T. Luminescence Properties of Red-Emitting $\text{M}_2\text{Si}_5\text{N}_8:\text{Eu}^{2+}$ ($\text{M} = \text{Ca}, \text{Sr}, \text{Ba}$) LED Conversion Phosphors. *J. Alloys Compd.* **2006**, *417*, 273–279.
- [35] Li, G.; Lin, C. C.; Chen, W.-T.; Molokeev, M. S.; Atuchin, V. V.; Chiang, C.-Y.; Zhou, W.; Wang, C.-W.; Li, W.-H.; Sheu, H.-S.; Chan, T.-S.; Ma, C.; Liu, R.-S. Photoluminescence Tuning via Cation Substitution in Oxonitridosilicate Phosphors: DFT Calculations, Different Site Occupations, and Luminescence Mechanisms. *Chem. Mater.* **2014**, *26*, 2991–3001.
- [36] Leano, J. L., Jr.; Mariano, C. O. M.; Huang, W. T.; Mahlik, S.; Lesniewski, T.; Grinberg, M.; Sheu, H. S.; Hu, S. F.; Liu, R. S. Thermally Stable and Deep Red Luminescence of $\text{Sr}_{1-x}\text{Ba}_x[\text{Mg}_2\text{Al}_2\text{N}_4]:\text{Eu}^{2+}$ ($x = 0-1$) Phosphors for Solid State and Agricultural Lighting Applications. *ACS Appl. Mater. Interfaces* **2020**, *12*, 23165–23171.
- [37] Lazarowska, A.; Mahlik, S.; Grinberg, M.; Lin, C. C.; Liu, R. S. Pressure effect on the zero-phonon line emission of Mn^{4+} in K_2SiF_6 . *J. Chem. Phys.* **2015**, *143*, 134704.
- [38] Höpfe, H. A.; Lutz, H.; Morys, P.; Schnick, W.; Seilmeier, A. Luminescence in Eu^{2+} -doped $\text{Ba}_2\text{Si}_5\text{N}_8$: Fluorescence, Thermoluminescence, and Upconversion. *J. Phys. Chem. Solids* **2000**, *61*, 2001–2006.
- [39] Sato, Y.; Kato, H.; Kobayashi, M.; Masaki, T.; Yoon, D. H.; Kakihana, M. Tailoring of deep-red luminescence in $\text{Ca}_2\text{SiO}_4:\text{Eu}^{2+}$. *Angew. Chem. Int. Ed.* **2014**, *53*, 7756–7759; *Angew. Chem.* **2014**, *30*, 7890–7893.
- [40] Watanabe, H.; Wada, H.; Seki, K.; Itou, M.; Kijima, N. Synthetic Method and Luminescence Properties of $\text{Sr}_x\text{Ca}_{1-x}\text{AlSiN}_3:\text{Eu}^{2+}$ Mixed Nitride Phosphors. *J. Electrochem. Soc.* **2008**, *155*, F31–F36.

6. Summary

The main research objective of this thesis was a fundamental investigation of nitridoberyllates and nitridoberylloaluminates in terms of their preparation and their applicability as phosphors. Prior to this work, neither ternary nitridoberyllates exhibiting Eu^{2+} luminescence, nor a single representative of the substance class of nitridoberylloaluminate were known. Formally, the presented thesis can be divided in two parts, addressing these topics.

The first section of the thesis covers the synthesis and crystal structure determination of the oxonitridoberyllate $\text{Eu}_3\text{Be}_{22}\text{N}_{16}\text{O}$ (Chapter 2) and the highly condensed nitrides $M\text{Be}_{20}\text{N}_{14}:\text{Eu}^{2+}$ ($M = \text{Sr}, \text{Ba}$) and $\text{EuBe}_{20}\text{N}_{14}$ (Chapter 3). The (pseudo)ternary (oxo)nitridoberyllates are synthesized at temperature of 1400 °C under N_2 atmosphere in a radio-frequency furnace. The crystal structure of $\text{Eu}_3\text{Be}_{22}\text{N}_{16}\text{O}$ illustrates how Be^{2+} can expand the structural diversity compared to other elements like Si^{4+} or Al^{3+} , since Be^{2+} occurs both threefold and fourfold coordinated by N^{3-} in the same compound. Meanwhile, Eu^{2+} doped samples of $M\text{Be}_{20}\text{N}_{14}$ ($M = \text{Sr}, \text{Ba}$) exhibit a remarkably narrow-band blue Eu^{2+} emission. Due to the high linkage of BeN_4 tetrahedra in $M\text{Be}_{20}\text{N}_{14}$, the anionic network is extremely rigid, thus, perfectly fulfilling one of the requirements for narrow-band emission (Chapter 1.2). Within the second part, covered by Chapters 4 and 5, the hot isostatic press is applied to formally substitute Al^{3+} by the lower charged Be^{2+} , thus preparing the first representatives of a new class of compounds, the nitridoberylloaluminates. The unprecedented structure of $M_2[\text{BeAl}_3\text{N}_5]:\text{Eu}^{2+}$ ($M = \text{Sr}, \text{Ba}$), as elucidated from single-crystal XRD analyses, reveals the presence of BeN_3 units and AlN_4 tetrahedra. Meanwhile, the study of luminescence properties of the solid solution of $\text{Sr}_{2-x}\text{Ba}_x[\text{BeAl}_3\text{N}_5]:\text{Eu}^{2+}$ ($x = 0-2$) exhibit inverse-tunable luminescence in the orange to red spectral region. More detailed information on the presented publications can be found in the summaries of the respective chapters:

6.1 $\text{Eu}_3\text{Be}_{22}\text{N}_{16}\text{O}$: A Highly Condensed Oxonitridoberyllate

6.2 $M\text{Be}_{20}\text{N}_{14}:\text{Eu}^{2+}$ ($M = \text{Sr}, \text{Ba}$): Highly Condensed Nitridoberyllates with Exceptional Highly Energetic Eu^{2+} Luminescence

6.3 Illuminating Nitridoberylloaluminates: The Highly Efficient Red-Emitting Phosphor $\text{Sr}_2[\text{BeAl}_3\text{N}_5]:\text{Eu}^{2+}$

6.4 Inverse-Tunable Red Luminescence and Electronic Properties of Nitridoberylloaluminates $\text{Sr}_{2-x}\text{Ba}_x[\text{BeAl}_3\text{N}_5]:\text{Eu}^{2+}$ ($x = 0-2$)

6.1 $\text{Eu}_3\text{Be}_{22}\text{N}_{16}\text{O}$: A Highly Condensed Oxonitridoberyllate

Published in: **E. Elzer**, M. Weidemann, W. Schnick

Eur. J. Inorg. Chem. **2021**, 4979

Access via: DOI: 10.1002/ejic.202100807

Reprinted at: Chapter 2, Supporting Information in Chapter A

The synthesis and the elucidation of the crystal structure of a highly condensed oxonitridoberyllate, namely $\text{Eu}_3\text{Be}_{22}\text{N}_{16}\text{O}$, is reported. Starting from stoichiometric amounts of $\text{Eu}(\text{NH}_2)_2$, Be_3N_2 and BeO a crystalline dark red powder sample was synthesized in a radio-frequency (rf) furnace under N_2 atmosphere at 1400°C . The crystal structure of the compound was elucidated from X-ray diffraction experiments and confirmed by Rietveld refinement methods and lattice-energy calculations (MAPLE). $\text{Eu}_3\text{Be}_{22}\text{N}_{16}\text{O}$ crystallizes in the monoclinic space group $C2/c$ (no. 15) with $Z = 8$, $a = 20.620(2)$, $b = 8.722(6)$, $c = 17.506(2)$ Å, $\beta = 120.782(3)^\circ$. The anionic network of $\text{Eu}_3\text{Be}_{22}\text{N}_{16}\text{O}$ exhibits simultaneous occurrence of BeN_4 and BeN_2O_2 tetrahedra, as well as trigonal-planar BeN_3 units, not yet observed in (oxo)nitridoberyllates. The high connectivity of the building units results in a high degree of condensation $\kappa = 1.29$. The charge of the anionic network is compensated by the incorporation of Eu^{2+} . The oxidation state of Eu^{II} was confirmed by magnetic susceptibility measurements.

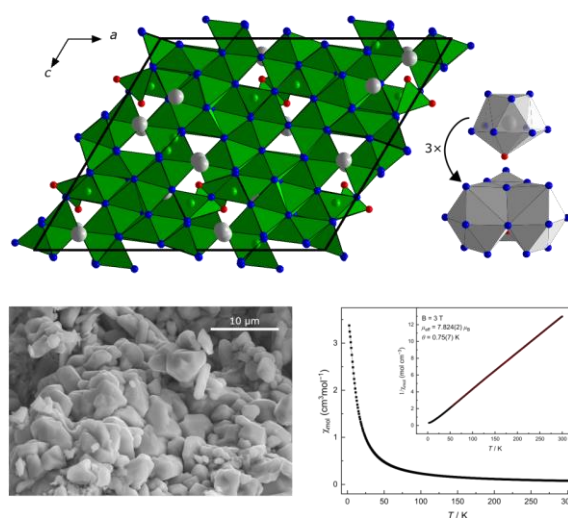


Figure 6.1: Crystal structure of $\text{Eu}_3\text{Be}_{22}\text{N}_{16}\text{O}$ with BeX_4 tetrahedra ($X = \text{N}, \text{O}$) (green), Eu (gray), N (blue), O (red), and coordination polyhedra around Eu^{2+} (gray), accompanied by an image of the typical sample morphology and a plot of the magnetic susceptibility, as well as the inverse susceptibility with the Curie-Weiss fit.

6.2 $M\text{Be}_{20}\text{N}_{14}:\text{Eu}^{2+}$ ($M = \text{Sr}, \text{Ba}$): Highly Condensed Nitridoberyllates with Exceptional Highly Energetic Eu^{2+} Luminescence

Published in: **E. Elzer**, R. Niklaus, P. J. Strobel, V. Weiler, P. J. Schmidt, W. Schnick

Chem. Mater. **2019**, *31*, 3174

Access via: DOI: 10.1021/acs.chemmater.8b05133

Reprinted at: Chapter 3, Supporting Information in Chapter B

The synthesis of the highly condensed nitridoberyllates $M\text{Be}_{20}\text{N}_{14}$ ($M = \text{Sr}, \text{Ba}, \text{Eu}$) is reported. Single crystals of the reported compounds were obtained from reaction of $M(\text{NH}_2)_2$ ($M = \text{Sr}, \text{Ba}, \text{or Eu}$) and Be_3N_2 in a rf furnace at 1400 °C. Furthermore, bulk samples of $M\text{Be}_{20}\text{N}_{14}:\text{Eu}^{2+}$ ($M = \text{Sr}, \text{Ba}$) were synthesized in a hot isostatic press (HIP) under a N_2 pressure of 50 MPa at 1400 °C. The crystal structures of $M\text{Be}_{20}\text{N}_{14}$ ($M = \text{Sr}, \text{Ba}, \text{Eu}$) were solved and refined from single-crystal X-ray diffraction data. The

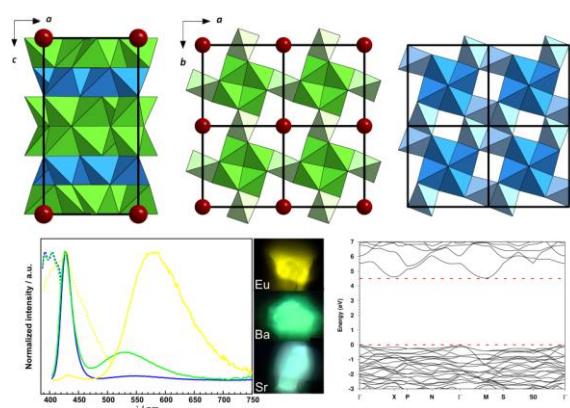


Figure 6.2: Crystal structure of $M\text{Be}_{20}\text{N}_{14}$ consisting of BeN_4 tetrahedra (green, blue) with respective luminescence spectra of $M\text{Be}_{20}\text{N}_{14}:\text{Eu}^{2+}$ ($M = \text{Sr}, \text{Ba}, \text{Eu}$), photographs of Eu^{2+} doped particles, as well as the band structure of $\text{SrBe}_{20}\text{N}_{14}$.

compounds crystallize isotypic in tetragonal space group $I4/m$ (no. 87) with $Z = 2$ and $a = 6.525(2)$ and $c = 12.133(4)$ Å for $M = \text{Sr}$, $a = 6.524(8)$ and $c = 12.136(2)$ Å for $M = \text{Eu}$, and $a = 6.540(6)$, $c = 12.214(11)$ Å for $M = \text{Ba}$, respectively. The crystal structure of $M\text{Be}_{20}\text{N}_{14}$ consists of both edge- and vertex-sharing BeN_4 tetrahedra, forming a highly condensed network. The anionic charge of the network is compensated by counterions Sr^{2+} , Ba^{2+} and Eu^{2+} , respectively. The high connectivity of the tetrahedra leads to an exceptionally high degree of condensation of $\kappa = n(\text{Be}):n(\text{N}) = 1.43$, a value which is, so far, only surpassed by the binary nitride Be_3N_2 ($\kappa = 1.5$). Eu^{2+} doped samples exhibit two emission bands in the blue-to-green spectral region, which can be attributed to a regular narrow-band blue Eu^{2+} emission ($\lambda_{\text{em}} \approx 426\text{--}428$ nm, $\text{fwhm} \approx 22\text{--}25$ nm/ $1180\text{--}1310$ cm^{-1}) and trapped exciton emission (ETE) in the blue-green spectral region ($\lambda_{\text{em}} \approx 530\text{--}540$ nm, $\text{fwhm} > 100$ nm). Large band gaps ($E_g = 4.6$ eV for $\text{SrBe}_{20}\text{N}_{14}$), high chemical and thermal stability, and rigid networks make nitridoberyllates promising candidates for narrow-band emitting phosphors.

6.3 Illuminating Nitridoberyllaluminates: The Highly Efficient Red-Emitting Phosphor $\text{Sr}_2[\text{BeAl}_3\text{N}_5]:\text{Eu}^{2+}$

Published in: **E. Elzer**, P. Strobel, V. Weiler, P. J. Schmidt, W. Schnick

Chem. Mater. **2020**, 32, 6611

Access via: DOI: 10.1021/acs.chemmater.0c02037

Reprinted at: Chapter 4, Supporting Information in Chapter C

The formal incorporation of Be^{2+} in nitridoaluminates led to the discovery of the first nitridoberyllaluminate with composition $\text{Sr}_2[\text{BeAl}_3\text{N}_5]:\text{Eu}^{2+}$. The compound was synthesized under elevated N_2 pressure of 50 MPa in a hot isostatic press (HIP) at 1400 °C starting from stoichiometric amounts of Sr_2N , AlN , and

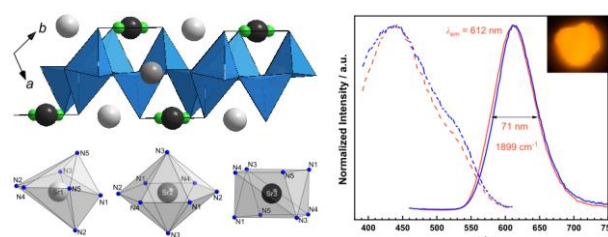


Figure 6.3: Crystal structure of $\text{Sr}_2[\text{BeAl}_3\text{N}_5]:\text{Eu}^{2+}$, and coordination polyhedra around Sr with AlN_4 tetrahedra (blue), BeN_3 units (green), Sr (light gray, gray, and black), N (blue) and luminescence spectra of $\text{Sr}_2[\text{BeAl}_3\text{N}_5]:\text{Eu}^{2+}$ with a photograph of a single particle.

Be_3N_2 . The crystal structure was determined based on single crystal X-ray diffraction data ($P\bar{1}$ (no. 2), $Z = 2$, $a = 6.061(2)$, $b = 6.982(3)$, $c = 7.872(4)$ Å and $\alpha = 102.22(3)$, $\beta = 112.62(2)$ and $\gamma = 104.02(2)^\circ$). $\text{Sr}_2[\text{BeAl}_3\text{N}_5]:\text{Eu}^{2+}$ is built up of AlN_4 tetrahedra and trigonal-planar BeN_3 units with a degree of condensation $\kappa = 0.8$ and provides three crystallographically independent sites for Sr^{2+} . Eu^{2+} doped samples exhibit strong red luminescence ($\lambda_{\text{em}} \approx 612$ nm, $\text{fwhm} = 65\text{--}73$ nm/ $1715\text{--}1966$ cm^{-1}) after irradiation with blue light. Luminescence measurements at lower temperatures (6 K) revealed three superimposing emission peaks, most probably originating from the different crystallographic sites for $\text{Sr}^{2+}/\text{Eu}^{2+}$. Considering the three different coordination spheres around Sr it is quite surprising that the band broadening of the emission band in $\text{Sr}_2[\text{BeAl}_3\text{N}_5]:\text{Eu}^{2+}$ turns out to be relatively moderate. In summary, $\text{Sr}_2[\text{BeAl}_3\text{N}_5]:\text{Eu}^{2+}$ as the first representative of the class of nitridoberyllaluminates is a promising start for the further search for efficient narrow-band red-emitting phosphors.

6.4 Inverse-Tunable Red Luminescence and Electronic Properties of Nitridoberylloaluminates $\text{Sr}_{2-x}\text{Ba}_x[\text{BeAl}_3\text{N}_5]:\text{Eu}^{2+}$ ($x = 0-2$)

Published in: **E. Elzer**, P. Strobel, V. Weiler, M. R. Amin, P. J. Schmidt, A. Moewes, W. Schnick

Chem. Eur. J. **2021**, e202104121

Access via: DOI: 10.1002/chem.202104121

Reprinted at: Chapter 5, Supporting Information in Chapter D

The synthesis of the nitridoberylloaluminates $\text{Ba}_2[\text{BeAl}_3\text{N}_5]:\text{Eu}^{2+}$ and solid solutions $\text{Sr}_{2-x}\text{Ba}_x[\text{BeAl}_3\text{N}_5]:\text{Eu}^{2+}$ ($x = 0.5, 1.0, 1.5$) in a hot isostatic press (HIP) under N_2 atmosphere at 1200°C are reported. The phosphors were obtained through reaction of stoichiometric amounts of $M_2\text{N}$ ($M = \text{Sr}, \text{Ba}$), and the binary nitrides AlN and Be_3N_2 . $\text{Ba}_2[\text{BeAl}_3\text{N}_5]:\text{Eu}^{2+}$ crystallizes isotypically to $\text{Sr}_2[\text{BeAl}_3\text{N}_5]:\text{Eu}^{2+}$ in the triclinic space group $P\bar{1}$ (no. 2) with $Z = 2$. The lattice parameters of $\text{Ba}_2[\text{BeAl}_3\text{N}_5]:\text{Eu}^{2+}$ are enlarged due to the larger radius of Ba^{2+} compared to Sr^{2+} ($a = 6.1869(10)$, $b = 7.1736(13)$, $c = 8.0391(14)$ Å, $\alpha = 102.754(8)$, $\beta = 112.032(6)$, $\gamma = 104.765(7)^\circ$). The lattice parameters of the solid solution series have been obtained from Rietveld refinements and show a nearly linear dependence on the atomic ratio Sr:Ba. A combination of soft X-ray spectroscopy and density functional theory (DFT) was used to investigate the electronic properties and to determine the band gaps of $M_2[\text{BeAl}_3\text{N}_5]$ ($M = \text{Sr}, \text{Ba}$). Eu^{2+} doped samples of the nitridoberylloaluminates exhibit emission in the range between 610 and 656 nm (fwhm = 1922–2025 cm^{-1} (72–87 nm)). Against the usual trend, substitution of the smaller Sr^{2+} by the larger Ba^{2+} results in inverse-tunable luminescence to higher wavelengths (red-shifted). Anomalous emission was excluded with low-temperature luminescence measurements.

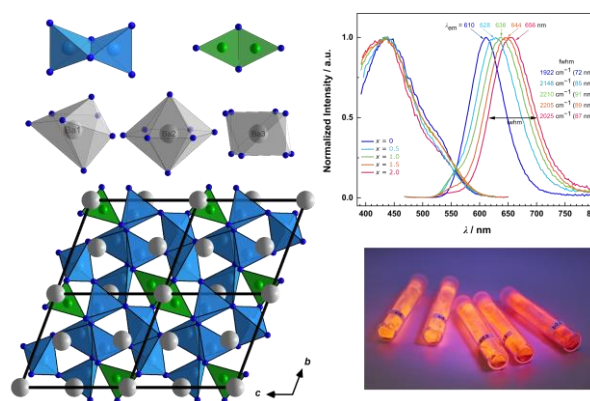


Figure 6.4: Crystal structure of $\text{Sr}_{2-x}\text{Ba}_x[\text{BeAl}_3\text{N}_5]:\text{Eu}^{2+}$, with AlN_4 tetrahedra (blue), BeN_3 units (green), Sr/Ba (gray) and N (blue) atoms and a luminescence spectra of the solid solution series with a photograph of the respective Eu^{2+} doped samples (irradiated with blue light).

7. Discussion and Outlook

Despite over 20 years of research into nitridometallates as promising candidates for application in pc LEDs, investigation of nitridoberyllates as possible host lattices for Eu^{2+} doping is still in its infancy. The number of known ternary nitridoberyllates so far is limited to two compositions – LiBeN and $M\text{Be}_2\text{N}_2$ ($M = \text{Mg}, \text{Ca}-\text{Ba}$) – both showing no luminescence when doped with Eu^{2+} .^[1, 2] However, recent investigations into (oxo)nitridoberyllates have proven that the sparsely studied materials class is highly promising in the search for further narrow-band emitting phosphors.^[3-5]

Therefore, as already discussed in the Chapter 6, the main objective of this thesis was the preparation of nitrides containing beryllium as a network building element and investigation of their promising luminescence properties. The key findings of this thesis will be summarized and discussed in terms of their relevance to the structural chemistry of nitridoberyllates and nitridoberylloaluminates, as well as their relevance for the application as phosphors in pc LEDs. Additionally, perspectives for further investigations in the field of Be/Al-N chemistry and future research on beryllium containing phosphors will be discussed.

The compounds presented in this work were obtained through reactions at high temperatures ($> 1200\text{ }^\circ\text{C}$) under nitrogen atmosphere. The reaction of binary compounds in a radio-frequency furnace has been a well-established synthesis route for nitrides for several decades,^[6, 7] whereas the implementation of a hot isostatic press (HIP), allowing elevated N_2 pressures (50–200 MPa), has only recently been established as a synthesis route for nitrides.^[8-12] Usually, HIPs are industrially employed for annealing and sintering processes of ceramics or alloys.^[13] As already discussed in Chapter 1, the incorporation of Be into anionic networks of nitrides paves the way for the synthesis of highly condensed structures, which in turn can be beneficial for narrow-band emitting phosphors. In Figure 7.1, the degrees of condensation κ of the hitherto known Be containing (oxo)nitrides are therefore compared with the new compounds presented within this thesis highlighted in green.

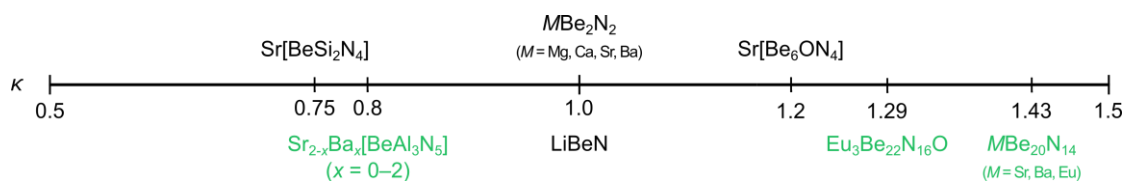


Figure 7.1: Overview of the degree of condensation κ for (oxo)nitridoberyllates, nitridoberyllosilicates and aluminates, respectively. (Oxo)nitrides prepared over the course of this work are highlighted in green.

Recapitulating, a new representative was found for the ternary nitridoberyllates, the quaternary oxonitridoberyllates and, the first member of a compound class containing only Be and Al as network building atoms in a nitride. In addition, structures with higher degrees of condensation κ than previously known for multinary nitrides could be prepared. Here, the incorporation of Be^{2+} with a lower formal charge allows higher crosslinking of the BeN_4 tetrahedra, thus resulting in highly condensed structures with κ values above 1.0. Due to the high atomic ratio of N:O, a degree of condensation κ closer to Be_3N_2 than to BeO is achieved in $\text{Eu}_3\text{Be}_{22}\text{N}_{16}\text{O}$, while $M\text{Be}_{20}\text{N}_{14}$ ($M = \text{Sr}, \text{Ba}, \text{Eu}$) exhibit the highest value observed so far ($\kappa = 1.43$), apart from the binary nitride Be_3N_2 ($\kappa = 1.5$).

Removing the two oxonitridoberyllates in Figure 7.1 the number of known ternary nitridoberyllates with an AE cation is reduced to two compositions – $AE\text{Be}_2\text{N}_2$ and $AE\text{Be}_{20}\text{N}_{14}$ – with an atomic ratio $AE:\text{Be}$ of 1:2 and 1:20, respectively. This offers great potential for finding new structures by examining different compositions ($AE:\text{Be}$), for example “ $AE\text{Be}_5\text{N}_4$ ” (1:5), “ $AE_3\text{Be}_{30}\text{N}_{22}$ ” (1:10), or “ $AE\text{Be}_{14}\text{N}_{10}$ ” (1:14). So far the preparation of the ternary nitridoberyllates was achieved either as a two-step synthesis, where the starting materials were processed at 1000 °C under N_2 flow, before completing the reaction in closed Ta ampoules (Ar atmosphere, 1000–1100 °C) or as a one-step synthesis in open systems (crucibles, N_2 atmosphere, 1400 °C).^[1-4, 14] In contrast to the synthesis of BaBe_2N_2 (60 h), the preparation of $\text{Eu}_3\text{Be}_{22}\text{N}_{16}\text{O}$ and $M\text{Be}_{20}\text{N}_{14}$ ($M = \text{Sr}, \text{Ba}, \text{Eu}$) in the rf furnace was successful despite relatively short reaction times of 1–2 h.^[14] Thus, the variables – composition, temperature and reaction time – open up a large area for ongoing investigations in search for further representatives from the substance class of nitridoberyllates. Additionally, pressure often plays a decisive role in the synthesis and stabilization of nitrides.^[15-17] Therefore, syntheses under elevated nitrogen pressure in a hot isostatic press could be a subject of future investigations. Nitrogen pressure could also be beneficial in search of highly condensed structures when combining high temperatures and starting materials (e. g. Mg_3N_2 , or $M(\text{NH}_2)_2$ ($M = \text{Ca}, \text{Sr}, \text{Ba}$)), which would decompose before reaching the reaction temperatures (> 1400 °C).

As already addressed in Chapter 1.4, Be^{2+} , in contrast to Al^{3+} or Si^{4+} , shows increased versatility with respect to its usually observed coordination numbers: CN = 3 is observed as often as CN = 4. Accordingly, trigonal planar BeN_3 units and BeN_4 tetrahedra are the typical coordination environments. In the present work, different combinations of these building units were observed.

Whereas $M\text{Be}_{20}\text{N}_{14}$ ($M = \text{Sr}, \text{Ba}, \text{Eu}$) is solely composed of edge- and vertex-sharing BeN_4 tetrahedra, $\text{Eu}_3\text{Be}_{22}\text{N}_{16}\text{O}$ is the first (oxo)nitridoberyllate exhibiting the simultaneous occurrence of BeN_3 units and BeN_2O_2 and BeN_4 tetrahedra. Thus, both compounds illustrate the structural versatility of (oxo)nitridoberyllates.

In addition to the synthesis of (oxo)nitridoberyllates, the structural chemistry of nitrides incorporating Be and Al was investigated. The incorporation of lower charged Li^+ and Mg^{2+} into nitridoaluminates contributed to the increase of the degree of condensation (Figure 1.8) from 0.5 in ternary nitridoaluminates to 1.0 in quaternary systems (e. g. $M[\text{LiAl}_3\text{N}_4]$ ($M = \text{Ca}, \text{Sr}$), $M[\text{Mg}_2\text{Al}_2\text{N}_4]$ ($M = \text{Ca}-\text{Ba}$)).^[18-20] Therefore, in the second part of this thesis the incorporation of Be^{2+} into the anionic networks of nitridoaluminates was investigated in the search for new, highly condensed structures. By applying a N_2 pressure of 50 MPa in a hot isostatic press, the synthesis of the first nitridoberylloaluminate with the composition $M_2[\text{BeAl}_3\text{N}_5]$ ($M = \text{Sr}, \text{Ba}$) was achieved. Theoretically, the composition $M_2[\text{BeAl}_3\text{N}_5]$ ($M = \text{Sr}, \text{Ba}$) can be derived from $\text{Ca}_2[\text{MgGa}_3\text{N}_5]$ through a formal substitution of Ca^{2+} , Mg^{2+} and Ga^{3+} by $\text{Sr}^{2+}/\text{Ba}^{2+}$, Be^{2+} and Al^{3+} , respectively. However, the obtained structure is not isotypic to $\text{Ca}_2[\text{MgGa}_3\text{N}_5]$, since Be^{2+} is not tetrahedrally coordinated like Mg^{2+} . While a mixed occupation of the tetrahedral positions is observed in $\text{Ca}_2[\text{MgGa}_3\text{N}_5]$, two different CN are observed in $M_2[\text{BeAl}_3\text{N}_5]$ ($M = \text{Sr}, \text{Ba}$) for the network building ions. Be^{2+} is threefold coordinated, forming trigonal planar BeN_3 units and Al^{3+} is fourfold coordinated, exhibiting AlN_4 tetrahedra. Recapitulating, the incorporation of Be^{2+} into nitridoaluminates, hence the preparation of nitridoberylloaluminates led to the discovery of a previously unknown structure with a higher degree of condensation ($\kappa = 0.8$), compared to values obtained in ternary nitridoaluminates.

For future investigations compositions of known nitrides, such as $\text{Ca}[\text{Mg}_2\text{GaN}_3]$, $\text{Ba}[\text{Mg}_2\text{Ga}_2\text{N}_4]$, or $\text{Sr}[\text{MgAl}_5\text{N}_7]$ can serve as a starting point for the preparation of nitridoberylloaluminates. Formally replacing the elements Mg^{2+} or Ga^{3+} with Be^{2+} and Al^{3+} would lead to the sum formulas “ $M[\text{Be}_2\text{AlN}_3]$ ”, “ $M[\text{Be}_2\text{Al}_2\text{N}_4]$ ”, or “ $M[\text{BeAl}_5\text{N}_7]$ ” with $M = \text{Ca}, \text{Sr}, \text{Ba}$. As illustrated by the example above, the discovery of new structures is very likely, due to the special and flexible role of Be (BeN_3 units or BeN_4 tetrahedra). With only one representative of nitridoberylloaluminates known so far, it is difficult to conclude whether the occurrence of different coordination numbers for Be^{2+} and Al^{3+} is common, or an exception. A comparison with Al and Be containing oxides shows that structures with BeO_4 and AlO_4 tetrahedra (for example $\text{Na}_3\text{AlBe}[\text{SiO}_4]_2$) as well as compounds containing BeO_4 tetrahedra and AlO_6 octahedra (e. g. $\text{Be}_3\text{Al}_2[\text{Si}_6\text{O}_{18}]$, $\text{Al}_2[\text{BeO}_4]$) are known.^[21-23] Meanwhile, trigonal-

planar BeO_3 units mainly appear in ternary oxoberyllates.^[14, 24, 25] Since higher coordination numbers are usually observed in compounds prepared at higher pressures – according to the pressure coordination rule – studies of the synthesis of nitridoberylloaluminates could be carried out at higher pressures, either in hot isostatic presses in the range of 50–200 MPa or in large volume presses allowing typical pressures in the GPa range. This could result in nitridoberylloaluminates consisting of both BeN_4 and AlN_4 tetrahedra or even BeN_4 tetrahedra and AlN_6 octahedra.

As already mentioned at the beginning of this chapter, the focus of this thesis was not only on extending the structural diversity of nitridoberyllates, but also on the investigation of their promising luminescence properties. Structural prerequisites such as highly condensed anionic networks, cation ordering, and a highly symmetric crystallographic site for the dopant with uniform dopant-ligand distances have been evaluated in the literature as beneficial for narrow band emission. In this context, previous investigations of the narrow-band cyan-emitting $\text{Sr}[\text{Be}_6\text{ON}_4]:\text{Eu}^{2+}$ or the ultranarrow-band blue-emitting $\text{AELi}_2[\text{Be}_4\text{O}_6]:\text{Eu}^{2+}$ ($\text{AE} = \text{Sr}, \text{Ba}$) already illustrated the potential of beryllium containing host lattices as narrow-band emitting phosphors.

As discussed in Chapter 1.2, nitride anions feature a higher covalence of the dopant-ligand interaction and cause a high crystal field splitting, which usually result in red-shifted excitation and lower emission energies. Therefore, in this thesis, the synthesis of highly condensed nitridoberyllates and nitridoberylloaluminates as possible host lattices for doping with Eu^{2+} was targeted, resulting in the synthesis of $M\text{Be}_{20}\text{N}_{14}:\text{Eu}^{2+}$ ($M = \text{Sr}, \text{Ba}$). Due to the high connectivity of the BeN_4 tetrahedra, $\text{SrBe}_{20}\text{N}_{14}:\text{Eu}^{2+}$ and $\text{BaBe}_{20}\text{N}_{14}:\text{Eu}^{2+}$ exhibit an extremely rigid anionic network with very similar lattice parameters and metal–ligand distances. Thus, the structure perfectly fulfills the requirements for narrow-band emission. The highly condensed, rigid network, and the cage like, cuboctahedral substitutional site for the incorporation of the activator ion Eu^{2+} in the structure of $M\text{Be}_{20}\text{N}_{14}:\text{Eu}^{2+}$ limits lattice relaxation, resulting in a small Stokes shift and a narrow emission band. Even though, nitrides, in contrast to oxides, usually shift the emission to higher wavelengths, here the nephelauxetic effect is reduced due to the high degree of condensation of the anionic network. Additionally, a high coordination number ($\text{CN} = 12$) around the activator results in a weak crystal field splitting. Therefore, the typical red-shift for nitrides is significantly reduced. Compared to other nitrides, $M\text{Be}_{20}\text{N}_{14}:\text{Eu}^{2+}$ ($M = \text{Sr}, \text{Ba}$), along with $\text{BaP}_8\text{N}_{14}$, is one of the first nitrides with an emission band so far in the blue spectral region.^[26] Currently, however, the occurrence of Eu^{2+} trapped exciton emission (ETE) in addition to normal Eu^{2+} emission (Chapter 3.3) prevents a possible application of

$M\text{Be}_{20}\text{N}_{14}:\text{Eu}^{2+}$ as a narrow-band blue-emitting phosphor. Usually, ETE is observed in compounds with long activator–ligand distance.^[27] Since the intensity of ETE decreases from $\text{BaBe}_{20}\text{N}_{14}:\text{Eu}^{2+}$ to $\text{SrBe}_{20}\text{N}_{14}:\text{Eu}^{2+}$ further improvement of the materials emission properties is conceivable by a further gradual reduction of the *AE* cation size. Possible approaches would be the synthesis of solid solution series ($\text{Sr}_{1-x}\text{Ca}_x\text{Be}_{20}\text{N}_{14}:\text{Eu}^{2+}$) or a complete substitution of Sr/Ba with the smaller *AE* metal Ca ($\text{CaBe}_{20}\text{N}_{14}:\text{Eu}^{2+}$).

Meanwhile, Eu^{2+} doped samples of the nitridoberylloaluminates $M_2[\text{BeAl}_3\text{N}_5]:\text{Eu}^{2+}$ ($M = \text{Sr}, \text{Ba}$) exhibit intense orange to red luminescence. In contrast to the usual trend, the emission maximum in the nitridoberylloaluminates $\text{Sr}_{2-x}\text{Ba}_x[\text{BeAl}_3\text{N}_5]:\text{Eu}^{2+}$ ($x > 0$) is inversely shifted to higher wavelengths by the incorporation of the larger cation Ba^{2+} . Thus, resulting in an inverse-tunable emission between 610 to 656 nm through the compositional variable x . Thorough investigations of the luminescence properties of the solid solution series ruled out activator concentration and anomalous trapped exciton emission as possible causes for the red-shifted emission. Therefore, the uncommon, inverse-tunable red emission of $\text{Sr}_{2-x}\text{Ba}_x[\text{BeAl}_3\text{N}_5]:\text{Eu}^{2+}$ is attributed to structural changes in the local Eu^{2+} coordination. The study of the solid solution series emphasizes that the Eu^{2+} emission can be significantly influenced by small local changes and distortions of the environment without necessarily changing the symmetry of the crystal. In this context, a substitution of Sr/Ba with smaller cations like Ca could be the subject of further investigations, resulting in possible sum formulas “ $\text{Ca}_2M_4[\text{Be}_3\text{Al}_9\text{N}_{15}]:\text{Eu}^{2+}$ ” or “ $\text{Ca}_4M_2[\text{Be}_3\text{Al}_9\text{N}_{15}]:\text{Eu}^{2+}$ ” ($M = \text{Sr}, \text{Ba}$). Shorter metal–ligand distance could lead to preferential occupation of the Sr/Ba site when doped, due to similar ionic radii of Sr^{2+} and Eu^{2+} , resulting in smaller fwhm values, when Eu^{2+} is located only on one (or two) crystallographic site(s), instead of three.

Recapitulating, this thesis introduced several new representatives from the substance class of nitridoberyllates and the synthesis of the first nitridoberylloaluminate. The incorporation of Be into the anionic networks allowed the preparation of highly condensed structures with high degrees of condensation κ , such as $\kappa = 1.29$ in $\text{Eu}_3\text{Be}_{22}\text{N}_{16}\text{O}$ and $\kappa = 1.43$ in $M\text{Be}_{20}\text{N}_{14}$ ($M = \text{Sr}, \text{Ba}, \text{Eu}$). The examined Eu^{2+} doped samples showed promising luminescence properties with exceptional narrow-band blue emission in case of $M\text{Be}_{20}\text{N}_{14}:\text{Eu}^{2+}$ ($M = \text{Sr}, \text{Ba}$) and inverse-tunable orange to red emission of the solid solution series $\text{Sr}_{2-x}\text{Ba}_x[\text{BeAl}_3\text{N}_5]:\text{Eu}^{2+}$ ($x = 0-2$). In conclusion, the synthesis of the presented compounds and the study of their electronic and optical properties contributes to the elucidation of the hitherto scarcely studied class of nitridoberyllates and nitridoalumoberyllates and

underline their role in the discovery and development of new phosphors. By combining the properties of the here presented phosphors, such as high thermal and chemical stability, narrow band emission, small Stokes shift and emission in the range between 610 and 650 nm, the discovery of a red phosphor with a fwhm of 30 nm is within reach. Structurally, Be based nitrides appear to be perfectly suited for this purpose, due to their highly condensed, rigid networks. The future challenge is to discover a compound that, in addition to the rigid network, has a highly symmetric crystallographic position for an *AE* cation with suitable metal–ligand distances for a red-emitting phosphor.

7.1 References

- [1] Somer, M.; Carrillo-Cabrera, W.; Peters, E.-M.; Peters, K.; von Schnering, H. Crystal structure of lithium beryllium nitride, LiBeN. *Z. Kristallogr.-Cryst. Mater.* **1996**, *211*, 635–635.
- [2] Somer, M.; Yarasik, A.; Akselrud, L.; Leoni, S.; Rosner, H.; Schnelle, W.; Kniep, R. Ae[Be₂N₂]: nitridoberyllates of the heavier alkaline-earth metals. *Angew. Chem. Int. Ed.* **2004**, *43*, 1088–1092; *Angew. Chem.* **2004**, *116*, 1108–1112.
- [3] Strobel, P.; de Boer, T.; Weiler, V.; Schmidt, P. J.; Moewes, A.; Schnick, W. Luminescence of an Oxonitridoberyllate: A Study of Narrow-Band Cyan-Emitting Sr[Be₆ON₄]:Eu²⁺. *Chem. Mater.* **2018**, *30*, 3122–3130.
- [4] Strobel, P.; Weiler, V.; Schmidt, P. J.; Schnick, W. Sr[BeSi₂N₄]:Eu²⁺/Ce³⁺ and Eu[BeSi₂N₄]: Nontypical Luminescence in Highly Condensed Nitridoberyllosilicates. *Chem. Eur. J.* **2018**, *24*, 7243–7249.
- [5] Strobel, P.; Maak, C.; Weiler, V.; Schmidt, P. J.; Schnick, W. Ultra-Narrow-Band Blue-Emitting Oxoberyllates AELi₂[Be₄O₆]:Eu²⁺ (AE = Sr, Ba) Paving the Way to Efficient RGB pc-LEDs. *Angew. Chem. Int. Ed.* **2018**, *57*, 8739–8743; *Angew. Chem.* **2018**, *130*, 8875–8879.
- [6] Zeuner, M.; Pagano, S.; Schnick, W. Nitridosilicates and oxonitridosilicates: from ceramic materials to structural and functional diversity. *Angew. Chem. Int. Ed.* **2011**, *50*, 7754–7775; *Angew. Chem.* **2011**, *123*, 7898–7920.
- [7] Wang, L.; Xie, R. J.; Suehiro, T.; Takeda, T.; Hirosaki, N. Down-Conversion Nitride Materials for Solid State Lighting: Recent Advances and Perspectives. *Chem. Rev.* **2018**, *118*, 1951–2009.
- [8] Wagatha, P.; Pust, P.; Weiler, V.; Wochnik, A. S.; Schmidt, P. J.; Scheu, C.; Schnick, W. Ca_{18.75}Li_{10.5}[Al₃₉N₅₅]:Eu²⁺ — Supertetrahedron Phosphor for Solid-State Lighting. *Chem. Mater.* **2016**, *28*, 1220–1226.
- [9] Wagatha, P.; Weiler, V.; Schmidt, P. J.; Schnick, W. Tailoring Emission Characteristics: Narrow-Band Red Luminescence from SLA to CaBa[Li₂Al₆N₈]:Eu²⁺. *Chem. Mater.* **2018**, *30*, 7885–7891.
- [10] Wagatha, P.; Weiler, V.; Schmidt, P. J.; Schnick, W. Tunable Red Luminescence in Nitridomagnesoaluminates α -Sr₂[MgAl₅N₇]:Eu²⁺, β -Sr₂[MgAl₅N₇]:Eu²⁺, and Sr₈[LiMg₂Al₂₁N₂₈]:Eu²⁺. *Chem. Mater.* **2018**, *30*, 1755–1761.
- [11] Wendl, S.; Zipkat, M.; Strobel, P.; Schmidt, P. J.; Schnick, W. Synthesis of Nitride Zeolites in a Hot Isostatic Press. *Angew. Chem. Int. Ed.* **2021**, *60*, 4470–4473; *Angew. Chem.* **2021**, *133*, 4520–4523.
- [12] Wendl, S.; Mardazad, S.; Strobel, P.; Schmidt, P. J.; Schnick, W. HIP to be Square: Simplifying Nitridophosphate Synthesis in a Hot Isostatic Press. *Angew. Chem. Int. Ed.* **2020**, *59*, 18240–18243; *Angew. Chem.* **2020**, *132*, 18397–18400.
- [13] Bocanegra-Bernal, M. H. Hot Isostatic Pressing (HIP) technology and its application to metals and ceramics. *J. Mater. Sci.* **2004**, *39*, 6399–6420.
- [14] Leoni, S.; Niewa, R.; Akselrud, L.; Prots, Y.; Schnelle, W.; Tahsin, G.; Cetinkol, M.; Somer, M.; Kniep, R. Novel Barium Beryllates Ba[Be₂N₂] and Ba₃[Be₅O₈]: Syntheses, Crystal Structures and Bonding Properties. *Z. Anorg. Allg. Chem.* **2005**, *631*, 1818–1824.
- [15] Horvath-Bordon, E.; Riedel, R.; Zerr, A.; McMillan, P. F.; Auffermann, G.; Prots, Y.; Bronger, W.; Kniep, R.; Kroll, P. High-pressure chemistry of nitride-based materials. *Chem. Soc. Rev.* **2006**, *35*, 987–1014.
- [16] Kloss, S. D.; Schnick, W. Nitridophosphates: A Success Story of Nitride Synthesis. *Angew. Chem. Int. Ed.* **2019**, *58*, 7933–7944; *Angew. Chem.* **2019**, *131*, 8015–8027.

- [17] Wang, P.; Wang, S.; Zou, Y.; Zhu, J.; He, D.; Wang, L.; Zhao, Y. Novel Nitride Materials Synthesized at High Pressure. *Crystals* **2021**, *11*.
- [18] Pust, P.; Wochnik, A. S.; Baumann, E.; Schmidt, P. J.; Wiechert, D.; Scheu, C.; Schnick, W. Ca[LiAl₃N₄]:Eu²⁺ — A Narrow-Band Red-Emitting Nitridolithoaluminate. *Chem. Mater.* **2014**, *26*, 3544–3549.
- [19] Pust, P.; Weiler, V.; Hecht, C.; Tucks, A.; Wochnik, A. S.; Henss, A. K.; Wiechert, D.; Scheu, C.; Schmidt, P. J.; Schnick, W. Narrow-band red-emitting Sr[LiAl₃N₄]:Eu²⁺ as a next-generation LED-phosphor material. *Nat. Mater.* **2014**, *13*, 891–896.
- [20] Pust, P.; Hintze, F.; Hecht, C.; Weiler, V.; Locher, A.; Zitnanska, D.; Harm, S.; Wiechert, D.; Schmidt, P. J.; Schnick, W. Group (III) Nitrides M[Mg₂Al₂N₄] (M = Ca, Sr, Ba, Eu) and Ba[Mg₂Ga₂N₄] — Structural Relation and Nontypical Luminescence Properties of Eu²⁺ Doped Samples. *Chem. Mater.* **2014**, *26*, 6113–6119.
- [21] Razmanova, Z. P.; Rastsvetaeva, R. K.; Kharitonov, Y. A.; Belov, N. V. Refined crystal structure of Na₃AlBeSi₂O₈ with three-dimensional skeleton from tetrahedrons of three types. *Kristallografiya* **1982**, *27*, 675–679.
- [22] Bragg, W. L.; West, J. The Structure of Beryl, Be₃Al₂Si₆O₁₈. *Proc. R. Soc. London, Ser. A* **1926**, *111*, 691–714.
- [23] Bragg, W. L.; Brown, G. B. V. Die Kristallstruktur von Chrysoberyll (BeAl₂O₄). *Z. Kristallogr. Cryst. Mater.* **1926**, *63*, 122–143.
- [24] Strobel, P.; Niklaus, R.; Schmidt, P. J.; Schnick, W. Oxoberyllates SrBeO₂ and Sr₁₂Be₁₇O₂₉ as Novel Host Materials for Eu²⁺ Luminescence. *Chem. Eur. J.* **2018**, *24*, 12678–12685.
- [25] Gifftthaler, T.; Strobel, P.; Schnick, W. Synthesis and Crystal Structure of the Strontium Beryllate Sr₃Be₂O₅. *Z. Anorg. Allg. Chem.* **2020**, *646*, 103–105.
- [26] Wendl, S.; Eisenburger, L.; Strobel, P.; Gunther, D.; Wright, J. P.; Schmidt, P. J.; Oeckler, O.; Schnick, W. Nitridophosphate-Based Ultra-Narrow-Band Blue-Emitters: Luminescence Properties of AEP₈N₁₄:Eu²⁺ (AE=Ca, Sr, Ba). *Chem. Eur. J.* **2020**, *26*, 7292–7298.
- [27] Dorenbos, P. Anomalous luminescence of Eu²⁺ and Yb²⁺ in inorganic compounds. *J. Phys.: Condens. Matter* **2003**, *15*, 2645–2665.

A. Supporting Information for Chapter 2

A.1 Results and Discussion

Synthesis

Table A.1. List of chemicals used for the synthesis of $\text{Eu}_3\text{Be}_{22}\text{N}_{16}\text{O}$ and weighed starting materials for the synthesis of $\text{Eu}_3\text{Be}_{22}\text{N}_{16}\text{O}$.

Substance	Producer	weight (amount of substance)
$\text{Eu}(\text{NH}_2)_2$	Synthesized according to literature from Eu in supercritical ammonia ^[1,2]	44.16 mg (0.240 mmol)
Be_3N_2	Synthesized from Be in a hot isostatic press at 1400 °C under 50 MPa N_2 atmosphere ^[3]	30.83 mg (0.560 mmol)
BeO	AlfaAesar, 99.95%	2.0 mg (0.080 mmol)

Table A.2. EDX results of $\text{Eu}_3\text{Be}_{22}\text{N}_{16}\text{O}$ with standard deviations in parentheses.

Element	calculated atom-%	measured atom-%
Eu	15	15(3)
N	80	77(3)
O	5	7(3)

FTIR

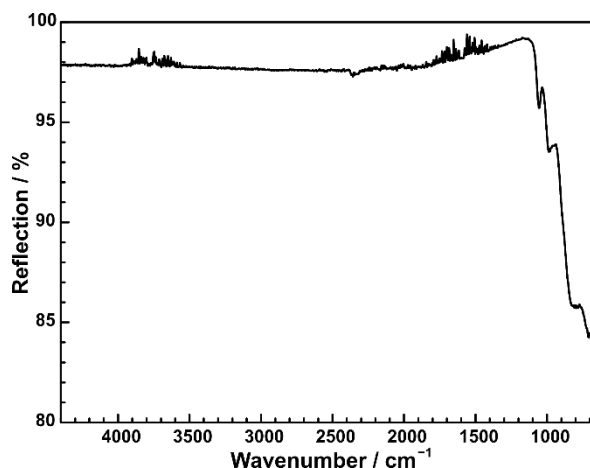


Figure A.1. FTIR-spectra (ATR) of $\text{Eu}_3\text{Be}_{22}\text{N}_{16}\text{O}$ powder sample. Bands at 2345 cm^{-1} belong to the asymmetric stretching vibration of CO_2 . No O–H and N–H bands are observed in the typical region. The absorption bands between 500 and 1300 cm^{-1} can be attributed to symmetric and asymmetric stretching modes of the Be-X-framework ($X = \text{N}, \text{O}$).

Crystallographic data for $\text{Eu}_3\text{Be}_{22}\text{N}_{16}\text{O}$ **Table A.3.** Atomic coordinates and equivalent isotropic displacement parameters (U_{eq}) of $\text{Eu}_3\text{Be}_{22}\text{N}_{16}\text{O}$ with standard deviations in parentheses.

Atom	Wyckoff	x	y	z	$U_{\text{eq}}/\text{\AA}^3$	sof
Eu1	8f	0.32790(2)	0.33996(4)	0.22378(2)	0.00755(10)	1
Eu2	8f	0.11968(2)	0.04269(4)	0.42413(3)	0.00934(10)	1
Eu3	8f	0.39643(2)	0.12011(5)	0.09449(3)	0.01182(11)	1
N1	8f	0.0280(3)	0.3298(7)	0.1238(4)	0.0051(7)	1
N2	8f	0.1167(3)	0.3287(7)	0.4106(4)	0.0051(7)	1
N3	4e	0	0.4894(9)	$\frac{1}{4}$	0.0024(14)	1
N4	8f	0.0813(3)	0.1738(6)	0.5347(4)	0.0029(6)	1
N5	8f	0.2630(3)	0.0049(7)	0.4362(4)	0.0043(6)	1
N6	8f	0.0753(3)	0.1625(6)	0.0273(4)	0.0029(6)	1
N7	8f	0.0781(3)	0.5097(7)	0.0301(4)	0.0051(7)	1
N8	8f	0.3002(3)	0.1578(6)	0.3267(4)	0.0029(6)	1
N9	8f	0.1510(3)	0.4927(7)	0.2855(4)	0.0043(6)	1
N10	8f	0.0335(3)	0.0051(7)	0.6358(4)	0.0032(7)	1
N11	8f	0.2577(3)	0.3240(6)	0.4315(4)	0.0029(6)	1
N12	8f	0.1979(3)	0.0110(6)	0.1648(4)	0.0029(6)	1
N13	4e	0	0.1775(9)	$\frac{1}{4}$	0.0032(7)	1
N14	8f	0.1810(3)	0.3353(6)	0.1677(4)	0.0029(6)	1
N15	8f	0.5355(3)	0.1761(7)	0.1407(4)	0.0043(6)	1
N16	8f	0.1486(3)	0.1739(6)	0.2799(4)	0.0032(7)	1
N17	8f	0.2336(3)	0.1727(7)	0.0538(4)	0.0043(6)	1
O1	8f	0.4325(3)	0.3447(7)	0.1926(4)	0.0129(11)	1
Be1	8f	0.1203(5)	0.3342(10)	0.2130(6)	0.0055(10)	1
Be2	8f	0.2600(5)	0.0123(11)	0.1184(6)	0.0055(10)	1
Be3	8f	0.2053(5)	0.1698(10)	0.2327(6)	0.0043(16)	1
Be4	8f	0.0076(5)	0.1665(10)	0.5710(6)	0.0054(16)	1
Be5	8f	0.0976(5)	0.0021(10)	0.5913(6)	0.0060(16)	1
Be6	8f	0.0103(5)	0.1542(10)	0.0659(6)	0.0062(17)	1
Be7	8f	0.0266(5)	0.3317(10)	0.3213(6)	0.0055(10)	1
Be8	8f	0.1575(5)	0.3311(10)	0.3490(6)	0.0053(16)	1
Be9	8f	0.0859(6)	0.3338(11)	0.0769(7)	0.0078(18)	1
Be10	8f	0.2926(5)	0.0014(11)	0.2580(6)	0.0061(16)	1
Be11	8f	0.2914(5)	0.1574(10)	0.5092(6)	0.0043(11)	1
Be12	8f	0.0711(5)	0.3328(11)	0.4655(7)	0.0073(17)	1
Be13	8f	0.4017(6)	0.1661(11)	0.3958(7)	0.0088(18)	1
Be14	8f	0.2352(5)	0.1538(10)	0.3673(6)	0.0043(11)	1
Be15	8f	0.3176(6)	0.3300(11)	0.3902(6)	0.0063(17)	1
Be16	8f	0.1764(5)	0.4913(10)	0.1012(6)	0.0048(16)	1
Be17	8f	0.1725(5)	0.1782(11)	0.0921(6)	0.0058(16)	1
Be18	8f	0.5111(7)	0.0114(13)	0.0666(8)	0.019(2)	1
Be19	8f	0.5158(6)	0.3440(14)	0.1983(8)	0.016(2)	1
Be20	8f	0.2507(5)	0.3479(10)	0.0296(6)	0.0057(16)	1
Be21	8f	0.0591(6)	0.1153(14)	0.2209(7)	0.015(2)	1
Be22	8f	0.4391(5)	0.0534(11)	0.2764(6)	0.0075(17)	1

Table A.4. Anisotropic displacement parameters for $\text{Eu}_3\text{Be}_{22}\text{N}_{16}\text{O}$ with standard deviations in parentheses.

Atom	$U_{11}/\text{\AA}^2$	$U_{22}/\text{\AA}^2$	$U_{33}/\text{\AA}^2$	$U_{12}/\text{\AA}^2$	$U_{13}/\text{\AA}^2$	$U_{23}/\text{\AA}^2$
Eu1	0.00721(18)	0.00957(18)	0.00698(17)	0.00072(13)	0.00443(14)	0.00098(12)
Eu2	0.01022(19)	0.00663(18)	0.01312(19)	-0.00068(13)	0.00738(15)	-0.00275(13)
Eu3	0.0145(2)	0.00703(18)	0.01079(19)	-0.00067(14)	0.00418(16)	-0.00121(14)
N1	0.0014(15)	0.0085(17)	0.0044(15)	0.0009(12)	0.0008(13)	-0.0017(12)
N2	0.0014(15)	0.0085(17)	0.0044(15)	0.0009(12)	0.0008(13)	-0.0017(12)
N3	0.001(3)	0.003(4)	0.002(3)	0.00000	0.000(3)	0.00000
N4	0.0014(15)	0.0018(15)	0.0042(15)	-0.0006(11)	0.0006(12)	0.0002(11)
N5	0.0027(14)	0.0039(14)	0.0043(14)	0.0011(10)	0.0003(11)	0.0021(10)
N6	0.0014(15)	0.0018(15)	0.0042(15)	-0.0006(11)	0.0006(12)	0.0002(11)
N7	0.0014(15)	0.0085(17)	0.0044(15)	0.0009(12)	0.0008(13)	-0.0017(12)
N8	0.0035(15)	0.0023(15)	0.0022(15)	-0.0007(11)	0.0010(13)	-0.0007(11)
N9	0.0027(14)	0.0039(14)	0.0043(14)	0.0011(10)	0.0003(11)	0.0021(10)
N10	0.0017(16)	0.0035(17)	0.0030(16)	0.0014(14)	0.0002(14)	0.0012(14)
N11	0.0014(15)	0.0018(15)	0.0042(15)	-0.0006(11)	0.0006(12)	0.0002(11)
N12	0.0035(15)	0.0023(15)	0.0022(15)	-0.0007(11)	0.0010(13)	-0.0007(11)
N13	0.0017(16)	0.0035(17)	0.0030(16)	0.0014(14)	0.0002(14)	0.0012(14)
N14	0.0035(15)	0.0023(15)	0.0022(15)	-0.0007(11)	0.0010(13)	-0.0007(11)
N15	0.0027(14)	0.0039(14)	0.0043(14)	0.0011(10)	0.0003(11)	0.0021(10)
N16	0.0017(16)	0.0035(17)	0.0030(16)	0.0014(14)	0.0002(14)	0.0012(14)
N17	0.0027(14)	0.0039(14)	0.0043(14)	0.0011(10)	0.0003(11)	0.0021(10)
O1	0.009(3)	0.022(3)	0.009(3)	0.001(2)	0.005(2)	0.001(2)
Be1	0.006(2)	0.005(2)	0.006(2)	-0.0011(18)	0.004(2)	-0.0016(18)
Be2	0.006(2)	0.005(2)	0.006(2)	-0.0011(18)	0.004(2)	-0.0016(18)
Be3	0.004(4)	0.003(4)	0.006(4)	0.001(3)	0.003(3)	-0.001(3)
Be4	0.004(4)	0.003(4)	0.010(4)	0.001(3)	0.004(3)	0.000(3)
Be5	0.005(4)	0.003(4)	0.010(4)	0.002(3)	0.004(3)	0.000(3)
Be6	0.007(4)	0.006(4)	0.005(4)	0.002(3)	0.002(3)	0.000(3)
Be7	0.006(2)	0.005(2)	0.006(2)	-0.0011(18)	0.004(2)	-0.0016(18)
Be8	0.006(4)	0.004(4)	0.006(4)	0.001(3)	0.002(3)	0.001(3)
Be9	0.013(5)	0.004(4)	0.009(4)	-0.003(3)	0.007(4)	-0.001(3)
Be10	0.005(4)	0.006(4)	0.006(4)	0.000(3)	0.001(3)	0.000(3)
Be11	0.004(3)	0.004(3)	0.005(3)	0.000(2)	0.003(2)	-0.002(2)
Be12	0.009(4)	0.004(4)	0.009(4)	-0.001(3)	0.005(4)	0.000(3)
Be13	0.009(4)	0.010(4)	0.006(4)	-0.004(3)	0.003(4)	-0.002(3)
Be14	0.004(3)	0.004(3)	0.005(3)	0.000(2)	0.003(2)	-0.002(2)
Be15	0.010(4)	0.006(4)	0.006(4)	-0.001(3)	0.006(4)	-0.002(3)
Be16	0.005(4)	0.004(4)	0.008(4)	0.000(3)	0.005(3)	0.001(3)
Be17	0.003(4)	0.006(4)	0.007(4)	-0.001(3)	0.002(3)	-0.002(3)
Be18	0.017(5)	0.011(5)	0.027(6)	0.000(4)	0.009(5)	0.001(4)
Be19	0.008(5)	0.029(6)	0.013(5)	-0.005(4)	0.007(4)	0.002(4)
Be20	0.007(4)	0.005(4)	0.006(4)	-0.001(3)	0.004(3)	0.000(3)
Be21	0.006(4)	0.024(6)	0.015(5)	-0.004(4)	0.007(4)	-0.013(4)
Be22	0.004(4)	0.010(4)	0.006(4)	-0.003(3)	0.001(3)	-0.002(3)

BVS calculations

Table A.5. Cation (Eu^{2+} , Be^{2+}) and anion (N^{3-} , O^{2-}) BVS for $\text{Eu}_3\text{Be}_{22}\text{N}_{16}\text{O}$.

Atom	Bond Valence Sum	Atom	Bond Valence Sum	Atom	Bond Valence Sum
Eu1	1.88	Be13	2.03	N6	2.99
Eu2	2.02	Be14	2.25	N7	3.34
Eu3	2.02	Be15	1.94	N8	3.00
Be1	2.11	Be16	2.07	N9	3.00
Be2	1.97	Be17	1.96	N10	2.80
Be3	1.99	Be18	1.87	N11	3.00
Be4	2.06	Be19	1.67	N12	2.94
Be5	1.97	Be20	2.12	N13	2.78
Be6	1.95	Be21	2.09	N14	3.06
Be7	2.11	Be22	2.06	N15	2.96
Be8	2.09	N1	3.04	N16	3.10
Be9	2.20	N2	3.29	N17	2.85
Be10	2.01	N3	2.95	O1	2.27
Be11	2.02	N4	2.99		
Be12	2.12	N5	3.10		

MAPLE calculations

Table A.6. Results of MAPLE calculations (kJ/mol) for $\text{Eu}_3\text{Be}_{22}\text{N}_{16}\text{O}$. Δ = deviation of the sum of MAPLE values of constituting binary or ternary oxides/nitrides to the total MAPLE value of $\text{Eu}_3\text{Be}_{22}\text{N}_{16}\text{O}$.

	$\text{Eu}_3\text{Be}_{22}\text{N}_{16}\text{O}$	Reference	Typical values from literature
Eu^{2+}	1604–1828	[4]	1700–2100
N^{3-}	4868–6172	[4]	$\text{N}^{[2]}$: 4600–6000, $\text{N}^{[3]}$ 5000–6200 ^[1]
O^{2-}	2506	[4]	$\text{O}^{[2]}$: 2400–2800
Be^{2+}	2303–3211	[5–7]	Be^{2+} : 2698–3261
Total	158115		
Δ	[1] 1.67%, [2] 0.09%		
Total MAPLE	[1] $3 \text{EuCl}_2 + \text{Mg}_3\text{N}_2 + \text{BeO} + 7 \text{Be}_3\text{N}_2 - 3 \text{MgCl}_2 = 160799 \text{ kJ/mol}$ [2] $3 \text{EuBe}_{20}\text{N}_{14} + \text{BeO} - 13 \text{Be}_3\text{N}_2 = 158261 \text{ kJ/mol}$		

Rietveld refinement of $\text{Eu}_3\text{Be}_{22}\text{N}_{16}\text{O}$ **Table A.7.** Data of Rietveld refinements for $\text{Eu}_3\text{Be}_{22}\text{N}_{16}\text{O}$ with least squares standard deviations in parentheses.

formula	$\text{Eu}_3\text{Be}_{22}\text{N}_{16}\text{O}$
Formula mass/ $\text{g}\cdot\text{mol}^{-1}$	894.26
Crystal system	monoclinic
Space group	$C2/c$ (no. 15)
Lattice parameters/ $\text{\AA}, ^\circ$	$a = 20.6094(3)$
	$b = 8.7310(1)$
	$c = 17.4985(3)$
	$\beta = 120.7071(13)$
Volume/ \AA^3	2707.20(9)
Z	8
X-ray density / $\text{g}\cdot\text{cm}^{-3}$	4.38796
Diffractometer	Stoe Stadi P
Radiation	Mo $K\alpha_1 = 0.71073 \text{\AA}$
Monochromator	Ge(111)
Detector	MYTHEN 1K
2θ -range/ $^\circ$	5–70
Data points	4623
Number of observed reflections	6421
Number of parameters	51
Program used	TOPAS Academic V6
Structure refinement	Rietveld-method
Background function	Shifted Chebyshev (12 polynomials)
R_{wp}	7.3031
R_{exp}	3.0725
R_{p}	4.7878
R_{Bragg}	3.2223
χ^2	2.3769

Structure Description

Table A.8. Selected atomic distances in $\text{Eu}_3\text{Be}_{22}\text{N}_{16}\text{O}$ in Å with standard deviations in parentheses.

Atom 1	Atom 2	Distance	Atom 1	Atom 2	Distance	Atom 1	Atom 2	Distance	Atom 1	Atom 2	Distance
Eu1	O1	2.482(8)	Be1	N16	1.723(11)	Be8	N16	1.775(12)	Be16	N5	1.686(15)
Eu1	N14	2.664(7)	Be1	N1	1.738(9)	Be8	N11	1.818(10)	Be16	N7	1.761(10)
Eu1	N8	2.674(8)	Be1	N9	1.761(11)	Be9	N6	1.686(12)	Be16	N14	1.761(12)
Eu1	N12	2.716(8)	Be1	N14	1.792(16)	Be9	N7	1.708(13)	Be16	N8	1.820(11)
Eu1	N5	2.838(6)	Be2	N17	1.704(12)	Be9	N1	1.762(18)	Be17	N17	1.704(15)
Eu1	N16	2.959(6)	Be2	N9	1.752(9)	Be9	N14	1.784(11)	Be17	N6	1.731(10)
Eu1	N15	2.961(6)	Be2	N11	1.808(12)	Be10	N9	1.687(16)	Be17	N12	1.827(12)
Eu1	N17	2.974(6)	Be2	N12	1.834(16)	Be10	N8	1.772(13)	Be17	N14	1.850(13)
Eu1	N10	2.974(5)	Be3	N16	1.743(16)	Be10	N12	1.795(9)	Be18	N7	1.759(12)
Eu1	N9	3.076(7)	Be3	N14	1.745(11)	Be10	N14	1.834(12)	Be18	N7	1.79(2)
Eu2	O1	2.463(7)	Be3	N12	1.780(12)	Be11	N2	1.689(10)	Be18	N1	1.810(14)
Eu2	N2	2.504(7)	Be3	N8	1.803(9)	Be11	N5	1.726(11)	Be18	N15	1.825(14)
Eu2	N4	2.693(8)	Be4	N6	1.695(9)	Be11	N11	1.790(16)	Be19	O1	1.643(14)
Eu2	N11	2.756(5)	Be4	N10	1.713(11)	Be11	N11	1.865(11)	Be19	O1	1.669(16)
Eu2	N10	2.804(7)	Be4	N15	1.728(11)	Be12	N2	1.653(17)	Be19	N10	1.863(17)
Eu2	N5	2.872(8)	Be4	N4	1.925(15)	Be12	N7	1.738(13)	Be19	N15	1.935(16)
Eu2	N17	2.957(6)	Be5	N4	1.731(11)	Be12	N4	1.782(13)	Be20	N5	1.577(12)
Eu2	N6	2.999(8)	Be5	N6	1.732(11)	Be12	N1	1.830(10)	Be20	N17	1.659(15)
Eu2	N13	3.011(4)	Be5	N12	1.795(10)	Be13	N15	1.715(17)	Be20	N17	1.671(12)
Eu2	N16	3.096(8)	Be5	N10	1.846(15)	Be13	N4	1.765(13)	Be21	N13	1.635(15)
Eu3	O1	2.457(7)	Be6	N10	1.749(12)	Be13	N7	1.779(13)	Be21	N16	1.668(12)
Eu3	N2	2.553(7)	Be6	N1	1.768(11)	Be13	N8	1.805(12)	Be21	N10	1.672(14)
Eu3	N15	2.597(7)	Be6	N6	1.785(15)	Be14	N5	1.662(11)	Be22	N3	1.642(13)
Eu3	N3	2.706(4)	Be6	N4	1.815(9)	Be14	N16	1.662(9)	Be22	N15	1.658(12)
Eu3	N7	2.737(8)	Be7	N2	1.710(9)	Be14	N11	1.774(11)	Be22	N9	1.687(11)
Eu3	N5	2.939(5)	Be7	N13	1.722(11)	Be14	N8	1.810(15)			
Eu3	N9	2.951(8)	Be7	N3	1.746(11)	Be15	N11	1.722(17)			
Eu3	N17	3.090(7)	Be7	N1	1.816(16)	Be15	N12	1.791(12)			
Eu3	N6	3.123(8)	Be8	N2	1.673(16)	Be15	N8	1.792(12)			
Eu3	N17	3.174(6)	Be8	N9	1.757(12)	Be15	N4	1.808(11)			

Table A.9. Average bond lengths Be–X (X = N, O) in the BeX_4 tetrahedra and trigonal planar BeN_3 units.

Tetrahedral central atom	Average bond length/ Å	Tetrahedral central atom	Average bond length/ Å
Be1	1.7533	Be12	1.7508
Be2	1.7741	Be13	1.7658
Be3	1.7680	Be14	1.7273
Be4	1.7652	Be15	1.7282
Be5	1.7761	Be16	1.7569
Be6	1.7791	Be17	1.7779
Be7	1.7487	Be18	1.7973
Be8	1.7557	Be19	1.7776
Be9	1.7345	Be20	1.6356
Be10	1.7716	Be21	1.6585
Be11	1.7675	Be22	1.6621

Table A.10. Selected angles between Be atoms and the coordinating N and O atoms in $\text{Eu}_3\text{Be}_{22}\text{N}_{16}\text{O}$ in $^\circ$ with standard deviations in parentheses. Angles between Atoms 2-1-3, respectively

Atom 1	Atom 2	Atom 3	Angle	Atom 1	Atom 2	Atom 3	Angle	Atom 1	Atom 2	Atom 3	Angle
Be1	N16	N1	115.3(6)	Be7	N3	N1	109.5(6)	Be14	N16	N8	107.4(7)
Be1	N16	N9	106.0(6)	Be8	N2	N9	121.2(7)	Be14	N11	N8	103.1(6)
Be1	N16	N14	103.6(6)	Be8	N2	N16	121.3(7)	Be15	N11	N12	106.5(7)
Be1	N1	N9	119.4(6)	Be8	N2	N11	103.3(7)	Be15	N11	N8	106.1(7)
Be1	N1	N14	107.2(7)	Be8	N9	N16	104.0(6)	Be15	N11	N4	120.2(9)
Be1	N9	N14	103.9(6)	Be8	N9	N11	102.6(6)	Be15	N12	N8	118.8(6)
Be2	N17	N9	122.7(7)	Be8	N16	N11	101.2(6)	Be15	N12	N4	103.3(6)
Be2	N17	N11	120.6(7)	Be9	N6	N7	126.5(7)	Be15	N8	N4	103.1(6)
Be2	N17	N12	104.0(6)	Be9	N6	N1	106.5(7)	Be16	N5	N7	122.3(8)
Be2	N9	N11	103.3(6)	Be9	N6	N14	105.1(7)	Be16	N5	N14	120.8(7)
Be2	N9	N12	101.6(7)	Be9	N7	N1	108.8(7)	Be16	N5	N8	103.2(6)
Be2	N11	N12	101.3(6)	Be9	N7	N14	102.3(6)	Be16	N7	N14	101.0(6)
Be3	N16	N14	104.7(6)	Be9	N1	N14	106.5(8)	Be16	N7	N8	102.7(6)
Be3	N16	N12	118.9(7)	Be10	N9	N8	120.0(7)	Be16	N14	N8	104.7(6)
Be3	N16	N8	104.3(7)	Be10	N9	N12	105.9(7)	Be17	N17	N6	125.6(8)
Be3	N14	N12	108.1(6)	Be10	N9	N14	105.2(6)	Be17	N17	N12	104.3(6)
Be3	N14	N8	117.3(6)	Be10	N8	N12	105.0(6)	Be17	N17	N14	118.9(7)
Be3	N12	N8	104.3(6)	Be10	N8	N14	103.7(6)	Be17	N6	N12	102.5(6)
Be4	N6	N10	117.8(6)	Be10	N12	N14	118.2(6)	Be17	N6	N14	100.5(6)
Be4	N6	N15	122.2(7)	Be11	N2	N5	118.9(7)	Be17	N12	N14	101.8(6)
Be4	N6	N4	102.9(7)	Be11	N2	N11	103.8(7)	Be18	N7	N7	105.9(9)
Be4	N10	N15	107.9(6)	Be11	N2	N11	113.1(6)	Be18	N7	N1	104.6(7)
Be4	N10	N4	102.4(6)	Be11	N5	N11	114.9(6)	Be18	N7	N15	122.6(8)
Be4	N15	N4	100.0(6)	Be11	N5	N11	101.7(6)	Be18	N7	N1	103.0(8)
Be5	N4	N6	116.0(6)	Be11	N11	N11	104.1(6)	Be18	N7	N15	106.1(8)
Be5	N4	N12	106.3(6)	Be12	N2	N7	120.9(8)	Be18	N1	N15	113.0(7)
Be5	N4	N10	105.0(6)	Be12	N2	N4	118.3(7)	Be19	O1	O1	96.1(8)
Be5	N6	N12	103.8(6)	Be12	N2	N1	102.9(7)	Be19	O1	N10	118.4(8)
Be5	N6	N10	106.0(6)	Be12	N7	N4	103.4(6)	Be19	O1	N15	115.1(8)
Be5	N12	N10	120.7(8)	Be12	N7	N1	104.6(6)	Be19	O1	N10	117.9(9)
Be6	N10	N1	112.7(6)	Be12	N4	N1	105.2(6)	Be19	O1	N15	117.1(9)
Be6	N10	N6	108.0(6)	Be13	N15	N4	107.2(7)	Be19	N10	N15	94.2(7)
Be6	N10	N4	122.1(6)	Be13	N15	N7	111.8(7)	Be20	N5	N17	125.6(7)
Be6	N1	N6	102.0(6)	Be13	N15	N8	126.2(9)	Be20	N5	N17	126.7(8)
Be6	N1	N4	106.4(6)	Be13	N4	N7	102.4(6)	Be20	N17	N17	106.6(7)
Be6	N6	N4	103.9(7)	Be13	N4	N8	104.3(7)	Be21	N13	N16	118.1(9)
Be7	N2	N13	116.5(6)	Be13	N7	N8	102.6(7)	Be21	N13	N10	122.7(8)
Be7	N2	N3	117.6(6)	Be14	N5	N16	124.1(7)	Be21	N16	N10	119.3(8)
Be7	N2	N1	101.2(7)	Be14	N5	N11	108.3(6)	Be22	N3	N15	121.5(7)
Be7	N13	N3	103.3(5)	Be14	N5	N8	104.5(6)	Be22	N3	N9	117.6(8)
Be7	N13	N1	108.9(6)	Be14	N16	N11	107.8(6)	Be22	N15	N9	121.1(7)

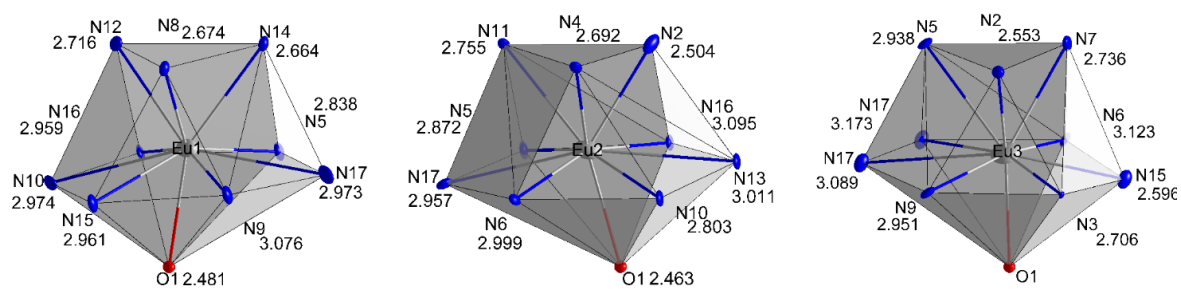


Figure A.2. Coordination polyhedra around Eu1, Eu2 and Eu3 with the Eu–N/O distances in Å.

Magnetization Measurements of $\text{Eu}_3\text{Be}_{22}\text{N}_{16}\text{O}$

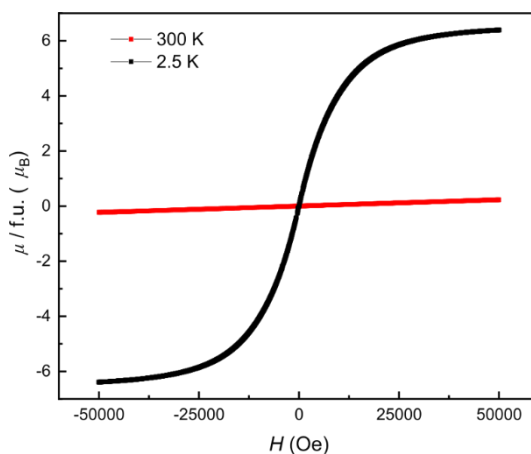


Figure A.3. Magnetization isotherms of $\text{Eu}_3\text{Be}_{22}\text{N}_{16}\text{O}$ at 300 K (red) and 2.5 K (black).

A.2 Author Contributions

E.E. Formal analysis: Lead; Investigation: Lead; Validation: Lead; Writing – original draft: Lead; Writing – review & editing: Lead

M.W. Formal analysis: Supporting; Investigation: Supporting

W.S. Funding acquisition: Lead; Project administration: Lead; Resources: Lead; Supervision: Lead; Writing – original draft: Supporting; Writing – review & editing: Supporting

A.3 References

- [1] Zeuner, M.; Hintze, F.; Schnick, W. Low temperature precursor route for highly efficient spherically shaped LED-phosphors $M_2Si_5N_8:Eu^{2+}$ ($M = Eu, Sr, Ba$). *Chem. Mater.* **2009**, *21*, 336–342.
- [2] Senker, J.; Jacobs, H.; Müller, M.; Press, W.; Müller, P.; Mayer, H.; Ibberson, R. Reorientational dynamics of amide ions in isotopic phases of strontium and calcium amide. 1. Neutron diffraction experiments. *J. Phys. Chem. B* **1998**, *102*, 931–940.
- [3] García-Gutiérrez, R.; Barboza-Flores, M.; Berman-Mendoza, D.; Contreras-López, O. E.; Ramos-Carrasco, A. Synthesis and characterization of highly luminescent beryllium nitride. *Mater. Lett.* **2014**, *132*, 179–181.
- [4] Zeuner, M.; Pagano, S.; Schnick, W. Nitridosilicates and oxonitridosilicates: from ceramic materials to structural and functional diversity. *Angew. Chem. Int. Ed.* **2011**, *50*, 7754–7775; *Angew. Chem.* **2011**, *123*, 7898–7920.
- [5] Strobel, P.; Weiler, V.; Schmidt, P. J.; Schnick, W. $Sr[BeSi_2N_4]:Eu^{2+}/Ce^{3+}$ and $Eu[BeSi_2N_4]:$ Nontypical Luminescence in Highly Condensed Nitridoberyllosilicates. *Chem. Eur. J.* **2018**, *24*, 7243–7249.
- [6] Strobel, P.; Niklaus, R.; Schmidt, P. J.; Schnick, W. Oxoberyllates $SrBeO_2$ and $Sr_{12}Be_{17}O_{29}$ as Novel Host Materials for Eu^{2+} Luminescence. *Chem. Eur. J.* **2018**, *24*, 12678–12685.
- [7] Elzer, E.; Niklaus, R.; Strobel, P. J.; Weiler, V.; Schmidt, P. J.; Schnick, W. $MBe_{20}N_{14}:Eu^{2+}$ ($M = Sr, Ba$) - Highly Condensed Nitridoberyllates with Exceptional Highly Energetic Eu^{2+} Luminescence. *Chem. Mater.* **2019**, *31*, 3174–3182.

B. Supporting Information for Chapter 3

B.1 Results and Discussion

Synthesis and Chemical Analysis

Table B.1. List of chemicals for this work.

Substance	Information	Producer
$M(\text{NH}_2)_2$	$M = \text{Sr, Eu, Ba}$	Synthesized according to literature from metals in supercritical ammonia ^[1,2]
Be	99+%, 325 mesh	ABCR
Be_3N_2		Synthesized from Be in a radio frequency furnace at 1400 °C under N_2 -atmosphere ^[3]
EuF_3	99.95%	Sigma-Aldrich
Sr_2N	99+%	Taiheiyo Cement Corp
Ba_2N	99.7%	Materion

Table B.2. Weighted sample for the reaction leading to single crystals of $M\text{Be}_{20}\text{N}_{14}:\text{Eu}^{2+}$ ($M = \text{Sr, Ba}$) and $\text{EuBe}_{20}\text{N}_{14}$, synthesized in an rf furnace.

Substance	$M = \text{Sr}$	$\text{EuBe}_{20}\text{N}_{14}$	$M = \text{Ba}$
$M(\text{NH}_2)_2$	18.7 mg (0.156 mmol)	26.5 mg (0.144 mmol)	26.4 mg (0.156 mmol)
Be_3N_2	10.7 mg (0.195 mmol)	9.9 mg (0.180 mmol)	10.7 mg (0.195 mmol)
EuF_3	ca. 2 mol% of M	-	ca. 2 mol% of M

Table B.3. Temperature program of the rf furnace for the reaction leading to $M\text{Be}_{20}\text{N}_{14}:\text{Eu}^{2+}$ ($M = \text{Sr, Ba}$) and $\text{EuBe}_{20}\text{N}_{14}$.

Step	Temperature range	t/ h		
		$M = \text{Sr}$	$M = \text{Eu}$	$M = \text{Ba}$
1	RT \rightarrow 1400 °C	1	0.75	0.5
2	1400 \rightarrow 1400 °C	1	1	1
3	1400 \rightarrow 500 °C	1	1	0.5

Table B.4. Weighted sample for the reaction leading to the bulk samples of $M\text{Be}_{20}\text{N}_{14}:\text{Eu}^{2+}$ ($M = \text{Sr, Ba}$), synthesized in a hot isostatic press.

Substance	$M = \text{Sr}$	$M = \text{Ba}$
$M_2\text{N}$	28.4 mg (0.150 mmol)	43.3 mg (0.150 mmol)
Be_3N_2	88.1 mg (1.600 mmol)	88.1 mg (1.600 mmol)
EuF_3	ca. 2 mol% of M	ca. 2 mol% of M

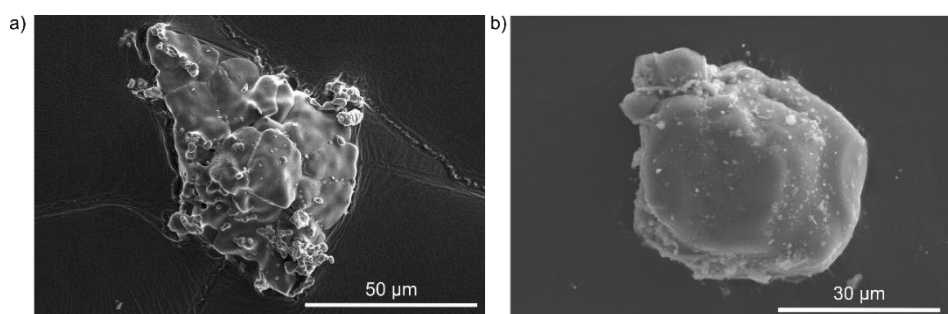


Figure B.1. SEM image of a) $\text{SrBe}_{20}\text{N}_{14}:\text{Eu}^{2+}$ and b) $\text{BaBe}_{20}\text{N}_{14}:\text{Eu}^{2+}$.

Table B.5. EDX results of $M\text{Be}_{20}\text{N}_{14}$ ($M = \text{Sr}, \text{Ba}, \text{Eu}$) with standard deviations in parentheses.

	Theoretical atom %	Experimental atom %		
	$M\text{Be}_{20}\text{N}_{14}$	$M = \text{Sr}$	$M = \text{Eu}$	$M = \text{Ba}$
M	7	8(1)	9(1)	15(1)
N	93	92(1)	91(1)	85(1)

FTIR

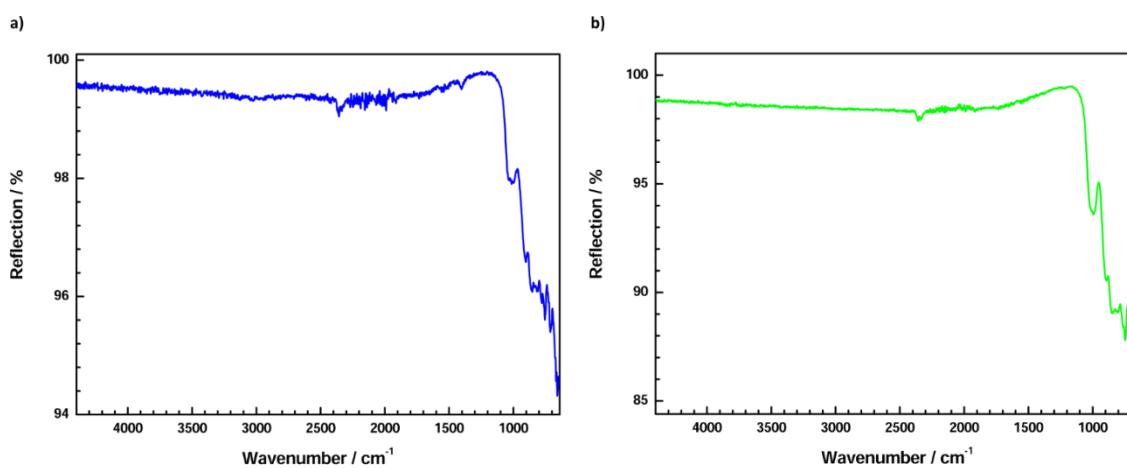


Figure B.2. FTIR-spectra of a) $\text{SrBe}_{20}\text{N}_{14}:\text{Eu}^{2+}$ and b) $\text{BaBe}_{20}\text{N}_{14}:\text{Eu}^{2+}$ powder sample. Bands at 2345 cm^{-1} belong to the asymmetric stretching vibration of CO_2 . No O–H and N–H bands are observed in the typical region.

Crystallographic Data for $M\text{Be}_{20}\text{N}_{14}$ **Table B.6.** Atomic coordinates and equivalent isotropic displacement parameters (U_{eq}) of $\text{SrBe}_{20}\text{N}_{14}:\text{Eu}^{2+}$ with standard deviations in parentheses.

Atom	Wyckoff	x	y	z	$U_{\text{eq}}/\text{\AA}^3$	sof
Sr1	$2a$	0	0	0	0.01053(11)	1
Be1	$16i$	0.0896(3)	0.2264(3)	0.23392(14)	0.0082(3)	1
Be2	$16i$	0.1353(3)	0.1943(2)	0.41450(13)	0.0080(3)	1
Be3	$8g$	0	1/2	0.0924(2)	0.0076(4)	1
N1	$16i$	0.2985(2)	0.1170(2)	0.16725(8)	0.0056(2)	1
N2	$8h$	0.2053(2)	0.4400(2)	0	0.0051(3)	1
N3	$4e$	0	0	0.3296(2)	0.0059(4)	1

Table B.7. Anisotropic displacement parameters for $\text{SrBe}_{20}\text{N}_{14}:\text{Eu}^{2+}$ with standard deviations in parentheses.

Atom	$U_{11}/\text{\AA}^2$	$U_{22}/\text{\AA}^2$	$U_{33}/\text{\AA}^2$	$U_{23}/\text{\AA}^2$	$U_{13}/\text{\AA}^2$	$U_{12}/\text{\AA}^2$
Sr1	0.01184(13)	0.01184(13)	0.0080(2)	0	0	0
Be1	0.0066(7)	0.0093(7)	0.0088(7)	0.0011(5)	-0.0007(5)	-0.0007(6)
Be2	0.0077(7)	0.0070(7)	0.0094(8)	0.0010(5)	0.0000(5)	0.0008(5)
Be3	0.0069(10)	0.0069(10)	0.009(1)	0.0009(8)	0	0
N1	0.0055(4)	0.0055(4)	0.0057(4)	-0.0006(3)	0.0011(3)	-0.0002(4)
N2	0.0055(6)	0.0045(6)	0.0055(6)	0.0000(4)	0	0
N3	0.0056(5)	0.0056(5)	0.0066(9)	0	0	0

Table B.8. Atomic coordinates and equivalent isotropic displacement parameters (U_{eq}) of $\text{EuBe}_{20}\text{N}_{14}$ with standard deviations in parentheses.

Atom	Wyckoff	x	y	z	$U_{\text{eq}}/\text{\AA}^3$	sof
Eu1	$2a$	0	0	0	0.01249(5)	1
Be1	$16i$	0.2255(2)	0.0898(2)	0.23377(11)	0.0075(2)	1
Be2	$16i$	0.1944(2)	0.1355(2)	0.41455(11)	0.0075(2)	1
Be3	$8g$	0	1/2	0.0928(2)	0.0063(3)	1
N1	$16i$	0.11687(12)	0.29865(12)	-0.16767(7)	0.00469(13)	1
N2	$8h$	0.2049(2)	0.56044(18)	0	0.0045(2)	1
N3	$4e$	0	0	0.32934(14)	0.0051(3)	1

Table B.9. Anisotropic displacement parameters for $\text{EuBe}_{20}\text{N}_{14}$ with standard deviations in parentheses.

Atom	$U_{11}/\text{\AA}^2$	$U_{22}/\text{\AA}^2$	$U_{33}/\text{\AA}^2$	$U_{23}/\text{\AA}^2$	$U_{13}/\text{\AA}^2$	$U_{12}/\text{\AA}^2$
Eu1	0.01386(6)	0.01386(6)	0.00975(7)	0	0	0
Be1	0.0088(5)	0.0060(5)	0.0078(5)	0.0002(4)	-0.0007(4)	-0.0014(4)
Be2	0.0073(5)	0.0081(5)	0.0071(5)	0.0006(4)	0.0017(4)	0.0003(4)
Be3	0.0056(7)	0.0065(7)	0.0067(7)	0.0006(6)	0	0
N1	0.0038(3)	0.0044(3)	0.0059(3)	-0.0002(2)	-0.0002(2)	-0.0010(2)
N2	0.0039(4)	0.0053(4)	0.0042(4)	-0.0002(3)	0	0
N3	0.0051(4)	0.0051(4)	0.0052(6)	0	0	0

Table B.10. Atomic coordinates and equivalent isotropic displacement parameters (U_{eq}) of $\text{BaBe}_{20}\text{N}_{14}:\text{Eu}^{2+}$ with standard deviations in parentheses.

Atom	Wyckoff	x	y	z	$U_{\text{eq}}/\text{\AA}^3$	sof
Ba1	$2a$	0	0	0	0.00886(8)	1
Be1	$16i$	0.2262(4)	0.0895(3)	0.2341(2)	0.0110(4)	1
Be2	$16i$	0.1939(3)	0.1340(3)	0.4143(2)	0.0092(3)	1
Be3	$8g$	0	1/2	0.0924(3)	0.0101(5)	1
N1	$16i$	0.1167(2)	0.3025(2)	0.16966(11)	0.0047(2)	1
N2	$8h$	0.2053(3)	0.5611(3)	0	0.0057(3)	1
N3	$4e$	0	0	0.3298(2)	0.0071(4)	1

Table B.11. Anisotropic displacement parameters for $\text{BaBe}_{20}\text{N}_{14}:\text{Eu}^{2+}$ with standard deviations in parentheses.

Atom	$U_{11}/\text{\AA}^2$	$U_{22}/\text{\AA}^2$	$U_{33}/\text{\AA}^2$	$U_{23}/\text{\AA}^2$	$U_{13}/\text{\AA}^2$	$U_{12}/\text{\AA}^2$
Ba1	0.00914(9)	0.00914(9)	0.00829(13)	0	0	0
N1	0.0031(4)	0.0051(5)	0.0059(5)	-0.0014(3)	-0.0005(4)	0.0026(4)
N2	0.0052(7)	0.0070(7)	0.0048(7)	-0.0005(5)	0	0
N3	0.0067(6)	0.0067(6)	0.0078(11)	0	0	0
Be1	0.0134(9)	0.0088(8)	0.0107(9)	0.0018(7)	-0.0018(7)	-0.0004(7)
Be2	0.0086(8)	0.0093(8)	0.0095(9)	0.0001(6)	0.0011(7)	0.0008(7)
Be3	0.0077(11)	0.0104(12)	0.0124(13)	0.0022(9)	0	0

MAPLE calculations

Table B.12. Results of MAPLE Calculations (all values in kJ/mol) for SrBe₂₀N₁₄:Eu²⁺. Partial MAPLE values, total MAPLE values and deviation (Δ) to sums of total MAPLE values of binary/ternary ionic compounds, forming SrBe₂₀N₁₄ in a hypothetical reaction.^a

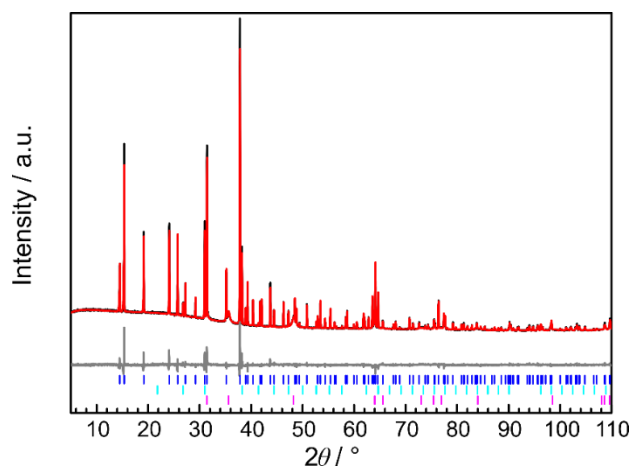
SrBe ₂₀ N ₁₄ :Eu ²⁺								$\Delta = 0.09\%$
Sr1 ²⁺	Be1 ²⁺	Be2 ²⁺	Be3 ²⁺	N1 ^{[3]3-}	N2 ^{[3]3-}	N3 ^{[3]3-}	total MAPLE	
1656	2769	2698	2796	5703	5817	5746	137024	
Hypothetical reaction: 0.5 SrBe ₂ N ₂ ^[4] + 6 α -Be ₃ N ₂ ^[5] = 0.5·19876 kJ/mol + 6·35792 kJ/mol = 137154 kJ/mol								

^aTypical MAPLE values (in kJ/mol): Sr²⁺: 1500–2100; Be²⁺: 2759–2947; N^{[3]3-}: 5000–6200.^[6,7]

Partial MAPLE values were calculated for each site and compared to typical (empirical) partial MAPLE values.^[6] The values for N atoms as well as for Be and Sr atoms (Table B.12) are in the reported typical ranges (Table B.12).^[6] Total MAPLE values for the whole crystal structures were compared to the sum of total MAPLE values of SrBe₂N₂ and α -Be₃N₂, forming SrBe₂₀N₁₄ in a hypothetical reaction (Table B.12). These total MAPLE values must be equal or within a deviation of < 1%.^[6] SrBe₂₀N₁₄ shows a small deviation of 0.09% therefore supporting the crystal structure model refined from single-crystal X-ray data.

Rietveld Refinement of $M\text{Be}_{20}\text{N}_{14}$ **Table B.13.** Data of Rietveld refinements for $M\text{Be}_{20}\text{N}_{14}\text{Eu}^{2+}$ ($M = \text{Sr}, \text{Ba}$) with least squares standard deviations in parentheses. Only lattice parameters were refined.

formula	$M = \text{Sr}$	$M = \text{Ba}$
Formula mass / $\text{g}\cdot\text{mol}^{-1}$	463.96	513.68
Crystal system	tetragonal	
Space group	$I4/m$ (no. 87)	
Lattice parameters / Å	$a = 6.5253(4), c = 12.1363(1)$	$a = 6.54124(3), c = 12.2206(1)$
Volume / Å^3	516.753(6)	522.891(7)
Z	2	
X-ray density / $\text{g}\cdot\text{cm}^{-3}$	2.9818(1)	3.26248(4)
Diffractometer	Stoe StadiP	
Radiation	Cu-K α 1 ($\lambda = 1.54056 \text{ Å}$)	
Monochromator	Ge(111)	
Detector	MYTHEN 1K	
F(000)	432	468
2θ -range / $^\circ$	5–110	
Data points	7035	7035
Number of observed reflections	177	179
Number of parameters	34	34
Constraints	0	0
Program used	TOPAS Academic V6	
Structure refinement	Rietveld-Method	
Background function	Shifted Chebyshev (12 polynomials)	
R_{wp}	5.066	5.255
R_{exp}	2.123	2.336
R_{p}	3.734	3.514
R_{Bragg}	2.615	3.649
χ^2	2.386	2.249

**Figure B.3.** Rietveld refinement of $\text{BaBe}_{20}\text{N}_{14}$ (Cu K α 1 = 1.54056 Å). Experimental data (black line), calculated pattern (red line) and difference curve (gray line). Tick marks: position of Bragg reflections of $\text{BaBe}_{20}\text{N}_{14}$ (blue), Be_3N_2 (cyan) and WC (magenta).

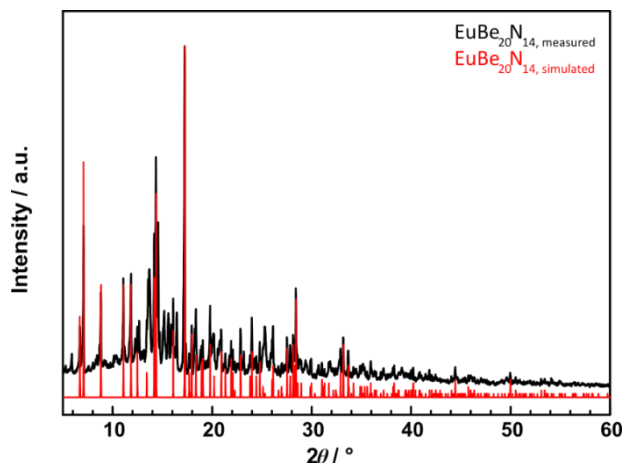


Figure B.4. Powder diffraction data of $\text{EuBe}_{20}\text{N}_{14}$ ($\text{Mo K}\alpha = 0.71073 \text{ \AA}$). Experimental data (black line), calculated pattern (red line). $\text{EuBe}_{20}\text{N}_{14}$ was obtained as part of a product with a yet not further identified side phase.

Structure Description

Table B.14. Selected atomic distances in $M\text{Be}_{20}\text{N}_{14}$ ($M = \text{Sr, Eu, Ba}$) in \AA with standard deviations in parentheses.

	$M = \text{Sr}$	$M = \text{Eu}$	$M = \text{Ba}$
$M1\text{-N}1$	2.9143(12)	2.9186(9)	2.965(3)
$M1\text{-N}2$	3.168(2)	3.1639(12)	3.169(4)
$\text{Be}1\text{-N}1$	1.641(2)	1.640(2)	1.639(3)
$\text{Be}1\text{-N}1$	1.737(2)	1.733(2)	1.714(3)
$\text{Be}1\text{-N}1$	1.739(3)	1.738(2)	1.754(3)
$\text{Be}1\text{-N}3$	1.968(3)	1.963(2)	1.975(4)
$\text{Be}2\text{-N}1$	1.640(2)	1.643(2)	1.661(3)
$\text{Be}2\text{-N}2$	1.710(2)	1.710(2)	1.720(3)
$\text{Be}2\text{-N}2$	1.770(2)	1.773(2)	1.778(3)
$\text{Be}2\text{-N}3$	1.857(2)	1.860(2)	1.855(3)
$\text{Be}3\text{-N}1$	1.772(2)	1.771(2)	1.773(3)
$\text{Be}3\text{-N}2$	1.790(2)	1.7909(14)	1.799(4)

UV-vis Spectroscopy

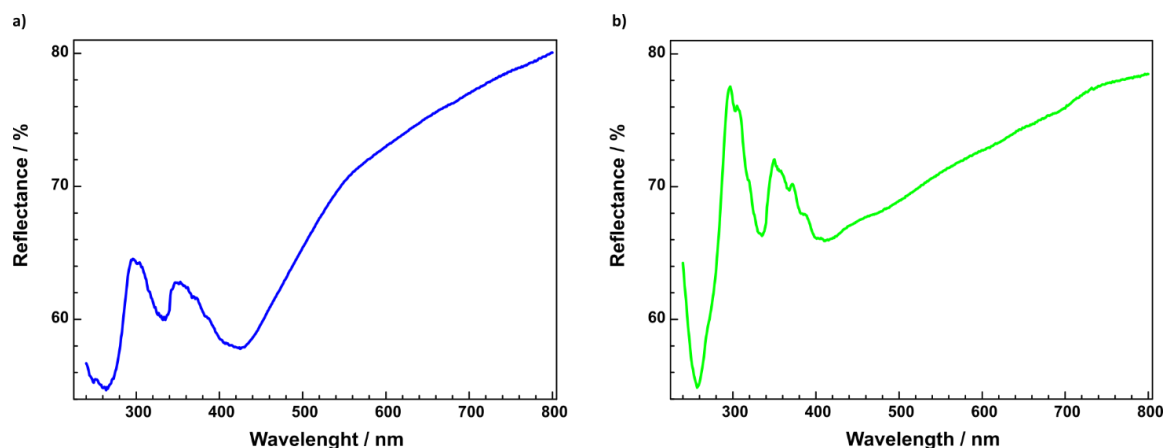


Figure B.5. Diffuse reflectance UV-Vis spectra of a) $\text{SrBe}_{20}\text{N}_{14}:\text{Eu}^{2+}$ and b) $\text{BaBe}_{20}\text{N}_{14}:\text{Eu}^{2+}$. The artifacts around 340 nm correspond to the lamp-switch.

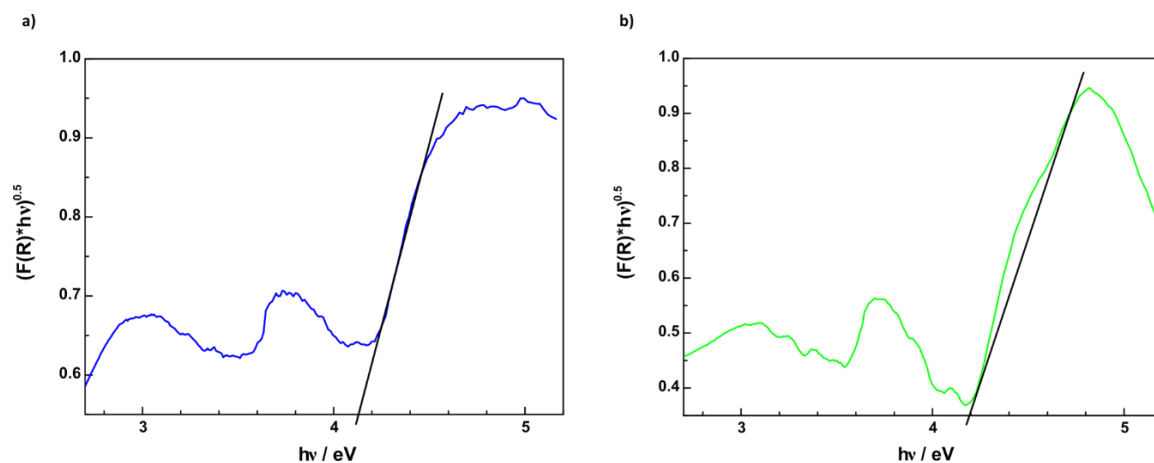


Figure B.6. Tauc plots for a) $\text{SrBe}_{20}\text{N}_{14}:\text{Eu}^{2+}$ and b) $\text{BaBe}_{20}\text{N}_{14}:\text{Eu}^{2+}$, tangents at the inflection points (black).

Electronic Properties

Table B.15. Calculated elastic constants C_{nm} , bulk (B), shear (G) and Young's (Y) moduli in GPa, Debye temperature (θ_D) in K and Poisson's ratio (ν) for $\alpha\text{-Be}_3\text{N}_2$. Bulk and shear moduli according to the Voigt (B_V , G_V); Reuss (B_R , G_R) and Voigt-Reuss-Hill (B_{VRH} , G_{VRH}) approach. C_{nm} obtained from C_{ijkl} according to the Voigt notation $xx \rightarrow 1$, $yy \rightarrow 2$, $zz \rightarrow 3$, $yz \rightarrow 4$, $zx \rightarrow 5$, $xy \rightarrow 6$.^[8]

Elastic Moduli		Elastic Constants	
B_V	215.0	C_{11}	438.9
B_R	215.0	C_{22}	438.9
B_{VRH}	215.0	C_{33}	438.9
G_V	187.0	C_{44}	196.6
G_R	185.6	C_{55}	196.6
G_{VRH}	186.3	C_{66}	196.6
Y_{VRH}	433.6	C_{12}	103.0
ν	0.16	C_{13}	103.0
θ_D	1438.2	C_{23}	103.0

Luminescence

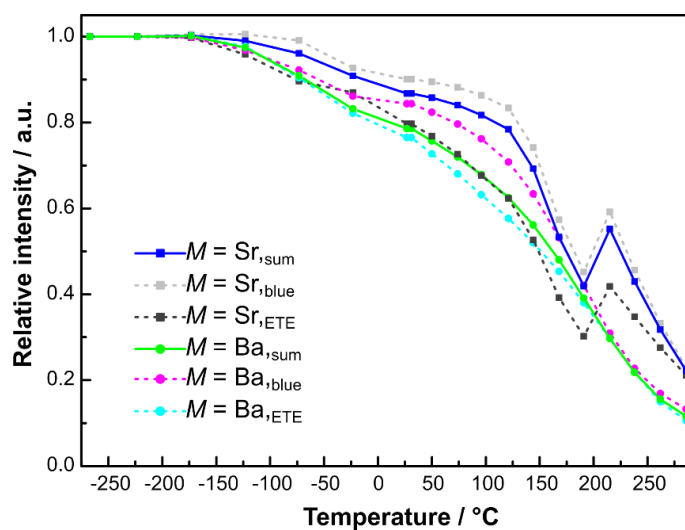


Figure B.7. Thermal quenching data for $M\text{Be}_{20}\text{N}_{14}:\text{Eu}^{2+}$ ($M = \text{Sr}, \text{Ba}$). The thermal quenching was analyzed for the entire spectrum (line: blue for $M = \text{Sr}$ and green for $M = \text{Ba}$), as well as the two emission maxima (blue = 410–480 nm; ETE = 480–700 nm) separately from each other (dashed lines: black and gray for $M = \text{Sr}$ and cyan and magenta for $M = \text{Ba}$).

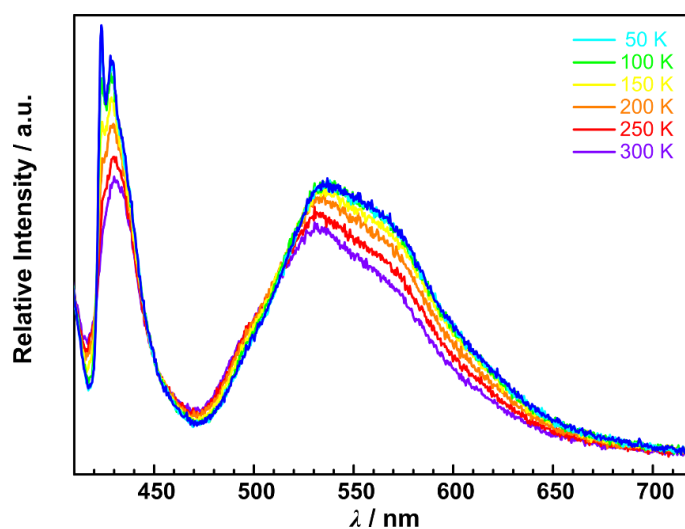


Figure B.8. Photoluminescence spectrum of a powder sample of $\text{BaBe}_{20}\text{N}_{14}:\text{Eu}^{2+}$ ($\lambda_{\text{exc}} = 380 \text{ nm}$) at different temperatures from 6–300 K.

B.2 References

- [1] Zeuner, M.; Hintze, F.; Schnick, W. Low temperature precursor route for highly efficient spherically shaped LED-phosphors $M_2Si_5N_8:Eu^{2+}$ ($M = Eu, Sr, Ba$). *Chem. Mater.* **2009**, *21*, 336–342.
- [2] Senker, J.; Jacobs, H.; Müller, M.; Press, W.; Müller, P.; Mayer, H.; Ibberson, R. Reorientational dynamics of amide ions in isotopic phases of strontium and calcium amide. 1. Neutron diffraction experiments. *J. Phys. Chem. B* **1998**, *102*, 931–940.
- [3] García-Gutiérrez, R.; Barboza-Flores, M.; Berman-Mendoza, D.; Contreras-López, O. E.; Ramos-Carrasco, A. Synthesis and characterization of highly luminescent beryllium nitride. *Mater. Lett.* **2014**, *132*, 179–181.
- [4] Somer, M.; Yarasik, A.; Akselrud, L.; Leoni, S.; Rosner, H.; Schnelle, W.; Kniep, R. $Ae[Be_2N_2]$: nitridoberyllates of the heavier alkaline-earth metals. *Angew. Chem. Int. Ed.* **2004**, *43*, 1088–1092; *Angew. Chem.* **2004**, *116*, 1108–1112.
- [5] Stackelberg, M. v.; Paulus, R. Untersuchungen über die Kristallstruktur der Nitride und Phosphide zweiwertiger Metalle. *Z. Phys. Chem.* **1933**, *22*, 305–322.
- [6] Zeuner, M.; Pagano, S.; Schnick, W. Nitridosilicates and oxonitridosilicates: from ceramic materials to structural and functional diversity. *Angew. Chem. Int. Ed.* **2011**, *50*, 7754–7775; *Angew. Chem.* **2011**, *123*, 7898–7920.
- [7] Strobel, P.; Niklaus, R.; Schmidt, P. J.; Schnick, W. Oxoberyllates $SrBeO_2$ and $Sr_{12}Be_{17}O_{29}$ as Novel Host Materials for Eu^{2+} Luminescence. *Chem. Eur. J.* **2018**, *24*, 12678–12685.
- [8] Ashcroft, N. W.; Mermin, N. D., *Solid State Physics*. Saunders college Philadelphia, **1976**.

C. Supporting Information for Chapter 4

C.1 Results and Discussion

Synthesis and Chemical Analysis

Table C.1. List of chemicals for this work.

Substance	Information	Producer
Eu(NH ₂) ₂		Synthesized according to literature from metals in supercritical ammonia ^[1, 2]
Be	99%, pieces	ABCR
Be ₃ N ₂		Synthesized from Be in a radio frequency furnace at 1400 °C under N ₂ atmosphere ^[3]
EuF ₃	99.95%	Sigma-Aldrich
Sr ₂ N	99+%	Taiheiyo Cement Corp
AlN	Grade A	ABCR

Table C.2. Weighted sample for the reaction leading to the bulk samples Sr₂[BeAl₃N₅]:Eu²⁺, synthesized in a hot isostatic press.

Substance	
Sr ₂ N	189.25 mg (1.000 mmol)
Be ₃ N ₂	18.35 mg (0.333 mmol)
AlN	122.96 mg (3.000 mmol)
EuF ₃ / Eu(NH ₂) ₂	<i>x</i> mol-% referred to Sr (according to the desired doping grade)

Table C.3. EDX results of Sr₂[BeAl₃N₅]:Eu²⁺ with standard deviations in parentheses.

elements	calculated atom-%	measured atom-%
N	50	50(3)
Al	30	31(3)
Sr	20	19(1)

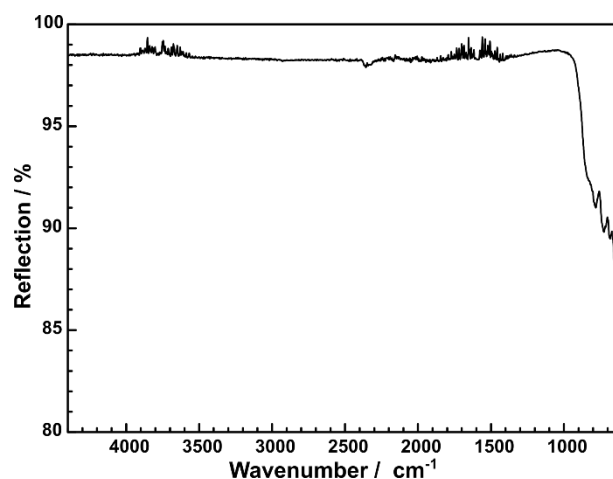


Figure C.1. FTIR spectrum of $\text{Sr}_2[\text{BeAl}_3\text{N}_5]:\text{Eu}^{2+}$. Bands at 2345 cm^{-1} belong to the asymmetric stretching vibration of CO_2 . No O–H and N–H bands are observed in the typical region.

Crystal Structure Determination

Table C.4. Wyckoff positions, Atomic coordinates, equivalent isotropic displacement parameters (U_{eq}) and site occupation factors (sof) of $\text{Sr}_2[\text{BeAl}_3\text{N}_5]:\text{Eu}^{2+}$ with standard deviations in parentheses.

Atom	Wyckoff	x	y	z	$U_{\text{eq}}/\text{\AA}^3$	sof
Sr1	$2i$	0.00422(4)	0.50057(3)	0.22359(3)	0.00894(4)	1
Sr2	$1a$	0	0	0	0.01437(6)	1
Sr3	$1f$	$\frac{1}{2}$	0	$\frac{1}{2}$	0.01751(6)	1
Al1	$2i$	0.01550(11)	0.15913(9)	0.44542(9)	0.00616(10)	1
Al2	$2i$	0.57348(11)	0.69898(9)	0.10634(9)	0.00647(10)	1
Al3	$2i$	0.53989(11)	0.42013(9)	0.35670(9)	0.00620(10)	1
N1	$2i$	0.2939(3)	0.3141(3)	0.4330(2)	0.0079(3)	1
N2	$2i$	0.3835(3)	0.4393(2)	0.1111(2)	0.0076(3)	1
N3	$2i$	0.3629(3)	0.8590(3)	0.0483(2)	0.0081(3)	1
N4	$2i$	0.0928(3)	0.1330(2)	0.6953(2)	0.0077(3)	1
N5	$2i$	0.7495(3)	0.2617(2)	0.3711(2)	0.0075(2)	1
Be1	$2i$	0.5929(5)	0.0959(4)	0.1447(4)	0.0091(4)	1

Table C.5. Anisotropic displacement parameters for $\text{Sr}_2[\text{BeAl}_3\text{N}_5]:\text{Eu}^{2+}$ with standard deviations in parentheses.

Atom	$U_{11}/\text{\AA}^2$	$U_{22}/\text{\AA}^2$	$U_{33}/\text{\AA}^2$	$U_{12}/\text{\AA}^2$	$U_{13}/\text{\AA}^2$	$U_{23}/\text{\AA}^2$
Sr1	0.00843(8)	0.00871(7)	0.00889(7)	0.00381(6)	0.00297(6)	0.00263(6)
Sr2	0.01151(12)	0.01739(13)	0.01825(13)	0.00949(10)	0.00823(10)	0.00598(10)
Sr3	0.01552(13)	0.01306(13)	0.03371(18)	0.00751(10)	0.01616(13)	0.01414(12)
Al1	0.0059(2)	0.0060(2)	0.0066(2)	0.00225(19)	0.00278(19)	0.00208(19)
Al2	0.0062(2)	0.0062(2)	0.0066(2)	0.00253(19)	0.00248(19)	0.00197(19)
Al3	0.0061(2)	0.0066(2)	0.0060(2)	0.00245(19)	0.00282(19)	0.00202(18)
N1	0.0073(6)	0.0077(6)	0.0090(6)	0.0021(5)	0.0048(5)	0.0020(5)
N2	0.0083(6)	0.0071(6)	0.0069(6)	0.0021(5)	0.0035(5)	0.0024(5)
N3	0.0073(6)	0.0080(6)	0.0088(6)	0.0033(5)	0.0034(5)	0.0027(5)
N4	0.0077(6)	0.0071(6)	0.0062(6)	0.0015(5)	0.0017(5)	0.0023(5)
N5	0.0070(6)	0.0073(6)	0.0075(6)	0.0032(5)	0.0027(5)	0.0017(5)
Be1	0.0081(10)	0.0083(10)	0.0093(10)	0.0035(8)	0.0029(8)	0.0015(8)

MAPLE calculations

Table C.6. Results of MAPLE Calculations (all values in kJ/mol) for $\text{Sr}_2[\text{BeAl}_3\text{N}_5]:\text{Eu}^{2+}$. Partial MAPLE values, total MAPLE values and deviation (Δ) to sums of total MAPLE values of binary/ternary ionic compounds, forming $\text{Sr}_2[\text{BeAl}_3\text{N}_5]:\text{Eu}^{2+}$ in a hypothetical reaction.^a

	$\text{Sr}_2[\text{BeAl}_3\text{N}_5]:\text{Eu}^{2+}$	$\text{SrBe}_{20}\text{N}_{14}$	$\alpha\text{-Be}_3\text{N}_2$ ^[4]	AlN
Sr^{2+}	1667–1796	1656	-	-
Be^{2+}	2874	2697–2795	2726	-
Al^{3+}	5415–5553	-	-	5499
N^{3-}	5000–5175	5702–5817	5796–5990	5499
Total	48170	137024	19876	11004
Δ	[1] 1%			
Total MAPLE:	[1] $2 \text{SrBe}_{20}\text{N}_{14} - 13 \alpha\text{-Be}_3\text{N}_2 + 3 \text{AlN} = 48667 \text{ kJ/mol}$			

^aTypical MAPLE values (in kJ/mol): Sr^{2+} : 1500–2100; Be^{2+} : 2759–2947; $\text{N}^{[3]3-}$: 5000–6200^[5, 6]

Partial MAPLE values were calculated for each site and compared to typical (empirical) partial MAPLE values.^[5] The values for all atoms (Table C.6) are in the reported typical ranges (Table C.6).^[5] Total MAPLE values for the entire crystal structures were compared with the sum of total MAPLE values of $\text{SrBe}_{20}\text{N}_{14}$ and $\alpha\text{-Be}_3\text{N}_2$, forming $\text{Sr}_2[\text{BeAl}_3\text{N}_5]:\text{Eu}^{2+}$ in a hypothetical reaction (Table C.6). These total MAPLE values must be equal or within a deviation of $< 1\%$.^[5] $\text{Sr}_2[\text{BeAl}_3\text{N}_5]:\text{Eu}^{2+}$ shows a deviation of 1%, which can be ascribed to the changed coordination of Be and N in $\text{Sr}_2[\text{BeAl}_3\text{N}_5]:\text{Eu}^{2+}$ (trigonal coordinated Be and $\text{N}^{[3]}$) compared to the binary and ternary nitrides AlN, $\alpha\text{-Be}_3\text{N}_2$ and $\text{SrBe}_{20}\text{N}_{14}$ (tetrahedral coordinated Be and N)^[4]. This leads to an increased deviation, as already discussed in literature.^[7, 8]

Crystal Structure Description.

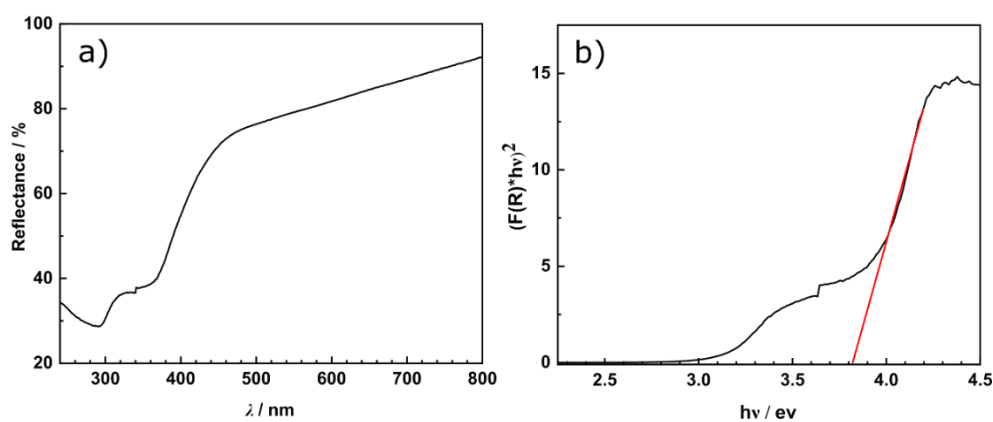
Table C.7. Selected atomic distances in Sr₂[BeAl₃N₅]:Eu²⁺ in Å with standard deviations in parentheses.

Atom 1	Atom 2	distance/ Å	Atom 1	Atom 2	distance/ Å
Sr1	N3	2.682(2)	Al1	N1	1.821(2)
Sr1	N1	2.700(3)	Al1	N5	1.862(2)
Sr1	N5	2.733(3)	Al1	N4	1.899(2)
Sr1	N4	2.762(2)	Al1	N4	1.912(2)
Sr1	N5	2.839(3)	Al2	N3	1.883(3)
Sr1	N2	2.853(3)	Al2	N4	1.884(2)
Sr1	N2	2.971(2)	Al2	N2	1.915(2)
Sr2	N3	2.553(3)	Al2	N2	1.922(2)
Sr2	N4	2.943(3)	Al3	N2	1.848(2)
Sr2	N2	3.069(2)	Al3	N5	1.863(2)
Sr2	N1	3.142(3)	Al3	N1	1.863(2)
Sr3	N5	2.699(2)	Al3	N1	1.926(2)
Sr3	N1	2.822(3)	Be1	N5	1.647(3)
Sr3	N4	3.109(2)	Be1	N3	1.672(3)
Sr3	N3	3.186(3)	Be1	N3	1.719(4)

Table C.8. Data of Rietveld refinement for $\text{Sr}_2[\text{BeAl}_3\text{N}_5]:\text{Eu}^{2+}$ with least squares standard deviations in parentheses. Only lattice parameters were refined.

formula	$\text{Sr}_2\text{BeAl}_3\text{N}_5:\text{Eu}^{2+}$
Formula mass/ $\text{g}\cdot\text{mol}^{-1}$	335.24
Crystal system	triclinic
Space group	$P\bar{1}$ (no. 2)
Lattice parameters/ $\text{\AA}, ^\circ$	$a = 6.0745(2)$
Volume/ \AA^3	281.73(0)
Z	2
X-ray density/ $\text{g}\cdot\text{cm}^{-3}$	4.01559
Diffractometer	Stoe StadiP
Radiation	Cu-K α 1 ($\lambda = 1.54056 \text{\AA}$)
Monochromator	Ge(111)
Detector	MYTHEN 1K
F(000)	308
2θ -range/ $^\circ$	5–110
Data points	7035
Number of observed reflections	729
Number of parameters	92
Constraints	0
Program used	TOPAS Academic V6
Structure refinement	Rietveld-Method
Background function	Shifted Chebyshev (12 polynomials)
R_{wp}	0.06178
R_{exp}	0.02289
R_{p}	0.04321
R_{Bragg}	0.02764
χ^2	2.699

UV-vis Spectroscopy

**Figure C.2.** a) Diffuse reflectance UV-Vis spectra of $\text{Sr}_2[\text{BeAl}_3\text{N}_5]$. The artifacts around 340 nm correspond to the lamp-switch. b) Tauc plot of $\text{Sr}_2[\text{BeAl}_3\text{N}_5]$, tangent at the inflection points (red).

Luminescence

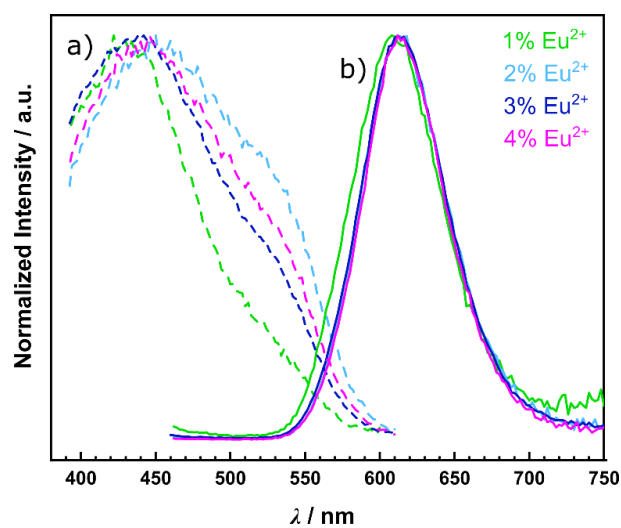


Figure C.3. Normalized photoluminescence spectra of single crystals from samples with 1 mol-% (green), 2 mol-% (light blue), 3 mol-% (dark blue) and 4 mol-% (magenta) Eu^{2+} concentration referred to Sr. a) Excitation spectra ($\lambda_{\text{obs}} = 628 \text{ nm}$); b) Emission spectra ($\lambda_{\text{exc}} = 440 \text{ nm}$).

Table C.9. Emission maximum and fwhm of samples with different Eu^{2+} concentration.

x mol-% Eu^{2+}	$\lambda_{\text{em}} / \text{nm}$	fwhm/ nm	fwhm/ cm^{-1}
1	608	73	1966
2	612	69	1827
3	612	69	1827
4	612	65	1715

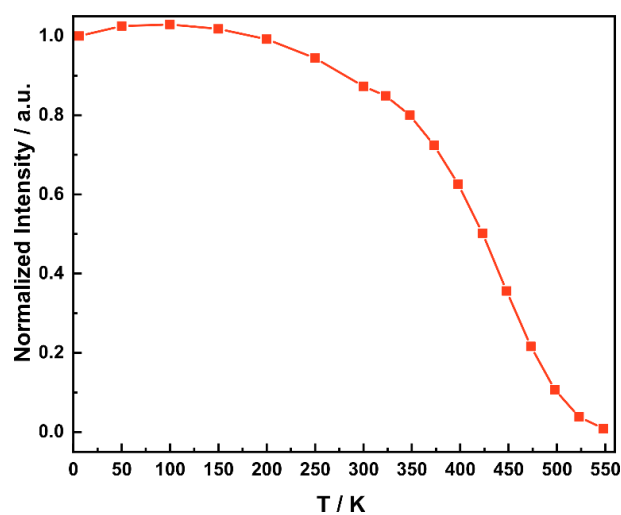


Figure C.4. Temperature dependence of the relative integrated photoluminescence intensity for $\text{Sr}_2[\text{BeAl}_3\text{N}_5]:\text{Eu}^{2+}$ (6–550 K).

C.2 References

- [1] Zeuner, M.; Hintze, F.; Schnick, W. Low temperature precursor route for highly efficient spherically shaped LED-phosphors $M_2Si_5N_8:Eu^{2+}$ ($M = Eu, Sr, Ba$). *Chem. Mater.* **2009**, *21*, 336–342.
- [2] Senker, J.; Jacobs, H.; Müller, M.; Press, W.; Müller, P.; Mayer, H.; Ibberson, R. Reorientational dynamics of amide ions in isotypic phases of strontium and calcium amide. 1. Neutron diffraction experiments. *J. Phys. Chem. B* **1998**, *102*, 931–940.
- [3] García-Gutiérrez, R.; Barboza-Flores, M.; Berman-Mendoza, D.; Contreras-López, O. E.; Ramos-Carrasco, A. Synthesis and characterization of highly luminescent beryllium nitride. *Mater. Lett.* **2014**, *132*, 179–181.
- [4] Stackelberg, M. v.; Paulus, R. Untersuchungen über die Kristallstruktur der Nitride und Phosphide zweiwertiger Metalle. *Z. Phys. Chem.* **1933**, *22*, 305–322.
- [5] Zeuner, M.; Pagano, S.; Schnick, W. Nitridosilicates and oxonitridosilicates: from ceramic materials to structural and functional diversity. *Angew. Chem. Int. Ed.* **2011**, *50*, 7754–7775; *Angew. Chem.* **2011**, *123*, 7898–7920.
- [6] Strobel, P.; Niklaus, R.; Schmidt, P. J.; Schnick, W. Oxoberyllates $SrBeO_2$ and $Sr_{12}Be_{17}O_{29}$ as Novel Host Materials for Eu^{2+} Luminescence. *Chem. Eur. J.* **2018**, *24*, 12678–12685.
- [7] Strobel, P.; Weiler, V.; Schmidt, P. J.; Schnick, W. $Sr[BeSi_2N_4]:Eu^{2+}/Ce^{3+}$ and $Eu[BeSi_2N_4]:$ Nontypical Luminescence in Highly Condensed Nitridoberyllsilicates. *Chem. Eur. J.* **2018**, *24*, 7243–7249.
- [8] Strobel, P.; Maak, C.; Weiler, V.; Schmidt, P. J.; Schnick, W. Ultra-Narrow-Band Blue-Emitting Oxoberyllates $AELi_2[Be_4O_6]:Eu^{2+}$ ($AE = Sr, Ba$) Paving the Way to Efficient RGB pc-LEDs. *Angew. Chem. Int. Ed.* **2018**, *57*, 8739–8743; *Angew. Chem.* **2018**, *130*, 8875–8879.

D. Supporting Information for Chapter 5

D.1 Experimental Section

Safety Assessment

Exposure to Be and Be containing compounds is known to be harmful as it can cause diseases, such as acute berylliosis, chronic beryllium disease (CBD) and cancer. While beryllium is poorly absorbed after oral and dermal exposure the inhalation of Be dusts or soluble salts is especially hazardous.^[1] To prevent possible exposure to Be all samples containing Be were handled in closed systems like gloveboxes or Schlenk-glassware.

Synthesis of $\text{Sr}_{2-x}\text{Ba}_x[\text{BeAl}_3\text{N}_5]:\text{Eu}^{2+}$ ($x = 0-2.0$)

To prevent hydrolysis or oxidation of the starting materials and products, all experiments were carried out under the exclusion of moisture and oxygen in an Ar filled glovebox (Unilab, MBraun, Garching, $\text{O}_2 < 0.1$ ppm, $\text{H}_2\text{O} < 1$ ppm) or in dry Schlenk-type glassware attached to a vacuum line (10^{-3} mbar). Argon (Air Liquide, 5.0) was dried and purified in columns filled with KOH (Merck, $\geq 85\%$), silica gel (Merck), molecular sieve (Fluka, 4 Å), P_4O_{10} (Roth, $\geq 99\%$) mixed with pumice, and titanium sponge (700 °C, Johnsen Matthey, 99.5%). The synthesis of solid solutions with the nominal composition $\text{Sr}_{2-x}\text{Ba}_x[\text{BeAl}_3\text{N}_5]:\text{Eu}^{2+}$ ($x = 0, 0.5, 1.0, 1.5, 2.0$) was carried out as described in the literature for $\text{Sr}_2[\text{BeAl}_3\text{N}_5]:\text{Eu}^{2+}$ with small modifications.^[2] The starting materials Sr_2N (Taiheiyo Cement Corp, 99+%), Ba_2N (Materion, 99.7%), AlN (abcr, grade B) and Be_3N_2 (synthesized from Be (abcr, 99+%, 325 mesh) at 1400 °C under 50 MPa N_2 atmosphere)^[3-5] were thoroughly ground in a tungsten carbide mortar and transferred into tantalum crucibles, which were then placed in a tungsten crucible. A list of chemicals and the amounts used for the synthesis are listed in Table D.1 and Table D.2.

Table D.1. List of chemicals used for the synthesis of $\text{Sr}_{2-x}\text{Ba}_x[\text{BeAl}_3\text{N}_5]:\text{Eu}^{2+}$ ($x = 0, 0.5, 1.0, 1.5$ and 2.0).

Substance	Information	Producer
AlN	grade B	ABCR
Ba ₂ N	99.7%	Materion
Be	99+%, 325 mesh	ABCR
Be ₃ N ₂	Synthesized from Be in a hot isostatic press at 1400 °C under 50 MPa N ₂ -atmosphere ^[5]	
Eu(NH ₂) ₂	Synthesized according to literature from Eu in infercritical ammonia ^[3,4]	
Sr ₂ N	99+%	Taiheiyo Cement Corp

Table D.2. Weighed starting materials for the synthesis of $\text{Sr}_{2-x}\text{Ba}_x[\text{BeAl}_3\text{N}_5]:\text{Eu}^{2+}$ ($x = 0, 0.5, 1.0, 1.5$ and 2.0) in a hot isostatic press.

Substance	$x = 0$	$x = 0.5$	$x = 1.0$	$x = 1.5$	$x = 2.0$
Sr ₂ N	189.25 mg (1.000 mmol)	141.94 mg (0.750 mmol)	94.63 mg (0.500 mmol)	47.31 mg (0.250 mmol)	-
Ba ₂ N	-	72.17 mg (0.250 mmol)	144.33 mg (0.500 mmol)	216.50 mg (0.750 mmol)	288.66 mg (1.000 mmol)
AlN	122.96 mg (3.000 mmol)				
Be ₃ N ₂	18.35 mg (0.333 mmol)				
Eu(NH ₂) ₂	ca. 2 mol% of Sr/Ba				

For doping a small amount of Eu(NH₂)₂ was added to the reaction mixture. All samples have been prepared with a 2 mol% Eu²⁺ concentration referred to Sr/Ba, unless otherwise stated in the manuscript. The tungsten crucibles were placed in a corundum crucible and transferred into a hot isostatic press (HIP, AIP6-30H, American Isostatic Presses, Inc., Columbus, Ohio, USA). The starting materials were heated with 300 °C·h⁻¹ to 1400 ($x = 0$) or 1200 °C ($x = 0.5, 1.0, 1.5, 2.0$), kept at that temperature for 2–10 h, cooled down to 500 °C in 0.5–10 h and subsequently quenched to room temperature by shutting down the furnace. During synthesis the nitrogen pressure was maintained at 50 MPa. The heterogeneous products consist of orange crystals showing luminescence and some colorless as well as dark red by-products exhibiting no luminescence, when illuminated with blue light. To reduce the amount of impurity phases the products have been washed under Ar atmosphere with a 1:2 mixture of acetic acid and isopropanol, then sedimented in isopropanol and dried under vacuum (Figure D.1). The resulting samples are sensible against moisture, therefore the dried products were stored under Ar in a glovebox or Schlenk-type glassware.



Figure D.1. Pictures of the washing steps of $\text{Sr}_2[\text{BeAl}_3\text{N}_5]:\text{Eu}^{2+}$ as an example how all samples have been handled during the washing steps. a) powder sample before the washing steps in a WC mortar, b) suspension of the product in a mixture of acetic acid/ isopropanol at daylight c) same step as in (b) irradiated with a UV-lamp, d) samples dried under vacuum, e) washed samples in a WC mortar in a glovebox.

Electron Microscopy

To investigate the morphology and the chemical composition of the synthesized samples a scanning electron microscope (SEM) NanoLab G3 (Helios), equipped with a X-Mas 80 SDD (Oxford Instruments) energy-dispersive X-ray (EDX) detector, was used. The EDX data were collected on multiple particles with an accelerating voltage of 20 kV.

Single Crystal X-Ray Diffraction

The preparation of single crystals of $\text{Ba}_2[\text{BeAl}_3\text{N}_5]:\text{Eu}^{2+}$ was conducted in a glovebox. Single crystals were isolated under a microscope and mounted on MicroMounts (MiTeGen) with an aperture size of 20–30 μm . To prevent exposure to oxygen outside the glovebox the MicroMounts were covered with clear polyester capillaries (MiTeGen), which are sealed at one end. X-ray diffraction data were obtained using a Bruker D8 Venture diffractometer with a rotating anode (Mo $K\alpha$ radiation). The program package APEX3 was used to carry out the integration and absorption correction (SADABS).^[6, 7] The crystal structure was solved using Direct Methods and refined by least-squares method (SHELX-2014) neglecting Eu^{2+} during the refinement process due to the insignificant scattering density resulting from the low content.^[8-10]

Powder X-Ray Diffraction

The collection of X-ray diffraction data was conducted with a STOE Stadi P diffractometer (parafocusing Debye–Scherrer geometry, Ge(111) monochromator, Mythen 1K detector) with Cu $K\alpha_1$ radiation ($\lambda = 1.5406 \text{ \AA}$) for $\text{Sr}_2[\text{BeAl}_3\text{N}_5]:\text{Eu}^{2+}$ or Mo $K\alpha_1$ radiation ($\lambda = 0.71073 \text{ \AA}$) for all samples containing Ba. Glass capillary (Hilgenberg, Germany) with a diameter of 0.1–0.3 mm and

wall thickness of 0.01 mm were used to seal the powder samples. Rietveld refinements were run with the TOPAS Academic 6 package, applying the fundamental parameters approach.^[11-14]

XAS and XES Measurements

X-ray absorption spectroscopy (XAS) and X-ray emission spectroscopy (XES) measurements were conducted at the REIXS beamline at the Canadian Light Source in Saskatoon, Saskatchewan, Canada.^[15] The absorption was measured in the partial fluorescence yield mode (PFY), determined by postprocessing the emission spectra collected by silicon drift detectors. The resolving power, $E/\Delta E$, for the monochromator at REIXS is 8000, which corresponds to an energy resolution value, ΔE , of 0.1 eV at N K-edge (400 eV) XAS. XAS and XES spectra were collected at room temperature with the incoming beam under 45° angle to the sample surface. The $E/\Delta E$ for the emission spectrometer at REIXS is 2000, which is equivalent to an energy resolution of 0.2 eV at 400 eV for XES. For the measurements, the powder sample was first pressed into indium foil before transferring it to the ultra-high vacuum chambers. The XAS spectrum was calibrated using an initial peak of hexagonal boron nitride (h-BN) at 402.1 eV, while the XES spectra were initially calibrated using elastic scattering peaks and then shifted further to obtain the final calibration by the same amount as the absorption spectrum was shifted with respect to the h-BN peak at 402.1 eV.^[16]

Density Functional Theory (DFT) Calculations

The ab initio density functional theory (DFT) calculations were used to calculate the band gaps, band structures, XAS and XES spectra, and partial density of states (pDOS). The calculations were carried out using the commercially available WIEN2k DFT software package.^[17, 18] This code uses Kohn-Sham methodology with spherical wave functions to model core orbitals, linearized augmented plane waves, semi-core and valence states.^[17, 18] Crystal structures of $\text{Sr}_2[\text{BeAl}_3\text{N}_5]:\text{Eu}^{2+}$ ^[2] and $\text{Ba}_2[\text{BeAl}_3\text{N}_5]:\text{Eu}^{2+}$ obtained from X-ray single crystal measurements were used as input for the calculations, neglecting the incorporated activator Eu^{2+} in the process. For the exchange-correlation functional, the Perdew-Burke-Ernzerhof variant of the generalized gradient approximation (PBE-GGA) was used.^[19, 20] To obtain a more accurate estimate of the band gaps, calculations were performed using the modified Becke-Johnson (mBJ) exchange-correlation potential.^[21] The spectra were calculated by multiplying the pDOS with the dipole transition matrix and the radial transition matrix^[22] and broadened using the combination of a Lorentzian function to mimic the core-hole lifetime broadening, and a Gaussian function to account for the instrumentation-related

broadening.^[23] Since the PBE-GGA functionals usually underestimate the band gap of semiconductors, the calculated XAS-XES spectra were rigidly shifted by a constant amount to facilitate comparison with the carefully calibrated experimental spectra.^[23] In the measurements, the XAS and XES spectra depend on the final state and for the N K-edge absorption, the final state has a core-hole in the 1s level,^[24, 25] which tends to shift spectral weight to lower energies. To account for this effect, a core hole calculation was performed for each non-equivalent N site, where $2 \times 1 \times 1$ supercell was created and one core electron (1s) was removed from the corresponding N atom in the supercell and a background lattice charge was added to the supercell to preserve charge neutrality.

Nitrogen K-edge Spectra

Soft X-ray spectroscopy and DFT calculations can elucidate the electronic structure of the materials. To get insight into the electronic structure, N K_{α} XES and 1s XAS spectra for $M_2[\text{BeAl}_3\text{N}_5]:\text{Eu}^{2+}$ ($M = \text{Sr}, \text{Ba}$) were collected. Absorption measurements were collected in the bulk sensitive partial fluorescence yield (PFY) mode and the emission measurements are divided into two types based on the excitation energy that was used. When the excitation energies are near to the absorption threshold, these emissions are referred to resonant inelastic X-ray scattering spectra (RIXS). On the other hand, when the excitation energy is well above the absorption edge, the spectrum is termed a non-resonant X-ray emission spectrum (NXES).

During RIXS measurements, the incident energy is chosen to be close to one of the absorption edges. Therefore, the changes in emission spectra are observed when the excitation energy is varied. This RIXS technique can be used to investigate whether the material has a direct or an indirect band gap. The authors in Ref.^[26, 27] state that for materials with a direct band gap, the RIXS spectrum with the highest emission energy is obtained by threshold excitation, while for a material with an indirect band gap material, the highest emission energy is obtained by excitation with a higher energy compared to the threshold excitation.

Luminescence

Luminescence measurements of single crystals were carried out on small particles in air. The data was obtained from a HORIBA Fluoromax4 spectrofluorimeter system, which was attached to an Olympus BX51 microscope (via optical fibers). The crystals were excited with blue light ($\lambda_{\text{exc}} = 450 \text{ nm}$) to capture emission spectra up to 800 nm (2 nm step size).

Thick-bed powder layers were used to obtain room and low temperature measurements. Room temperature luminescence properties were investigated with the help of an in-house-built system, consisting of a 5.3'' integrating sphere and a spectrofluorimeter equipped with a 75 W Xe lamp and a monochromator model 101 and a fiber spectrometer AvaSpec-2048 TEC-USB1.0 (Avantes). The internal quantum efficiency (IQE) of the samples was determined by comparing integrated emission and absorption intensities at excitation wavelength with BaSO₄ white standard, and SrSi₂O₂N₂:Eu²⁺ (Lumileds) reference samples.

An Ocean Optics HR2000 + ES spectrometer (2048 pixels, grating UA (200–1100 nm), slit 50) was used for luminescence measurements between 6 and 300 K. The samples were placed in an evacuated cooling chamber and the temperature was adjusted through a liquid-He compressor system (Advance Research System Inc. (ARS4HW)).

UV-Vis Spectroscopy

A UV/vis spectrophotometer (Jasco V-650) with a deuterium and a halogen lamp (JASCO, Pfungstadt, Germany, Czerny–Turner monochromator with 1200 lines/mm, concave grating, photomultiplier tube detector) was used to measure the diffuse reflectance UV-vis spectra.

D.2 Results and Discussion

Chemical analysis

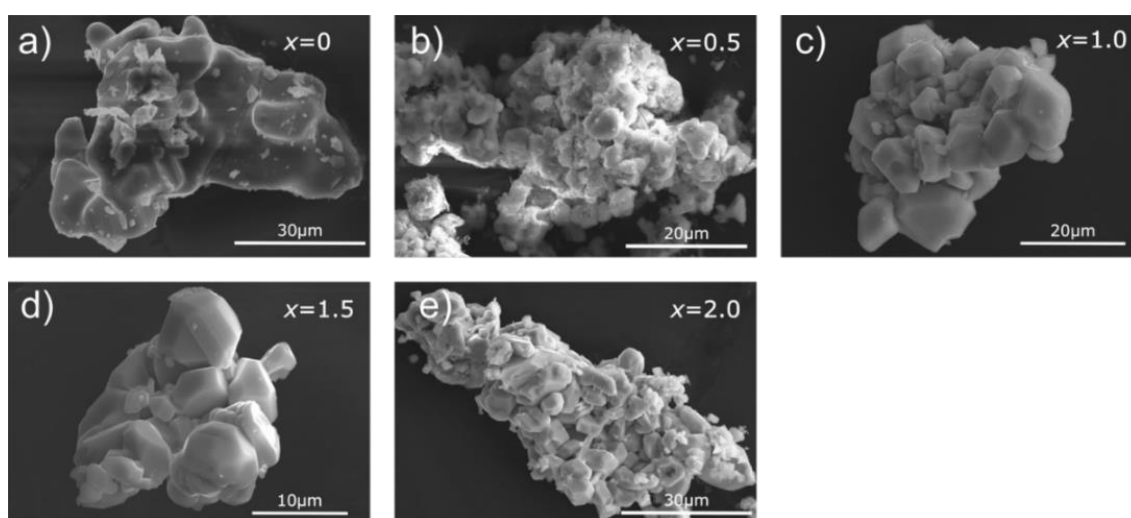


Figure D.2. Sample morphology of Sr_{2-x}Ba_x[BeAl₃N₅]:Eu²⁺ with a) $x = 0$, b) $x = 0.5$, c) $x = 1.0$, d) $x = 1.5$ and e) $x = 2.0$.

Crystal Structure

Table D.3. Detailed Crystallographic Data of $\text{Ba}_2[\text{BeAl}_3\text{N}_5]:\text{Eu}^{2+}$. Standard deviations in parentheses.

	$\text{Ba}_2[\text{BeAl}_3\text{N}_5]:\text{Eu}^{2+}$
Formula mass/ $\text{g}\cdot\text{mol}^{-1}$	434.68
Crystal system	triclinic
Space group	$P\bar{1}$ (no. 2)
Cell parameters/ \AA , $^\circ$	$a = 6.1869(10)$ $b = 7.1736(13)$ $c = 8.0391(14)$ $\alpha = 102.754(8)$ $\beta = 112.032(6)$ $\gamma = 104.765(7)$
Volume/ \AA^3	299.24(9)
Formula units/ cell	2
X-ray density/ $\text{g}\cdot\text{cm}^{-3}$	4.824
Abs. coefficient/ $\mu\cdot\text{mm}^{-1}$	13.427
F(000)	380
Crystal dimensions/ mm^3	$0.004 \times 0.003 \times 0.003$
Diffractometer	Bruker D8 Venture
Radiation	Mo $K\alpha$ ($\lambda = 0.71073 \text{\AA}$)
Temperature/ K	293(2)
Absorption correction	Multi-scan
θ range/ $^\circ$	2.92–38.28
Observed reflections	9163
Independent reflections	5720
Independent reflections with $I \geq 2\sigma(I)$	4885
Min./ max. transmission	0.847 / 1.000
Refined parameters	104
Goof	1.038
R indices ($F_0^2 \geq 2\sigma(F_0^2)$)	$R1 = 0.0354 /$ $wR2 = 0.0747$
R indices (all data)	$R1 = 0.0458 /$ $wR2 = 0.0795$
Min./ max. residual electron density/ $\text{e}\cdot\text{\AA}^{-3}$	-2.832 / 1.667

Table D.4. Atomic coordinates and equivalent isotropic displacement parameters (U_{eq}) of $Ba_2[BeAl_3N_5]:Eu^{2+}$ with standard deviations in parentheses.

Atom	Wyckoff	x	y	z	$U_{eq}/\text{\AA}^3$	sof
Ba1	2i	0.00939(5)	0.50633(4)	0.21982(4)	0.00861(6)	1
Ba2	1a	0	0	0	0.01153(8)	1
Ba3	1f	1/2	0	1/2	0.01428(8)	1
Al1	2i	0.0163(3)	0.1589(2)	0.44471(19)	0.0057(2)	1
Al2	2i	0.5766(3)	0.6982(2)	0.1074(2)	0.0060(2)	1
Al3	2i	0.5458(3)	0.4209(2)	0.35886(19)	0.0055(2)	1
N1	2i	0.2950(7)	0.3161(6)	0.4328(6)	0.0076(6)	1
N2	2i	0.4036(8)	0.4409(6)	0.1180(5)	0.0083(6)	1
N3	2i	0.3805(7)	0.8594(6)	0.0528(5)	0.0085(6)	1
N4	2i	0.0974(7)	0.1321(6)	0.6915(5)	0.0076(6)	1
N5	2i	0.7529(7)	0.2625(6)	0.3671(5)	0.0071(6)	1
Be1	2i	0.5930(11)	0.0979(9)	0.1431(9)	0.0090(9)	1

Table D.5. Anisotropic displacement parameters for $Ba_2[BeAl_3N_5]:Eu^{2+}$ with standard deviations in parentheses.

Atom	$U_{11}/\text{\AA}^2$	$U_{22}/\text{\AA}^2$	$U_{33}/\text{\AA}^2$	$U_{23}/\text{\AA}^2$	$U_{13}/\text{\AA}^2$	$U_{12}/\text{\AA}^2$
Ba1	0.00893(11)	0.00805(11)	0.00844(10)	0.00277(8)	0.00328(8)	0.00372(8)
Ba2	0.01066(16)	0.01335(17)	0.01373(16)	0.00524(13)	0.00685(13)	0.00692(13)
Ba3	0.01140(17)	0.01215(17)	0.0252(2)	0.01230(15)	0.01041(15)	0.00538(13)
Al1	0.0059(5)	0.0047(5)	0.0059(5)	0.0018(4)	0.0025(4)	0.0015(4)
Al2	0.0058(5)	0.0058(5)	0.0060(5)	0.0023(4)	0.0023(4)	0.0021(4)
Al3	0.0054(5)	0.0057(5)	0.0054(5)	0.0017(4)	0.0026(4)	0.0020(4)
N1	0.0077(14)	0.0069(14)	0.0098(14)	0.0027(12)	0.0057(12)	0.0026(12)
N2	0.0106(15)	0.0098(15)	0.0066(14)	0.0039(12)	0.0052(12)	0.0042(12)
N3	0.0089(15)	0.0085(15)	0.0068(13)	0.0023(12)	0.0025(12)	0.0035(12)
N4	0.0099(15)	0.0069(14)	0.0081(14)	0.0039(12)	0.0050(12)	0.0039(12)
N5	0.0073(14)	0.0066(14)	0.0067(13)	0.0009(11)	0.0029(11)	0.0030(11)
Be1	0.008(2)	0.007(2)	0.010(2)	0.0022(18)	0.0029(19)	0.0020(18)

Table D.6. Selected atomic distances in $Ba_2[BeAl_3N_5]:Eu^{2+}$ in \AA with standard deviations in parentheses.

Atom 1	Atom 2	Count	Distance	Atom 1	Atom 2	Count	Distance
Ba1	N3	1x	2.789(4)	Al1	N1	1x	1.854(5)
Ba1	N5	1x	2.809(5)	Al1	N5	1x	1.912(5)
Ba1	N1	1x	2.812(5)	Al1	N4	1x	1.923(5)
Ba1	N4	1x	2.844(5)	Al1	N4	1x	1.928(4)
Ba1	N5	1x	2.933(4)	Al2	N3	1x	1.882(5)
Ba1	N2	1x	2.959(6)	Al2	N4	1x	1.897(3)
Ba1	N2	1x	3.129(4)	Al2	N2	1x	1.922(5)
Ba2	N3	2x	2.719(5)	Al2	N2	1x	1.930(5)
Ba2	N4	2x	3.047(5)	Al3	N2	1x	1.859(5)
Ba2	N2	2x	3.164(4)	Al3	N1	1x	1.903(6)
Ba2	N1	2x	3.197(4)	Al3	N5	1x	1.911(6)
Ba3	N5	2x	2.789(5)	Al3	N1	1x	1.938(4)
Ba3	N1	2x	2.922(5)	Be1	N5	1x	1.657(7)
Ba3	N4	2x	3.199(4)	Be1	N3	1x	1.665(7)
Ba3	N3	2x	3.243(4)	Be1	N3	1x	1.727(10)

Table D.7. Selected angles in $\text{Ba}_2[\text{BeAl}_3\text{N}_5]:\text{Eu}^{2+}$ in $^\circ$ with standard deviations in parentheses.

Atom 1	Atom 2	Atom 3	Angle between Atoms 1-2-3
N1	Al1	N5	110.8(3)
N1	Al1	N4	112.5(2)
N1	Al1	N4	113.6(2)
N5	Al1	N4	112.3(2)
N5	Al1	N4	112.3(3)
N4	Al1	N4	94.6(2)
N3	Al2	N4	109.5(2)
N3	Al2	N2	113.9(2)
N3	Al2	N2	110.8(3)
N4	Al2	N2	119.1(2)
N4	Al2	N2	110.5(2)
N2	Al2	N2	91.7(2)
N2	Al3	N1	111.2(2)
N2	Al3	N5	110.8(2)
N2	Al3	N1	113.4(2)
N1	Al3	N5	112.4(2)
N1	Al3	N1	93.6(2)
N5	Al3	N1	114.6(2)
N5	Be1	N3	130.1(5)
N5	Be1	N3	125.9(5)
N3	Be1	N3	104.1(5)

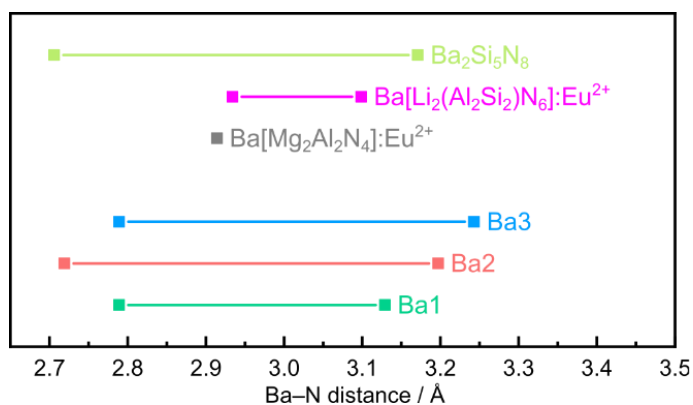
**Figure D.3.** Comparison of the interatomic distances between Ba atoms and N atoms in $\text{Ba}_2[\text{BeAl}_3\text{N}_5]$ (Ba1–N distance in green, Ba2–N in red, Ba3–N in light blue) $\text{Ba}[\text{Mg}_2\text{Al}_2\text{N}_4]:\text{Eu}^{2+}$ (gray),^[28] $\text{Ba}[\text{Li}_2(\text{Al}_2\text{Si}_2)\text{N}_6]:\text{Eu}^{2+}$,^[29] $\text{Ba}_2\text{Si}_5\text{N}_8$ (blue).^[30]

Table D.8. Data of Rietveld refinements for $\text{Sr}_{2-x}\text{Ba}_x[\text{BeAl}_3\text{N}_5]:\text{Eu}^{2+}$ ($x = 0, 0.5, 1.0, 1.5$ and 2.0) with least squares standard deviations in parentheses. Lattice parameters were refined for all samples. In addition, the occupation of the sites Sr/Ba1, Sr/Ba2 and Sr/Ba3 for samples with $x = 0.5, 1.0, 1.5$ was refined under the restriction that every site is fully occupied.

formula	$\text{Sr}_{2-x}\text{Ba}_x\text{BeAl}_3\text{N}_5:\text{Eu}^{2+}$				
x	0	0.5	1.0	1.5	2.0
Formula mass/ $\text{g}\cdot\text{mol}^{-1}$	335.23	374.25	385.78	401.89	434.645
Crystal system	triclinic				
Space group	$P\bar{1}$ (no. 2)				
Lattice parameters/ $\text{\AA}, ^\circ$	$a = 6.0740(2)$ $b = 6.9859(2)$ $c = 7.8864(2)$ $\alpha = 102.1014(8)$ $\beta = 112.6680(9)$ $\gamma = 104.1190(8)$	$a = 6.1259(1)$ $b = 7.0651(2)$ $c = 7.9688(2)$ $\alpha = 102.614(2)$ $\beta = 112.481(18)$ $\gamma = 104.222(2)$	$a = 6.1477(2)$ $b = 7.0992(2)$ $c = 7.9970(2)$ $\alpha = 102.721(2)$ $\beta = 112.376(2)$ $\gamma = 104.345(2)$	$a = 6.1685(1)$ $b = 7.1336(2)$ $c = 8.0200(2)$ $\alpha = 102.774(2)$ $\beta = 112.228(2)$ $\gamma = 104.529(2)$	$a = 6.1926(1)$ $b = 7.1772(1)$ $c = 8.0425(1)$ $\alpha = 102.7367(6)$ $\beta = 111.9943(6)$ $\gamma = 104.7907(6)$
Volume/ \AA^3	281.69(1)	289.53(1)	292.78(2)	295.92(1)	299.87(1)
Z	2				
X-ray density/ $\text{g}\cdot\text{cm}^{-3}$	3.9524(2)	4.29(1)	4.38(1)	4.52(1)	4.8136(1)
Diffractometer	Stoe StadiP				
Radiation	Cu $K\alpha_1$ $= 1.54056 \text{ \AA}$		Mo $K\alpha_1 = 0.71073 \text{ \AA}$		
Monochromator	Ge(111)				
Detector	MYTHEN 1K				
2θ -range/ $^\circ$	5–110				5–70
Data points	7035	4623	4623	4623	4623
Number of observed reflections	729	2752	2785	2815	2852
Number of parameters	87	55	42	42	45
Program used	TOPAS Academic V6				
Structure refinement	Rietveld-Method				
Background function	Shifted Chebyshev (12 polynomials)				
R_{wp}	10.252	0.9829	2.3637	2.6908	4.5328
R_{exp}	4.764	0.8230	1.3544	1.9598	2.8701
R_{p}	7.287	0.7531	1.4634	1.8596	3.3838
R_{Bragg}	5.154	0.2954	0.8910	0.8939	1.8416
χ^2	2.152	1.1942	1.7452	1.3729	1.5793

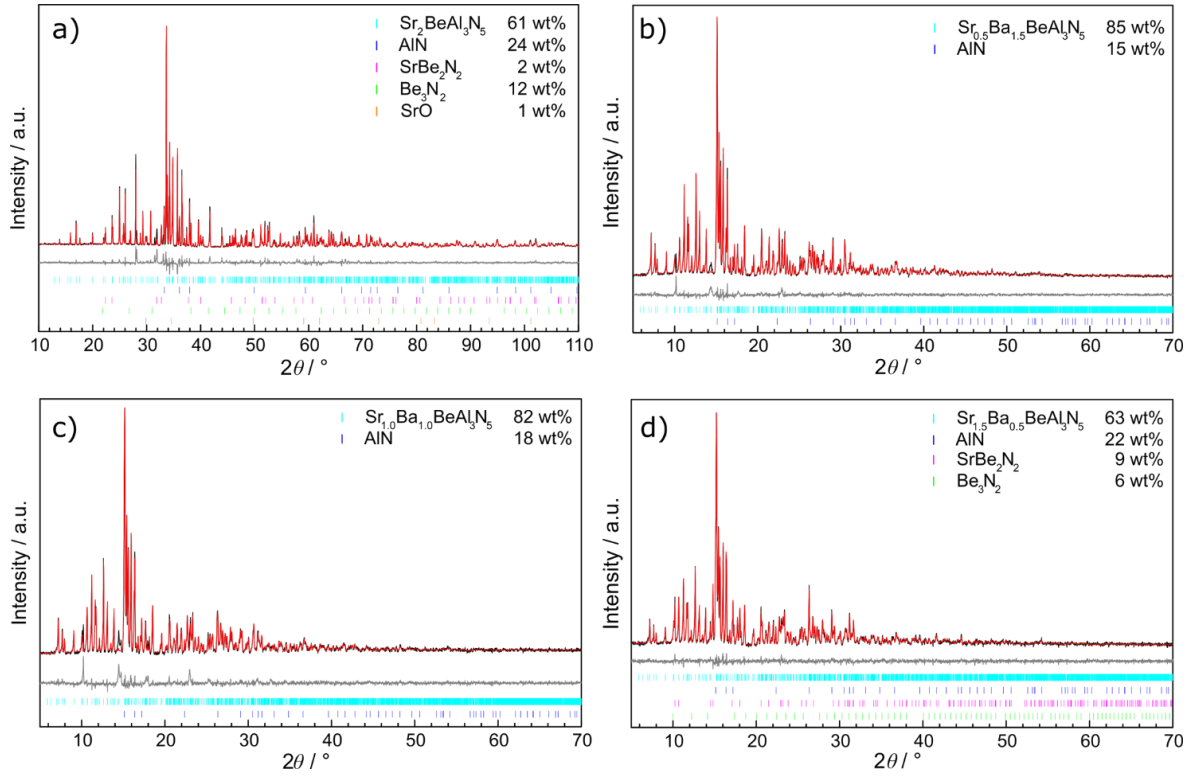


Figure D.4. Rietveld refinements of $\text{Sr}_{2-x}\text{Ba}_x[\text{BeAl}_3\text{N}_5]:\text{Eu}^{2+}$ ($x = 0, 0.5, 1.0$ and 1.5). Experimental data (black line), calculated pattern (red line) and difference curve (gray line). Tick marks: position of Bragg reflections of $\text{Sr}_{2-x}\text{Ba}_x[\text{BeAl}_3\text{N}_5]:\text{Eu}^{2+}$ ($x = 0, 0.5, 1.0$ and 1.5) (cyan), AlN (blue), SrBe_2N_2 (magenta), $\alpha\text{-Be}_3\text{N}_2$ (green), and SrO (orange). a) Rietveld refinements of $\text{Sr}_2[\text{BeAl}_3\text{N}_5]:\text{Eu}^{2+}$ ($\text{Cu K}\alpha_1 = 1.54056 \text{ \AA}$), b) Rietveld refinements of $\text{Sr}_{0.5}\text{Ba}_{1.5}[\text{BeAl}_3\text{N}_5]:\text{Eu}^{2+}$ ($\text{Mo K}\alpha = 0.71073 \text{ \AA}$), c) Rietveld refinement of $\text{Sr}_{1.0}\text{Ba}_{1.0}[\text{BeAl}_3\text{N}_5]:\text{Eu}^{2+}$ ($\text{Mo K}\alpha = 0.71073 \text{ \AA}$), d) Rietveld refinement of $\text{Sr}_{1.5}\text{Ba}_{0.5}[\text{BeAl}_3\text{N}_5]:\text{Eu}^{2+}$ ($\text{Mo K}\alpha = 0.71073 \text{ \AA}$).

Table D.9. Selected atomic distances in $\text{Sr}_{2-x}\text{Ba}_x[\text{BeAl}_3\text{N}_5]:\text{Eu}^{2+}$ ($x = 0.5, 1.0$ and 1.5) in Å with standard deviations in parentheses obtained from Rietveld refinements.

$x = 0.5$				$x = 1.0$				$x = 1.5$			
Atom 1	Atom 2	Count	Distance	Atom 1	Atom 2	Count	Distance	Atom 1	Atom 2	Count	Distance
Sr1 Ba1	N1	1x	2.6895(239)	Sr1 Ba1	N5	1x	2.5872(386)	Sr1 Ba1	N3	1x	2.6404(141)
Sr1 Ba1	N3	1x	2.7304(156)	Sr1 Ba1	N3	1x	2.6005(206)	Sr1 Ba1	N5	1x	2.6505(266)
Sr1 Ba1	N4	1x	2.7406(224)	Sr1 Ba1	N4	1x	2.7279(317)	Sr1 Ba1	N1	1x	2.7496(207)
Sr1 Ba1	N5	1x	2.7826(304)	Sr1 Ba1	N1	1x	2.7839(337)	Sr1 Ba1	N4	1x	2.7596(223)
Sr1 Ba1	N5	1x	2.8154(203)	Sr1 Ba1	N5	1x	2.9113(282)	Sr1 Ba1	N5	1x	2.8964(208)
Sr1 Ba1	N2	1x	2.9226(282)	Sr1 Ba1	N2	1x	2.9528(361)	Sr1 Ba1	N2	1x	2.9457(213)
Sr1 Ba1	N2	1x	3.0763(221)	Sr1 Ba1	N2	1x	3.0963(292)	Sr1 Ba1	N2	1x	3.1288(178)
Sr2 Ba2	N3	2x	2.6042(257)	Sr2 Ba2	N3	2x	2.6186(333)	Sr2 Ba2	N3	2x	2.6712(217)
Sr2 Ba2	N4	2x	2.9815(259)	Sr2 Ba2	N1	2x	2.9769(244)	Sr2 Ba2	N2	2x	3.0998(178)
Sr2 Ba2	N2	2x	3.1180(194)	Sr2 Ba2	N2	2x	3.0779(257)	Sr2 Ba2	N1	2x	3.1144(178)
Sr2 Ba2	N1	2x	3.1520(186)	Sr2 Ba2	N4	2x	3.0898(355)	Sr2 Ba2	N4	2x	3.1278(197)
Sr3 Ba3	N5	2x	2.7309(298)	Sr3 Ba3	N1	2x	2.7977(339)	Sr3 Ba3	N1	2x	2.9141(197)
Sr3 Ba3	N1	2x	2.9191(244)	Sr3 Ba3	N5	2x	2.9546(379)	Sr3 Ba3	N5	2x	2.9217(257)
Sr3 Ba3	N3	2x	3.1763(235)	Sr3 Ba3	N4	2x	3.1664(276)	Sr3 Ba3	N4	2x	3.1903(167)
Sr3 Ba3	N4	2x	3.2034(164)	Sr3 Ba3	N3	2x	3.3547(311)	Sr3 Ba3	N3	2x	3.3386(159)

Electronic Properties

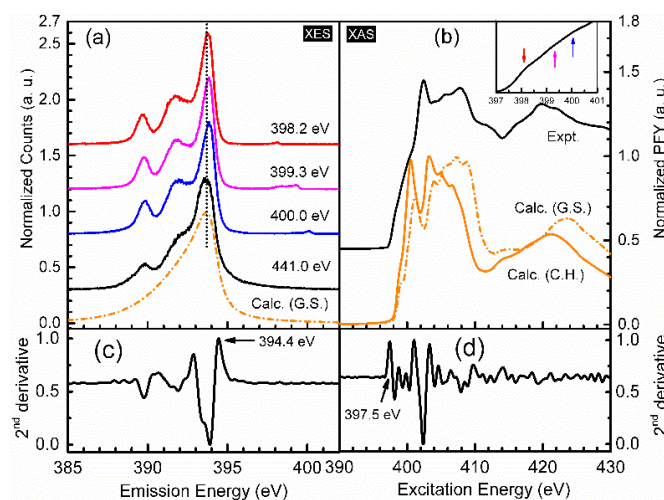


Figure D.5. N K-edge XAS and XES spectra of $\text{Ba}_2[\text{BeAl}_3\text{N}_5]:\text{Eu}^{2+}$. The XES (a) and XAS (b) spectra are shown alongside DFT calculations. The calculated ground state (Calc. G.S.) and excited state (Calc. C.H.) XAS spectra are shown as dash-dotted orange and solid orange lines, respectively. The vertical dotted black line in (a) is used to guide the eye in finding the highest emission energy among the RIXS spectra. The second derivatives of the experimental NXES spectrum excited at 441.0 eV and the XAS spectrum are shown in panel (c) and (d), respectively.

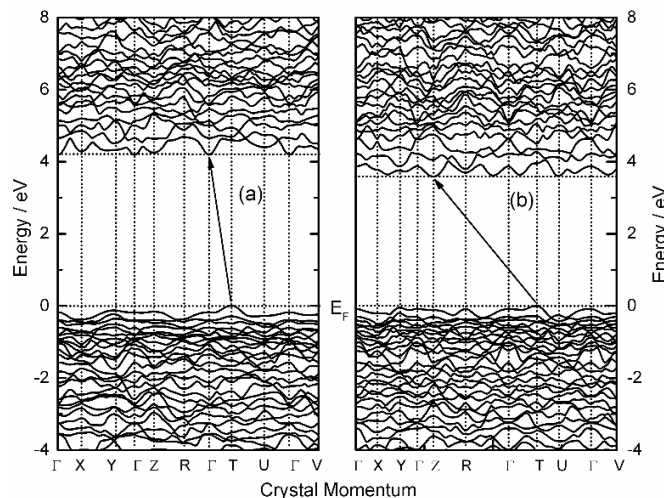


Figure D.6. Calculated band structure of a) $\text{Sr}_2[\text{BeAl}_3\text{N}_5]$ and b) $\text{Ba}_2[\text{BeAl}_3\text{N}_5]$ based on ground state mBJ exchange-correlation potential calculations. Energy scale is set with respect to the Fermi energy (E_F). The black arrow indicates the transition between the valence band maximum and the conduction band minimum. Both samples show an indirect band gap.

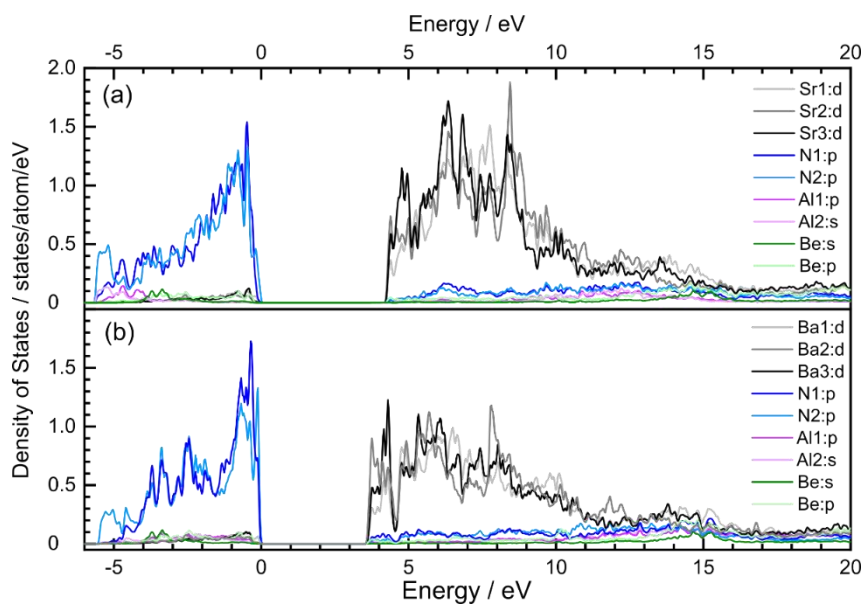


Figure D.7. Calculated partial density of states of a) $\text{Sr}_2[\text{BeAl}_3\text{N}_5]$ and b) $\text{Ba}_2[\text{BeAl}_3\text{N}_5]$ using the mBJ exchange-correlation potential. The energy zero is taken at the Fermi level.

UV-vis Spectroscopy

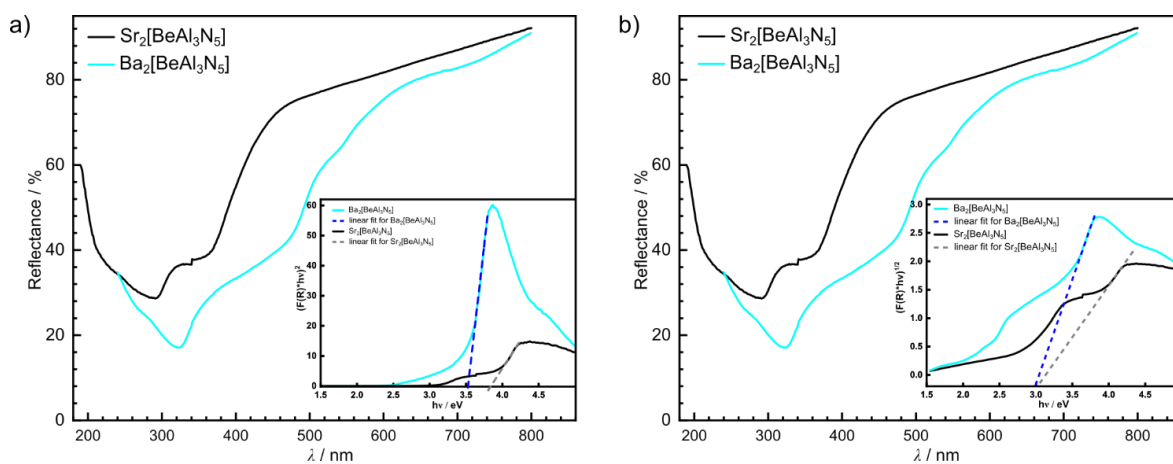


Figure D.8. Diffuse reflectance UV-Vis spectra of undoped $\text{Sr}_2[\text{BeAl}_3\text{N}_5]$ (black) and $\text{Ba}_2[\text{BeAl}_3\text{N}_5]$ (cyan) with insets of the respective Tauc plots for a) direct and b) indirect band gaps. The artifacts in the UV-Vis spectra around 340 nm correspond to the lamp-switch.

Luminescence

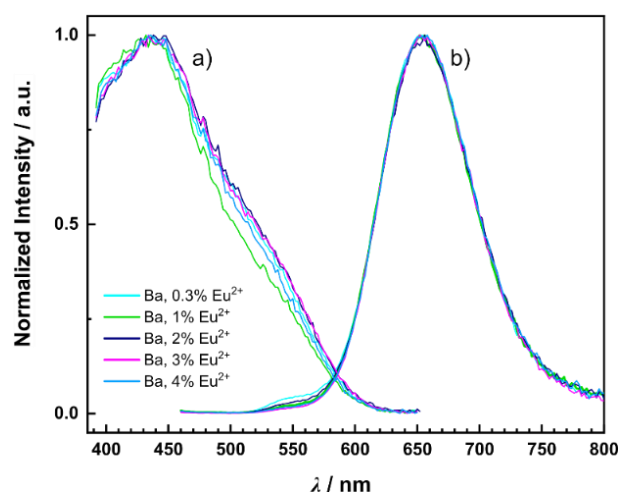


Figure D.9. Normalized photoluminescence spectra of bulk samples of $\text{Ba}_2[\text{BeAl}_3\text{N}_5]:\text{Eu}^{2+}$ with 0.3 mol% (cyan), 1 mol% (green), 2 mol% (dark blue), 3 mol% (magenta) and 4 mol% (light blue) Eu^{2+} concentration referred to Ba. a) Excitation spectra ($\lambda_{\text{obs}} = 668\text{--}672\text{ nm}$); b) Emission spectra ($\lambda_{\text{exc}} = 440\text{ nm}$).

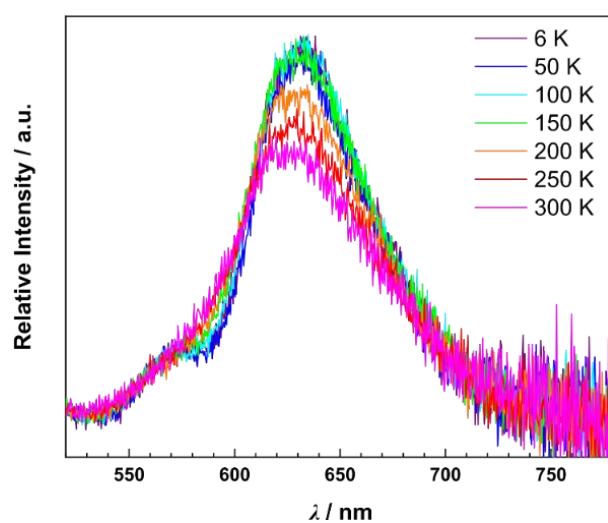


Figure D.10. Relative photoluminescence spectra of a powder sample of $\text{Sr}_{2-x}\text{Ba}_x[\text{BeAl}_3\text{N}_5]:\text{Eu}^{2+}$ with $x = 0.5$ at different temperatures from 6–300 K ($\lambda_{\text{exc}} = 450\text{ nm}$).

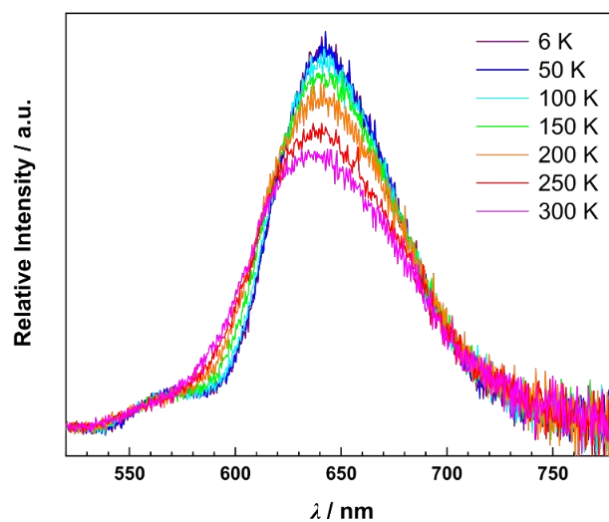


Figure D.11. Relative photoluminescence spectra of a powder sample of $\text{Sr}_{2-x}\text{Ba}_x[\text{BeAl}_3\text{N}_5]:\text{Eu}^{2+}$ with $x = 1.0$ at different temperatures from 6–300 K ($\lambda_{\text{exc}} = 450$ nm).

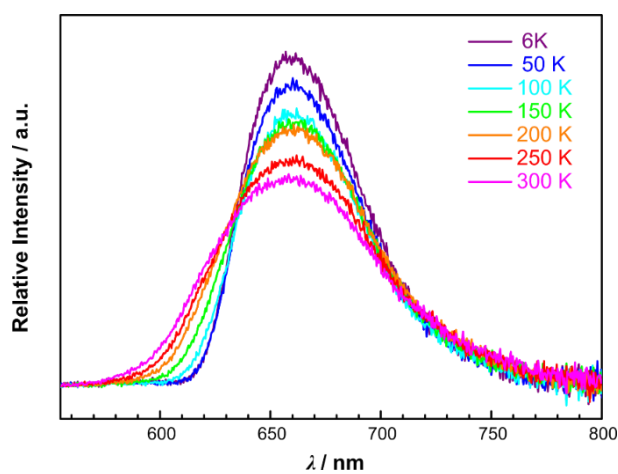


Figure D.12. Relative photoluminescence spectra of a powder sample of $\text{Ba}_2[\text{BeAl}_3\text{N}_5]:\text{Eu}^{2+}$ ($\lambda_{\text{exc}} = 380$ nm) at different temperatures from 6–300 K ($\lambda_{\text{exc}} = 450$ nm).

D.3 Author Contributions

E.E. Formal analysis: Lead; Investigation: Lead; Validation: Lead; Visualization: Lead; Writing – original draft: Lead; Writing – review & editing: Lead

P.S. Formal analysis: Supporting; Investigation: Supporting; Validation: Supporting; Writing – original draft: Supporting; Writing – review & editing: Supporting

V.W. Formal analysis: Supporting; Investigation: Supporting; Validation: Supporting; Writing – review & editing: Supporting

M.A. Conceptualization: Supporting; Investigation: Supporting; Validation: Supporting; Writing – original draft: Supporting; Writing – review & editing: Supporting

P.S. Conceptualization: Supporting; Funding acquisition: Equal; Investigation: Supporting; Methodology: Supporting; Project administration: Supporting; Resources: Supporting; Supervision: Supporting; Validation: Supporting; Writing –original draft: Supporting; Writing – review & editing: Supporting

A.M. Conceptualization: Supporting; Formal analysis: Supporting; Funding acquisition: Supporting; Methodology: Supporting; Project administration: Supporting; Resources: Supporting; Supervision: Supporting; Validation: Supporting; Writing – original draft: Supporting; Writing – review & editing: Supporting

W.S. Conceptualization: Equal; Funding acquisition: Lead; Project administration: Lead; Resources: Lead; Supervision: Lead; Validation: Supporting; Writing – original draft: Supporting; Writing – review & editing: Supporting

D.4 References

- [1] Kumberger, O.; Schmidbauer, H. Warum ist Beryllium so toxisch? *Chem. Unserer Zeit* **1993**, *27*, 310–316.
- [2] Elzer, E.; Strobel, P.; Weiler, V.; Schmidt, P. J.; Schnick, W. Illuminating Nitridoberyllaluminates: The Highly Efficient Red-Emitting Phosphor $\text{Sr}_2[\text{BeAl}_3\text{N}_5]:\text{Eu}^{2+}$. *Chem. Mater.* **2020**, *32*, 6611–6617.
- [3] Zeuner, M.; Hintze, F.; Schnick, W. Low temperature precursor route for highly efficient spherically shaped LED-phosphors $\text{M}_2\text{Si}_5\text{N}_8:\text{Eu}^{2+}$ (M = Eu, Sr, Ba). *Chem. Mater.* **2009**, *21*, 336–342.
- [4] Senker, J.; Jacobs, H.; Müller, M.; Press, W.; Müller, P.; Mayer, H.; Ibberson, R. Reorientational dynamics of amide ions in isotopic phases of strontium and calcium amide. 1. Neutron diffraction experiments. *J. Phys. Chem. B* **1998**, *102*, 931–940.
- [5] García-Gutiérrez, R.; Barboza-Flores, M.; Berman-Mendoza, D.; Contreras-López, O. E.; Ramos-Carrasco, A. Synthesis and characterization of highly luminescent beryllium nitride. *Mater. Lett.* **2014**, *132*, 179–181.
- [6] BrukerAXS APEX3, version 2018.1-0.; 2018.
- [7] Sheldrick, G. M. *SADABS, Multi-Scan Absorption Correction*, Bruker AXS, version 2; Madison, WI, USA, 2012.
- [8] Sheldrick, G. M. Crystal structure refinement with SHELXL. *Acta Crystallogr., Sect. C: Struct. Chem.* **2015**, *71*, 3–8.
- [9] Sheldrick, G. M. SHELXS-97: A Program for Crystal structure solution. University of Göttingen, Germany, 1997.
- [10] Sheldrick, G. M. SHELXL-97: A Program for Crystal structure refinement. University of Göttingen, Germany, 1997.
- [11] Coelho, A. A. *TOPAS: A Program for Rietveld Refinement*, version 6; 2016.
- [12] Cheary, R. W.; Coelho, A. A.; Cline, J. P. Fundamental Parameters Line Profile Fitting in Laboratory Diffractometers. *J. Res. Natl. Inst. Stand. Technol.* **2004**, *109*, 1–25.
- [13] Bergmann, J.; Kleeberg, R.; Haase, A.; Breidenstein, B. In *Advanced Fundamental Parameters Model for Improved Profile Analysis*, Materials Science Forum, Trans Tech Publications: 2000; pp 303–308.
- [14] Rietveld, H. M. A profile refinement method for nuclear and magnetic structures. *J. Appl. Crystallogr.* **1969**, *2*, 65–71.
- [15] Boots, M.; Muir, D.; Moewes, A. Optimizing and Characterizing Grating Efficiency for a Soft X-ray Emission Spectrometer. *J. Syn. Rad.* **2013**, *20*, 272–285.
- [16] Amin, M. R.; de Boer, T.; Becker, P.; Hertrampf, J.; Niewa, R.; Moewes, A. Bandgap and Electronic Structure Determination of Oxygen-Containing Ammonothermal InN: Experiment and Theory. *J. Phys. Chem. C* **2019**, *123*, 8943–8950.
- [17] Schwarz, K.; Blaha, P.; Madsen, G. K. Electronic Structure Calculations of Solids Using the WIEN2k Package for Material Sciences. *Comput. Phys. Commun* **2002**, *147*, 71–76.
- [18] Schwarz, K.; Blaha, P. Solid State Calculations Using WIEN2k. *Comput. Mater. Sci.* **2003**, *28*, 259–273.
- [19] Perdew, J. P.; Burke, K.; Ernzerhof, M. Generalized Gradient Approximation Made Simple. *Phys. Rev. Lett.* **1996**, *77*, 3865–3868.
- [20] Perdew, J. P.; Burke, K.; Ernzerhof, M. Generalized Gradient Approximation Made Simple [Phys. Rev. Lett. 77, 3865 (1996)]. *Phys. Rev. Lett.* **1997**, *78*, 1396–1396.

-
- [21] Tran, F.; Blaha, P. Accurate Band Gaps of Semiconductors and Insulators with a Semilocal Exchange-Correlation Potential. *Phys. Rev. Lett.* **2009**, *102*, 226401.
- [22] Schwarz, K.; Neckel, A.; Nordgren, J. On the X-ray Emission Spectra from FeAl. *J. Phys. F: Metal Phys.* **1979**, *9*, 2509–2521.
- [23] McLeod, J.; Green, R.; Kurmaev, E.; Kumada, N.; Belik, A.; Moewes, A. Band-gap Engineering in TiO₂-based Ternary Oxides. *Phys. Rev. B* **2012**, *85*, 195201.
- [24] Mahan, G. Final-state Potential in X-ray Spectra. *Phys. Rev. B* **1980**, *21*, 1421–1431.
- [25] von Barth, U.; Grossmann, G. Dynamical Effects in X-ray Spectra and the Final-State Rule. *Phys. Rev. B* **1982**, *25*, 5150–5179.
- [26] Green, R.; Regier, T.; Leedahl, B.; McLeod, J.; Xu, X.; Chang, G.; Kurmaev, E.; Moewes, A. Adjacent Fe-Vacancy Interactions as the Origin of Room Temperature Ferromagnetism in (In_{1-x}Fe_x)₂O₃. *Phys. Rev. Lett.* **2015**, *115*, 167401.
- [27] Eisebitt, S.; Eberhardt, W. Band Structure Information and Resonant Inelastic Soft X-ray Scattering in Broad Band Solids. *J. Electron Spectrosc. Relat. Phenom.* **2000**, *110*, 335–358.
- [28] Pust, P.; Hintze, F.; Hecht, C.; Weiler, V.; Locher, A.; Zitnanska, D.; Harm, S.; Wiechert, D.; Schmidt, P. J.; Schnick, W. Group (III) Nitrides M[Mg₂Al₂N₄] (M = Ca, Sr, Ba, Eu) and Ba[Mg₂Ga₂N₄] — Structural Relation and Nontypical Luminescence Properties of Eu²⁺ Doped Samples. *Chem. Mater.* **2014**, *26*, 6113–6119.
- [29] Strobel, P.; Schmiechen, S.; Siegert, M.; Tücks, A.; Schmidt, P. J.; Schnick, W. Narrow-Band Green Emitting Nitridolithoalumosilicate Ba[Li₂(Al₂Si₂)N₆]:Eu²⁺ with Framework Topology whj for LED/ LCD-Backlighting Applications. *Chem. Mater.* **2015**, *27*, 6109–6115.
- [30] Schlieper, T.; Milius, W.; Schnick, W. Hochtemperatur-Synthesen und Kristallstrukturen von Sr₂Si₅N₈ und Ba₂Si₅N₈. *Z. Anorg. Allg. Chem.* **1995**, *621*, 1380–1384.

E. Miscellaneous

E.1 List of Publications

The following list contains all publications of this thesis in chronological order, including authors, citations, and author contributions.

1. $M\text{Be}_{20}\text{N}_{14}:\text{Eu}^{2+}$ ($M = \text{Sr}, \text{Ba}$): Highly Condensed Nitridoberyllates with Exceptional Highly Energetic Eu^{2+} Luminescence

Eugenia Elzer, Robin Niklaus, Philipp J. Strobel, Volker Weiler, Peter J. Schmidt, and Wolfgang Schnick

Chem. Mater. **2019**, *31*, 3174–3182

DOI: 10.1021/acs.chemmater.8b05133

Conceptualization, syntheses and formal analyses were performed by Eugenia Elzer. DFT calculations and the interpretation of the results were carried out by Robin Niklaus. Philipp Strobel and Volker Weiler conducted the luminescence measurements, while Philipp Strobel and Peter J. Schmidt helped with the interpretation of the luminescence data. Wolfgang Schnick supervised the project. Eugenia Elzer wrote the manuscript, except for the part regarding DFT calculations and the discussion of the electronic properties, which was written by Robin Niklaus. All authors contributed to the discussion of the results and the revision of the manuscript.

2. Illuminating Nitridoberylloaluminates: The Highly Efficient Red-Emitting Phosphor $\text{Sr}_2[\text{BeAl}_3\text{N}_5]:\text{Eu}^{2+}$

Eugenia Elzer, Philipp Strobel, Volker Weiler, Peter J. Schmidt, and Wolfgang Schnick

Chem. Mater. **2020**, *32*, 6611–6617

DOI: 10.1021/acs.chemmater.0c02037

Conceptualization, syntheses, and formal analyses were done by Eugenia Elzer. Philipp Strobel and Volker Weiler carried out the measurements of luminescence properties. Philipp Strobel and Peter J. Schmidt supported with the interpretation of the luminescence data. Wolfgang Schnick supervised the work. The manuscript was written by Eugenia Elzer. All authors contributed to the discussion of the results and revised the manuscript

3. $\text{Eu}_3\text{Be}_{22}\text{N}_{16}\text{O}$: A Highly Condensed Oxonitridoberyllate

Eugenia Elzer, Martin Weidemann, and Wolfgang Schnick

Eur. J. Inorg. Chem. **2021**, 4979

DOI: 10.1002/ejic.202100807

Conceptualization, synthesis, analysis and composition of the manuscript was done by Eugenia Elzer. Martin Weidemann carried out the magnetization measurements and helped with the interpretation of the obtained data. Wolfgang Schnick supervised the project. The manuscript was written by Eugenia Elzer. All authors contributed to the discussion of the results and revised the manuscript.

4. Inverse-Tunable Red Luminescence and Electronic Properties of Nitridoberylloaluminates $\text{Sr}_{2-x}\text{Ba}_x[\text{BeAl}_3\text{N}_5]:\text{Eu}^{2+}$ ($x = 0-2$)

Eugenia Elzer, Philipp Strobel, Volker Weiler, Muhammad R. Amin, Peter J. Schmidt, Alexander Moewes, Wolfgang Schnick

Chem. Eur. J. **2022**, e202104121

DOI: 10.1002/chem.202104121

Conceptualization of the project, syntheses and formal analyses were performed by Eugenia Elzer. Philipp Strobel and Volker Weiler carried out luminescence measurements and helped – supported by Peter J. Schmidt - with the interpretation of the data. Muhammad R. Amin and Alexander Moewes executed the collection and interpretation of the soft X-ray spectroscopy data. The manuscript was written by Eugenia Elzer, except for the electronic properties part, which was written by Muhammad R. Amin. Wolfgang Schnick directed and supervised the work. All authors contributed to the discussion of the results and revised the manuscript.

E.2 Publications beyond this Thesis

The following list contains the publications beyond this thesis in chronological order.

1. Unraveling the Energy Levels of Eu^{2+} Ions in $M\text{Be}_{20}\text{N}_{14}:\text{Eu}^{2+}$ ($M = \text{Sr}, \text{Ba}$) Phosphors

Muhammad R. Amin, **Eugenia Elzer**, Wolfgang Schnick, Alexander Moewes

J. Phys. Chem. C **2021**, 125, 11828

DOI: 10.1021/acs.jpcc.1c01085

E.3 Conference Contributions and Presentations

How to publish – and what to do with a “do not publish”

***Eugenia Elzer** and Wolfgang Schnick*

Talk, Seminar Schnick Group, **2022**, Munich, Germany

Das Glühwürmchen-Thema

***Eugenia Elzer** and Wolfgang Schnick*

Talk, Seminar Schnick Group, **2021**, Munich, Germany

Ein leuchtendes Nitridoberylloaluminat

***Eugenia Elzer** and Wolfgang Schnick*

Talk, 5. Obergurgl-Seminar Festkörperchemie, **2020**, Obergurgl, Austria

Nitridoberyllate und Nitrido(beryllo)aluminat

***Eugenia Elzer** and Wolfgang Schnick*

Talk, Seminar Schnick Group, **2019**, Munich, Germany

$MBe_{20}N_{14}:Eu^{2+}$ – hochkondensiert und leuchtend

***Eugenia Elzer** and Wolfgang Schnick*

Talk, 4. Obergurgl-Seminar Festkörperchemie, **2019**, Obergurgl, Austria

Von A nach B nach X

***Eugenia Elzer** and Wolfgang Schnick*

Talk, Seminar Schnick Group, **2018**, Munich, Germany

E.4 Deposited Crystallographic Data

The Crystallographic Information Files (CIFs) of compounds discussed in this thesis can be accessed free of charge at the joint Cambridge Crystallographic Data Centre (Cambridge, United Kingdom) and Fachinformationszentrum Karlsruhe (Germany) online deposition service by quoting the corresponding deposition number.

Table 1: List of compound introduced in this thesis with the corresponding deposition numbers.

Compound	CSD
$\text{SrBe}_{20}\text{N}_{14}$	1883227
$\text{BaBe}_{20}\text{N}_{14}$	1883228
$\text{EuBe}_{20}\text{N}_{14}$	1883229
$\text{Sr}_2[\text{BeAl}_3\text{N}_5]$	2002561
$\text{Eu}_3\text{Be}_{22}\text{N}_{16}\text{O}$	2104949
$\text{Ba}_2[\text{BeAl}_3\text{N}_5]$	2121521

E.5 Curriculum Vitae

Eugenia Elzer

December 25th, 1990

Kustanaj, Kazakhstan

Education:

- 05/2021 **PhD Thesis:** *Nitridoberyllates and Nitridoberylloaluminates for Solid-State Lighting*, Ludwig-Maximilians-Universität München, Germany (Prof. Dr. W. Schnick)
- Since 07/2017 PhD studies and research assistant, Ludwig-Maximilians-Universität München, Germany (Prof. Dr. W. Schnick)
- 05/2017 **Master Thesis:** *Synthese und Charakterisierung einer Ordnungsvariant des Ca[LiAlN₂]-Typs und neue Synthesestrategie zu quaternären Nitridomagnesogermanaten*, Ludwig-Maximilians-Universität München, Germany (Prof. Dr. W. Schnick)
- 10/2013-05/2017 Master of Science in Chemistry Ludwig-Maximilians-Universität München, Germany
- 09/2013 **Bachelor Thesis:** *Versuche zur Darstellung der Nitridogallate „Sr₂Ga₃MgN₅:Eu²⁺“ und „CaGaMg₂N₃“ unter Hochdruck-Hochtemperatur-Bedingungen sowie Optimierung der Synthese von „CaGaMg₂N₃:Eu²⁺“, Ludwig-Maximilians-Universität München, Germany (Prof. Dr. W. Schnick)*
- 09/2011-09/2013 Bachelor of Science in Chemistry and Biochemistry, Ludwig-Maximilians-Universität München, Germany
- 05/2011 Allgemeine Hochschulreife, Hildegardis-Gymnasium Kempten, Germany

